A STATE DYNAMICS METHOD FOR INTEGRATED GPS/INS NAVIGATION AND ITS APPLICATION TO AIRCRAFT PRECISION APPROACH

BY

FANG-CHENG CHAN

Submitted in partial fulfillment of the
requirements for the degree of
Doctor of Philosophy in Mechanical and Aerospace Engineering
in the Graduate College of the
Illinois Institute of Technology

Approved _____
Adviser

Chicago, Illinois
May 2008

ACKNOWLEDGEMENT

I would like to thank my advisor, Professor Boris Pervan, for giving me the opportunity and support to pursue this research. His intellectual advice, technical insight and clear guidance, not only in GPS and inertial navigation, but also in general academic research, have made this thesis possible and will benefit my career for life. Especially his patient and precious time spent on giving me recommendation while I was working on this research. I can't say thanks enough to him. I learned a great deal of inertial navigation from Professor Demoz Gebre-Egziabher's dissertation. His valuable and beneficial recommendations are very much appreciated. I would also like to thank my defense and reading committees, Professor Sudhakar Nair, Professor John Kallend and Professor Xiaoping Qian for their valuable advice on this dissertation.

I would like to thank all my colleagues in the Navigation and Guidance Lab, Livio Gratton, Mathieu Joerger, Samer Khanafseh and Steven Langel for their helpful assistance and advantageous discussion during the time of my research, and constructive comments while tirelessly reviewing this lengthy dissertation. I would also like to express my appreciation to the Federal Aviation Administration (FAA) for sponsoring my research, and people working in FAA William J. Hughes Technical Center for providing valuable flight data.

Finally, I would like to thank all my family members and friends in Taiwan as well as in US for their encouragement and supports during my journey of pursuing Ph.D degree. Especially thank my parents, Yi-Ming and Hsiao-Yin Chan, and my elder brothers, Fang-Guan, Fang-Wei and Fang-Hsin Chan, for their unlimited support both on financial and emotional. I dedicate this dissertation to them, my dear family.

TABLE OF CONTENT

LIST OF TABLES

LIST OF FIGURES

LIST OF SYMBOLS

Symbol	Definition
ρ_k^i	code-phase range measurement between receiver antenna phase center and satellite *i* at time epoch *k*
r_k^i	true or geometric range between receiver antenna phase center and satellite *i* at time epoch *k*
${}_{clk}\tau_k^r$	receiver clock offset from nominal GPS time at time epoch *k*
${}_{clk}\tau_k^i$	satellite *i* clock offset from nominal GPS time at time epoch *k*
I_k^i	ionospheric delay for satellite *i* at time epoch *k*
T_k^i	tropospheric delay for satellite *i* at time epoch *k*
$v_{\rho_k}^{\ i}$	code-phase measurement error primarily due to the multipath and receiver noise
λ	the carrier wavelength
ϕ_k^i	carrier-phase range measurement
N^i	unknown constant integer ambiguity for satellite *i* in cycles
$v_{\phi_k}^{\ i}$	carrier-phase measurement error due to the multipath and receiver noise
Δ	single difference operation
$\Delta\tau_k^{clk}$	clock offset between reference and user GPS receivers
Δn^i	local refraction index decorrelation
ΔV_{ig}^i	vertical ionospheric gradient
$\vec{V}_e^n$	a relative velocity expressed in *n* frame

$\vec{f}$	specific force
$\vec{w}$	rotation measurement
$\vec{E}$	attitude
$\vec{B}_g$	gyroscope measurement bias
$\vec{B}_a$	accelerometer measurement bias
$\vec{g}$	gravity vector
S_f	IMU scale factor
M_{is}	IMU mis-alignment

ABSTRACT

In recent years, GPS navigation systems have found widespread use in many diverse applications. The achievements of GPS navigation systems in positioning and navigation services have been nothing short of extraordinary. With the use of carrier phase measurements and Differential GPS (DGPS), centimeter-level performance is achievable today. Therefore, the principal issues for modern navigation are not related to accuracy per se, but *robustness*. Unfortunately in this regard, all radionavigation systems are subject to Radio Frequency Interference (RFI). In response, this research is focused on the development of interference-robust navigation systems for aviation applications.

A new dual-frequency Carrier-phase DGPS (CDGPS) architecture has been developed in this research and its performance was evaluated relative to the requirements for a unique shipboard landing application. RFI vulnerability was addressed for this application by directly incorporating a single frequency architecture as a back-up in the event of hostile jamming on one frequency.

For critical civil aviation applications without access to dual frequency GPS signals, a novel method for tightly-coupling GPS and Inertial Navigation Sensors (INS) was developed to address the signal vulnerability issue. The new hybrid navigation system, based on the direct fusion of GPS and INS using state dynamics, is a mathematically rigorous approach, yet it is more direct and simpler to implement than existing GPS/INS integration schemes. The hybrid navigation system was validated with flight data, and predicted system performance was evaluated using a covariance analysis method. Necessary conditions on INS sensor and gravity model quality were derived to

ensure that the hybrid system performance is compliant with navigation requirements for aircraft precision approach and landing.

In addition, a new fault detection algorithm, based on integrated Kalman filter innovations, was developed and evaluated against other existing GPS fault detection methods and radar altimeter detection technique. It is shown that the new algorithm outperforms existing methods in the detection of slowly developing ranging errors, such as those caused by ionospheric and tropospheric anomalies. It is also demonstrated that the radar detection technique can provide a significant benefit to navigation system integrity.

CHAPTER 1

INTRODUCTION

The Global Positioning System (GPS) has become a widespread technology since it was declared fully operational in 1995. There is a large diversity of GPS-based applications such as land surveying, Geographical Information System (GIS), ship navigation, Intelligent Transportation Systems (ITS), precision agriculture, and in the near future, aircraft precision approach and landing. Its unlimited user capacity and worldwide applicability ensure that the system will be the basis of modern civil navigation throughout the 21st century.

Differential GPS (DGPS) can provide 10 times more accurate position information than standard GPS to fulfill more demanding applications. Moreover, the ultimate in GPS positioning accuracy can be obtained by using highly precise differential carrier-phase measurements. With carrier-phase measurements, centimeter-level navigation performance is possible when the associated integer cycle ambiguities are correctly resolved.

Given that GPS can provide centimeter-level performance today, the principal issues for modern navigation are not related to accuracy per se, but *robustness*. Unfortunately, all radio wave navigation systems are subject to Radio Frequency Interference (RFI). In response, this research is focused on the development of a robust navigation system for aviation applications that is immune to RFI during the most critical stage of the application. The robustness of this system is achieved by integration of inertial navigation sensors with carrier phase DGPS.

1.1 Background

1.1.1 GPS Overview. GPS is a passive, satellite-based, radio wave ranging system. The GPS satellite nominal constellation, illustrated in Figure 1.1, consists of 24 spacecraft in nearly circular, half-synchronous (11.97 hr period) orbits. The satellites are distributed among six orbital planes that are inclined at 55 degrees and separated by 60 degrees ascending node increments. Each plane contains four satellites whose nominal phasing (mean anomaly) within each plane has been selected to minimize the impact of a single satellite failure [Misra01].

GPS satellites transmit radio ranging code signals along with navigation data at two different frequencies in the L band (frequencies between 1-2G Hz): one is centered at 1575.42 MHz called Link 1 (L1) and the other is centered at 1227.6 MHz called Link 2 (L2). Although the accessible GPS signals to civilian applications are limited to L1

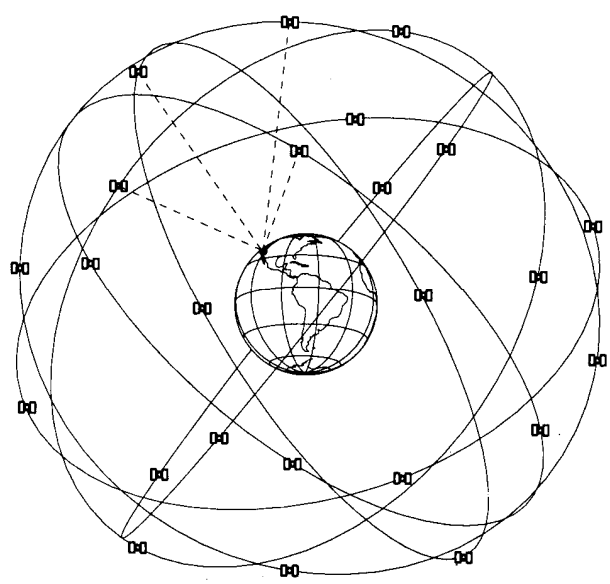

Figure 1.1. GPS Constellation

ranging code and carrier, in the near future modernized Block IIR-M/IIF GPS satellites will broadcast civil GPS signals at the L2 frequency. Additional ranging signals at the L5 frequency (1176.45 MHz) will be transmitted by Block III GPS satellites, which will bring the number of GPS satellites up to over 30.

Generally, the L1 carrier for each satellite is modulated by a unique, 37 week-long pseudorandom noise (PRN) code, known as the P (precision) code, which has a chip rate of 10.23 MHz. In addition, the phase quadrature component of the L1 carrier is modulated by another 1 msec long PRN code, known as the C/A (clear acquisition) code with a chip rate of 1.023 MHz. Both the in-phase and quadrature components of the L1 carrier are also modulated with a 50 bps navigation data stream. The L2 signal is identical to L1 with a notable exception that the C/A code is not present. Since 1994, the P-code has been encrypted by the Department of Defense (DoD) to provide a measure of "anti-spoofing" (A/S) capability for military applications; the encrypted version is known as Y-code. Civil users can only access C/A code. The services provided by C/A and P(Y) codes are defined by the Standard Position Service (SPS) and Precise Position Service (PPS) respectively.

The 50 bps navigation data stream contains spacecraft health data, satellite clock and ionosphere corrections, detailed orbital ephemeris information for the broadcasting spacecraft, and coarse orbital almanac information for all spacecraft in the constellation [Spilker96]. The ephemeris data provide information on spacecraft locations necessary to obtain a GPS position fix.

The fundamental principle behind GPS satellite ranging is measuring the phase offset between the received PRN code from a given satellite and an identical code

generated internally in the receiver. The measured code phase delay, known as the pseudorange, is the sum of the signal traveling time and the receiver's clock offset from GPS satellite time. With code-phase measurements and navigation data from four or more satellites, users are able to compute the receiver position and clock offset.

This same measuring principle can be applied to the signal carrier to generate carrier-phase measurements which are much more precise. However, carrier-phase measurements contain an unknown number of carrier cycles, which renders the measurement ambiguous.

1.1.2 Inertial Navigation Overview. Inertial Navigation Systems (INS) compute a vehicle's position, velocity and attitude by measuring the vehicle's rotation and acceleration with respect to an inertial reference frame. The primary measurement sensors employed are the gyroscope and accelerometer, which can sense the system's rotation and acceleration respectively. A strapdown Inertial Navigation System (INS) typically consists of three gyroscopes and three accelerometers rigidly and orthogonally mounted on a sensor frame installed on a vehicle. This sensor cluster is recognized as the Inertial Measurement Unit (IMU). Strapdown INS is based on a computed platform which has no sophisticated mechanism of stabilization, and is contrary to traditional INS units which need complex stable platforms. This makes strapdown INS attractive because it is easier to build and therefore less expensive and consumes much less volume. On the computed platform, the measurements from the gyroscopes are first compensated to exclude the effect of the earth's rotation and then integrated to determine the orientation of the vehicle and hence the orientation of the accelerometer triad rigidly

attached to it. The accelerometer measurements are preconditioned to eliminate the gravitational effect and are then integrated to determine vehicle's velocity and position.

A platform INS uses a sophisticated gimbal structure for the gyroscopes to maintain tracking of the vehicle attitude. The platform INS accomplishes this tracking by directly measuring the relative angles of gimbal frames. A high quality platform INS normally needs very expensive hardware which has prevented it from being considered in low cost applications, such as automobile navigation systems. Nevertheless, rapid advancements in computer technology have made it both technologically and economically feasible to achieve the high computational power that is essential for strapdown INS. In addition, incorporating miniature solid state inertial sensors made from Micro-Electro-Mechanical Systems (MEMS) technology has pushed the expansion of strapdown INS applications to include the low cost, compact size consumer market.

The performance of INS is mostly based on the quality and stability of IMU outputs. The IMU quality is roughly graded into different categories based on the demands of different applications. The root-mean-square (rms) value of the gyroscope drift rate is normally used to approximately represent the quality of an IMU. Consumer grade is for applications pertaining to consumer products. Automotive grade is mainly for ground vehicle navigation. Tactical grade and Navigation grade are both for high precision applications like aircraft navigation, missile guidance, under water navigation

Table 1.1. IMU Grades and Approximate Costs

	Consumer	Automotive	Tactical	Navigation
Drift rate Range	1~0.01^{o}/sec	1~0.1^{o}/hr	0.01^{o}/hr	0.001^{o}/hr
Cost Range	$50~1000	$2~5k	$10~40k	> $50k

etc. Table 1.1 lists the approximate market price range corresponding to the associated IMU grades.

1.1.3 GPS/INS Integration Scheme. It is widely recognized that inertial systems are naturally complementary to satellite navigation systems for several important reasons. First, GPS systems are based on point positioning by using microwave signals, whereas inertial systems operate on dead reckoning (integrating) principles and are impervious to jamming, interference and blockage of radio signals. Therefore, with the aid of INS, the potential exists to mitigate GPS navigation continuity risk. Second, inertial instruments, like GPS, are globally functional in the sense that they are able to support essentially all aerospace, terrestrial, and maritime navigation applications. There is effectively no navigation application for which GPS can function but INS cannot. The two systems fundamentally differ in that when the GPS signal is available (interference, jamming, or signal blockage is not present), position output is stable and reliable. In contrast, INS position outputs drift over time due to the integration of imperfect acceleration and angular rate measurements. Nevertheless, the two systems can, for example, be combined in such a way that INS errors are calibrated by GPS when satellite signals are available. In this way, any subsequent temporary GPS signal outage can be bridged by relatively accurate INS position outputs.

The integration of GPS and INS is achievable in varying depths [Greenspan96]. At the simplest level, the position outputs from a GPS receiver can be combined with time-matching position outputs of an independent INS through a Kalman filter [Greenspan96] [Scherzinger00]. System integration at this level is typically referred to as ‘loosely coupled.’ The obvious advantage of such an implementation is simplicity.

Minimal effort is needed to implement the system and relatively little knowledge of the internal operation of either GPS receivers or INS sensors are required. The principal disadvantage of this implementation lies in the fact that whenever fewer than four GPS satellite signals are tracked, no position output will be available from the GPS receiver. In this case navigation must be based only on the INS sensor, whose position output will drift with time. For applications that do not require high accuracy, the resulting position error drift may be acceptable for brief GPS outages.

Performance can be improved at the expense of loss of simplicity by implementing a 'tightly coupled' integration. In this case, direct sensor measurement outputs (rather than finished position outputs) are forwarded from the GPS receiver and INS sensor to a Kalman filter for estimations of position, cycle ambiguities, and INS error states (e.g., biases and scale factors) [Greenspan96] [Scherzinger00]. In this case, when fewer than four GPS satellites are available, code phase and carrier phase measurements from those satellites which are being tracked can still be used in the Kalman filter, ultimately providing improved positioning performance during GPS satellite outages.

The tightly coupled integration can be extended by using INS to *aid* the GPS receiver in such a way that satellite tracking outages are reduced in the first place. In this case, Kalman filter state outputs (whose continuity is ensured by the presence of the inertial sensor) can be used to directly aid carrier phase and code phase tracking loops within the GPS receiver [Soloviev04] [Gebre03]. Because INS is capable of accurately tracking user dynamics over short time frames, it becomes possible to reduce the receiver tracking loop bandwidths, thereby attenuating noise and interference power relative to the

desired GPS signal power to provide a better single-to-noise ratio inside the tracking loop. In this way, the receiver will be capable of receiving weaker than normal GPS signals. Nevertheless, strong RFI can still interrupt the GPS receiver output, which will degrade navigation system performance.

1.1.4 Navigation Requirements for Aircraft Precision Landing. Allocation of specific requirements of the navigation system is based on four fundamental parameters [Davis93] [Pervan96a]:

Accuracy. Accuracy is the system's capability to provide navigation solutions within an error bound under fault-free conditions. The error bound value is normally associated with a 95% probability.

Integrity. Integrity is the indication of trustworthiness of the information supplied by a navigation system. A system's integrity is measured through the quality of the navigation solution under fault-free conditions and the ability to alert users when the system should not be used for navigation in a timely fashion. Integrity risk is the probability of an undetected failure or system error that results in an unacceptable navigation error.

Continuity. Continuity is the ability of a navigation system to comply with the accuracy and integrity requirements without unintentional interruptions during the intended operation. Continuity risk is the probability of an unscheduled operation interruption during an approach.

Availability. Availability is the probability that a navigation system is available to initiate an approach at any time, which is determined by its compliance with the accuracy, integrity, and continuity requirements.

The actual performance achievable from a navigation system is a trade-off among these requirements. An extremely tight accuracy requirement can be very difficult to achieve with a navigation system, which will lead to significant degradation of availability performance. We can also impose a high integrity requirement on the navigation system by setting up a tight integrity monitoring threshold, but this will result in frequent false alarms that will interrupt the system service and consequently affect the system continuity performance.

One example of a navigation system requirement is the Signal-in-Space (SIS) performance for Local Area Augmentation System (LAAS) Approach Service for different levels of precision approaches defined by the International Civil Aviation Organization (ICAO). Table 1.2 shows the LAAS SIS requirements.

1.2 Differential GPS and Carrier-Phase Differential GPS

The typical precision of code phase measurements with receiver thermal noise is about 0.25-0.5 m (1σ) –less than 1% of the code chip length of 300 m. In addition to thermal noise, a number of other ranging error sources exist: satellite clock and orbit

Table 1.2. LAAS Signal-in-Space Specifications

	95% Vertical Accuracy at DH - 95% (meter)	Vertical Alarm Limit (ft) / Integrity Risk (any 15 sec)	Continuity Risk (any 15 sec)
Category I	13 (DH=200 ft)	33 / 2×10^{-7}	8×10^{-6}-
Category II	10 (DH=100 ft)	33 / 1×10^{-9}	4×10^{-6}
Category IIIb	10 (DH=50 ft)	33 / 1×10^{-9}	2×10^{-6} (15 sec vertical, 30 sec lateral)

DH : Decision Height

errors, ionospheric and tropospheric delays, and multipath, which limit stand alone civil GPS positioning accuracy to roughly the 10-meter level. The effect of multipath, which is the reflection of GPS signals from environments, on ranging error will vary depending on the specific antenna and receiver hardware, the line-of-sight to the spacecraft, and the local geography (which is the source of signal reflections). Typically, the magnitude of the resulting error is 0.5-1 m for code measurements and less than one centimeter for carrier-phase measurements. The remaining three errors can be much larger. However, these errors – ionospheric delay, tropospheric refraction and spacecraft clock error – can be traced back directly to a given spacecraft's transmission path. Therefore they are highly spatially correlated, in the sense that two receivers nearby (within a few kilometers) will experience essentially identical errors. It is precisely this spatial correlation in errors that inspires the concept of Differential GPS (DGPS).

In 1980, Teasley, Hoover, and Johnson [Teasley80] introduced DGPS with code measurements. The DGPS concept was further detailed by Beser and Parkinson in 1982 [Beser82] and developed broadly ever since. In a general DGPS architecture, DGPS users receive and apply the range corrections from a nearby DGPS reference station through a digital data link. One or more GPS receivers in the reference station estimate the highly correlated ranging errors in a precisely surveyed location. Positioning accuracy can be roughly improved to meter level [Misra01].

The range correction is essential to realize the advantages of DGPS. The specific content of the correction can vary according to the application requirements. One straightforward example is to broadcast the raw range measurements collected at the reference GPS receiver. This type of 'direct difference between measurements' is simple.

But it might require a large data-link bandwidth due to frequent positioning updates. Another approach that permits a smaller data transmission rate is to broadcast the message in the form of 'corrections' to the users' GPS measurements. This type of implementation relaxes the requirement on data-link bandwidth. The first widely used and standardized DGPS system using the correction-based approach was defined in 1986 by the Radio Technical Committee on Maritime Services (RTCM) Special Committee 104 [Kalafus86]. Code-based DGPS service using the RTCM data format is currently provided by the U.S. Coast Guard for ship navigation in inland waterways and coastal harbors. A more recent and significant application of code-based DGPS technology is the Local Area Augmentation System (LAAS) which will be discussed in more detail in section 1.2.1. Figure 1.2 serves two purposes: it shows the overall LAAS configuration and it also illustrates the general structure of a typical DGPS configuration.

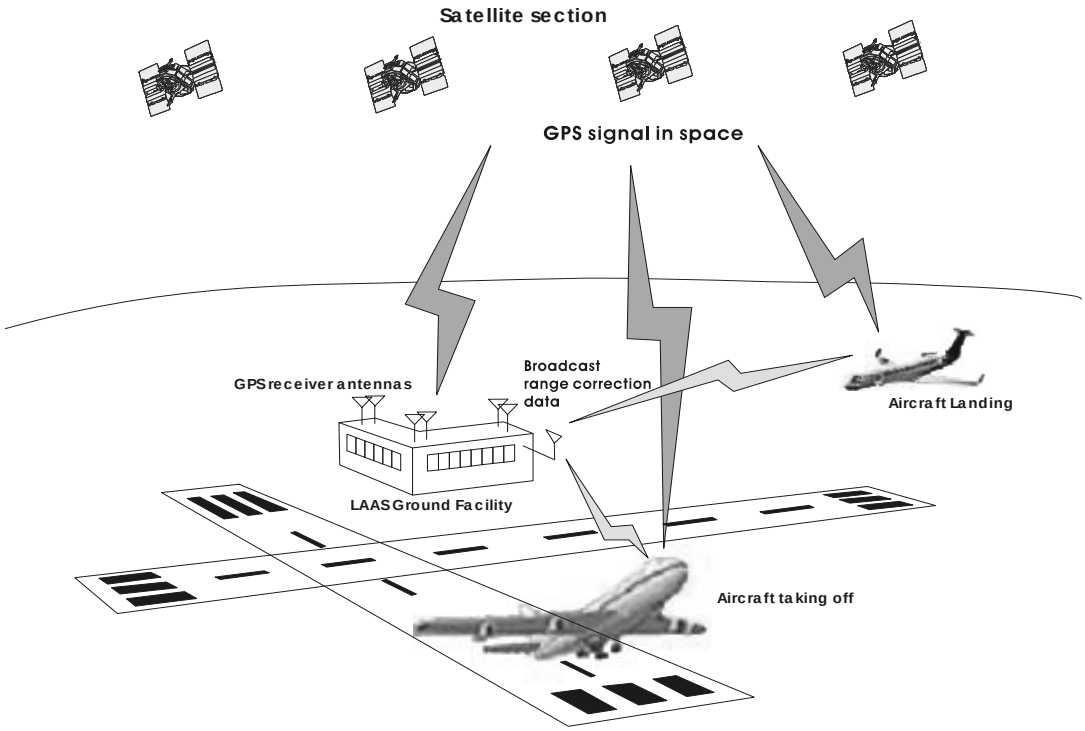

Figure 1.2. DGPS/LAAS System Overview

GPS carrier-phase measurements are generally available from a GPS receiver because the signal detection mechanisms inside the receiver are tracking GPS code and carrier signals at the same time. In 1979, the existing techniques of Very Long Baseline Interferometry (VLBI) were extended to GPS carrier-phase measurements by Counselman and Shapiro [Counselman79] and MacDoran [MacDoran79] independently, setting the stage for the use of high-precision carrier-phase differential GPS measurements for static surveying and geodetic applications. The carrier-phase differential GPS (CDGPS) concept has since been extended to kinematical survey [Remondi85] as well as navigation applications [vanGraas93] [Romrell95], and a widelane technique was exploited to seek a fast solution to the integer ambiguity problem [Jung00].

From the navigation point of view, the centimeter-level accuracy achievable by CDGPS has enabled a host of new navigation applications including precision agriculture [O'Connor96], vehicle attitude determination [Cohen92] [Hayward99], navigation for automatic landing on aircraft carriers [Pervan03] etc. The high precision of CDGPS is also beneficial to monitor system integrity [Pervan96b] [Pervan98]. In all cases, however, the realization of centimeter-level CDGPS performance requires the correct resolution of carrier-phase cycle ambiguities for GPS satellites in view.

1.2.1 Local Area Augmentation System (LAAS). GPS/LAAS is currently under research and development by the Federal Aviation Administration (FAA), which will serve as the next generation navigation aid for aircraft precision approach and landing with the objective to replace current Instrument Landing System (ILS) [Braff97]

[vanGraas95b]. There are two services provided by LAAS: an approach service and a differentially-corrected positioning service.

The approach service provides vertical and lateral deviation guidance with respect to a defined final approach segment, while the positioning service provides horizontal position, velocity and time information to support area navigation (RNAV) operations in the airport terminal area. The LAAS system is composed of three primary subsystems: a) satellite subsystem, which produces ranging signals; b) ground subsystem, which provides a VHF Data Broadcast (VDB) containing differential corrections and other pertinent information; c) airborne subsystem, which consists of aircraft equipment used to receive and process the LAAS/GPS signals in order to compute and to output position solutions, deviations relative to a desired reference path, and appropriate annunciation of the system status. All associated LAAS system requirements are specified in the *Minimum Aviation System Performance Standards for the Local Area Augmentation System* (MASPS) [RTCA/DO245A].

LAAS system design is driven by the desire to replace the current ILS. The navigation performance requirements for LAAS are, therefore, derived to meet the three-tiered structure (Category I, II, and III) of ILS Approach Services and ICAO Ground-

Table 1.3. GBAS Service Levels for Approach Service

ICAO GBAS Operation	GBAS Service Level
Category I (CAT I)	C
Category II (CAT II)	E
Category IIIa (CAT IIIa)	E
Category IIIb (CAT IIIb)	D / F
Category IIIc (CAT IIIc)	Not addressed

Based Augmentation System (GBAS) standards. In order to best specify LAAS ground and airborne subsystem performance, LAAS approach service performance is classified in terms of defined levels of service called GBAS service levels. A GBAS Service Level (GSL) defines a specific level of required Accuracy, Integrity, and Continuity. Table 1.3 specifies the LAAS GBAS service levels and the supported operations. We can see that LAAS GSL C is equivalent to Category I (CAT I) precision approach service, GSL F supports Category IIIb (CAT IIIb), and GSL D is the standard for aircraft augmented with navigation equipment in addition to GPS airborne receivers.

1.2.2 Cycle Resolution of Carrier-Phase Differential GPS (CDGPS). While a GPS receiver's code tracking delay-lock loop (DLL) generates code-phase (pseudorange) measurements, accumulated carrier-phase measurements are normally available to users from the phase-lock loop (PLL) which provides synchronized carrier phase to remove carrier in DLL for coherent code detection [Mirsa01]. The precision of carrier phase estimates can reach roughly 1% of the carrier wavelength of 19 cm. Millimeter-level carrier-phase measurement precision is possible. However, the sinusoidal nature of the carrier-phase measurement results in cycles that are identical, i.e. one cycle cannot be discerned from an adjacent cycle. This results in a precise carrier-phase measurement that is expressible in the form of a very accurate phase estimation plus an ambiguous number of whole carrier cycles number, known as an integer ambiguity or cycle ambiguity. The centimeter-level positioning capability of CDGPS can be realized only when the cycle ambiguities can be correctly resolved.

Resolution of the integer ambiguities is not a trivial problem. A great deal of research and effort has been invested in this area. For surveying and other time-

insensitive applications, a long-time filtering process can work very well to resolve the necessary integers for precise positioning. However, for kinematical CDGPS applications or a high-integrity navigation system based by CDGPS, the optimal method of correctly resolving the cycle ambiguities expediently in real time with high integrity is still a very active area of research in guidance and navigation.

A new Carrier-Phase DGPS (CDGPS) navigation system, called Shipboard-Relative GPS (SRGPS), is currently under development by the U.S. Navy. This system provides an excellent opportunity to explore the possibility of realizing ultimate-precision positioning performance by CDGPS architecture with a high integrity of correct cycle ambiguity resolution. Due to the military nature of SRGPS research, both code and carrier measurements are accessible at L1 and L2 frequencies. The benefits of a dual frequency system are fully explored in Chapter 2.

1.3 Previous Work

1.3.1 Kinematic Carrier-Phase Differential GPS Positioning and Cycle Resolution. Ever since Remondi (1986) expanded the CDGPS concept for kinematic survey, a tremendous amount of works have been done in kinematic CDGPS positioning research. Efforts on resolving carrier-phase integer ambiguities in real time have generated numerous approaches to ambiguity resolution. Some of these methods include search techniques, single [Landau92] or multiple widelane algorithms [Jung00], and even on-the-fly (OTF) search techniques which have been tested in a series of flight tests [Paielli93] [vanGraas93] [Romrell95]. The correlations among carrier-phase integers were studied and exploited by Teunissen and an effective way of evaluating the probability of correct integer resolution was presented in 1998 [Teunissen98]. The most

remarkable achievement is the successful demonstration of the Integrity Beacon Landing System (IBLS) which can resolve carrier-phase integers in seconds with high integrity when the landing aircraft flies over two ground pseudolites [Pervan96a] [Lawrence96].

Regardless of the great advances made in previous research, the unique shipboard environment has made the ground pseudolites in IBLS impossible to be installed. Therefore, in order to meet the high integrity requirement imposed on successful ambiguity resolution, one must reconsider the problem of defining a real-time cycle resolution algorithm.

1.3.2 Integration of GPS and INS for Aircraft Aviation. The concept of GPS/INS integration can be traced back as early as 1980 [Cox78] [Cox80]. The benefit of inertial sensors in navigation was not widely embraced during this time due to the high cost of IMU sensors. Only in the last two decades has the practical advantages of INS begun to emerge. As technology advances, GPS/INS integrations expand along with the increasing market share of cost effective IMU sensors. The majority of integrations are implemented using loosely coupled scheme described in section 1.1.3 for its advantages of simplicity and compatibility among different systems.

During the past 15 years, tightly coupled implementations for aviation have drawn more attention due to its superior performance during partial GPS signal outages. Military based research has the advantage of accessing high quality IMU sensors. However, the research normally is concentrated on GPS aided INS systems with stand alone GPS receivers [Cunningham88] [Johnson90]. Some research has focused solely on vehicle attitude determination [Tome99] [Fathy99], but the majority of the research is focused on the applications for general aviation aircraft [Lorga03] [Moafipoor04]. A

more general study was done by Gautier [Gautier03], which investigated the performance of different integration schemes with diverse grades of IMU. Despite this research, a high integrity GPS/INS tightly coupled navigation system for precision approach and landing has yet to be realized.

1.3.3 Precision Approach and Landing Application. A great amount of research has been done on using DGPS as the navigation resource in precision approach and landing applications. Nevertheless, the U.S. Department of Transportation (John A. Volpe National Transportation Systems Center) produced an influential report in September 2001 entitled "Vulnerability Assessment of the Transportation Infrastructure Relying on the Global Positioning System." [Volpe01]. While praising the achievements of GPS and its potential to meet the needs of a wide variety of users, the report also clearly identified the continuity and integrity threats involved with widespread reliance on GPS within the transportation infrastructure. This report has raised concerns on the risk of losing GPS signals for any type of GPS navigation system. This report also pointed out the possible catastrophic failure that could occur during an intentional jamming attempt on an aircraft approaching the touchdown point. It is these types of concerns that lead to the consideration of incorporating INS into the GPS navigation system for critical applications. Aircraft coasting on INS during the final phase of precision approach is one proposed solution to hostile events such as jamming.

Researchers have investigated the possibility of tightly coupled GPS/INS integration for LAAS. Lee's work is centered on improving system integrity by detecting slow growing errors in the GPS signal [Lee99]. Brenner has worked on reducing continuity risk [Brenner99]. Diesel has published a system for military aircraft to

perform CAT II operations even without any ground aids [Diesel99]. The most recent investigation of tightly coupled GPS/INS integration is Lee's analysis which evaluated the availability of a GPS/INS architecture with extra vertical guidance [Lee05]. However, a comprehensive study of precision approach coasting during the final segment in terms of optimal GPS/INS tightly coupled system architecture, IMU coasting performance, in-flight calibration performance and integrity risk has not yet been done. The most demanding LAAS CAT III requirements will be used as the standard scenario for system analysis unless noted otherwise.

1.4 Contributions

This research focuses on the performance of the high integrity navigation system using carrier-phase GPS and inertial navigation sensors. The main contributions of this work are briefly described below:

- A new high-performance dual-frequency GPS navigation architecture was developed and analyzed to obtain centimeter-level relative positioning accuracy with high integrity. The ultimate system performance was realized by resolving the carrier ambiguities with assured integrity in real time for a GPS-unfriendly shipboard precision landing application.
- A novel GPS/INS tight-coupling hybrid navigation system was devised and validated by flight data. The innovation of the GPS/INS hybrid architecture is a complete integration of all GPS and INS states in a single dynamic system model, rather than the conventional way of elaborating calibration models in the measurement domain. This novel system architecture enables positioning and INS calibration to be accomplished optimally using ordinary GPS measurement

updates, unlike the conventional GPS/INS integration schemes which needs additional sophisticated measurement processing for INS calibrations. In addition, an effective cycle slip detection mechanism was built into the system process.

- The sensitivity of the new hybrid navigation system to all system parameters was thoroughly analyzed and the required INS quality was quantified for precision approach applications. The hybrid navigation system performance was evaluated to ensure compliance with the LAAS CAT I/III accuracy, continuity and integrity requirements. Fault-free navigation system availability was evaluated for six major airports with a 24 satellite constellation.
- A new fault detection algorithm based on integrating innovation residuals was conceived and analyzed to show superior detection performance over other well known detection methods.

The details of the major contributions described above are explained in Chapter 7 (Conclusion).

CHAPTER 2

CARRIER-PHASE DIFFERENTIAL GPS NAVIGATION

A new dual-frequency high-performance navigation architecture applied to SRGPS is developed in this chapter. The system development starts from a general GPS measurement error analysis. The error sources which have noticeable effects on stand-alone GPS code-phase signal can be identified as receiver clock error, satellite clock error, ionosphere delay, troposphere delay and multipath: [Misra01]

$$\rho_k^i = r_k^i + {}_{clk}\tau_k^r + {}_{clk}\tau_k^i + I_k^i + T_k^i + v_{\rho_k}^{\ i} \tag{2.1}$$

where

ρ_k^i is the code-phase range measurement between receiver antenna phase center and satellite *i* at time epoch *k*.

r_k^i is the true or geometric range between receiver antenna phase center and satellite *i* at time epoch *k*.

${}_{clk}\tau_k^r$ is the receiver clock offset from nominal GPS time at time epoch *k*.

${}_{clk}\tau_k^i$ is the satellite *i* clock offset from nominal GPS time at time epoch *k*.

I_k^i is the ionospheric delay between receiver antenna phase center and satellite *i* at time epoch *k*.

T_k^i is the tropospheric delay between receiver antenna phase center and satellite *i* at time epoch *k*.

$v_{\rho_k}^{\ i}$ is the code-phase measurement error primarily due to the multipath and receiver noise for satellite *i* at time epoch *k*.

The same errors can be found in carrier-phase measurements, except the ionospheric delay working on the opposite way. The ambiguous cycle integers are also included in the measurements:

$$\lambda\phi_k^i = r_k^i + {}_{clk}\tau_k^r + {}_{clk}\tau_k^i - I_k^i + T_k^i + \lambda N^i + v_k^i \tag{2.2}$$

where

λ is the carrier wavelength, $\lambda_1 = 19.03\,cm$ for L1 frequency and $\lambda_2 = 24.42\,cm$ for L2 frequency.

ϕ_k^i is the carrier-phase range measurement between receiver antenna phase center and satellite *i* at time epoch *k* in cycles.

N^i is the unknown constant integer ambiguity for satellite *i* in cycles.

$v_{\phi_k}^{\ i}$ is the carrier-phase measurement error due to the multipath and receiver noise for satellite *i* at time epoch *k* in meters.

For differential GPS applications, single-difference (SD) GPS code and carrier measurements can be formed by differencing the measurements between user and reference station receivers corresponding to the same satellite, in which the satellite clock offset is canceled:

$$\Delta\rho_k^i = \Delta r_k^i + \Delta\tau_k^{clk} + \Delta I_k^i + \Delta T_k^i + \Delta v_{\rho_k}^{\ i} \tag{2.3}$$

where

Δ is the single difference operation,

$\Delta\tau_k^{clk}$ is the clock offset between reference and user GPS receivers at time epoch *k*.

Not only is the satellite clock error ${}_{clk}\tau_k^i$ eliminated completely in single difference between receivers, but a great portion of spatial correlated ionospheric and tropospheric delays is canceled out as well. The true range difference, Δr_k^i, corresponding to the satellite *i* can be linearized with respect to the reference station location while the distances between the reference station and the user is in tens of kilometers. This linearized range difference can be mathematically expressed by projecting a relative displacement vector, $\vec{x}_k$, onto a line-of-sight vector, $\vec{e}_k^i$. The relative displacement vector is the vector from the reference station to the user and the line-of-sight vector is the unit vector which indicates the direction from the reference station to the satellite *i*:

$$\Delta r_k^i = -\vec{e}_k^i \cdot \vec{x}_k \tag{2.4}$$

Linearized single difference code and carrier phase measurements can be written as:

$$\Delta\rho_k^i = -\vec{e}_k^i \cdot \vec{x}_k + \Delta\tau_k^{clk} + \Delta I_k^i + \Delta T_k^i + \Delta v_{\rho_k}^{\ i} \tag{2.5}$$

$$\lambda\Delta\phi_k^i = -\vec{e}_k^i \cdot \vec{x}_k + \Delta\tau_k^{clk} - \Delta I_k^i + \Delta T_k^i + \lambda\Delta N^i + \Delta v_{\phi_k}^{\ i} \tag{2.6}$$

where ΔI_k^i and ΔT_k^i are the remaining ionosheric and troposheric delays due to spatial decorrelations; ΔN^i is the single difference cycle ambiguity in the carrier-phase measurement to satellite *i*; and $\Delta v_{\phi_k}^{\ i}$ is the carrier-phase measurement error (typically at the sub-centimeter level) due to the receiver noise and multipath. In contrast, the

differential code-phase measurement is free from cycle ambiguities, but the measurement error is typically at the sub-meter level.

Under normal conditions, decorrelation errors from ionosphere and troposphere delays in SD code-phase measurement are small and are grouped together into the measurement error term. A single standard deviation (sigma) value is used to bound the summation of the grouped error sigmas:

$$\Delta\rho_k^i = -\vec{e}_k^{\,i} \cdot \vec{x}_k + \Delta\tau_k^{clk} + \Delta\tilde{v}_{\rho_k}^{\;i},\ \Delta\tilde{v}_{\rho_k}^{\;i} \sim N(0,\sigma_i^2) \tag{2.7}$$

where $\sigma_i^2 = \sigma_{\Delta Ii}^2 + \sigma_{\Delta Ti}^2 + \sigma_{\Delta v_\rho^i}^2$, $\sigma_{\Delta Ii}$ is the sigma of SD ionosphere decorrelation, $\sigma_{\Delta Ti}$ is the sigma of SD troposphere decorrelation, and $\sigma_{\Delta v_\rho^i}$ is the sigma of SD code multipath plus receiver noise.

With four or more satellite measurements being available at each time epoch, a weighed least square solution to a stack of observation equation 2.7 can lead to a position estimate with submeter-level accuracy:

$$\begin{bmatrix} \vdots \\ \Delta\rho_k^i \\ \vdots \end{bmatrix}_{n\times 1} = \begin{bmatrix} \vdots & \vdots \\ -\vec{e}_k^{\,i} & 1 \\ \vdots & \vdots \end{bmatrix}_{n\times 4} \begin{bmatrix} \vec{x}_k \\ \Delta\tau_k \end{bmatrix}_{4\times 1} + \begin{bmatrix} \vdots \\ \Delta\tilde{v}_{\rho_k}^{\;i} \\ \vdots \end{bmatrix}_{n\times 1} \Rightarrow \Delta Z_k = H_k S_k + \Delta V_k \tag{2.8}$$

$$\begin{bmatrix} \hat{x}_k \\ \Delta\hat{\tau}_k \end{bmatrix}_{4\times 1} = \hat{S}_k = (H_k^{\,T} W_{\Delta V}^{-1} H_k)^{-1} H_k^{\,T} W_{\Delta V}^{-1} \Delta Z_k \text{, where } W_V = E(\Delta V \Delta V^T) \tag{2.9}$$

where $W_{\Delta V}$ is the covariance matrix of measurement error, $E(\ )$ is the expectation operation. $W_{\Delta V}$ is used as a 'whitening' process in least square estimation to account for measurement error correlations.

The same technique will encounter some difficulties when it comes to use SD carrier-phase measurements because of the integer ambiguities. If we stack the SD carrier-phase measurements in the same manner as equation 2.8:

$$\begin{bmatrix} \vdots \\ \lambda\Delta\phi_k^i \\ \vdots \end{bmatrix}_{n\times 1} = \begin{bmatrix} \vdots & \vdots & 1 & 0 & \cdots \\ -\bar{e}_k^i & 1 & 0 & \ddots & 0 \\ \vdots & \vdots & \cdots & 0 & 1 \end{bmatrix}_{n\times(n+4)} \begin{bmatrix} \bar{x}_k \\ \Delta\tau_k \\ \vdots \\ \lambda\Delta N_i \\ \vdots \end{bmatrix}_{(n+4)\times 1} + \begin{bmatrix} \vdots \\ \Delta\tilde{v}_{\phi k}^{\ i} \\ \vdots \end{bmatrix}_{n\times 1} \tag{2.10}$$

At time epoch k, there are four more states to be estimated than there are available measurements. It is not possible to obtain position estimations with this undetermined equation set without some prior knowledge of the cycle integers. But once the cycle ambiguities are resolved, center-meter level positioning is available.

The cycle resolution problem, nevertheless, is non-trivial in general. Satellite motion can provide direct observation on carrier-phase integers and this effect is widely exploited in geodetic and surveying applications, for which time is not a significant constraint. Unfortunately, the satellite motion is relatively slow in comparison with the time scales of most real-time navigation applications.

2.1 Development of New Dual-frequency CDGPS System Architecture

To overcome the difficulty of resolving integer ambiguities in real time, a new CDGPS dual-frequency measurement model which incorporates with ionosphere and troposphere decorrelation models is developed. The dual-frequency SD code and carrier-phase measurements from a single satellite i at time epoch k are shown as:

$$
\begin{aligned}
\Delta_{L1}\rho_k^i &= -\vec{e}_k^{\,i}\cdot\vec{x}_k + \Delta\tau_k^{clk} + \Delta tc_k^i\cdot\Delta n^i + \Delta_{L1}ic_k^i\cdot\Delta V_{ig}^i + \Delta_{L1}v_{\rho_k}^{\;i} \\
\lambda_1\Delta\phi_k^i &= -\vec{e}_k^{\,i}\cdot\vec{x}_k + \Delta\tau_k^{clk} + \Delta tc_k^i\cdot\Delta n^i - \Delta_{L1}ic_k^i\cdot\Delta V_{ig}^i + \Delta N_{L1}^i + \Delta_{L1}v_{\phi_k}^{\;i} \\
\Delta_{L2}\rho_k^i &= -\vec{e}_k^{\,i}\cdot\vec{x}_k + \Delta\tau_k^{clk} + \Delta tc_k^i\cdot\Delta n^i + \Delta_{L2}ic_k^i\cdot\Delta V_{ig}^i + \Delta_{L2}v_{\rho_k}^{\;i} + b_{\rho 2} \\
\lambda_2\Delta\phi_k^i &= -\vec{e}_k^{\,i}\cdot\vec{x}_k + \Delta\tau_k^{clk} + \Delta tc_k^i\cdot\Delta n^i - \Delta_{L2}ic_k^i\cdot\Delta V_{ig}^i + \Delta N_{L2}^i + \Delta_{L2}v_{\phi_k}^{\;i} + b_{\phi 2}
\end{aligned}
\tag{2.11}
$$

where Δn^i and ΔV_{ig}^i are the local refraction index error and vertical ionospheric gradient correspondingly used in the tropospheric and ionospheric decorrelation models; Δtc_k^i is the coefficient of the tropospheric decorrelation model, $\Delta_{L1}ic_k^i$ and $\Delta_{L2}ic_k^i$ are the coefficients of the ionospheric decorrelation models for L1 and L2 measurements, respectively; $b_{\rho 2}$ and $b_{\phi 2}$ are the interfrequency biases which only exist in L2 measurements and are the same for all satellites; all the measurements (L1 code and carrier, and L2 code and carrier) are corresponding to the satellite *i*. The details of the ionospheric and tropospheric decorrelation models will be addressed in Sections 2.3.1 and 2.3.2.

Assuming there are *n* satellites in view and picking the nth satellite as the master satellite, (*n-1*)×4 Double Difference (DD) measurements between the satellites can be generated with the clock and interfrequency biases eliminated. The resulted measurement model is expressed in matrix form:

$$
\begin{bmatrix} \Delta^2\vec{\rho}_{L1} \\ \lambda_1\Delta^2\vec{\phi}_{L1} \\ \Delta^2\vec{\rho}_{L2} \\ \lambda_2\Delta^2\vec{\phi}_{L2} \end{bmatrix}_k
=
\begin{bmatrix}
\Delta G & \Delta^2 T_c & \Delta_{L1}^2 I_c & 0_{(n-1)\times n} & 0_{(n-1)\times n} \\
\Delta G & \Delta^2 T_c & -\Delta_{L1}^2 I_c & \lambda_1 dI & 0_{(n-1)\times n} \\
\Delta G & \Delta^2 T_c & \Delta_{L2}^2 I_c & 0_{(n-1)\times n} & 0_{(n-1)\times n} \\
\Delta G & \Delta^2 T_c & -\Delta_{L2}^2 I_c & 0_{(n-1)\times n} & \lambda_2 dI
\end{bmatrix}_k
\begin{bmatrix} \vec{x}_k \\ \Delta n \\ \Delta\vec{V}_{ig} \\ \Delta\vec{N}_{L1} \\ \Delta\vec{N}_{L2} \end{bmatrix}_k
+
\begin{bmatrix} \Delta^2\vec{v}_{\rho L1} \\ \Delta^2\vec{v}_{\phi L1} \\ \Delta^2\vec{v}_{\rho L2} \\ \Delta^2\vec{v}_{\phi L2} \end{bmatrix}_k
\tag{2.12}
$$

where $\Delta G = \begin{bmatrix} -(\vec{e}^{\,1}-\vec{e}^{\,n}) \\ \vdots \\ -(\vec{e}^{\,n-1}-\vec{e}^{\,n}) \end{bmatrix}$, $\Delta^2 T_c = \begin{bmatrix} \Delta tc^1 - \Delta tc^n \\ \vdots \\ \Delta tc^{n-1} - \Delta tc^n \end{bmatrix}$, $dI = \begin{bmatrix} 1 & 0 & \cdots & -1 \\ 0 & \ddots & 0 & \vdots \\ \vdots & 0 & 1 & -1 \end{bmatrix}_{(n-1)\times n}$,

$$\Delta^2_{L1/L2} I_c = \begin{bmatrix} \Delta_{L1/L2} ic^1 & 0 & \cdots & -\Delta_{L1/L2} ic^n \\ 0 & \ddots & 0 & \vdots \\ \vdots & 0 & \Delta_{L1/L2} ic^{n-1} & -\Delta_{L1/L2} ic^n \end{bmatrix}$$ is applicable to both L1 and L2.

A simplified notation is introduced to represent equation 2.12:

$$\Delta^2 Z_k = H_k S_k + \Delta^2 V_k \tag{2.13}$$

The corresponding measurement error model is expressed as:

$$\delta\Delta^2 Z_k = H_k \delta S_k + V_{\Delta^2 k}, P_k \equiv E(\delta S_k \delta S_k^T), W_k^{\Delta^2 V} \equiv E(\Delta^2 V_k \Delta^2 V_k^T) \tag{2.14}$$

where P_k is defined as the covariance of the estimated states, and $W_k^{\Delta^2 V}$ is defined as the covariance of the measurement noise. In this analysis, the code measurement error for each satellite is assumed to have the same sigma value, so does the carrier measurement error. No correlation between code and carrier measurements is assumed. The code or carrier measurements are correlated between each satellite pair because of the double difference process. The measurements between L1 and L2 frequencies are assumed to have no correlation. The measurement covariance matrix will have the form as below:

$$W_k^{\Delta^2 V} = \begin{bmatrix} W_k^{L1} & 0_{2(n-1)\times 2(n-1)} \\ 0_{2(n-1)\times 2(n-1)} & W_k^{L2} \end{bmatrix}$$

where $$W_k^{L1/L2} = \begin{bmatrix} \sigma^2_{\Delta^2\rho} \begin{bmatrix} 1 & 0.5 & \dots \\ 0.5 & \ddots & 0.5 \\ \vdots & 0.5 & 1 \end{bmatrix}_{(n-1)\times(n-1)} & 0_{(n-1)\times(n-1)} \\ 0_{(n-1)\times(n-1)} & \sigma^2_{\Delta^2\phi} \begin{bmatrix} 1 & 0.5 & \dots \\ 0.5 & \ddots & 0.5 \\ \vdots & 0.5 & 1 \end{bmatrix}_{(n-1)\times(n-1)} \end{bmatrix}$$

The sigma values of the measurement errors will be addressed in Section 2.3.3. Some elements in the observation matrix H need the knowledge of the relative position $\vec{x}_k$, but the sensitivity of observation matrix error to the relative position error is small.

Therefore, the observation matrix error is negligible. An iteration process might be necessary to eliminate the possibility of large observation matrix error during the initialization.

The major contributor to the DD measurement errors, $V_{\Delta^2 k}$, is the code and carrier multipath. Sampling dual-frequency measurements at 2 times the measurement correlation time constant, τ, can avoid taking improper advantage of over counting measurements as independent. Covariance analysis is performed through the Kalman filter process to evaluate the performance of the new system architecture.

The state covariance time update by Kalman filter is shown as:

$$\overline{P}_k = \Phi_{k-1}\hat{P}_{k-1}\Phi_{k-1}^T + \Sigma_{k-1} \tag{2.15}$$

where Φ_{k-1} is just an unit matrix, Σ_{k-1} is the process noise matrix which has large values on the corresponding position states to account for unknown system dynamics.

The measurement update on the state covariance by Kalman filter is expressed as:

$$\begin{aligned} K_k &= \overline{P}_k H_k^T (W_k^{\Delta^2 V} + H_k \overline{P}_k H_k^T)^{-1} \\ \hat{P}_k &= (I - K_k H_k)\overline{P}_k (I - K_k H_k)^T + K_k W_k^{\Delta^2 V} K_k^T \end{aligned} \tag{2.16}$$

where K_k is the Kalman filter gain. At this moment, the new dual-frequency CDGPS system architecture is only filtering the estimated states. The estimated carrier integers are floating numbers during the system filtering process. The new algorithm developed to fix the floating integers with required integrity starts here:

- The corresponding floating integer covariance is taken out from the system covariance matrix:

$$\hat{P}_k = \begin{bmatrix} \vdots & \vdots \\ \vdots & \hat{P}_k^{float\_Int} \end{bmatrix} \Rightarrow \hat{P}_k^{float\_Int}$$

- The floating integer covariance is decorrelated by LAMBDA process.
- Starting from the integer with the smallest variance after decorrelation, the Integer Bootstrapping algorithm is applied to the decorrelated integer states. The correct fix probability is computed and compared with the required integrity. The floating integer is fixed to the nearest integer if the integrity requirement is met.
- The system covariance matrix is updated if any integer is fixed during the above process.

With the new dual-frequency CDGPS system architecture and the high integrity integer fixing algorithm, a navigation system applied to the shipboard landing is developed in the following sections.

2.2 Shipboard-Relative CDGPS System Concept

Shipboard-Relative GPS (SRGPS) is an architectural variant of the Joint Precision Approach and Landing System (JPALS), which is being developed to provide high accuracy and high integrity differential GPS navigation for automatic shipboard landings. The required navigation system vertical accuracy is envisioned to be on the order of 0.3 m, and the vertical protection level is 1.1 m, with an associated integrity risk of approximately 10^{-7} [JPALS99]. In order to provide such navigation performance with adequate system availability—at least 99.7% [USAF002]—differential carrier phase solutions are presently being pursued [Waters01].

The full availability of both the L1 and L2 GPS signals for this military application is tempered by the simultaneous need to provide redundancy in the event of hostile jamming or interference. In this respect, although dual-frequency architectures may be acceptable for SRGPS, single-frequency carrier-phase solutions (if possible)

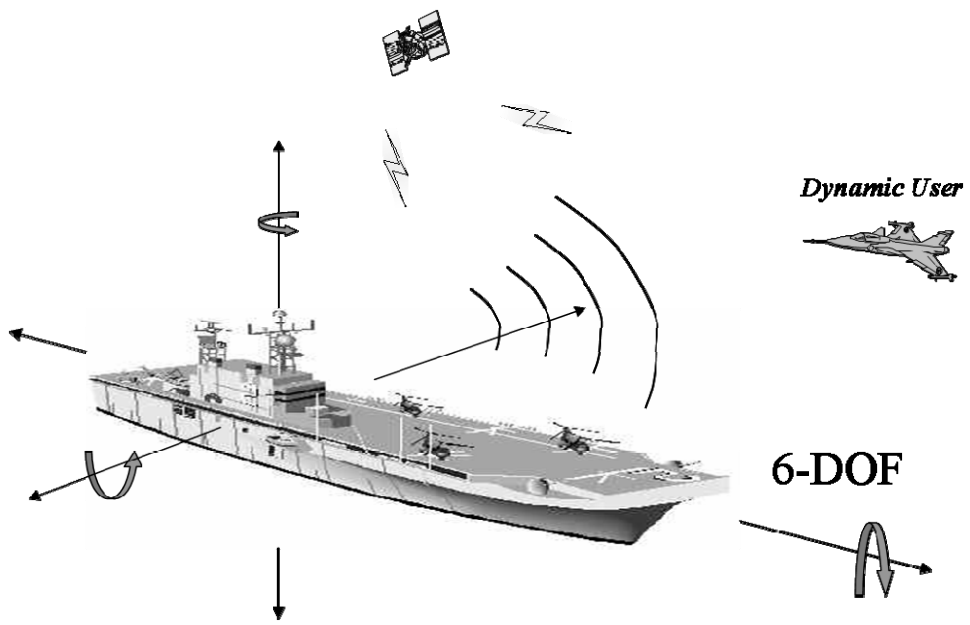

Figure 2.1. SRGPS System Overview

would be advantageous. In addition, controlled reception pattern (phased array) shipboard antennas will be implemented in SRGPS to provide superior performance in a jamming environment and to mitigate multipath. These antennas can also be expected to benefit SRGPS performance by providing exceptionally precise code and carrier measurements at the reference station for satellites at all elevations [Brown01]. A system overview of SRGPS is shown in Figure 2.1.

The use of differential carrier-phase for precise navigation is contingent upon the successful estimation or resolution of cycle ambiguities. While it is understood that fixed-integer implementations will provide better accuracy than floating-ambiguity implementations, the integrity of cycle resolution process must be ensured. In the most general sense, cycle resolution integrity will be a function of the quality of the raw code and carrier measurements, satellite geometry, and filter duration. For example, a large service volume can potentially provide sufficient time for averaging of noisy

measurements, and also for satellite motion, to improve cycle ambiguity observability. In this case, however, the spatial decorrelation of carrier phase measurement errors (over the resulting long baselines) must be carefully accounted for.

It is intuitively clear that the performance of carrier-phase DGPS (for both floating and fixed ambiguity implementations) will be best if:

- Dual-frequency measurements are used (instead of L1 or L2 alone).
- GPS data broadcast radius is large (ensuring longer filtering times and more satellite motion).
- High performance receivers and antennas are used (to provide small raw code and carrier measurement error).

While these observations are all qualitatively true, in this work we seek *quantitative* design guidelines and tradeoffs applicable to SRGPS. Some specific questions which require quantitative answers include:

- Given a specified GPS data broadcast radius (or maximum filter duration), how small must raw measurement errors should be to ensure adequate SRGPS availability? The answer to this question may be interpreted as a derived system requirement on antenna/receiver performance.
- Can we quantify the benefit to navigation availability due to fixing integers (relative to a floating implementation), given that the probability of incorrect integer fix must be consistent with integrity requirements? To what extent does integer fixing allow for relaxation of requirements on antenna/receiver quality and/or GPS data broadcast radius?

- How sensitive is SRGPS performance to time-correlated multipath, residual tropospheric error decorrelation, and ionospheric spatial gradients?
- How do the answers to the questions above differ for single and dual-frequency architectures?

In this research we seek to answer these questions to provide a basis for defining necessary conditions (i.e., derived requirements) to ensure adequate fault-free availability of SRGPS navigation. The development of fault detection methodologies for SRGPS is the subject of related work [Koenig02] [Heo04].

2.3 Analysis Methodology

To explore the sensitivity of SRGPS performance to variations in system and measurement error characteristics, we used a covariance analysis methodology. A nominal fixed-wing (airplane) approach model, illustrated in Figure 2.2, was assumed in this analysis [Colby01] [Wallac01]. The GPS data broadcast radius, also indicated in the

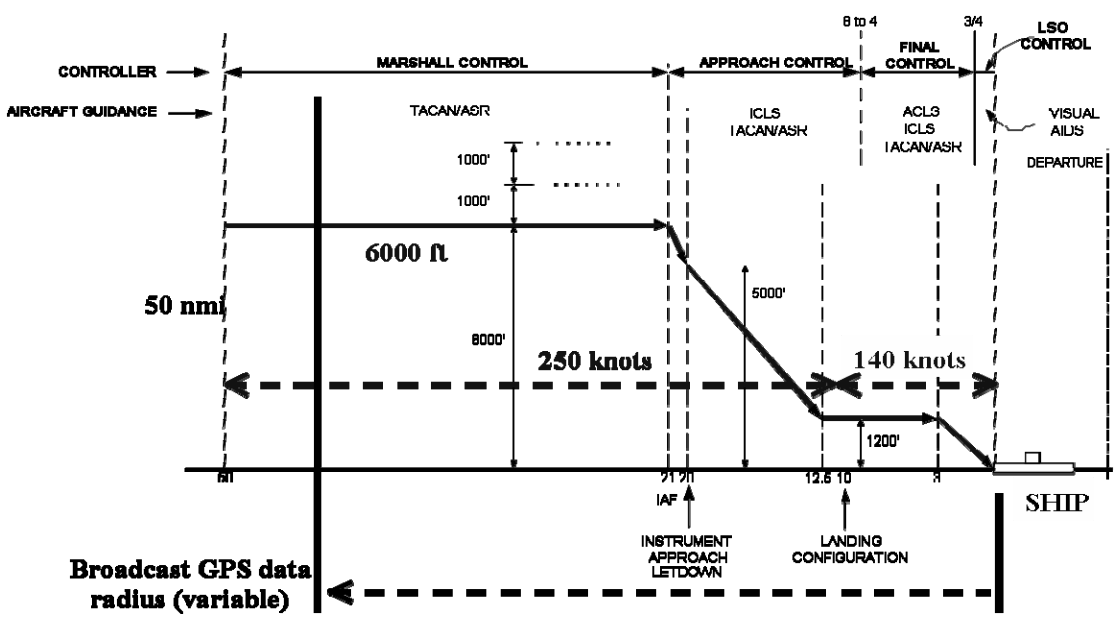

Figure 2.2. Nominal Airplane Approach Model

figure, was treated as a parameter. Within the broadcast radius, code and carrier measurements from the shipboard reference receiver(s) were assumed available for use at the aircraft. In this analysis, filtering of aircraft and shipboard measurements was initiated at broadcast radius entry. (The implications of filtering prior to broadcast radius entry, which can be particularly advantageous for dual-frequency architectures, will be addressed later.) The nominal DO-229D (WAAS MOPS) [RTCA/DO229D] GPS satellite constellation, a Central Pacific ship location (22 deg N, 158 deg W), and a satellite elevation mask of 7.5 deg were used in the analysis. Both single and dual-frequency implementations were considered in this work. The measurement error models used in the covariance analysis as well as details regarding the floating and fixed cycle ambiguity implementations are described below.

2.3.1 Residual Tropospheric Decorrelation. Residual differential tropospheric error (i.e., the ranging error remaining after tropospheric correction) was modeled using the Local Area Augmentation System (LAAS) tropospheric error model [McGraw00]:

$$\varepsilon_T(i,k) = \Delta n \cdot \frac{h_0\left[1-\exp\left(-h(k)/h_0\right)\right]}{\sqrt{0.002+\sin^2 E(i,k)}} \tag{2.17}$$

where ε_T is the tropospheric error, Δn is the error in knowledge of local index of refraction, h_0 is the troposphere scale height, h is the altitude of the airplane, E is satellite elevation angle in rad, and i and k are satellite and time indices, respectively. The coefficient of the tropospheric decorrelation model in equation 2.11 is defined as:

$$\Delta tc_k^i \equiv 10^{-6}\frac{h_0\left[1-\exp\left(-h(k)/h_0\right)\right]}{\sqrt{0.002+\sin^2 E(i,k)}}$$

The local refraction index error Δn was included as a *state* in the covariance analysis. At aircraft approach initiation, the uncertainty in knowledge of the refraction error state was defined by $\Delta n \sim N(0, 10^{-6}\sigma_{\Delta n})$. For the nominal error model, we assumed $\sigma_{\Delta n} = 10$ and $h_0 = 7000$ m, but these values were varied in the sensitivity analysis.

2.3.2 Ionospheric Spatial Gradient. The differential ranging error due to ionospheric spatial gradient was also modeled in this analysis using the associated LAAS model [McGraw00]:

$$\varepsilon_I(i,k) \;=\; VIG_i \cdot x(k) \Bigg/ \sqrt{1-\left(\frac{R_E \cos E(i,k)}{R_E + h_I}\right)^2} \tag{2.18}$$

where ε_I is the L1 ionospheric error (negative for carrier), *VIG* is the vertical ionospheric gradient, h_I is the ionospheric shell height (350 km), R_E is the earth radius, and x is the distance of the airplane from the ship. (E, i and k are as defined earlier.) The coefficient of the ionospheric decorrelation model in equation 2.11 is defined as:

$$\Delta ic_k^i = x(k) \Bigg/ \sqrt{1-\left(\frac{R_E \cos E(i,k)}{R_E + h_I}\right)^2}$$

In the covariance analysis, an independent *VIG* state was included for each satellite. At aircraft approach initiation, the uncertainty in knowledge of each *VIG* state was defined by $VIG_i \sim N(0, \sigma_{VIG})$. For a nominal error model, we assumed $\sigma_{VIG} = 1$ mm/km, but this parameter was also varied in the sensitivity analysis.

2.3.3 Multipath and Receiver Noise Error Model. Both code and carrier errors were modeled as first order Gauss-Markov Random Processes (GMRPs). Independent GMRPs were assumed for code and carrier for each frequency and for each satellite. The

associated GMRP standard deviations and time constants were treated as parameters which were varied in the analysis to quantify the effect of receiver/antenna quality on overall SRGPS performance. The time constants and standard deviations (for single difference measurement error) used in this work were:

- Time constant: $\tau \in \{40, 60, 120\}$ sec
- P(Y) Code: $\rho \in \{0.1, 0.15, 0.3\}$ m
- Carrier: $\lambda\phi \in \{0.5, 1.0, 1.5, 2.0\}$ cm

Each error standard deviation listed was applied to both L1 and L2 measurements for all satellites, independent of elevation. Each error time constant was applied to all measurement models.

2.3.4 Floating and Fixed Integer Implementation Model. During each simulated approach, both aircraft and satellite motion were modeled. The state covariance matrix (including floating cycle ambiguity, position, and error model states) was propagated in time during the approach. For floating implementation results, only the time history vertical position error standard deviation σ_{vert} (a direct output of the covariance propagation) was of interest. The basic performance criteria used in this analysis was the Vertical Protection Level under fault-free (*H0*) conditions (VPL_{H0}), defined by

$$\text{Prob}\left\{\left|\hat{x}_{vert} - x_{vert}\right| > VPL_{H0}\right\} = 10^{-7} \quad \Rightarrow \quad VPL_{H0} = 5.33\sigma_{vert}\,. \tag{2.19}$$

It is noted that in this initial analysis, we have allocated the total allowable navigation integrity risk (10^{-7}) entirely to the fault-free case. For navigation availability it is required that $VPL_{H0} < VAL$, where VAL is the specified Vertical Alert Limit (1.1 m). Overall fault-free service availability (A_{FF}) was defined as:

$$A_{FF} = \text{Prob}\{VPL_{H0} < VAL\}. \tag{2.20}$$

For fixed-integer implementations, a correct fix (*CF*) of the cycle ambiguities, or some subset linear combination of cycle ambiguities, will improve positioning performance such that $\sigma_{vert|CF} < \sigma_{vert}$. Obviously, for a fixed-integer implementation it is desired that the probability of incorrect fix (P_{IF}) is small. In mathematical terms, the associated VPL_{H0} is defined by:

$$\begin{aligned} &\text{Prob}\left\{\left|\hat{x}_{vert} - x_{vert}\right| > VPL_{H0} \,\middle|\, CF\right\} \cdot (1 - P_{IF}) \; + \\ &\text{Prob}\left\{\left|\hat{x}_{vert} - x_{vert}\right| > VPL_{H0} \,\middle|\, IF\right\} \cdot P_{IF} = 10^{-7} \end{aligned} \tag{2.21}$$

Given an incorrect fix, it is assumed that the resulting position error will generally be large, so that:

$$\text{Prob}\left\{\left|\hat{x}_{vert} - x_{vert}\right| > VPL_{H0} \,\middle|\, IF\right\} \approx 1 \tag{2.22}$$

Substituting (2.16) into (2.15), we obtain

$$\text{Prob}\left\{\left|\hat{x}_{vert} - x_{vert}\right| > VPL_{H0} \,\middle|\, CF\right\} = \frac{10^{-7} - P_{IF}}{1 - P_{IF}} \tag{2.23}$$

so that

$$VPL_{H0} = k(P_{IF}) \cdot \sigma_{vert|CF} \,. \tag{2.24}$$

The integrity multiplier k in equation 2.24 is plotted as a function of P_{IF} in Figure 2.3. For very small P_{IF}, the integrity multiplier approaches 5.33, the value in equation 2.19. However, as P_{IF} approaches 10^{-7}, the integrity multiplier, and hence VPL_{H0}, grows very large. For this analysis, we imposed a reasonable, intermediate requirement on the 'fixed' implementation: $P_{IF} < 10^{-8}$. In this case,

$$VPL_{H0} = 5.35\,\sigma_{vert|CF} \,. \tag{2.25}$$

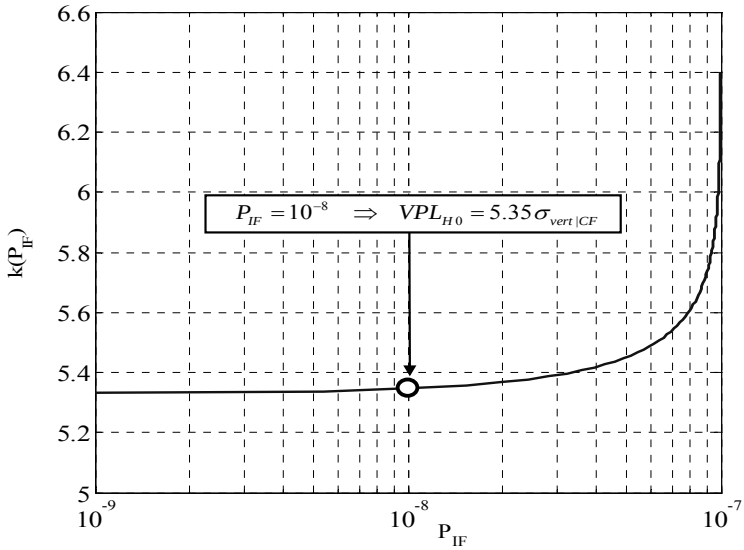

Figure 2.3. Integrity Multiplier as a Function of P_{IF}

The fixed-integer implementation model used in this analysis was Teunissen's 'Integer Bootstrapping' algorithm with LAMBDA cycle ambiguity decorrelation [Teunissen98]. The Integer Bootstrapping implementation is a successive rounding approach for which it is possible to directly compute the probability of correct fix (P_{CF}).

An illustrative example of a hypothetical airplane approach result is shown in Figure 2.4. The approach begins at the specified GPS data broadcast radius (at the far

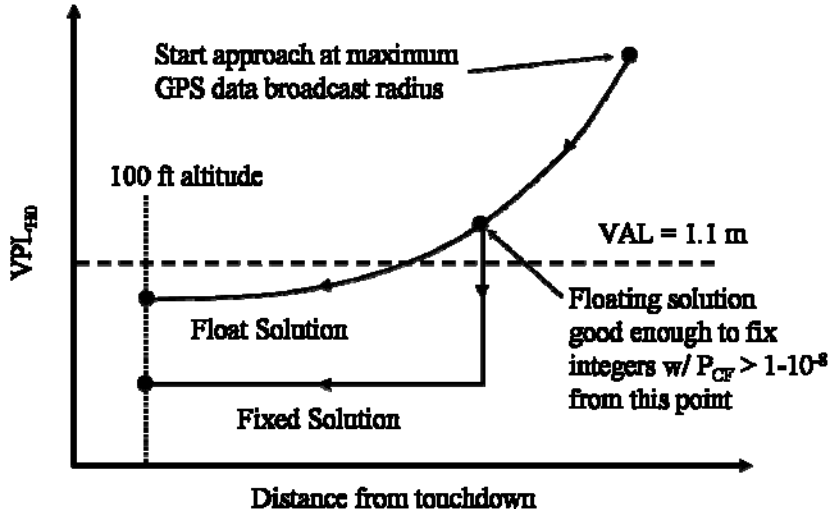

Figure 2.4. Evolution of VPL_{H0} for a Single Hypothetical Approach

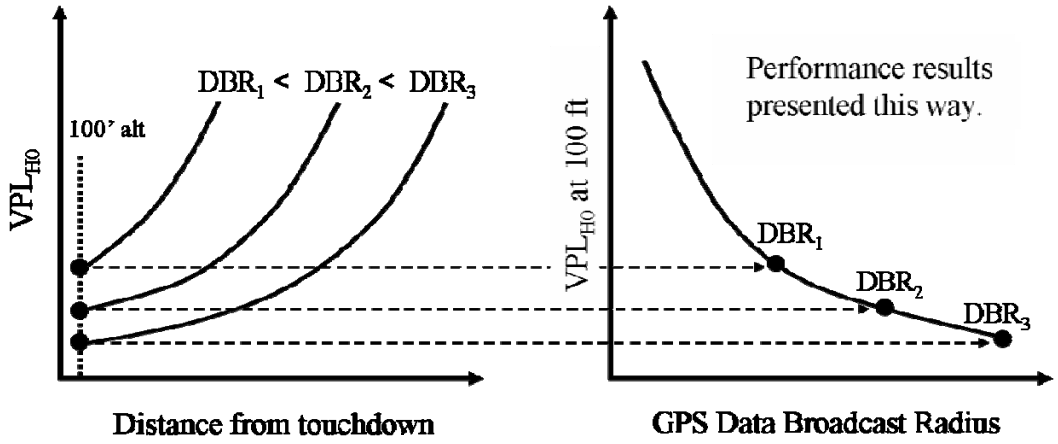

Figure 2.5. Format of Plotted Results

right in the figure). As time passes, the aircraft approaches the ship ('distance from touchdown' gets smaller) and the combined effect of filtering and satellite motion will cause σ_{vert} (floating), and therefore VPL_{H0}, to become smaller. At a certain point during the approach the probability of correct fix may become larger than the minimum required ($1-10^{-8}$). From this point on, a fixed solution is possible.

To consolidate the results from a large number of simulated approaches (associated with different satellite geometries and SRGPS parameter values) in a relatively compact way, VPL_{H0} results will be presented as illustrated in the right-hand plot in Figure 2.5. Here, a single curve is used to define the variation in VPL_{H0} at 100 ft altitude with GPS data broadcast radius (*DBR*), for a given satellite geometry. The satellite geometry is matched (for all of the approaches used to generate the right-hand curve) at the 100 ft altitude point; thus, as *DBR* increases the final geometry is the same, but there exists a longer prior exposure time for satellite motion and filtering. In this way, the results for many satellite geometries (many such curves) can be presented on a single plot.

2.4 Performance Results and Parameter Sensitivity

SRGPS fault-free availability was evaluated over an entire day of satellite geometries. Performance of single and dual-frequency architectures were assessed for both floating-ambiguity and fixed-integer implementations as functions of code-phase (pseudorange) and carrier-phase error standard deviations, measurement error time constant, and data broadcast radius. In all cases, fixed-integer implementations were constrained to achieve $P_{IF} < 10^{-8}$. Availability results were generated for both the full 24-satellite GPS constellation as well as depleted GPS constellations. The depleted constellation results were combined to compute overall average service availability based on the 'minimum standard' constellation state probability model given in the GPS Standard Positioning Service Performance Standard [GPSSPS]. The state probability model is shown in Table 2.1. The results for the full 24-satellite case, which may be interpreted as upper bounds on availability given the specified error models, were used principally to evaluate the sensitivity of availability results to variations in ionospheric and tropospheric error model parameters and processing architectures (i.e., fixed vs. floating). A 30-processor parallel PC cluster was used to manage computational load

Table 2.1. Satellite Constellation State Probability Model

Number of Operational Satellites (N)	Probability of N Operational Satellites
24	0.950
23	0.030
22	0.012
21	0.005
20	0.003

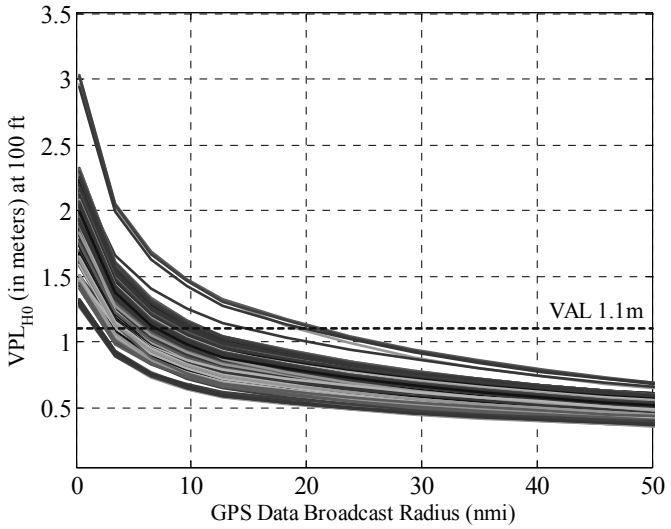

Figure 2.6. Full Day Results, Dual Frequency Floating Implementation

associated with the processing of aircraft approaches for the large number of satellite outage cases, error model parameter combinations and broadcast radii. The results described below quantify the tradeoffs between navigation system availability and derived requirements on receiver/antenna performance and data broadcast radius.

2.4.1 Dual-Frequency Performance. Example results for a complete day of satellite

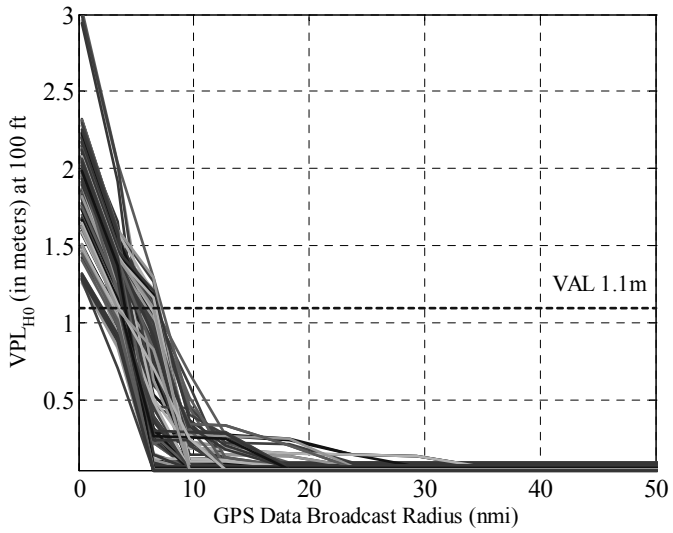

Figure 2.7. Full Day Results, Dual Frequency Fixed Implementation

geometries are shown in Figures 2.6 and 2.7 for floating and fixed-integer implementations, respectively. These results correspond to the full GPS constellation case with specific measurement error values of σ_ϕ = 1 cm, σ_{PR} = 0.3 m and τ = 40 sec. The nominal ionospheric and tropospheric error models described earlier were also used. By comparing the two figures, it is immediately clear that the fixed-integer performance (even with the P_{IF} constraint) is superior to the floating implementation in the sense that much smaller *DBR* values are required to achieve sub-*VAL* performance.

Figures 2.8 and 2.9 show 'unavailability' ($1-A_{FF}$) as a function of *DBR* using a full constellation for floating and fixed-integer implementations respectively. These results correspond to error model parameter values of σ_ϕ = 1 cm, $\sigma_{PR} \in \{0.1, 0.15, 0.3\}$ m, and $\tau \in \{40, 60, 120\}$sec. The figures quantify the relative benefits of fixed versus floating-integer implementations directly in terms of availability. Specifically, it is noted that when σ_{PR} is large, the availability provided by a fixed-integer implementation is

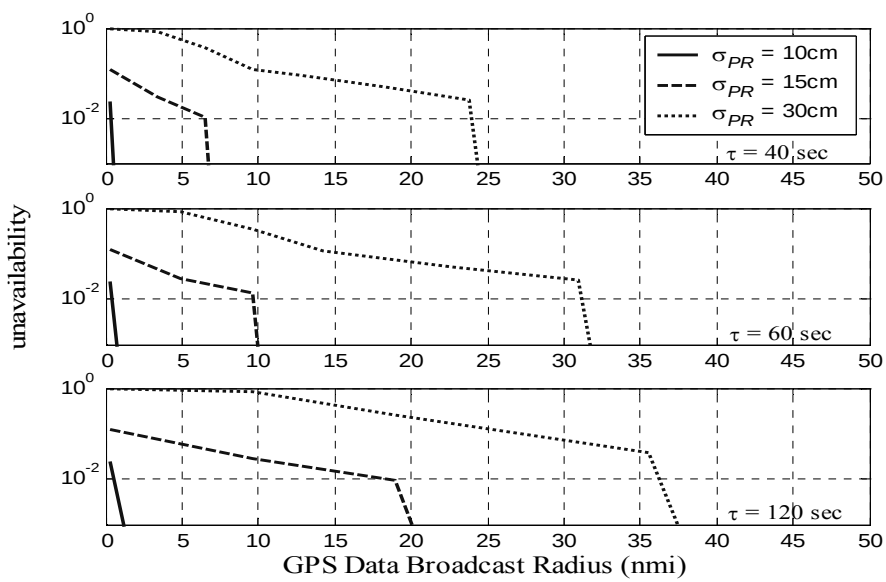

Figure 2.8. Availability of Dual Frequency Floating Implementation, σ_ϕ = 1 cm (Full Constellation)

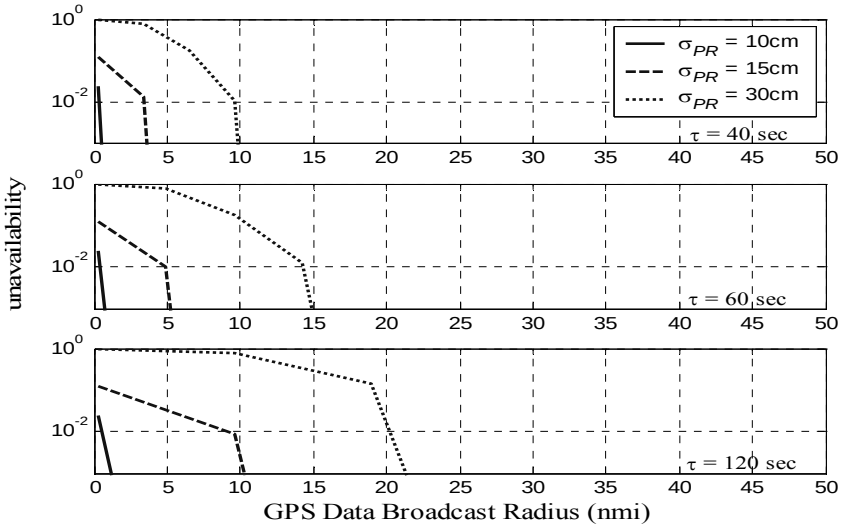

Figure 2.9. Availability of Dual Frequency Fixed Implementation, σ_ϕ= 1 cm (Full Constellation)

notably better than that by the floating implementation, but when σ_{PR} is small, roughly equivalent availability is achievable using either implementation.

This is true because when σ_{PR} is very small (~10 cm), the floating-integer implementation is typically good enough to ensure that VPL_{H0} is smaller than VAL (1.1

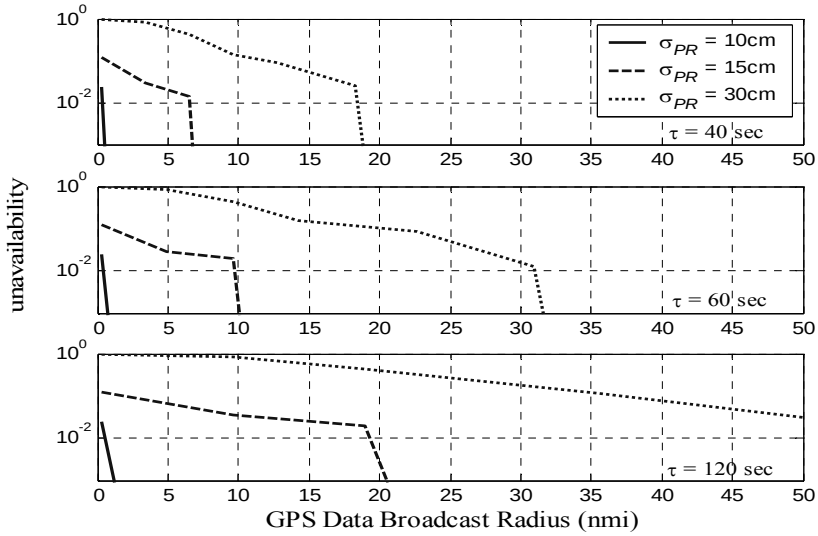

Figure 2.10. Availability of Dual Frequency Fixed Implementation, σ_ϕ= 1.5 cm (Full Constellation)

m). Thus any further improvement in accuracy provided by the fixed implementation will not significantly improve availability. Figure 2.10 shows analogous (fixed-integer implementation) results to Figure 2.9 for σ_ϕ = 1.5 cm. Comparing Figures 2.9 and 2.10, it is evident that availability (or equivalently, required *DBR*) is much more sensitive to σ_ϕ when σ_{PR} is large. This is true because for small σ_{PR} code-phase measurements provide a more reliable basis for cycle ambiguity estimation, whereas for large σ_{PR} cycle resolution performance is more heavily dependent on the quality of redundant carrier phase measurements.

Common to all three figures is an obvious dependence on measurement error time constant. In general, for a given *DBR*, the effectiveness of filtering during the approach decreases as the error time constant increases. Conversely, as error time constant is increased, larger *DBRs* are required to maintain a constant level of availability. As σ_{PR} is lowered, however, it is true that positioning performance near the ship is less dependent on prior filtering during the approach. In this case, sensitivity to measurement error time constant is reduced significantly.

Figure 2.11 shows an interpolated mapping of covariance simulation results using all combinations of error model parameter values derived from the nominal sets defined earlier: $\sigma_{PR} \in \{0.1, 0.15, 0.3\}$ m, $\sigma_\phi \in \{0.5, 1.0, 1.5, 2.0\}$ cm, and $\tau \in \{40, 60, 120\}$ sec. This figure specifically relates the receiver error performance characteristics (σ_{PR}, σ_ϕ, τ) and *DBR* required to provide availability of 99.7% using a full GPS constellation. For example, for given values of *DBR* (defined on the horizontal axis), σ_{PR} and τ (defined by the separate curves), the vertical axes defines the necessary values of σ_ϕ in

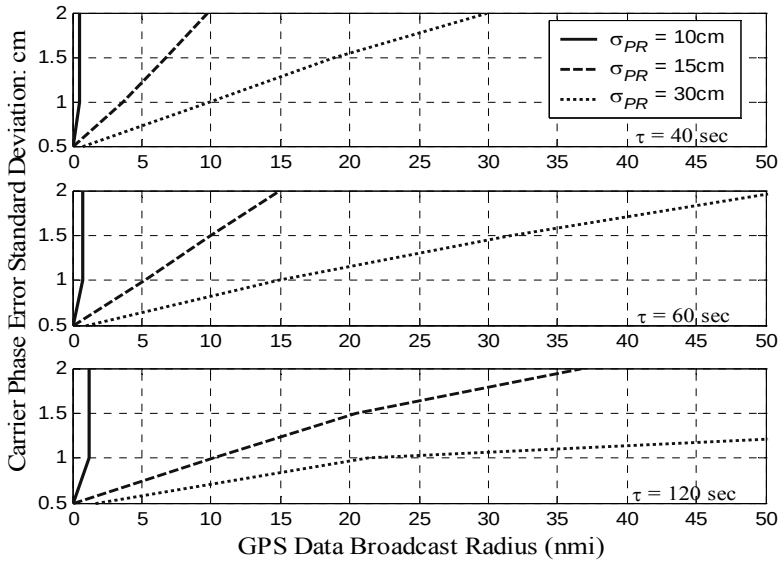

Figure 2.11. Dual Frequency Fixed Implementation System Requirements to Achieve 0.997 Availability (Full Constellation)

order to achieve the 0.997 availability. The results are encouraging in the sense that 99.7% availability is achievable with reasonable receiver error performance characteristics and data broadcast radius (e.g., σ_{PR} = 30 cm, σ_{ϕ} = 1 cm, τ = 2 min, and *DBR* = 20 nmi).

When satellite outages were considered, however, more stringent requirements on receiver error performance and *DBR* are required to achieve 99.7% availability. In this regard Figure 2.12 shows performance curves using the depleted constellation model in Table 2.1. The results are clearly quite different from those in Figure 2.11 (where all satellites were assumed functional). In particular, the poorer satellite geometries cause the system performance to become very sensitive to σ_{ϕ}, even when σ_{PR} is as small as 10 cm. This is due simply to the fact even when cycle ambiguities are correctly resolved,

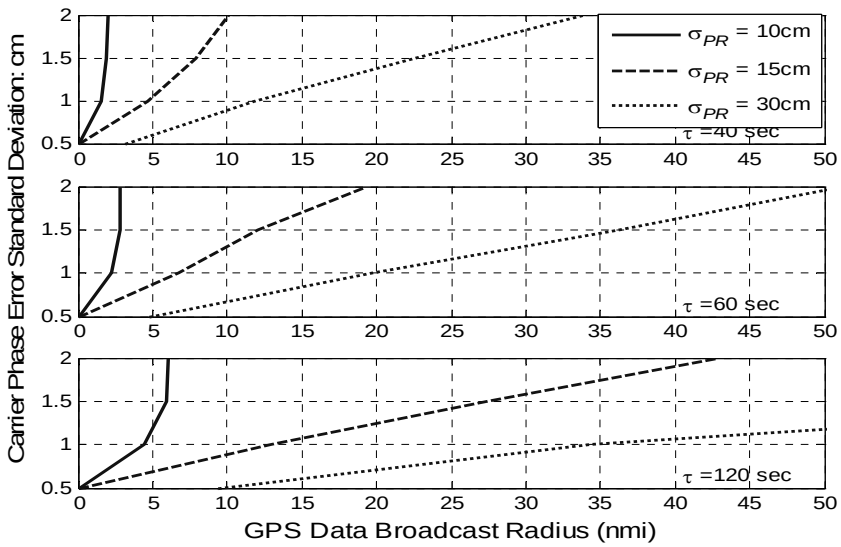

Figure 2.12. Dual Frequency Fixed Implementation System Requirements to Achieve 0.997 Availability (Depleted Constellation)

the achievable VPL_{H0} is still fundamentally limited by the quality of the satellite geometry and σ_{ϕ}

2.4.2 Dual-Frequency Performance Sensitivity. The sensitivity of dual-frequency SRGPS performance results to tropospheric and ionospheric error model parameters was also explored by varying each parameter directly. In addition, the dependency of performance on the effects of satellite motion was also examined. The results of these sensitivity analyses for the dual-frequency case are described below.

Satellite Motion. It is well known that satellite motion can be a helpful factor in cycle ambiguity estimation. However, over the time scale of an SRGPS aircraft approach, it is unclear whether such motion is significant enough to provide measurable benefits beyond those naturally realized from simply filtering code and carrier errors. To investigate the relative benefits of satellite motion for SRGPS, results comparable to those in Figure 2.9 were regenerated by holding fixed the satellite geometry during the course of each approach. The results of this exercise, shown in Figure 2.13, show little change in the performance relative to Figure 2.9. In general, the GPS satellite motion is not significant enough over the time scales of interest to affect the performance of a dual-frequency system. The only notable exception occurs for larger values of σ_{PR} and τ. In this case, filtering of code and carrier is less effective, making satellite motion relatively more beneficial.

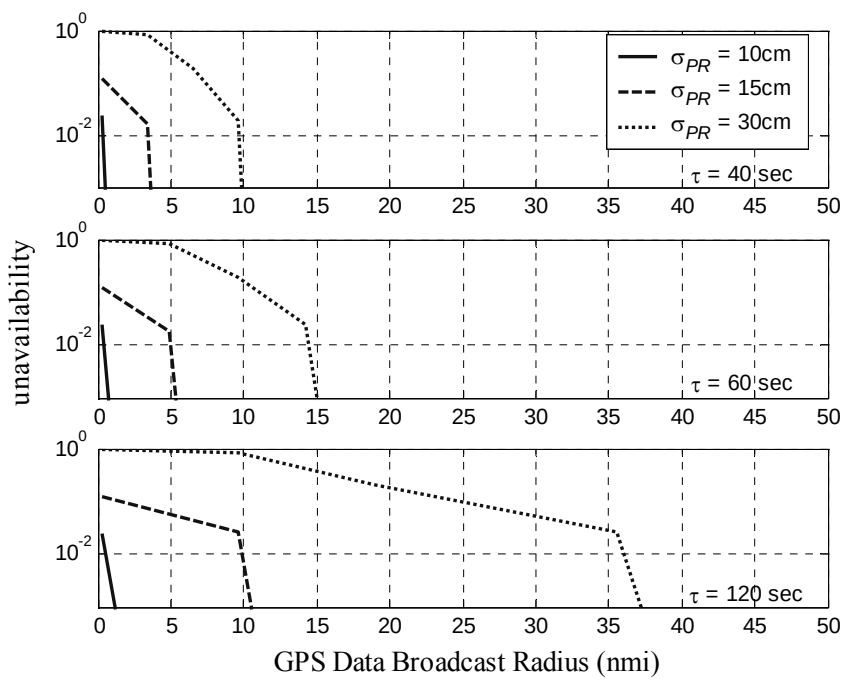

Figure 2.13. Dual Frequency Performance Sensitivity to Satellite Motion, Fixed Implementation, σ_ϕ = 1 cm (Full Constellation)

Ionospheric Spatial Gradient. The sensitivity of dual-frequency implementation performance to ionospheric spatial gradient was also investigated. In this regard, Figure 2.14 shows the availability results when uncertainty in prior knowledge of vertical ionospheric gradient (VIG) was increased to σ_{VIG} = 1 cm/km for each satellite. Because the dual-frequency architecture allows for direct observation of ionosphere gradient during each approach, the performance exhibited here is not significantly different from the nominal case in Figure 2.9, where σ_{VIG} = 1 mm/km.

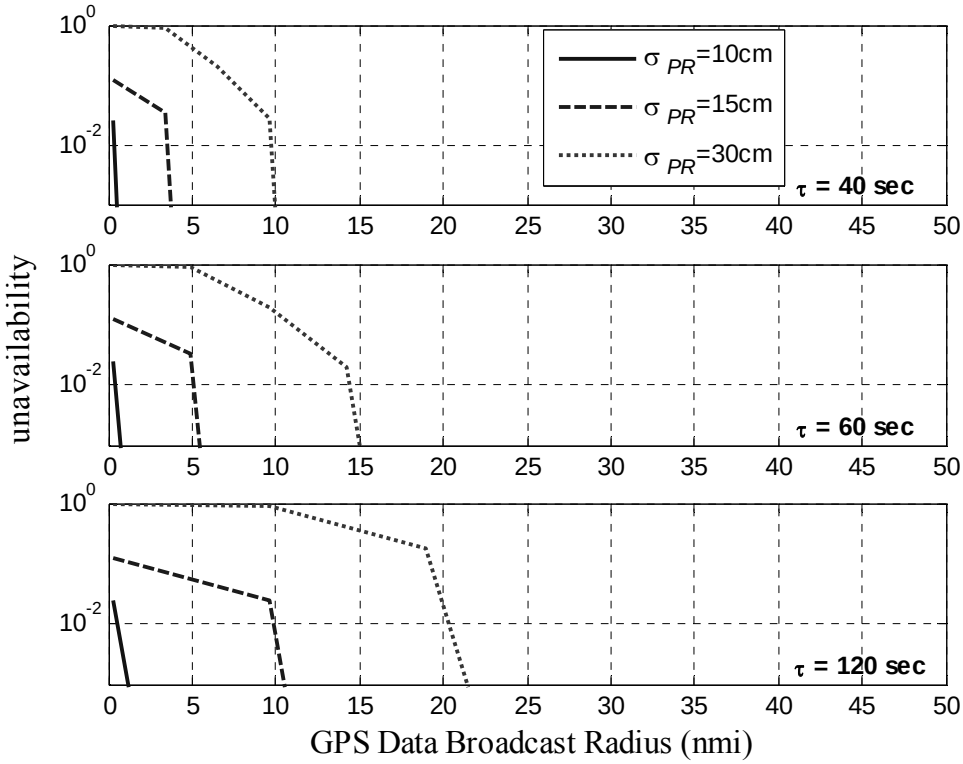

Figure 2.14. Dual Frequency Performance Sensitivity to Ionospheric Gradient Uncertainty, Fixed Implementation, σ_{th} = 1 cm (Full Constellation)

Tropospheric Decorrelation. Figure 2.15 shows the availability results when the uncertainty on prior knowledge of residual tropospheric refractivity was increased to σ_N = 100. When compared to the nominal model results (σ_N = 10) in Figure 2.9, the results show relatively low sensitivity to uncertainty in residual tropospheric refractivity. The only noteworthy exception occurs when both σ_{PR} and τ are large. In this case, a slightly longer filtering time (larger *DBR*) is required to achieve the same availability as the nominal case.

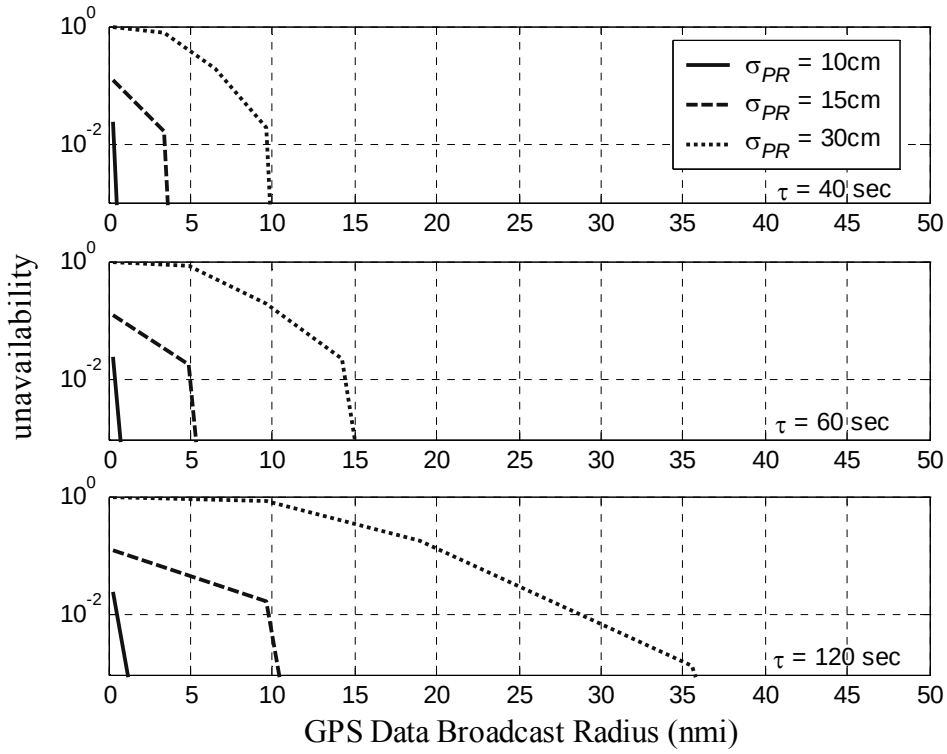

Figure 2.15. Dual Frequency Performance Sensitivity to Residual Tropospheric Decorrelation, Fixed Implementation, σ_ϕ = 1 cm (Full Constellation)

2.4.3 Single-Frequency Performance. The full-day system performance results for a single-frequency SRGPS implementation (using the full GPS constellation and the nominal error models with σ_ϕ =1 cm and 1.5 cm, respectively) are shown in Figures 2.16 and 2.17. It is not surprising that the performance here is significantly worse than that for the dual-frequency case (see for comparison Figures 2.9 and 2.10). In these results, differentiation between floating and fixed single-frequency implementations is unnecessary since the availability results for both cases are the same. This is true because whenever integer fixing is possible under the integrity constraint $P_{IF} < 10^{-8}$, the value of VPL_{H0} for the floating implementation is typically already below *VAL*. Therefore, while integer fixing can improve accuracy, it does not affect availability.

Figure 2.18 quantifies the required receiver error performance characteristics

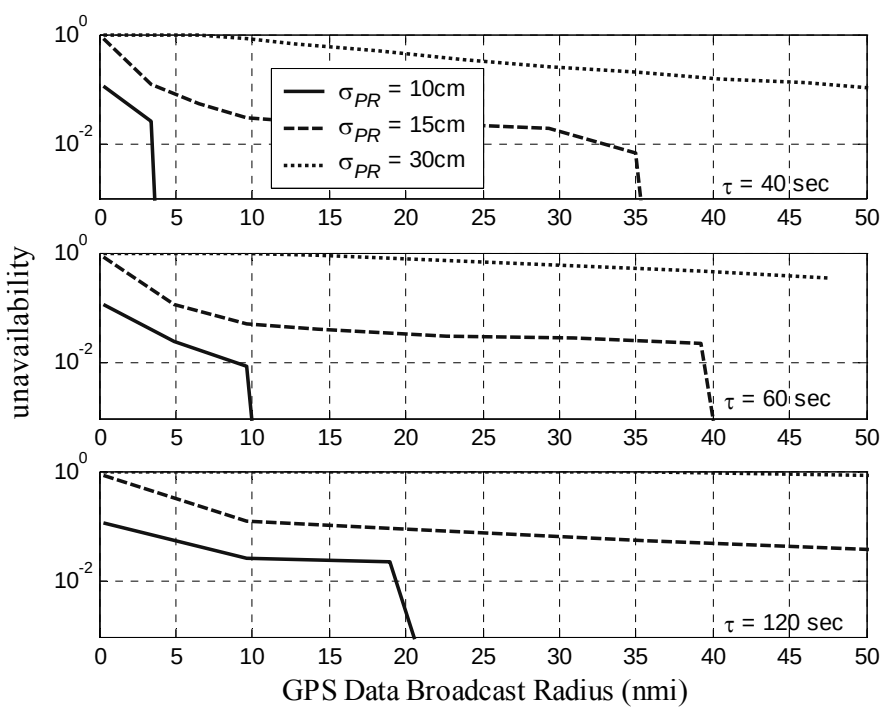

Figure 2.16. Availability of Single Frequency Implementation, σ_ϕ= 1 cm (Full Constellation)

(σ_{PR}, σ_{ϕ}, τ) and *DBR* to provide availability of 99.7% given a full GPS constellation. When compared to the dual-frequency system requirements seen earlier in Figure 2.11, the single-frequency results reveal that 99.7% availability is achievable only with significantly more stringent requirements on receiver measurement error performance and larger *DBR*. Furthermore, as seen in Figure 2.19, achieving 99.7% availability is even more difficult when satellite outages are considered. The stringent system requirements defined in the figure suggest that 99.7% availability is likely an unrealistic goal for a single-frequency SRGPS architecture. Nevertheless, the lower availability provided using single-frequency processing may be sufficient to provide backup capability for a nominal dual-frequency architecture in the event of interference or jamming at one of the two GPS frequencies. For example, Figure 2.20 shows that the single frequency system requirements to provide 95% availability are far less stringent.

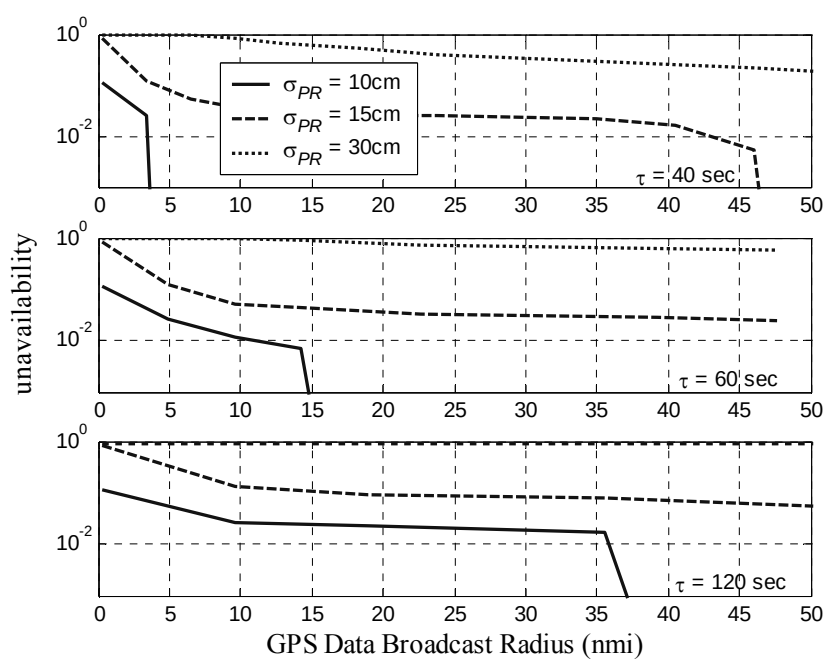

Figure 2.17. Availability of Single Frequency Implementation, σ_{ϕ}= 1.5 cm (Full Constellation)

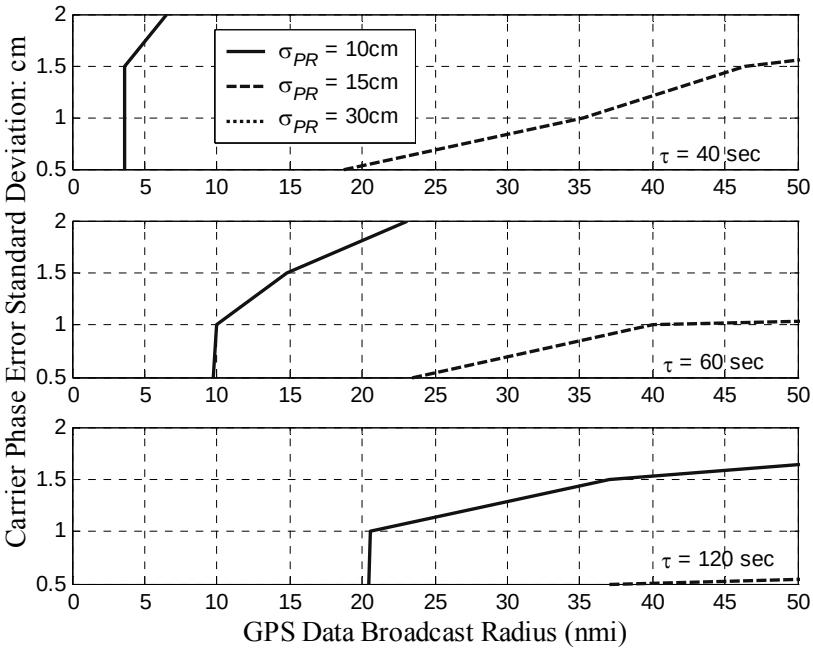

Figure 2.18. Single Frequency System Requirements to Achieve 0.997 Availability (Full Constellation)

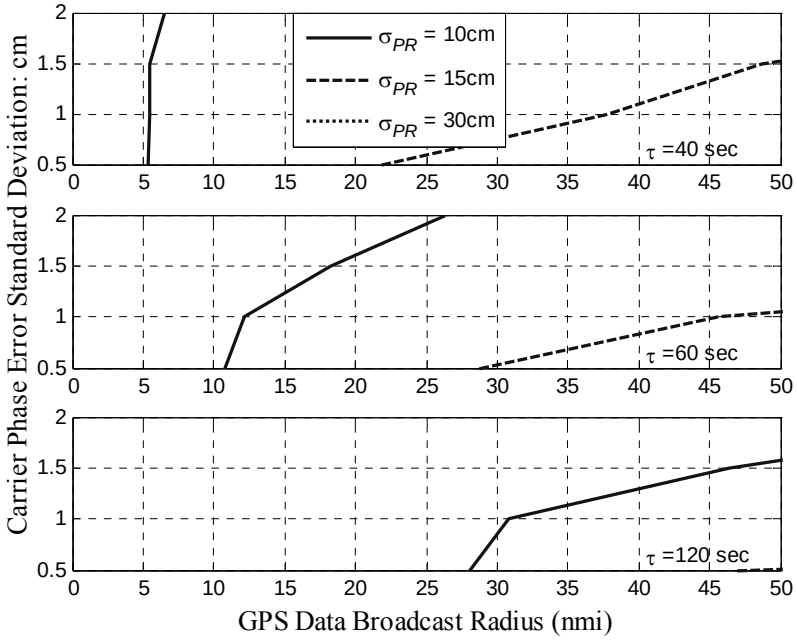

Figure 2.19. Single Frequency System Requirements to Achieve 0.997 Availability (Depleted Constellation Model)

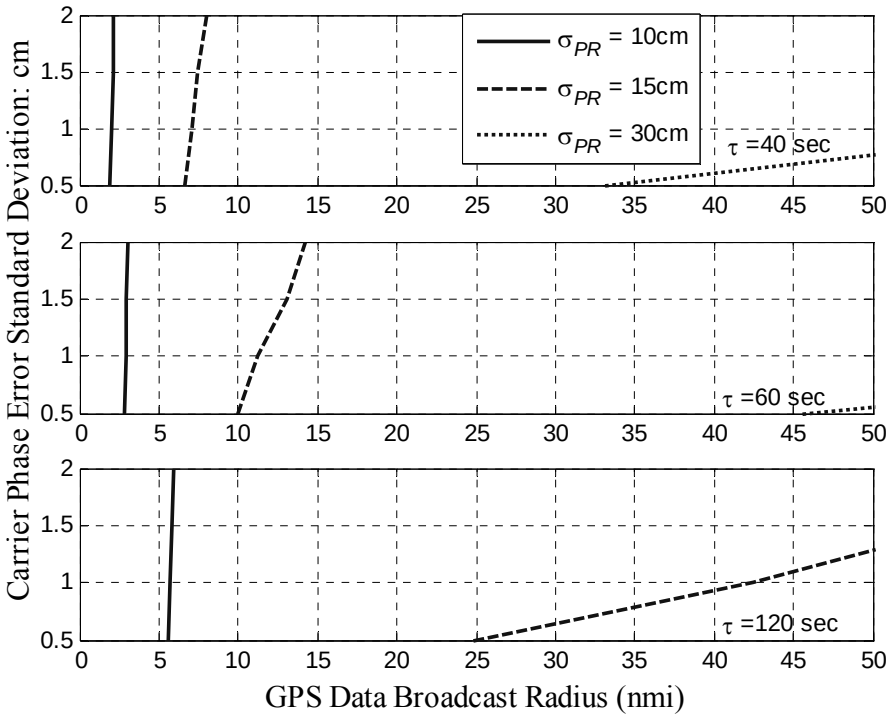

Figure 2.20. Single Frequency System Requirements to Achieve 0.95 Availability (Depleted Constellation Model)

2.4.4 Single-Frequency Performance Sensitivity. For completeness, the sensitivity analyses performed for the dual-frequency case were repeated for the single-frequency architecture. The performance of the single frequency were evaluated as the base to consider the possibility of using the single frequency system as a back-up during the hostile jamming at one of the two GPS frequencies. The results are described briefly in following pages.

Satellite Motion. As with the dual-frequency case, the relative benefit of satellite motion for a single-frequency SRGPS architecture was evaluated by holding fixed the satellite geometry during the course of each approach. The results are shown in Figure 2.21. When these are compared to the results in Figure 2.16 (where the effects of satellite motion were utilized), it is evident that performance is much worse for the single-frequency case when satellite motion is not exploited. While it is true that the geometry change over the timescale of a typical aircraft is no larger than that for the dual-frequency case, its relative importance to cycle ambiguity observability is clearly much greater for the single-frequency implementation.

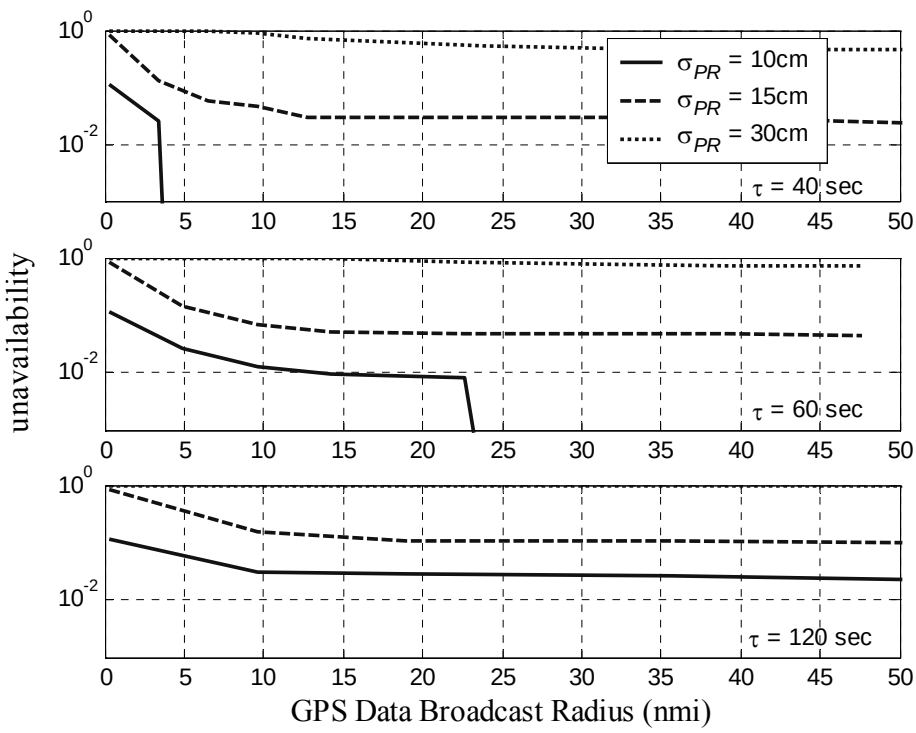

Figure 2.21. Single Frequency Performance Sensitivity to Satellite Motion, σ_ϕ = 1 cm (Full Constellation)

Ionospheric Spatial Gradient. In general, it is expected that a single-frequency implementation will be more susceptible to ionospheric effects than a dual-frequency implementation. This expectation is quantitatively supported in Figure 2.22, which shows single-frequency implementation availability when the assumed prior knowledge of vertical ionospheric gradient was increased to σ_{VIG} = 1 cm/km for each satellite. In comparison with the single-frequency results in Figure 2.16 for σ_{VIG} = 1 mm/km, Figure 2.22 shows much greater relative sensitivity to ionospheric spatial gradient than the dual-frequency case covered earlier.

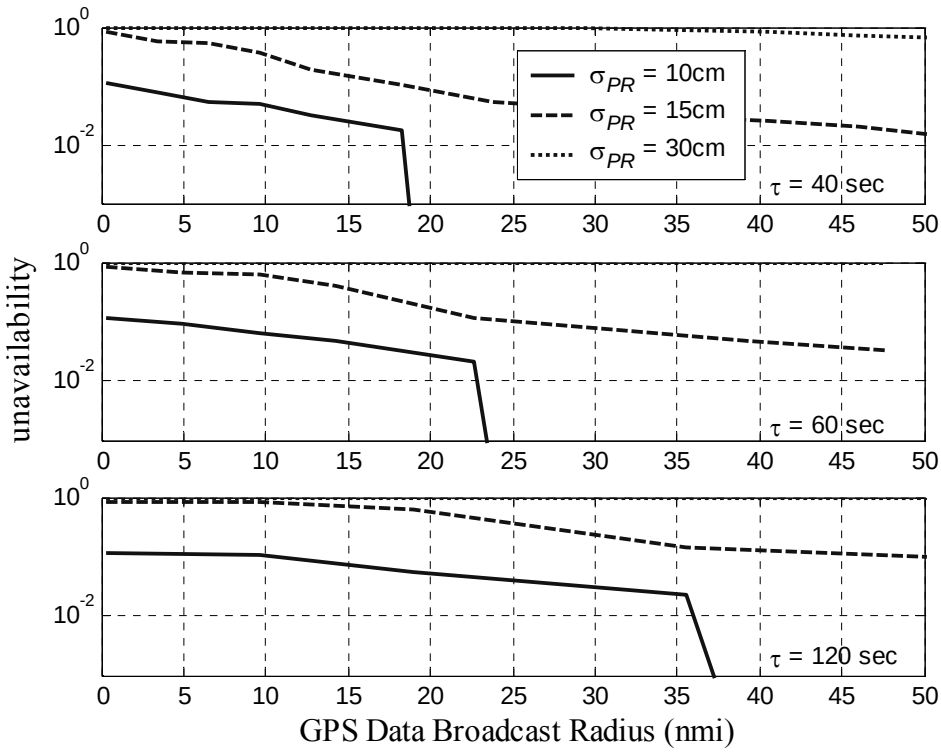

Figure 2.22. Single Frequency Performance Sensitivity to Ionospheric Gradient Uncertainty, σ_ϕ = 1 cm (Full Constellation)

Residual Tropospheric Decorrelation. Figure 2.23 shows the availability results when the uncertainty on prior knowledge of residual tropospheric refractivity was increased to σ_N = 100. When these results are compared to those for in Figure 2.16 (where σ_N = 10), it is evident that the availability is only mildly sensitive to residual tropospheric refractivity uncertainty. Recall that this was also true for the dual-frequency case.

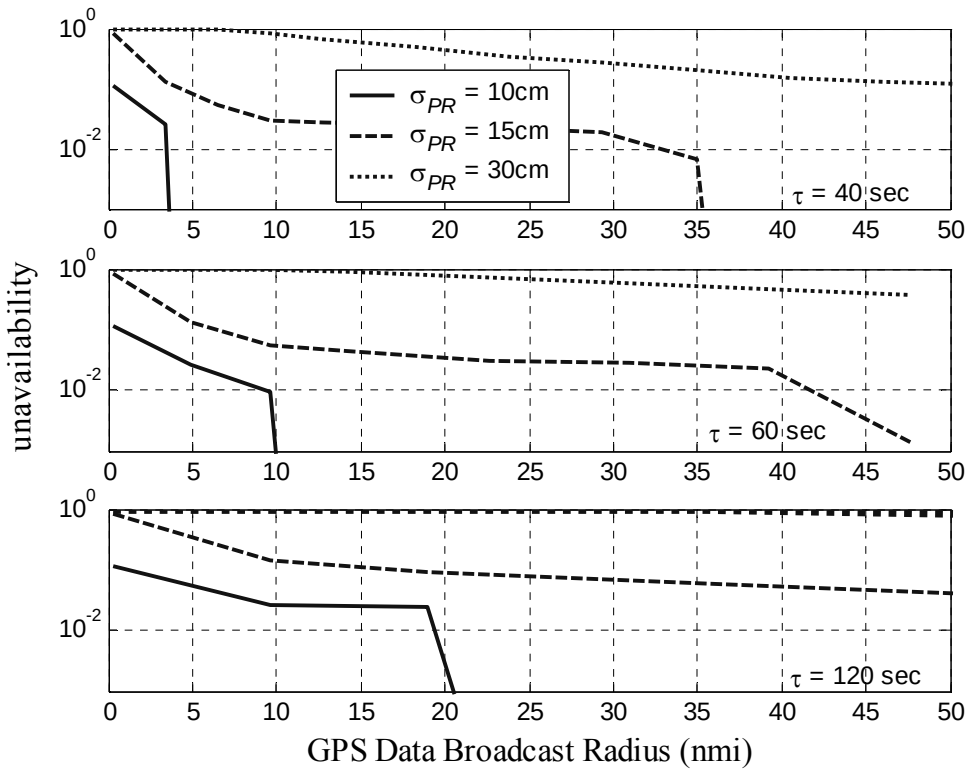

Figure 2.23. Single Frequency Performance Sensitivity to Residual Tropospheric Decorrelation, σ_ϕ = 1 cm (Full Constellation)

2.5 Summary of SRGPS Research

In this work, fault-free SRGPS performance was quantified as a function of data broadcast radius and relevant ranging error parameters, including raw code and carrier measurement error standard deviations and time constants, ionospheric spatial gradient uncertainty, and residual tropospheric decorrelation uncertainty. The results demonstrated that for dual-frequency architectures, a fixed-integer realization is superior to a floating-integer implementation, even when stringent constraints on the probability of correct integer resolution are applied. Moreover, the required receiver measurement error performance and data broadcast radius to achieve a system availability of 99.7% was parametrically quantified for both full and depleted GPS satellite constellations. It also shows that for a single-frequency architecture, no availability benefit is derived from the use of a fixed-integer implementation (relative to a floating-ambiguity processing). In addition, the performance of the single-frequency implementation was demonstrated to be highly sensitive to depleted satellite constellations. While achieving 99.7% availability is likely an unrealistic goal for a single-frequency architecture, in the event of interference or jamming at one of the two GPS frequencies, single-frequency processing may provide sufficient availability to function as a backup for a nominal dual-frequency/fixed-integer architecture.

To the concern of the stringent safety requirements for aviation applications, any aircraft landing system should be robust to external interferences. Unfortunately, for any navigation system which utilizes radio wave as the primary ranging source, RFI is an issue that needs to be addressed especially for low power radio wave system like GPS. Controlled reception pattern (phased array) shipboard antennas will be implemented in

SRGPS to provide superior performance in a jamming environment and to mitigate multipath [Kim04]. These antennas can also be expected to benefit SRGPS performance by providing exceptionally precise code and carrier measurements at the reference station for satellites at all elevations [Brown01]. On the system architecture level, a pre-filtering algorithm is analyzed by Heo [Heo06]. In his work, it shows that a much smaller data broadcast radius is needed to achieve the system requirements for the pre-filtering system architecture. A smaller data broadcast radius reduces the chance of exposing the system to the outside environment and, therefore, lower the likelihood of being interfered by intentional/unintentional RFI sources.

Even with all these precautious and thoroughly considered measures to mitigate the risk of RFI, the threat can't be eliminated completely. Moreover, for civil aviation applications, no option is currently available for a dual-frequency architecture; therefore, this excludes using a single-frequency system as back-up during an interference/jamming event. In response, a tightly coupled GPS/INS navigation system is designed to eliminate RFI threats by free-INS coasting during the most critical final approach segment. A novel GPS/INS hybrid navigation system based on the SRGPS single-frequency architecture is developed in the next chapter for precision approach and landing in civil aviation applications.

CHAPTER 3

A GPS/INS HYBRID NAVIGATION SYSTEM FOR PRECISION APPROACH AND LANDING

Innovative GPS/INS navigation system with tight-coupling integration implementation is described and the system error models are derived in detail in this chapter. The novel part of the proposed hybrid system is the way to fuse INS information with estimated DGPS states. Instead of conventionally calibrating INS and estimating position in separated processes, only linearized DGPS measurement updates (the same as the SRGPS measurement update in Section 2.1 with single frequency measurements only) are needed to calibrate INS errors and estimate system positions at the same time in a centralized Kalman filter. In the hybrid navigation system configuration, carrier-phase measurements are crucial for precise INS calibration. Although carrier-phase measurements are not included in the current LAAS broadcast message, message type six has been predefined in the Appendix C of *GNSS Based Precision Approach Local Area Augmentation System (LAAS) – Signal-in-Space Interface Control Document (ICD*) [RTCA/DO246C] for the future possibility of broadcasting carrier corrections. Explanations on the essentials of inertial navigation are presented in the beginning to facilitate the later derivation of the GPS/INS integration algorithm.

3.1 Inertial Navigation System (INS) Introduction

The mechanism behind an inertial navigation system is the dead reckoning process. The principle of "dead reckoning" is to propagate user positions based on the vehicle speed and heading information taken during the time after departing from previous known location. This process inevitably translates speed and heading errors into

position errors which continuously propagate with time. Therefore, the key point for this navigation system to work properly depends on the accuracy of the user dynamic information and the fast position-update rate to follow the user's motion faithfully. The time-growing position error in dead reckoning systems does not fit well for some applications, however the self-contained characteristic has made it very desirable to certain military operations, oceanic navigation or even the only choice for special missions, such as deep sea exploration.

With dramatic advances on modern technology, high quality inertial sensors, which can deliver user's acceleration and rotation information fast and accurately, have made themselves the perfect candidates for dead reckoning navigation. An inertial navigation system (INS) normally refers to a system that is able to generate user position, velocity and attitude information by applying the dead reckoning process on the measurements from inertial sensors. Normally, the sensor cluster unit within the INS is called inertial measurement unit (IMU). In other words, an INS is a self-contained dead reckoning navigation system based on propagating acceleration and rotation measurements from IMU to provide user position, velocity and attitude information in time.

3.1.1 Navigation Reference Frame. A proper coordinate system is the foundation of any navigation system. Through the development of GPS navigation system, an earth centered global datum was defined and refined several times to become the current World Geodetic System 1984 (WGS 84) by the Defense Mapping Agency, which became a part of the National Imagery and Mapping Agency (NIMA) in 1996, and reorganized as the National Geospatial-Intelligence Agency (NGA) in 2004. The basis of the WGS 84 earth

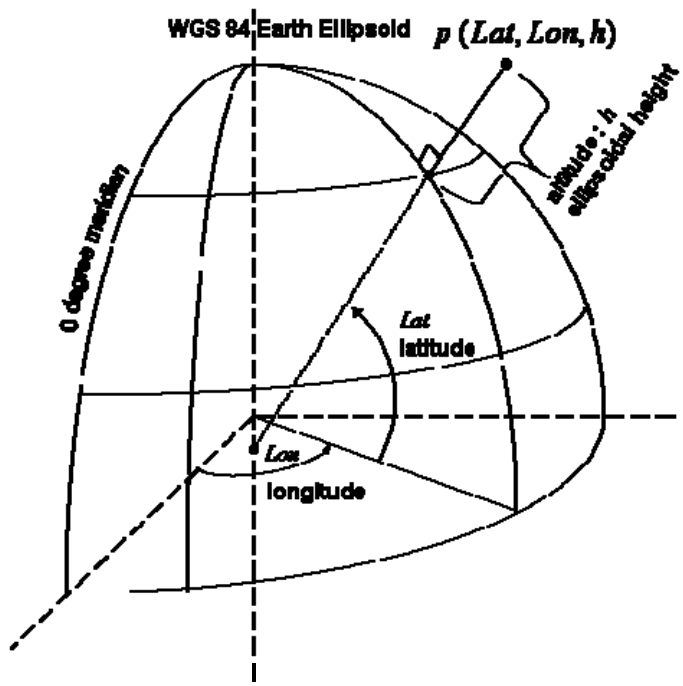

Figure 3.1. LLA Position on WGS 84 ellipsoid

model is a least-square fit ellipsoid to a set of globally distributed datum points in conjunction with an Earth-Centered Earth-Fixed (ECEF) Cartesian coordinates. This WGS 84 ECEF coordinate system is the standard for any GPS application. Based on the WGS 84 ellipsoidal datum, Latitude Longitude and Altitude (LLA) can be defined accordingly. Figure 3.1 illustrates an LLA position on WGS 84 ellipsoid.

Because WGS 84 has gradually become an international standard due to widespread GPS applications, it is natural to apply it as the navigation coordinate system for INS as well. As illustrated in Figure 3.2, a local-level frame derived from WGS 84 is the coordinate frame normally adopted for inertial navigation systems, which has three mutually perpendicular axes (x, y and z) pointing toward local north, east and normal-downward directions respectively. Customarily, geodetic latitude, longitude and altitude, which are defined on WGS 84, are used to present positions for INS. The local-level

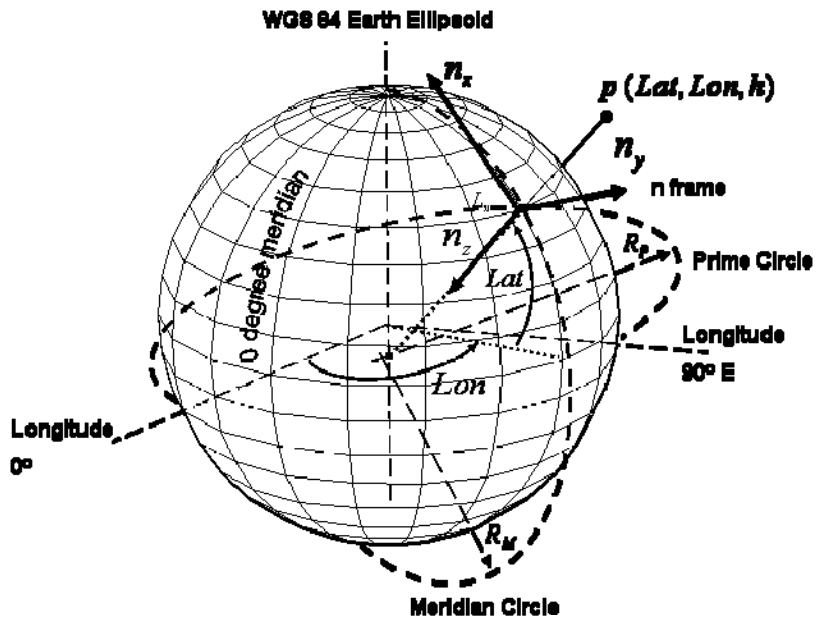

Figure 3.2 WGS 84 Ellipsoid and Navigation Frame

frame, whose origin coincides with the current LLA position, defines the navigation frame for INS. Speed and heading information that is presented in this navigation frame generally fit in with aircraft pilots' intuition of direction.

The transformation between ECEF and LLA frames can be easily accomplished with the currently available computational power. To compute ECEF position from LLA frame, equation 3.1 can be utilized:

$$\begin{bmatrix} x \\ y \\ z \end{bmatrix}_{ECEF} = \begin{bmatrix} (R_p + h)\cos(Lat)\sin(Lon) \\ (R_p + h)\cos(Lat)\cos(Lon) \\ (R_p(1-e^2) + h)\sin(Lat) \end{bmatrix} \tag{3.1}$$

where R_P is the prime radius of curvature and is a function of the latitude, the meridian radius is noted by R_M, and h is the ellipsoidal height. These two radii are expressed in equation 3.2 [IONtutorial02]:

Table 3.1. WGS-84 Earth Model Parameter

parameter name	symbol	value
eccentricity	e	0.0818191908426
ellipsoid major axis	r_e	6378137.0 meter
ellipsoid minor axis	r_n	$r_e(1-f) \approx 6356752.3142$ meter
flattening	f	$1/298.257223563$
earth rotation rate	w_{ie}	7.2921150×10^{-5} rad/s

$$R_P = \frac{r_e}{(1-e^2 \sin^2(Lat))^2}, \; R_M = \frac{r_e(1-e^2)}{(1-e^2 \sin^2(Lat))^{3/2}} \tag{3.2}$$

Other related parameters in these equations are defined by WGS-84 earth model and listed in Table 3.1 for reference.

To transfer an ECEF position into a corresponding LLA coordinates would need more effort because the latitude and longitude in equations 3.1 are the parameters inside trigonometric functions. Normally an iterative process is involved in order to get accurate transformation. More details about the coordinate transformation can be found in most of GPS or INS related books [Titterton04] [Misra01].

3.1.2 Navigation Equation in INS Navigation Frame. In order to correctly propagate user positions through IMU measurements, the system dynamic equations need to be derived. A notation clarification is necessary to avoid confusion afterward:

$\vec{V}_e^n$: a right superscript represents the coordinate frame in which the vector is expressed (*n* frame for this example). A subscript indicates the relativity of the vector. This example describes a velocity relative to an earth-fixed frame (ECEF for example) expressed in *n* frame (navigation frame) coordinates.

$\left.\frac{d\vec{V}_e^{\,n}}{dt}\right|^n \equiv {}^n\dot{\vec{V}}_e^{\,n}$: a left superscript represents that a derivative is taken with respect to that frame. This example describes a velocity relative to an earth-fixed frame differentiated with respect to the frame *n* and expressed in *n* frame coordinates.

$\vec{w}_{ie}^{\,n}$: two subscripts represent that the vector is the measure of the second subscript frame relative to the first subscript frame. This notation is generally applied to rotational measurements. For this example, it describes the angular velocity vector of an earth-fixed frame (*e* frame) relative to an inertial frame (*i* frame) expressed in *n* frame coordinates.

The inertial velocity is defined as the time derivative of the position vector, $\vec{r}$, with respect to an inertial frame. This inertial velocity can be decomposed into two terms: the ground speed, $\vec{V}_e$, and the cross product of the earth's rotation, $\vec{w}_{ie}$, with the position vector, $\vec{r}$. The ground speed, $\vec{V}_e$, is the derivative of the position vector with respect to the earth fixed frame, and the rotation vector, $\vec{w}_{ie}$, is the angular velocity of the earth-fixed frame relative to the earth-center inertial frame (ECI):

$$\left.\frac{d\vec{r}}{dt}\right|^I = \left.\frac{d\vec{r}}{dt}\right|^e + \vec{w}_{ie} \times \vec{r} = \vec{V}_e + \vec{w}_{ie} \times \vec{r} \tag{3.3}$$

The inertial acceleration is the second derivative of the position vector with respect to an inertial frame:

$$\left.\frac{d^2\vec{r}}{d^2t}\right|^I = \left.\frac{d(\vec{V}_e + \vec{w}_{ie} \times \vec{r})}{dt}\right|^e + \vec{w}_{ie} \times (\vec{V}_e + \vec{w}_{ie} \times \vec{r}) \tag{3.4}$$

Expanding equation 3.4, the Coriolis effect of a rotating frame on a moving object appears as shown in the second term of equation 3.5:

$$\left.\frac{d^2\vec{r}}{d^2t}\right|^I = {}^e\dot{\vec{V}}_e + 2\vec{w}_{ie} \times \vec{V}_e + \vec{w}_{ie} \times (\vec{w}_{ie} \times \vec{r}) \tag{3.5}$$

The left hand side term of equation 3.5 is the acceleration sensed by an IMU's accelerometers. The outputs of the IMU accelerometers, which is generally called specific force, $\vec{f}$, include the true acceleration and the effect from local gravity:

$$\left.\frac{d^2\vec{r}}{d^2t}\right|^I = \vec{f} + \vec{g} \tag{3.6}$$

Substituting the left hand side term of equation 3.5 with equation 3.6 and rearranging terms, the navigation equations in any earth-fixed frame is expressed as:

$${}^e\dot{\vec{V}}_e = \vec{f} + \vec{g} - 2\vec{w}_{ie} \times \vec{V}_e - \vec{w}_{ie} \times (\vec{w}_{ie} \times \vec{r}) \tag{3.7}$$

Since the preferable navigation frame is the local-level frame, the navigation equations above can be represented in the local-level frame by using relationship between the time derivative of the ground speed with respect to the earth-fixed frame and the time derivative of the ground speed with respect to the navigation frame (local-level frame):

$${}^e\dot{\vec{V}}_e = \left.\frac{d\vec{V}_e}{dt}\right|^e = \left.\frac{d\vec{V}_e}{dt}\right|^n + \vec{w}_{en} \times \vec{V}_e \tag{3.8}$$

where $\vec{w}_{en}$ is the angular velocity of the navigation frame relative to the earth-fixed frame. Replacing ${}^e\dot{\vec{V}}_e$ in equation 3.8 by equation 3.7 and rearranging terms, then equation 3.8 translates as:

$$\left.\frac{d\vec{V}_e}{dt}\right|^n = \vec{f} - 2\vec{w}_{ie} \times \vec{V}_e - \vec{w}_{en} \times \vec{V}_e + \vec{g} - \vec{w}_{ie} \times (\vec{w}_{ie} \times \vec{r}) \tag{3.9}$$

Rewriting equation 3.9 in such a way that the Coriolis effect terms are collected, the last two terms of equation 3.9 constitute the local gravity vector $\vec{g}_l$. The final results are expressed in the navigation frame as:

$$ {}^{n}\dot{\vec{V}}_e^n = \vec{f}^{\,n} - (2\vec{w}_{ie}^n + \vec{w}_{en}^n) \times \vec{V}_e^n + \vec{g}_l^n \tag{3.10} $$

Equation 3.10 is usually referred to as the navigation equation in the navigation frame.

The specific forces are generally measured by the IMU whose triad is normally aligned with the vehicle's body frame, $\vec{f}^{\,b}$. Hence, a transformation from the user body frame to the navigation frame needs to be applied on the sensed specific forces to convert the measured $\vec{f}^{\,b}$ to $\vec{f}^{\,n}$. Then the transformed specific forces, $\vec{f}^{\,n}$, can be used in the navigation equations to propagate user positions. Therefore timely user attitude information is needed for correct body-to-navigation frame transformation. The attitude information can be propagated through gyroscope measurements by three different implementations: Euler angles, quaternion and direction-cosine matrix. Any of these methods can be transformed into the other two in principle [Titterton04]. The choice of implementation is typically based on the application. Euler angle propagation and transformation provide an intuitive sense about the aircraft body's orientation, and are therefore used throughout this research. The drawback of the Euler angle implementation is the existence of singular points at the north and south poles, which can be avoided for our purpose in the research.

Euler angle transformation is normally defined by transforming navigation frame to user's body frame through a sequence of rotations about Z, Y and X axes by three

Euler angles: yaw (azimuth) angle, ψ, pitch angle, θ, and roll angle, ϕ, accordingly. As a result, the navigation to body frame transformation C_n^b matrix is derived as:

$$\begin{aligned} C_n^b &= R_x(\phi)R_y(\theta)R_z(\psi) \\ &= \begin{bmatrix} 1 & 0 & 0 \\ 0 & \cos(\phi) & \sin(\phi) \\ 0 & -\sin(\phi) & \cos(\phi) \end{bmatrix} \begin{bmatrix} \cos(\theta) & 0 & -\sin(\theta) \\ 0 & 1 & 0 \\ \sin(\theta) & 0 & \cos(\theta) \end{bmatrix} \begin{bmatrix} \cos(\psi) & \sin(\psi) & 0 \\ -\sin(\psi) & \cos(\psi) & 0 \\ 0 & 0 & 1 \end{bmatrix} \end{aligned} \tag{3.11}$$

where $R_z(\psi)$ is the single axis rotation, which rotates a frame with ψ angle about z axis. $R_y(\theta)$ and $R_x(\phi)$ are the same operations about *y* and *x* axes respectively. Executing the matrix multiplication in equation 3.11 results in:

$$C_n^b = \begin{bmatrix} c(\theta)c(\psi) & c(\theta)s(\psi) & -s(\theta) \\ -c(\phi)s(\psi)+s(\phi)s(\theta)c(\psi) & c(\phi)c(\psi)+s(\phi)s(\theta)s(\psi) & s(\phi)c(\theta) \\ s(\phi)s(\psi)+c(\phi)c(\psi)s(\theta) & -s(\phi)c(\psi)+c(\phi)s(\psi)s(\theta) & c(\phi)c(\theta) \end{bmatrix} \tag{3.12}$$

where $c(\theta)=\cos(\theta), s(\theta)=\sin(\theta)$. The reverse transformation (transfer from the body frame to the navigation frame) is equal to the transpose of the navigation-to-body transformation: $C_b^n = C_n^{b^T}$

$$C_b^n = \begin{bmatrix} c(\theta)c(\psi) & -c(\phi)s(\psi)+s(\phi)s(\theta)c(\psi) & s(\phi)s(\psi)+c(\phi)c(\psi)s(\theta) \\ c(\theta)s(\psi) & c(\phi)c(\psi)+s(\phi)s(\theta)s(\psi) & -s(\phi)c(\psi)+c(\phi)s(\psi)s(\theta) \\ -s(\theta) & s(\phi)c(\theta) & c(\phi)c(\theta) \end{bmatrix}$$

The Euler angle propagation for the timely attitude information is achieved by propagating IMU angular velocity measurements. The rates of Euler angles are connected to the body-to-navigation relative rotation rates by two sets of Euler angle transformations:

$$\vec{w}_{nb}^b = \begin{bmatrix} w_x \\ w_y \\ w_z \end{bmatrix} = R_x(\phi)R_y(\theta)\begin{bmatrix} 0 \\ 0 \\ \dot{\psi} \end{bmatrix} + R_x(\phi)\begin{bmatrix} 0 \\ \dot{\theta} \\ 0 \end{bmatrix} + \begin{bmatrix} \dot{\phi} \\ 0 \\ 0 \end{bmatrix} \tag{3.13}$$

After expanding equation 3.13 and re-organizing all terms, the changing rates of the three Euler angles can be derived as a function of body-to-navigation rotation rates, $\vec{w}_{nb}^{b}$:

$$\begin{bmatrix} \dot{\phi} \\ \dot{\theta} \\ \dot{\psi} \end{bmatrix} = \begin{bmatrix} 1 & \tan(\theta)\sin(\phi) & \tan(\theta)\cos(\phi) \\ 0 & \cos(\phi) & -\sin(\phi) \\ 0 & \sec(\theta)\sin(\phi) & \sec(\theta)\cos(\phi) \end{bmatrix} \begin{bmatrix} w_x \\ w_y \\ w_z \end{bmatrix} \Rightarrow [\dot{\vec{E}}] = [F_{Eu}][\vec{w}_{nb}^{b}] \tag{3.14}$$

Equation 3.14 is the fundamental dynamic equation for user attitude propagation in this research. A simplified notation is introduced above for future reference. The connection to the true IMU gyro measurements, $\vec{w}_{ib}^{b}$, can be found in the further break-down on $\vec{w}_{nb}^{b}$:

$$\vec{w}_{nb}^{b} = \vec{w}_{ib}^{b} - \vec{w}_{in}^{b} = \vec{w}_{ib}^{b} - C_n^b(\vec{w}_{ie}^{n} + \vec{w}_{en}^{n}) \tag{3.15}$$

where $\vec{w}_{ie}^{n}$ is the earth's rotation rate; $\vec{w}_{en}^{n}$ is the navigation-to-earth relative rotation rate, also known as transport rate; $\vec{w}_{ib}^{b}$ is the user's body rotation rate relative to the inertial frame measured by the three orthogonal gyroscopes.

The earth's rotation rate is constant and the value can be found in WGS 84 earth model, which is listed at table 3.1. The transport rate (navigation-to-earth rotation) is the result of a moving navigation frame following the curvature of the earth surface. Without showing the details of derivation [Titterton04], the transport rate is written below:

$$\vec{w}_{en}^{n} = \begin{bmatrix} \dfrac{v_E}{R_P + h} & \dfrac{-v_N}{R_M + h} & \dfrac{-v_E \tan(Lat)}{R_P + h} \end{bmatrix} \tag{3.16}$$

where v_N and v_E are the user's northern and eastern ground speeds, h is the ellipsoidal height. This equation can be presented in a matrix form, and a simplified notation is introduced as:

$$\vec{w}_{en}^{n} = \begin{bmatrix} 0 & \dfrac{1}{R_P + h} & 0 \\ \dfrac{-1}{R_M + h} & 0 & 0 \\ 0 & \dfrac{-\tan(Lat)}{R_P + h} & 0 \end{bmatrix} \begin{bmatrix} v_N \\ v_E \\ v_D \end{bmatrix} = [F_{V2T}][\vec{V}_e^{\,n}] \tag{3.17}$$

where v_D is the user's vertical velocity with positive direction defined toward the ground.

3.2 INS System Dynamics and Error Models

With the previously derived navigation equations (3.10), and attitude dynamic equations from equation 3.14 with $\vec{w}_{nb}^{b}$ been substituted by the results from equation 3.15 and 3.17, a complete system dynamics for INS can be formulized in matrix form:

$$\begin{bmatrix} {}^{n}\dot{\vec{V}}_e^{\,n} \\ \dot{\vec{E}} \end{bmatrix} = \begin{bmatrix} -(2\vec{w}_{ie}^{n} + \vec{w}_{en}^{n}) & 0_3 \\ -F_{Eu} \cdot C_n^b \cdot F_{V2T} & 0_3 \end{bmatrix} \begin{bmatrix} \vec{V}_e^{\,n} \\ \vec{E} \end{bmatrix} + \begin{bmatrix} C_b^n & 0_3 \\ 0_3 & F_{Eu} \end{bmatrix} \begin{bmatrix} \vec{f}^{\,b} \\ \vec{w}_{ib}^{b} \end{bmatrix} + \begin{bmatrix} \vec{g}_l^{\,n} \\ -F_{Eu} \cdot C_n^b \cdot \vec{w}_{ie}^{n} \end{bmatrix} \tag{3.18}$$

where $\vec{f}^{\,n} = C_b^n \vec{f}^{\,b}$ is used, and $\vec{f}^{\,b}$ is the specific force vector expressed in the body frame coordinates, and 0_3 is a 3×3 matrix of zeros.

The first term on the right hand side of equation 3.18 shows how the current velocity affects the changing rates of the attitude and itself. The third term explains the roles of gravity and the earth's rotation on the INS system dynamics. The major driving forces of the system dynamics come from the second term, which are the true vehicle accelerations and rotations that are to be measured by the IMU. However, like other sensors, IMU measurement outputs are contaminated with different types of sensor errors. These sensor errors can corrupt IMU measurements and result in wrong dynamic propagations. Therefore, a proper IMU measurement model which can account for measurement errors is necessary for any reliable INS.

A general IMU measurement model and the time history of IMU accelerometer measurements can be analyzed as below [IONtutorial02]:

$$\tilde{f}^b(t) = (I + S_f^a)\vec{f}^b(t) + \vec{b}_a^{all}(t) + M_{is}^a \vec{f}^b(t) + \vec{v}_a(t) \tag{3.19}$$

where S_f^a is the scale factor matrix; $\vec{f}^b(t)$ is the true specific forces; $\vec{b}_a^{all}(t)$ is the time history of true accelerometer biases; M_{is}^a is the misalignment matrix and $\vec{v}_a(t)$ is the measurement white noise.

All these measurement-related errors will be explained in detail in the next section. To complete the system dynamic analysis, a breakdown on gyro outputs is expressed similarly:

$$\tilde{w}_g^b(t) = (I + S_f^g)\vec{w}_{ib}^b(t) + \vec{b}_g^{all}(t) + M_{is}^g \vec{w}_{ib}^b(t) + \vec{v}_g(t) \tag{3.20}$$

where S_f^g and M_{is}^g are scale factor and misalignment matrices respectively, $\vec{b}_g^{all}(t)$ is the time history of true gyro biases and $\vec{v}_g(t)$ is the gyro measurement white noise.

The bias components in IMU outputs, $\vec{b}_a^{all}(t)$ and $\vec{b}_g^{all}(t)$, normally have constant null-shift values and time-varying components. The variation part of the bias can be modeled generally as first order Gauss-Markov Random Process (GMRP) [Gebre01]:

$$\vec{b}_{a/g}^{all}(t) = \vec{b}_{a0/g0} + \vec{b}_{a/g}(t),\ \dot{\vec{b}}_{a/g}(t) = -\frac{1}{\tau_{a/g}}\vec{b}_{a/g}(t) + \vec{n}_{a/g}(t) \tag{3.21}$$

where $\tau_{a/g}$ and $\vec{n}_{a/g}(t)$ are the time constant and the driving white noise of GMRP respectively.

In general, the best estimations of the bias, scale factor and misalignment are available from the IMU manufacturer or a calibration process [Titterton04] [Hou04]. An

internal or external process to remove the majority of the IMU errors can be performed by the following equations:

$$\begin{aligned} \bar{f}^b(t) &= (I + \hat{S}_f^a + \hat{M}_{is}^a)^{-1}[\tilde{f}^b(t) - \hat{b}_{a0}] \\ \bar{w}_g^b(t) &= (I + \hat{S}_f^g + \hat{M}_{is}^g)^{-1}[\tilde{w}_g^b(t) - \hat{b}_{g0}] \end{aligned} \tag{3.22}$$

The best estimations of the true specific forces and body frame rotation rates relative to the inertial frame are available by subtracting the estimated varying-biases from the compensated IMU measurements:

$$\hat{f}^b(t) = \bar{f}^b(t) - \hat{b}_a(t),\ \hat{w}_g^b(t) = \bar{w}_g^b(t) - \hat{b}_g(t) \tag{3.23}$$

Replacing the true specific forces, $\bar{f}^b$, and the true user's rotations, $\bar{w}_g^b$, with the best available estimates, $\hat{f}^b$ and $\hat{w}_g^b$, in equation 3.18, then substitute the estimates with the results from equation 3.23. The IMU biases are included in the INS state vector to account for their time-varying properties which can be modeled by equation 3.21. As a result, the system dynamic equations become:

$$\begin{bmatrix} {}^n\dot{\hat{V}}_e^n \\ \dot{\hat{E}} \\ \dot{\hat{b}}_g \\ \dot{\hat{b}}_a \end{bmatrix} = \begin{bmatrix} -(2\bar{w}_{ie}^n + \bar{w}_{en}^n) & 0_3 & 0_3 & -C_b^n \\ -F_{Eu} \cdot C_n^b \cdot F_{V2T} & 0_3 & -F_{Eu} & 0_3 \\ 0_3 & 0_3 & -I/\tau_g & 0_3 \\ 0_3 & 0_3 & 0_3 & -I/\tau_a \end{bmatrix} \begin{bmatrix} \hat{V}_e^n \\ \hat{E} \\ \hat{b}_g \\ \hat{b}_a \end{bmatrix} + \begin{bmatrix} C_b^n \bar{f}^b + \hat{g}_l^n \\ F_{Eu} \cdot (\bar{w}_g^b - C_n^b \bar{w}_{ie}^n) \\ 0_3 \\ 0_3 \end{bmatrix} + (\vec{W}) \tag{3.24}$$

Last term in the parenthesis is the total process noises which includes mis-modeling and uncompensated IMU measurement errors and is ignored in the state propagation. The function of process noise is to provide the compensation between real world systems and system models during covariance propagations. The detailed error analyses will be described in the next three sections, while the more well known velocity and attitude error dynamic derivations are shown in Appendix A. The notations of all states in

equation 3.24 are changed to estimated (^) symbols, because the measurement and modeling errors have been introduced.

The estimated local gravity, $\hat{g}_l^n$, is further analyzed here. Recalling equation 3.9, the local gravity consists of the gravity due to earth mass attraction and the centrifugal force due to the earth's rotation:

$$\hat{g}_l^n = \hat{g}_m^n - \vec{w}_{ie} \times (\vec{w}_{ie} \times \vec{r}) \tag{3.25}$$

where $\hat{g}_m^n$ is the estimated gravity value by a gravity model. Earth Gravity Model 96 (EGM96) is the global standard for WGS 84 earth model. For any high integrity application like LAAS, the high accuracy local gravity data by a local gravimetric survey should be considered. One popular earth gravity model which defines gravity as a function of height and deflection of vertical (DOV) parameters is adopted here [Titterton04] [Gebre01]:

$$\hat{g}_m^n(h) = \begin{bmatrix} -\hat{\xi} \cdot \hat{g}(h) & -\hat{\eta} \cdot \hat{g}(h) & \hat{g}(h) \end{bmatrix}^T \tag{3.26}$$

$$\begin{aligned} \hat{g}(h) &= g(0)\frac{R_0^2}{(R_0+h)^2} \approx g(0) - \frac{2g(0)}{R_0}h \\ g(0) &= 9.780318 \times [1 + 5.3024 \times 10^{-3} \sin^2(Lat) - 5.9 \times 10^{-6} \sin^2(2Lat)] \text{ m/sec}^2 \end{aligned} \tag{3.27}$$

where ξ, η are the DOV angles corresponding the north-south (positive toward north) and east-west (positive toward east) components of the deviation vector from the local true gravity vector to the ellipsoidal normal vector, R_0 is the earth radius at current position on WGS 84 earth ellipsoid.

Using the first order approximation of equation 3.27 to replace the corresponding terms in equation 3.26, neglecting the product between any DOV and height since they

are very small, then a vertical gravity deviation state, $\Delta\hat{g}(0)$, is added to account for irregular vertical gravity on rugged areas. Equation 3.26 in matrix form results in:

$$\hat{g}_m^n(h) = \begin{bmatrix} 0 \\ 0 \\ g(0) + \dfrac{-2g(0)}{R_0}\hat{h} \end{bmatrix} + \begin{bmatrix} -g(0) & 0 & 0 \\ 0 & -g(0) & 0 \\ 0 & 0 & 1 \end{bmatrix} \begin{bmatrix} \hat{\xi} \\ \hat{\eta} \\ \Delta\hat{g}(0) \end{bmatrix} \tag{3.28}$$

The added $\Delta\hat{g}(0)$ shown in the equation 3.28 is the first order approximation of the deviation between true gravity and gravity function g(0), and it is often called gravity anomaly. A simplified notation for equation 3.28 is assigned:

$$\hat{g}_m^n(h) = [\hat{g}_c^n(h)] + [F_{gm2V}] \begin{bmatrix} \hat{\xi} \\ \hat{\eta} \\ \Delta\hat{g}(0) \end{bmatrix}$$

It is expected that the gravity anomaly and the DOVs will change along with user's positions. To account for this change, first order GMRP is applied to model the variations when user motion exists:

$$\begin{bmatrix} \dot{\xi} \\ \dot{\eta} \\ \Delta\dot{g}(0) \end{bmatrix} = -\frac{1}{\tau_{gm}} \begin{bmatrix} 1 & 0 & 0 \\ 0 & 1 & 0 \\ 0 & 0 & 1 \end{bmatrix} \begin{bmatrix} \xi \\ \eta \\ \Delta g(0) \end{bmatrix} + \vec{n}_{gm}\text{, note } \vec{g}_{gm} = \begin{bmatrix} \xi \\ \eta \\ \Delta g(0) \end{bmatrix} \tag{3.29}$$

where τ_{gm} is the time constant converted from the correlated distance and user velocity, $\vec{n}_{gm}$ is the corresponding driving white noise. The derivation of these parameters will be discussed shortly in the derivation of equation 3.43.

By handling the time-varying states of gravity model similarly to the IMU biases, equation 3.29 is incorporated into system dynamic model (3.24) to become:

$$\begin{bmatrix} {}^n\dot{\hat{V}}_e^n \\ \dot{\hat{E}} \\ \dot{\hat{b}}_g \\ \dot{\hat{b}}_a \\ \dot{\hat{g}}_{gm} \end{bmatrix} = \begin{bmatrix} -(2\vec{w}_{ie}^n + \vec{w}_{en}^n) & 0_3 & 0_3 & -C_b^n & F_{gm2V} \\ -F_{Eu} \cdot C_n^b \cdot F_{V2T} & 0_3 & -F_{Eu} & 0_3 & 0_3 \\ 0_3 & 0_3 & -I/\tau_g & 0_3 & 0_3 \\ 0_3 & 0_3 & 0_3 & -I/\tau_a & 0_3 \\ 0_3 & 0_3 & 0_3 & 0_3 & -I/\tau_{gm} \end{bmatrix} \begin{bmatrix} \hat{V}_e^n \\ \hat{E} \\ \hat{b}_g \\ \hat{b}_a \\ \hat{g}_{gm} \end{bmatrix} + G \cdot \vec{u} \quad (3.30)$$

where $F_{gm2V} = \begin{bmatrix} -g(0) & 0 & 0 \\ 0 & -g(0) & 0 \\ 0 & 0 & 1 \end{bmatrix}$, $G \cdot \vec{u} = \begin{bmatrix} C_b^n \bar{f}^b + \hat{g}_c^n - \vec{w}_{ie}^n \times (\vec{w}_{ie}^n \times \hat{r}_{usr}^n) \\ F_{Eu} \cdot (\overline{w}_g^b - C_n^b \vec{w}_{ie}^n) \\ 0_{9\times1} \end{bmatrix}_{15\times1}$

To understand the inputs which drive the system dynamics, $G \cdot \vec{u}$ is factored as:

$$G \cdot \vec{u} = \begin{bmatrix} I_{6\times6} \\ 0_{9\times6} \end{bmatrix} \begin{bmatrix} C_b^n \bar{f}^b + \hat{g}_c^n - \vec{w}_{ie}^n \times (\vec{w}_{ie}^n \times \hat{r}_{usr}^n) \\ F_{Eu} \cdot (\overline{w}_g^b - C_n^b \vec{w}_{ie}^n) \end{bmatrix}_{6\times1}$$

$$\Rightarrow G = \begin{bmatrix} I_{6\times6} \\ 0_{9\times6} \end{bmatrix}, \ \vec{u} = \begin{bmatrix} C_b^n \bar{f}^b + \hat{g}_c^n - \vec{w}_{ie}^n \times (\vec{w}_{ie}^n \times \hat{r}_{usr}^n) \\ F_{Eu} \cdot (\overline{w}_g^b - C_n^b \vec{w}_{ie}^n) \end{bmatrix}_{6\times1} \quad (3.31)$$

where $\vec{u}$ is the vector of system commands generated by properly processing the compensated IMU outputs $\bar{f}^b$ and $\overline{w}_g^b$.

Equation 3.30 is the system dynamic equations in the state space realization for general inertial navigation systems. User's position propagations in real-time can be computed simply by integrating the velocity states, provided that IMU outputs are available and the states are initialized correctly in the first place. For a high integrity navigation system, however, it is not enough that the position propagations are implemented correctly according to the navigation equations, but the quality of propagating positions also needs to be assured. Therefore, a covariance analysis on INS will be deferred until after the error model derivations in the next two sections. Before continuing, a simplified notation for equation 3.30 is established for future reference:

$$\begin{bmatrix} {}^n\dot{\hat{V}}_e^n \\ \dot{\hat{E}} \\ \dot{\hat{b}}_g \\ \dot{\hat{b}}_a \\ \dot{\hat{g}}_{gm} \end{bmatrix} = \begin{bmatrix} -F_{V2V} & 0 & 0 & -C_b^n & F_{gm2V} \\ -F_{V2E} & 0 & -F_{Eu} & 0 & 0 \\ 0 & 0 & -I/\tau_g & 0 & 0 \\ 0 & 0 & 0 & -I/\tau_a & 0 \\ 0 & 0 & 0 & 0 & -I/\tau_{gm} \end{bmatrix} \begin{bmatrix} \hat{V}_e^n \\ \hat{E} \\ \hat{b}_g \\ \hat{b}_a \\ \hat{g}_{gm} \end{bmatrix} + G\vec{u} \tag{3.32}$$

where $F_{V2V} = 2\vec{w}_{ie}^n + \vec{w}_{en}^n$ and $F_{V2E} = F_{Eu} \cdot C_n^b \cdot F_{V2T}$.

3.2.1 IMU Error Model. IMU measurement errors impact INS accuracy directly. Without knowing the quality of IMU measurements and measurement error model, the system integrity would be compromised. A generalized IMU error model is established and analyzed in this section.

Generally speaking, a detailed and precise IMU model can make the propagations of INS states more accurate than a generalized IMU model. However, this approach also makes the system performance highly dependent on one specific type of IMU, which is not a desired path for this research. The methodology of this analysis is to parameterize the quality of the IMU and then to explore the sensitivity of the system performance to the quality parameters. The focus is to get a broader sense of how the INS performance varies with different IMU quality, instead of pursuing optimal system performance on one specific type of IMU.

A generalized IMU measurement model including bias variations has been described in equations 3.19, 3.20 and 3.21. The analysis below is developed for the accelerometer model, but the results can be extended to the gyro model as well. A matrix form of accelerometer measurements is described in detail below [IONtutorial02]:

$$\begin{bmatrix} \tilde{f}_x(t) \\ \tilde{f}_y(t) \\ \tilde{f}_z(t) \end{bmatrix} = \left(I + \begin{bmatrix} s_x & 0 & 0 \\ 0 & s_y & 0 \\ 0 & 0 & s_z \end{bmatrix} \right) \begin{bmatrix} f_x(t) \\ f_y(t) \\ f_z(t) \end{bmatrix} + \begin{bmatrix} 0 & m_{xy} & m_{xz} \\ m_{yx} & 0 & m_{yz} \\ m_{zx} & m_{zy} & 0 \end{bmatrix} \begin{bmatrix} f_x(t) \\ f_y(t) \\ f_z(t) \end{bmatrix} + \begin{bmatrix} b_x^{all}(t) \\ b_y^{all}(t) \\ b_z^{all}(t) \end{bmatrix} + \begin{bmatrix} v_x(t) \\ v_y(t) \\ v_z(t) \end{bmatrix} \quad (3.33)$$

$$\Rightarrow \tilde{\vec{f}}(t) = (I + S_f^a)\vec{f}(t) + M_{is}^a \vec{f}(t) + \vec{b}_a^{all}(t) + \vec{v}_a(t)$$

where $\tilde{\vec{f}}(t)$ is the direct accelerometer measurements with measurement noise $\vec{v}_a(t)$; $\vec{b}_a^{all}(t)$ is the true sensor bias including constant $\vec{b}_{a0}$ and time-varying $\vec{b}_a(t)$; S_f^a and M_{is}^a are the true scale factor and the misalignment coefficient matrices. The superscript *b* is omitted because that all vectors are expressed in the body frame coordinates. The relation between the true value and the estimated (or nominal) value is defined as:

(true value) = (estimated/nominal value) + (error)

In the real process, only the estimated or nominal values of all coefficients and biases are available. Expanding equation 3.33 row by row, the best available estimated specific force along the *x* axis in the body frame can be derived as:

$$\hat{f}_x(t) = [\tilde{f}_x(t) - \hat{b}_{x0} - \hat{m}_{xy}\hat{f}_y(t) - \hat{m}_{xz}\hat{f}_z(t)](1+\hat{s}_x)^{-1} - \hat{b}_x(t) \quad (3.34)$$

Expanding $(1+\hat{s}_x)^{-1}$ term in the Taylor series at $s_x = 0$ point (because all scale factor and misalignment coefficients are generally very small) and taking the first order approximation, the second and higher order terms are negligible. The estimation error along the *x* axis specific force can be expressed as:

$$\begin{aligned} \delta f_x(t) &= f_x(t) - \hat{f}_x(t) = f_x(t) - \{[\tilde{f}_x(t) - \hat{b}_{x0} - \hat{m}_{xy}\hat{f}_y(t) - \hat{m}_{xz}\hat{f}_z(t)](1-\hat{s}_x) - \hat{b}_x(t)\} \\ &= f_x(t) - (1-\hat{s}_x)\tilde{f}_x(t) + (1-\hat{s}_x)\hat{b}_{x0} + \hat{b}_x(t) + (1-\hat{s}_x)[\hat{m}_{xy}\hat{f}_y(t) + \hat{m}_{xz}\hat{f}_z(t)] \end{aligned} \quad (3.35)$$

Substituting $\tilde{f}_x$ from equation 3.33 into above equation, and using the definitions of $f_y = \hat{f}_y + \delta f_y$, $f_z = \hat{f}_z + \delta f_z$, $s_x = \hat{s}_x + \delta s_x$, $m_{xy} = \hat{m}_{xy} + \delta m_{xy}$, $m_{xz} = \hat{m}_{xz} + \delta m_{xz}$, equation

3.35 are expanded and approximated by assuming zero for any product between any state error and any coefficient, any bias and any coefficient, and any two coefficients. The estimation error of the constant null-shift bias, δb_{x0}, can be incorporated into the estimation error of the variation part of the bias, $\delta b_x(t)$. The final result is expressed as:

$$\delta f_x(t) = -\delta b_x(t) - \delta s_x f_x(t) - \delta m_{xy} f_y(t) - \delta m_{xz} f_z(t) - v_x(t) \tag{3.36}$$

The same format can be obtained for the specific forces along the *y* and *z* axes, and then the combined results can be expressed in the matrix form as:

$$\delta \vec{f}^{\,b}(t) = -\delta \vec{b}_a(t) - \delta S_f^a \vec{f}^{\,b}(t) - \delta M_{is}^a \vec{f}^{\,b}(t) - \vec{v}_a(t) \tag{3.37}$$

where $\delta S_f^a = \begin{bmatrix} \delta s_x & 0 & 0 \\ 0 & \delta s_y & 0 \\ 0 & 0 & \delta s_z \end{bmatrix}$ and $\delta M_{is}^a = \begin{bmatrix} 0 & \delta m_{xy} & \delta m_{xz} \\ \delta m_{yx} & 0 & \delta m_{yz} \\ \delta m_{zx} & \delta m_{zy} & 0 \end{bmatrix}$

The first term on the right hand side of equation 3.37 is the sensor bias estimation error which can be derived from GMRP in equation 3.21 and the definition of bias error:

$$\left.\begin{aligned} \dot{\vec{b}}_a(t) &= -1/\tau_a \cdot \vec{b}_a(t) + \vec{n}_a(t) \\ \dot{\hat{b}}_a(t) &= -1/\tau_a \cdot \hat{b}_a(t) \end{aligned}\right\} \Rightarrow \delta \dot{\vec{b}}_a(t) = -1/\tau_a \cdot \delta \vec{b}_a(t) + \vec{n}_a(t) \tag{3.38}$$

The relationship between the power spectral density (Q) of the driving white noise and the standard deviation (sigma) of the state variation (σ) for a general first order GMRP is $Q = 2\sigma^2/\tau$ [Brown97], where τ is the time constant. Therefore, the power spectral density (PSD), Q_{na}, of the driving white noise, $\vec{n}_a$, can be derived as $Q_{na} = 2\sigma_{ba}^2/\tau_a$, where σ_{ba} is the sigma of bias variation. Equation 3.37 and 3.38 defined the accelerometer error model of the IMU. A similar result can be applied to the gyroscopes to construct a complete IMU error model:

$$\delta\vec{w}_{ib}^{b}(t) = -\delta\vec{b}_g(t) - \delta S_f^g \vec{w}_{ib}^{b}(t) - \delta M_{is}^g \vec{w}_{ib}^{b}(t) - \vec{v}_g(t) \tag{3.39}$$

$$\delta\dot{\vec{b}}_g(t) = -1/\tau_g \cdot \delta\vec{b}_g(t) + \vec{n}_g(t) \tag{3.40}$$

The gyroscope measurement error $\vec{v}_g$ can be presented in different ways; power spectral density and Angle Random Walk (ARW) are the two most often seen. ARW describes the average angle deviation caused by the integration of a gyroscope sensor measurement noise. The conversion between PSD and ARW can be done by the following equation [Stockwell]:

$$\mathrm{ARW}(\mathrm{deg}/\mathrm{hr}^{1/2}) = 1/60 \times \sqrt{\mathrm{PSD}(\mathrm{deg}^2/\mathrm{hr}^2/\mathrm{hz})}$$

Evaluating an IMU error model is not a trivial task; different methods can be found in numerous books and research papers [Titterton04] [Jekeli01] [Gebre01][Hou04]. In addition, IEEE has defined standard procedures for design, modeling and testing for certain types of IMU sensor components [IEEEstd97].

3.2.2 Gravity Error Model. The same methodology for developing the IMU error model is utilized on gravity error model. As mentioned in equation 3.29, first order GMRP is applied to model the time-variation of the gravity model parameters. A distance-to-time conversion is necessary for gravity GMRP modeling, because that the DOVs and gravity anomaly errors are correlated in location, instead of time. By taking perturbation on both side of equation 3.25:

$$\delta\vec{g}_l^n = \delta\vec{g}_m^n - \delta(\vec{w}_{ie} \times (\vec{w}_{ie} \times \vec{r})) \approx \delta\vec{g}_m^n \tag{3.41}$$

The term $\delta(\vec{w}_{ie} \times (\vec{w}_{ie} \times \vec{r}))$ is negligibly small. With the help of equation 3.28, the gravity error can be modeled as:

$$\delta\bar{g}_l^n(h) = \delta\bar{g}_m^n(h) = \begin{bmatrix} 0 \\ 0 \\ \dfrac{-2g(0)}{R_0}\delta h \end{bmatrix} + \begin{bmatrix} -g(0) & 0 & 0 \\ 0 & -g(0) & 0 \\ 0 & 0 & 1 \end{bmatrix} \begin{bmatrix} \delta\xi \\ \delta\eta \\ \delta\Delta g(0) \end{bmatrix} \tag{3.42}$$

The first term on the right hand side of the above equation can be ignored for the applications which do not require high accuracy on the gravity anomaly; it is kept here due to the demanding nature of the precision approach applications. Rewrite this equation with simplified notation from equation 3.30:

$$\delta\bar{g}_l^n = F_{gm2V} \cdot \delta\bar{g}_{gm} - F_{h2V} \cdot \delta h \text{, where } F_{h2V} = \begin{bmatrix} 0 \\ 0 \\ \dfrac{2g(0)}{R_0} \end{bmatrix} \tag{3.43}$$

The time variation of $\delta\bar{g}_{gm}$ can be derived by a distance-to-time conversion. If a vehicle is moving at the ground speed v_e in an area with gravity error correlation distance d_{gm} and sigma σ_{gm}, the correlation time constant τ_{gm} can be acquired by the relation $v_e\tau_{gm} = d_{gm}$. By applying the formula $Q = 2\sigma^2/\tau$, the PSD, Q_{ngm}, of the driving white noise for the gravity error model can be computed from the corresponding pair of τ_{gm} and σ_{gm}. Assuming all gravity model parameters (DOVs and gravity anomaly) have the same correlation distance, the gravity state error dynamics can be derived in the similar form as the IMU bias error model in equation 3.38:

$$\begin{bmatrix} \delta\dot{\xi} \\ \delta\dot{\eta} \\ \delta\Delta\dot{g}(0) \end{bmatrix} = -\frac{1}{\tau_{gm}} \begin{bmatrix} 1 & 0 & 0 \\ 0 & 1 & 0 \\ 0 & 0 & 1 \end{bmatrix} \begin{bmatrix} \delta\xi \\ \delta\eta \\ \delta\Delta g(0) \end{bmatrix} + \vec{n}_{gm}, \; Q_{ngm} = 2\sigma_{gm}^2/\tau_{gm} \tag{3.44}$$

3.2.3 INS Error Propagation. With the IMU and gravity error models derived in the previous two sections, and velocity error and attitude error derived in Appendix A, the INS system performance can be analyzed quantitatively by covariance analysis. Consequently, the connection between the IMU and gravity model quality and the INS performance can be established.

For easy reference, velocity and attitude error dynamic equations from Appendix A are presented here:

$$\begin{aligned}\delta\,{}^{n}\dot{\vec{V}}_e^{\,n}(t) &= {}^{n}\dot{\vec{V}}_e^{\,n}(t) - {}^{n}\dot{\tilde{\vec{V}}}_e^{\,n}(t) \\ &= \left[\vec{f}^{\,n}(t)\times\right]\delta\vec{E}(t) + C_b^n(t)\delta\vec{f}^{\,b}(t) + \delta\vec{g}_l^{\,n}(t)\end{aligned} \tag{3.45}$$

$$\delta\dot{\vec{E}}(t) = -\left[\vec{w}_{in}^{n}(t)\times\right]\delta\vec{E}(t) - C_b^n(t)\delta\vec{w}_{ib}^{b}(t) + \delta\vec{w}_{in}^{n}(t) \tag{3.46}$$

where $[\vec{f}^{\,n}(t)\times]$ is the matrix form of the cross product with vector $\vec{f}^{\,n}$, and $\delta\vec{w}_{in}^{n} \approx \delta\vec{w}_{en}^{n}$ because of $\delta\vec{w}_{ie}^{n} \approx 0$. $\delta\vec{w}_{en}^{n}$ can be further expressed by taking perturbation operation on equation 3.17:

$$\delta\vec{w}_{en}^{n} = \begin{bmatrix} 0 & \dfrac{1}{R_P+h} & 0 \\ \dfrac{-1}{R_M+h} & 0 & 0 \\ 0 & \dfrac{-\tan(Lat)}{R_P+h} & 0 \end{bmatrix} \begin{bmatrix} \delta v_N \\ \delta v_E \\ \delta v_D \end{bmatrix} = F_{V2T}\cdot\delta\vec{V}_e^{\,n} \tag{3.47}$$

A collection of all INS dynamic error equations is presented:

$$\begin{aligned}
&\delta\,{}^{n}\dot{\vec{V}}_e^{\,n}(t) = \left[\vec{f}^{\,n}(t)\times\right]\delta\vec{E}(t) + C_b^n(t)\delta\vec{f}^{\,b}(t) + \delta\vec{g}_l^{\,n}(t) \\
&\delta\dot{\vec{E}}(t) = -\left[\vec{w}_{in}^{n}(t)\times\right]\delta\vec{E}(t) - C_b^n(t)\delta\vec{w}_{ib}^{b}(t) + F_{V2T}\cdot\delta\vec{V}_e^{\,n}(t) \\
&\delta\dot{\vec{b}}_g(t) = -1/\tau_g\cdot\delta\vec{b}_g(t) + \vec{n}_g(t) \\
&\delta\dot{\vec{b}}_a(t) = -1/\tau_a\cdot\delta\vec{b}_a(t) + \vec{n}_a(t) \\
&\delta\dot{\vec{g}}_{gm}(t) = -1/\tau_{gm}\cdot\delta\vec{g}_{gm}(t) + \vec{n}_{gm}(t)
\end{aligned} \tag{3.48}$$

The matrix form of the state space realization for the INS dynamic errors can then be shown to be:

$$\begin{bmatrix} \delta^n\dot{\vec{V}}_e^n \\ \delta\dot{\vec{E}} \\ \delta\dot{\vec{b}}_g \\ \delta\dot{\vec{b}}_a \\ \delta\dot{\vec{g}}_{gm} \end{bmatrix} = \begin{bmatrix} 0 & \vec{f}^{\,n}\times & 0 & 0 & 0 \\ F_{V2T} & -\vec{w}_{in}^n\times & 0 & 0 & 0 \\ 0 & 0 & -\dfrac{I}{\tau_g} & 0 & 0 \\ 0 & 0 & 0 & -\dfrac{I}{\tau_a} & 0 \\ 0 & 0 & 0 & 0 & -\dfrac{I}{\tau_{gm}} \end{bmatrix} \begin{bmatrix} \delta\vec{V}_e^n \\ \delta\vec{E} \\ \delta\vec{b}_g \\ \delta\vec{b}_a \\ \delta\vec{g}_{gm} \end{bmatrix} + \begin{bmatrix} C_b^n\delta\vec{f}^{\,b} + \delta\vec{g}_l^n \\ -C_b^n\delta\vec{w}_{ib}^b \\ \vec{n}_g \\ \vec{n}_a \\ \vec{n}_{gm} \end{bmatrix} \tag{3.49}$$

A further expansion is done by replacing $\delta\vec{f}^{\,b}$, $\delta\vec{w}_{ib}^b$ and $\delta\vec{g}_l^n$ in the last column with the results from equation 3.37, 3.39 and 3.43. The INS error dynamic model with process noise is presented as:

$$\begin{bmatrix} \delta^n\dot{\vec{V}}_e^n \\ \delta\dot{\vec{E}} \\ \delta\dot{\vec{b}}_g \\ \delta\dot{\vec{b}}_a \\ \delta\dot{\vec{g}}_{gm} \end{bmatrix} = \begin{bmatrix} 0 & \vec{f}^{\,n}\times & 0 & -C_b^n & F_{gm2V} \\ F_{V2T} & -\vec{w}_{in}^n\times & C_b^n & 0 & 0 \\ 0 & 0 & -\dfrac{I}{\tau_g} & 0 & 0 \\ 0 & 0 & 0 & -\dfrac{I}{\tau_a} & 0 \\ 0 & 0 & 0 & 0 & -\dfrac{I}{\tau_{gm}} \end{bmatrix} \begin{bmatrix} \delta\vec{V}_e^n \\ \delta\vec{E} \\ \delta\vec{b}_g \\ \delta\vec{b}_a \\ \delta\vec{g}_{gm} \end{bmatrix} + \vec{W}_{INS} \tag{3.50}$$

where $\vec{W}_{INS} = \begin{bmatrix} C_b^n(-\delta S_f^a\vec{f}^{\,b} - \delta M_{is}^a\vec{f}^{\,b} - \vec{v}_a) + F_{h2V}\cdot\delta h \\ -C_b^n(-\delta S_f^g\vec{w}_{ib}^b - \delta M_{is}^g\vec{w}_{ib}^b - \vec{v}_g) \\ \vec{n}_g \\ \vec{n}_a \\ \vec{n}_{gm} \end{bmatrix}$ is the process noise for the INS error dynamics.

Equation 3.50 is the continuous time version of the INS error propagation equations written in state space form. With the proper initialization on state errors, a high enough sampling frequency, and the correct handling on process noise, the state

covariance propagation can be performed in a discrete time version of this equation to serve as a tool for performance analysis. The system covariance propagation process will be derived in the GPS/INS hybrid system analysis in the next section.

3.3 Novel System Model for Tightly Coupled GPS/INS Integration

INS navigation systems have to be properly initialized and calibrated by external sources before providing navigation information. Differential GPS L1 code and carrier measurements are used as the external source in this research. A calibration scheme which can maximize the INS calibration performance is necessary, so that the INS can become a reliable navigation resource in the final approach stage. Based on the DGPS and INS system backgrounds elucidated earlier, a centralized Kalman filter fusing all INS and GPS states is constructed in a novel way so that only the measurement update process for DGPS positioning is necessary to accomplish range domain INS calibration

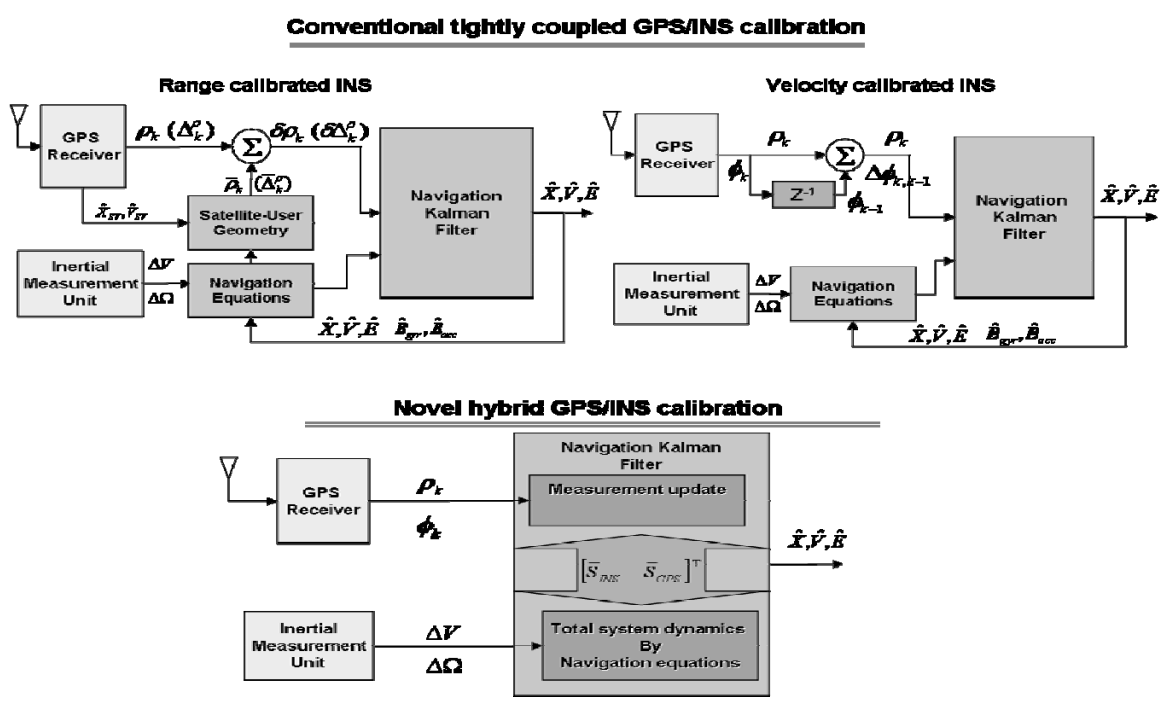

Figure 3.3. Tightly Couple GPS/INS Integration Architectures

and position estimation at the same time. The DGPS measurement update is precisely the same as the measurement update for GPS-only system. The system architectures of two conventional tight-coupled GPS/INS integrations and the hybrid GPS/INS integration are shown in Figure 3.3 for easy understanding. The conventional GPS/INS integration scheme normally utilizes the comparison between GPS and INS navigation outputs. In tightly coupled sense of the conventional GPS/INS integration systems, this comparison is realized in range domain by either using GPS range measurements or time-differenced carrier measurements to compare with the corresponding 'pseudo measurements' generated from INS. The novel hybrid navigation system removes any necessity of this kind of explicit comparison by comprehensively integrating INS dynamic information with the single frequency DGPS system model developed from Chapter 2. The advantage of the novel system architecture is that the calibration scheme is simple and straightforward and still can achieve high accuracy on the INS calibration performance. A more elaborate comparison will be described in Section 5.3. The detailed processes to accomplish this novel hybrid navigation system architecture are illustrated in the following section.

3.3.1 Centralized Hybrid System Dynamic and Error Dynamic Models. The most apparent difference of this novel hybrid navigation system from a traditional GPS-only system is that the vehicle dynamic information is available to the Kalman filter during the time propagations of the states. The centralized filter consists of 15 INS states plus one inertial height state (which is not necessary but very convenient for implementation purposes, therefore it is chosen to be implemented), three DGPS relative position states ($\Delta\vec{X}$), one tropospheric refractivity residual state for all satellites in view (Δn), one

ionospheric gradient state for each satellite (ΔV_{ig}), plus carrier-phase integers and code and carrier multipath states ($\Delta N, \Delta M_p, \Delta m_p$). For easier elaboration and notation on the system equations, all equations are derived in vector or matrix forms to avoid lengthy expansions on the elements. All the detailed derivations of the dynamic error equations and the process noises can be found in Sections 3.1, 3.2 and Appendices A, and C. The final results of equation derivations are applied here without further explanations.

The correlations between INS and DGPS states inside the centralized filter are the keys to this hybrid system's success. It works through two physical mechanisms: one is the gravity model that needs the ellipsoid height for gravity compensation (3.28), which can be derived from DGPS positions (Adding an inertial height state can facilitate this process); another is that the DGPS positions, $\Delta\vec{X}$, can be propagated in time through the integration of the INS velocity state. Using INS to propagate GPS positions is not a new scheme, but a complete DGPS state model propagation by INS integration is a new implementation. This new comprehensive GPS/INS state integration architecture enables the proper correlations connected among states, and therefore the INS can be calibrated implicitly in GPS positioning process without any special observation matrix for INS error calibration.

The differential equation to connect this time propagation from the INS velocity to the DGPS position can be derived as:

$$\left.\frac{d\Delta\vec{X}^{nr}}{dt}\right|^{e} = \left.\frac{d\Delta\vec{X}^{nr}}{dt}\right|^{nr} + \vec{w}_{e-nr}^{nr} \times \Delta\vec{X}^{nr} \Rightarrow \vec{V}_{e}^{nr} = \vec{V}_{nr}^{nr} + \vec{w}_{e-nr}^{nr} \times \Delta\vec{X}^{nr} \tag{3.51}$$

where $\Delta\vec{X}^{nr}$ is the vector of the DGPS position between the reference station and the user vehicle in the reference station's local-level nr frame.

Because there is no relative motion or rotation between the earth's ground surface and the ground reference station's local-level frame, the cross product term in equation 3.51 is vanished. Hence, the derivative of GPS position in the nr frame is equivalent to the ground speed:

$$ {}^{e}\Delta\dot{\vec{X}}^{nr} = \vec{V}_{nr}^{nr} = \vec{V}_{e}^{nr} = C_{n}^{nr}\vec{V}_{e}^{n} \tag{3.52} $$

A coordinate transformation, C_n^{nr}, is needed for the above equation and it is addressed in the following content. In stand alone (i.e. non-differential) GPS navigation systems, GPS measurements are usually handled in ECEF coordinates. The estimated positions can be transformed into any desired coordinates. In contrast, for DGPS applications, normally the relative position is processed in the local East-North-Up (ENU) coordinates with the origin at the reference station. Meanwhile, the INS navigation equations are generally derived in the aircraft/user local-level coordinates, North-East-Down (NED). To avoid the confusion and to ensure consistency, the local-level coordinates at the reference station (NED) is adopted for DGPS positioning instead of east-north-up. When the distance between the reference station and users is less than 50 kilometers, the orientation deviation between these two frames is less than 0.5 degree. Propagating position error caused by neglecting the transformation in a short period of time between GPS measurement updates, like 1 sec, has one sigma value smaller than 1 cm for navigation grade INS. Nevertheless, considering to maximize the INS calibration performance and maintaining this analysis as general as possible for different INS quality, this transformation between two local frames is retained. The derivation of the transformation is illustrated in Appendix B. The error dynamics of the DGPS position from equation 3.52 can be established as:

$$\delta\Delta\dot{\vec{X}}^{nr} = C_n^{nr}\delta\vec{V}_e^n \tag{3.53}$$

The errors caused by inaccurate transformation are negligibly small in magnitude.

The dynamic model of the centralized hybrid navigation system can be structured by attaching the DGPS states after the INS states, meanwhile the correlated states are connected through the gravity model and the ground velocity. At present, a set of the estimated states from a L1 single frequency DGPS, which is the same as the single frequency SRGPS system architecture, is collected and appended with extra code and carrier multipath states. The total estimated states in the hybrid system are listed below:

$$S = [ih \quad \vec{V}_e^n \quad \vec{E} \quad \vec{b}_g \quad \vec{b}_a \quad \vec{g}_{gm} \quad \Delta X^{nr} \quad \Delta n \quad \Delta Vig \quad \Delta N \quad \Delta M_p \quad \Delta m_p]$$

The augmentation of the multipath states is the way to enable 1Hz or faster INS calibration by accounting for the time correlated errors in DGPS measurement in the state model. This was not necessary for the analysis in Chapter 2 because the multipath correlation time was handled as a parameter and independent samples were used (two times correlation time). The DGPS state dynamics can be established by applying the GMRP model on code and carrier multipath with time constants τ_{code} and τ_{carr} respectively. The residual tropospheric refractivity, ionospheric gradient and carrier integer states are assumed to remain unchanged during time propagation. The INS and DGPS state dynamics models are presented in the following to explain the procedure of dynamic integration between GPS and INS states.

The INS system dynamics for the hybrid system has two changes from equation 3.32 which is derived for general INS dynamics. One is to add the inertial height state, and the other is that the aircraft/user attitude propagation is replaced by three estimated Euler angle attitude deviation states, $\Delta\hat{E}$. The reason for replacing the Euler angle

attitude with the Euler angle attitude deviation in the system dynamic model is that the attitude error model in the system dynamic error equations (3.50) is linearized. If there was no intention to calibrate INS state errors, the INS dynamic model from equation 3.32 would work fine. Since GPS measurements will be used to calibrate INS for the hybrid navigation system, only the linear attitude deviation states will match the prediction from the linearized attitude error propagation, and therefore can be used to correct Euler angle attitude errors properly. The dynamic model of the attitude deviation states can be derived analytically by applying perturbation on equation 3.14, however a zero order hold approximation (a constant) is good enough and implemented here. The actual Euler angle attitude propagation is implemented independently by the corresponding equations from equation 3.24:

$$\dot{\hat{E}} = -F_{Eu} \cdot C_n^b \cdot F_{V2T} \cdot \hat{V}_e^n + F_{Eu} \cdot (\overline{w}_g^b - \hat{b}_g - C_n^b \vec{w}_{ie}^n) \tag{3.54}$$

The INS system dynamics for the hybrid system is described below along with the simplified notations:

$$\begin{bmatrix} i\dot{\hat{h}} \\ \dot{\hat{V}}_e^n \\ \Delta\dot{\hat{E}} \\ \dot{\hat{b}}_g \\ \dot{\hat{b}}_a \\ \dot{\hat{g}}_{gm} \end{bmatrix} = \begin{bmatrix} 0 & -F_{V2h} & 0_{1\times3} & 0_{1\times3} & 0_{1\times3} & 0_{1\times3} \\ -F_{h2V} & -F_{V2V} & 0_3 & 0_3 & -C_b^n & F_{gm2V} \\ 0_{3\times1} & 0_3 & 0_3 & 0_3 & 0_3 & 0_3 \\ 0_{3\times1} & 0_3 & 0_3 & -I/\tau_g & 0_3 & 0_3 \\ 0_{3\times1} & 0_3 & 0_3 & 0_3 & -I/\tau_a & 0_3 \\ 0_{3\times1} & 0_3 & 0_3 & 0_3 & 0_3 & -I/\tau_{gm} \end{bmatrix} \begin{bmatrix} i\hat{h} \\ \hat{V}_e^n \\ \Delta\hat{E} \\ \hat{b}_g \\ \hat{b}_a \\ \hat{g}_{gm} \end{bmatrix} + G_I \vec{u}_I \tag{3.55}$$

$$\Rightarrow \dot{\hat{S}}_I = F_I \hat{S}_I + G_I \vec{u}_I$$

where $G_I = \begin{bmatrix} 0_{1\times3} \\ I_{3\times3} \\ 0_{12\times3} \end{bmatrix}$ and $\vec{u}_I = [C_b^n \bar{f}^b + [0 \quad 0 \quad g(0)]^T - \vec{w}_{ie}^n \times (\vec{w}_{ie}^n \times \hat{r}_{usr}^n)]_{3\times1}$. $F_{V2h} = [0 \quad 0 \quad 1]$ is introduced to describe the relationship $i\dot{h} = -v_z^n$, and $i\hat{h}(0)$ can be initialized by $\Delta\hat{X}_0^{nr}$.

$F_{h2V} = [0 \quad 0 \quad 2g(0)/R_0]^T$ was defined in equation 3.43. The DGPS system dynamics for the hybrid navigation system is illustrated:

$$\begin{bmatrix} \Delta\dot{\hat{X}}^{nr} \\ \Delta\dot{\hat{n}} \\ \Delta\dot{\hat{V}}_{ig} \\ \Delta\dot{\hat{N}} \\ \Delta\dot{\hat{M}}_p \\ \Delta\dot{\hat{m}}_p \end{bmatrix} = \begin{bmatrix} 0 & 0 & 0 & 0 & 0 & 0 \\ 0 & 0 & 0 & 0 & 0 & 0 \\ 0 & 0 & 0 & 0 & 0 & 0 \\ 0 & 0 & 0 & 0 & 0 & 0 \\ 0 & 0 & 0 & 0 & -1/\tau_{code} & 0 \\ 0 & 0 & 0 & 0 & 0 & -1/\tau_{carr} \end{bmatrix} \begin{bmatrix} \Delta\hat{X}^{nr} \\ \Delta\hat{n} \\ \Delta\hat{V}_{ig} \\ \Delta\hat{N} \\ \Delta M_p \\ \Delta m_p \end{bmatrix} + \begin{bmatrix} C_n^{nr} \\ 0 \\ 0 \\ 0 \\ 0 \\ 0 \end{bmatrix} \hat{V}_e^n \tag{3.56}$$

$$\Rightarrow \dot{\hat{S}}_G = F_G \hat{S}_G + \begin{bmatrix} C_n^{nr} \\ 0 \\ \vdots \end{bmatrix} \hat{V}_e^n$$

where the DGPS-related states include: $\Delta\hat{X}^{nr}$ as DGPS position; $\Delta\hat{n}$ as residual tropospheric refractivity index; $\Delta\hat{V}_{ig}$ as vertical ionospheric gradient; $\Delta\hat{N}$ as single difference carrier-phase integer, plus code and carrier multipath $\Delta\hat{M}_p, \Delta\hat{m}_p$.

The complete state space realization of the hybrid system dynamic model is the consolidation of equations 3.55 and 3.56. The results are presented in the simplified block matrix form:

$$\begin{bmatrix} \dot{\hat{S}}_I \\ \dot{\hat{S}}_G \end{bmatrix}_{(19+4+4\cdot sn)\times 1} = \begin{bmatrix} F_I & 0_{19\times(4+4\cdot sn)} \\ F_{I2G} & F_G \end{bmatrix} \begin{bmatrix} \hat{S}_I \\ \hat{S}_G \end{bmatrix}_{(19+4+4\cdot sn)\times 1} + G_{h(19+4+4\cdot sn)\times 3} \vec{u}_{I\,3\times 1} \tag{3.57}$$

where $F_{I2G} = \begin{bmatrix} 0_{3\times 1} & C_n^{nr} & 0_3 & \cdots \\ \vdots & 0_3 & 0_3 & \vdots \\ \vdots & \cdots & \cdots & \ddots \end{bmatrix}_{(4+4\cdot sn)\times 19}$, $G_h = \begin{bmatrix} G_I \\ 0_{(4+4\cdot sn)\times 3} \end{bmatrix}$ and sn is the number of the satellites in view.

Since the hybrid navigation system dynamic model is completed in equation 3.57, our attention is now turned toward the hybrid system error dynamic model in order to

perform the covariance propagation of the Kalman filter. Similar to the way of constructing the hybrid system dynamic model, the INS system error dynamic model for the hybrid system and a simplified notation are described:

$$\begin{bmatrix} \delta\dot{\hat{h}} \\ \delta\dot{\hat{V}}_e^n \\ \delta\dot{\hat{E}} \\ \delta\dot{\hat{b}}_g \\ \delta\dot{\hat{b}}_a \\ \delta\dot{\hat{g}}_{gm} \end{bmatrix} = \begin{bmatrix} 0 & -F_{V2h} & 0 & 0 & 0 & 0 \\ -F_{h2V} & 0 & \vec{f}^n\times & 0 & -C_b^n & F_{gm2V} \\ 0 & F_{V2T} & -\vec{w}_{in}^n\times & C_b^n & 0 & 0 \\ 0 & 0 & 0 & -I/\tau_g & 0 & 0 \\ 0 & 0 & 0 & 0 & -I/\tau_a & 0 \\ 0 & 0 & 0 & 0 & 0 & -I/\tau_{gm} \end{bmatrix} \begin{bmatrix} \delta\hat{h} \\ \delta\hat{V}_e^n \\ \delta\hat{E} \\ \delta\hat{b}_g \\ \delta\hat{b}_a \\ \delta\hat{g}_{gm} \end{bmatrix} + \vec{W}_I \tag{3.58}$$

$$\Rightarrow \delta\dot{\hat{S}}_I = F_e\delta\hat{S}_I + \vec{W}_I$$

where $\vec{W}_I$ is the $\vec{W}_{INS}$ in equation 3.50 without $F_{h2V}\cdot\delta h$ term. The DGPS system error dynamic model for the hybrid system is illustrated below:

$$\begin{bmatrix} \delta\Delta\dot{\hat{X}}^{nr} \\ \vdots \\ \delta\Delta\dot{\hat{M}}_p \\ \delta\Delta\dot{\hat{m}}_p \end{bmatrix} = [F_G] \begin{bmatrix} \delta\Delta\hat{X}^{nr} \\ \vdots \\ \delta\Delta\hat{M}_p \\ \delta\Delta\hat{m}_p \end{bmatrix} + \begin{bmatrix} C_n^{nr}\delta\hat{V}_e^n \\ 0_{(1+2\cdot sn)\times 1} \\ \vec{n}_{Mp} \\ \vec{n}_{mp} \end{bmatrix} \tag{3.59}$$

where n_{Mp} and n_{Mp} are the driving white noise for code and carrier multipath GMRP models. A simplified notation similar to equation 3.57 is introduced to represent the consolidation results of equations 3.58 and 3.59:

$$\begin{bmatrix} \delta\dot{\hat{S}}_I \\ \delta\dot{\hat{S}}_G \end{bmatrix}_{(19+4+4\cdot sn)\times 1} = \begin{bmatrix} F_e & 0 \\ F_{I2G} & F_G \end{bmatrix} \begin{bmatrix} \delta\hat{S}_I \\ \delta\hat{S}_G \end{bmatrix}_{(19+4+4\cdot sn)\times 1} + \vec{W} \tag{3.60}$$

where $\vec{W}$ is the process noise for the whole hybrid navigation system; the details are derived in Appendix C.

In the DGPS-only system model, position states would have big process noises to account for uncertainty during the time propagation because of the vehicle movement.

However in this hybrid GPS/INS navigation system, DGPS position uncertainties are bonded to the INS position propagation errors. This unique system architecture by comprehensively integrating GPS and INS states builds up correlations inside the hybrid navigation filter during time propagation, which are beneficial in the way that INS can provide prediction information on DGPS states and DGPS positioning information is utilized for INS velocity, attitude and biases estimation.

3.3.2 DGPS Measurement and Measurement Error Models. With the comprehensive GPS/INS integration in the system dynamic model, the INS calibration is achieved by simply updating the DGPS state estimations at each epoch. The INS can become a reliable navigation resource in the final approach stage without any special or sophisticated calibration scheme for the hybrid navigation system.

GPS code and carrier phase measurements at the L1 frequency are assumed to be available to the GPS/INS hybrid navigation system before the final approach stage. Code-phase measurements basically are used to estimate the DGPS positions. Recall the equations 2.5 and 2.6 in Chapter 2, DGPS measurements for code and carrier phases are re-shown with added multipath states here:

$$\Delta\rho_k^i = -\vec{e}_k^i \cdot \vec{x}_k^r + \Delta\tau_k + \Delta I_k^i + \Delta T_k^i + \Delta M_{p_k}^{\ i} + \Delta v_{\rho_k}^{\ i}$$

$$\lambda_1 \Delta\phi_k^i = -\vec{e}_k^i \cdot \vec{x}_k^r + \Delta\tau_k - \Delta I_k^i + \Delta T_k^i + \lambda_1 \Delta N^i + \Delta m_{p_k}^{\ i} + \Delta v_{\phi_k}^{\ i}$$

A master satellite is chosen to form Double Difference (DD) GPS measurements, which eliminate the clock bias:

$$\Delta^2\rho_k^{ij} = -(\vec{e}_k^i - \vec{e}_k^j) \cdot \vec{x}_k^r + \Delta^2 I_k^{ij} + \Delta^2 T_k^{ij} + \Delta^2 M_{p_k}^{\ ij} + \Delta^2 v_{\rho_k}^{\ ij} \tag{3.61}$$

$$\lambda_1 \Delta^2 \phi_k^{ij} = -(\vec{e}_k^{\,i} - \vec{e}_k^{\,j}) \cdot \vec{x}_k^{\,r} - \Delta^2 I_k^{ij} + \Delta^2 T_k^{ij} + \lambda_1 \Delta^2 N^{ij} + \Delta^2 m_{p_k}^{\;ij} + \Delta^2 v_{\phi_k}^{\;ij} \qquad (3.62)$$

Whenever there are *n* satellites in view from both GPS receivers (user and reference station), *n-1* DD code and carrier-phase measurements are available to construct the measurement equations as:

$$\begin{bmatrix} Z_\rho \\ Z_\phi \end{bmatrix} = \begin{bmatrix} 0 & H_1 \\ 0 & H_2 \end{bmatrix} \begin{bmatrix} S_I \\ S_G \end{bmatrix} + \begin{bmatrix} \Delta^2 \vec{v}_\rho \\ \Delta^2 \vec{v}_\phi \end{bmatrix} \Rightarrow Z = HS + v \qquad (3.63)$$

where the DD code and carrier measurements are represented as:

$$Z_p = \begin{bmatrix} \Delta^2 \rho_k^{ij} \\ \vdots \end{bmatrix}_{(n-1)\times 1}, Z_\phi = \begin{bmatrix} \lambda_1 \Delta^2 \phi_k^{ij} \\ \vdots \end{bmatrix}_{(n-1)\times 1} \qquad (3.64)$$

The submatrix H_1 is the observation matrix for DD code measurements :

$$H_1 = \begin{bmatrix} -(e_k^1 - e_k^n) & \Delta tc_k^1 - \Delta tc_k^n & \Delta ic_k^1 & \cdots & 0 & -\Delta ic_k^n & & & \\ \vdots & \vdots & \vdots & \ddots & 0 & \vdots & 0_{(n-1)\times n} & dI & 0_{(n-1)\times n} \\ -(e_k^{n-1} - e_k^n) & \Delta tc_k^{n-1} - \Delta tc_k^n & 0 & \cdots & \Delta ic_k^{n-1} & -\Delta ic_k^n & & & \end{bmatrix} \qquad (3.65)$$

where the definitions of Δtc_k^i and Δic_k^i are the same as in Sections 2.3.1 and 2.3.2. Another submatrix H_2 is the observation matrix for DD carrier measurements:

$$H_2 = \begin{bmatrix} -(e_k^1 - e_k^n) & \Delta tc_k^1 - \Delta tc_k^n & -\Delta ic_k^1 & \cdots & 0 & \Delta ic_k^n & & & \\ \vdots & \vdots & \vdots & \ddots & 0 & \vdots & \lambda_1 dI & 0_{(n-1)\times n} & dI \\ -(e_k^{n-1} - e_k^n) & \Delta tc_k^{n-1} - \Delta tc_k^n & 0 & \cdots & -\Delta ic_k^{n-1} & \Delta ic_k^n & & & \end{bmatrix} \qquad (3.66)$$

The master satellite was chosen as the last satellite *n* for easier illustration. *dI* is the result of performing the measurement difference between satellites on an unit matrix *I*. It appears as below in this example:

$$dI = \begin{bmatrix} 1 & 0 & 0 & -1 \\ 0 & \ddots & 0 & -1 \\ 0 & 0 & 1 & -1 \end{bmatrix}_{(n-1)\times n}$$

The measurement error model derived from equation 3.63 for covariance analysis is:

$$\begin{bmatrix} \delta Z_\rho \\ \delta Z_\phi \end{bmatrix} = \begin{bmatrix} 0 & H_1 \\ 0 & H_2 \end{bmatrix} \begin{bmatrix} \delta S_I \\ \delta S_G \end{bmatrix} + \begin{bmatrix} \Delta^2 \bar{v}_\rho \\ \Delta^2 \bar{v}_\phi \end{bmatrix} \Rightarrow \delta Z = H \delta S + v \tag{3.67}$$

The correlations between all single difference measurements are assumed to be zeros. However, the measurement noise v in equation 3.67 is correlated between each satellite pair due to the double difference operation. The covariance of the double difference measurement noise for equation 3.67 can be derived as:

$$\Sigma_G = E\left[vv^T\right] = \begin{bmatrix} \Sigma_\rho & 0_{(n-1)\times(n-1)} \\ 0_{(n-1)\times(n-1)} & \Sigma_\phi \end{bmatrix} \tag{3.68}$$

where $\Sigma_{\rho/\phi} = \begin{bmatrix} \sigma_1^2 + \sigma_n^2 & \sigma_n^2 & \cdots & \sigma_n^2 \\ \sigma_n^2 & \sigma_2^2 + \sigma_n^2 & \ddots & \vdots \\ \vdots & \ddots & \ddots & \sigma_n^2 \\ \sigma_n^2 & \cdots & \sigma_n^2 & \sigma_n^2 + \sigma_n^2 \end{bmatrix}_{(n-1)\times(n-1)}$, and that σ_i is either the DD code measurement sigma or DD carrier-phase measurement sigma for the satellite i.

At this moment, the system error dynamic model (3.60) and measurement error model (3.64) of the GPS/INS integrated navigation system have been well established. This hybrid system performance can be simulated by the well-known Kalman filter implementation described in Section 3.3.3.

3.3.3 Kalman Filter Implementation. Kalman filter is widely used in the navigation due to its versatile capability of processing time-varying and multiple-input/output (I/O) systems [Brown97]. Nevertheless, reliable results can be achieved by a Kalman filter only when system dynamic and measurement errors are properly modeled in terms of time, state and measurement correlations. An overly optimistic system model would generate results which are not realistic, yet an overly conservative system model could

produce the system performance so poor that the system requirements would not be met. Properly handling the system process noise to accommodate modeling errors and appropriately assessing the covariance relationship among measurement data are the key points of a successfully working Kalman filter.

In navigation systems, Kalman filters are usually implemented in a discrete time form. Although the system dynamic model is constructed in continuous time, converting a continuous system to a discrete time system is straightforward [Franklin97]. Therefore, following derivations are handled in the discrete time domain.

After the system states have been initialized by setting all states to proper values (all of the states are set to zero except the initial attitude Euler angles, which are propagated independently by equation 3.54 and will be addressed in Section 5.2 for system evaluation), one epoch of time propagation on the states, which run through the system dynamic model, is carried out by the Kalman filter time-update as shown below:

$$\overline{S}_k = \Phi_{k-1}\hat{S}_{k-1} + \Gamma_{k-1}\hat{u}_{I(k-1)} \tag{3.69}$$

$$\overline{P}_k = \Phi e_{k-1}\hat{P}_{k-1}\Phi e_{k-1}^{-1} + \Sigma_{k-1}^{W} \tag{3.70}$$

where Φ_{k-1} and Φe_{k-1} are the discrete time version of the system and system error dynamic matrices in equations 3.57 and 3.60 respectively. Γ_{k-1} is the discrete time version of the G_h matrix and $\hat{u}_{I(k-1)}$ is the compensated system accelerations in equation 3.57. $\hat{S}_{k-1}$ and $\hat{P}_{k-1}$ are the best estimated states and associated covariance matrix after measurement update at time epoch *k*-1. Σ_{k-1}^{W} is the process noise covariance matrix at time epoch *k*-1. $\overline{S}_k$ and $\overline{P}_k$ are the time-propagated states and the covariance matrix at time epoch *k*.

Due to the nonlinearity of the INS dynamic equations, the Extended Kalman Filter (EKF) technique is used in equations 3.69 and 3.70. An iteration process is necessary on the measurement update during the first few epochs EKF process. If the vehicle has very high dynamic motions, the iteration process might be necessary for the period of high dynamic maneuvers.

To properly cope with the process noise in the system model, the covariance matrix of process noise from equation 3.60 is defined as:

$$\Sigma_k^W = E(\vec{W}_k \vec{W}_k^{\,T}) \tag{3.71}$$

The content and derivation of Σ_k^W is provided in Appendix C.

Once the state propagation from time epoch *k*-1 to *k* is complete, GPS measurements with the associated noise are available at time epoch *k*:

$$Z_k = H_k S_k + v_k \tag{3.72}$$

The optimal state estimation can be generated by the filter measurement update formulas:

$$\hat{S}_k = \overline{S}_{k-1} + K_k (Z_k - H_k \overline{S}_k) \tag{3.73}$$

$$\hat{P}_k = (I - K_k H_k)\overline{P}_k (I - K_k H_k)^T + K_k \Sigma_k^v K_k^T \tag{3.74}$$

$$K_k = \overline{P}_k H_k^T (\Sigma_k^v + H_k \overline{P}_k H_k^T)^{-1} \tag{3.75}$$

$\hat{S}_k$ and $\hat{P}_k$ are the optimal estimated states and the state covariance matrix after extracting information from the available measurements; K_k is the Kalman filter gain; Σ_k^v is the correlation matrix of the measurement noise at epoch *k* as defined in equation 3.68.

One special correction technique is applied to the Euler angle calibration. From equations A.1 and A.2 in Appendix A, the true body-to-navigation transformation matrix,

C_b^n, can be transformed into the estimated body-to-navigation transformation matrix, $\hat{C}_b^n$, by another transformation matrix, *B*, using three Euler angle attitude deviations:

$$\hat{C}_b^n = R_3(-\Delta\psi)R_2(-\Delta\theta)R_1(-\Delta\phi)C_b^n = BC_b^n \tag{3.76}$$

where $\Delta\phi$, $\Delta\theta$, and $\Delta\psi$ are the three elements of $\Delta\vec{E}$ and corresponding to roll, pitch and yaw angle deviations. The calibrated Euler angles $\hat{E}_k$ can be obtained by applying the inverse trigonometric function on the elements of updated transformation matrix $\hat{C}_{b\,k}^n$. The $\hat{C}_{b\,k}^n$ is updated by this formula:

$$\hat{C}_{b\,k}^n = \hat{B}_k^{-1}\overline{C}_{b\,k}^n \tag{3.77}$$

where $\hat{B}_k$ can be computed by using the three Euler angle transformations in equation 3.76 or in a linearized version by utilizing equation A.3. In general, the linearized version in equation A.3 is good enough for high quality gyroscopes. The estimated Euler angle deviation state vector $\Delta\hat{E}_k$ is set to be zeros after the Euler angle attitude is calibrated by using equation 3.77.

At this point, the updated states are the currently best estimates provided by the Kalman filter. Any state can be taken as a system output if desired or used as an input for vehicle control.

In summary, a novel hybrid GPS/INS system architecture has been completely developed. The Kalman filter implementation used in the hybrid system is illustrated as well. The innovative part of the hybrid system architecture is the way of utilizing the system dynamic information provided by INS. A conventional INS is generally calibrated explicitly by the differences between GPS and INS navigation outputs, which are either the time differenced carrier-phase GPS measurements or the differences

between the GPS range measurements and the computed ranges from INS and satellite positions [Ko00] for range domain integration. This explicit calibration process generally needs an observation matrix to best account for the errors contributed from each INS state, which is not a trivial task [Farrell02]. In contrast, the proposed hybrid navigation system only performs the measurement update process for DGPS state estimation, which is clear, simple and straightforward. The INS states in the hybrid system are calibrated implicitly by the position update process through the correlation among states.

The unique way of fusing INS information enables a seamless transition on the system position outputs from fully GPS positioning accuracy when 4 or more satellites are in view to completely INS free-coasting positions if no GPS measurement is available without any intervention. In the case that the INS information is not available, which can have very low probability by installing redundant IMUs on the vehicle, all IMU inputs have to be set to zeros and additional process noise needs to be added on velocity and attitude states. As long as the proper process noise is propagated into DGPS position states, the hybrid navigation system will work as a GPS-only navigation system. An INS integrity mechanism should be implemented to enable this switch or to eliminate the INS continuity risk by any means, which is beyond the scope of this research. The transition on the system outputs captures the essence of the "hybrid" system: GPS and INS are coexisting in the system and working together smoothly, yet each one can still work independently if the other is not available.

To more fully understand the properties of this novel GPS/INS hybrid navigation system, nominal system performance and sensitivity analysis are carried out in the next chapter through covariance analyses.

CHAPTER 4

PERFORMANCE AND SENSITIVITY ANALYSIS OF THE GPS/INS HYBRID NAVIGATION SYSTEM

A tightly coupled GPS/INS integration scheme is chosen to be the core of the GPS/INS hybrid navigation system. The purpose of this work is to address the vulnerability of GPS-only navigation systems during the most critical stage of the precision approach. The quality of IMU and gravity models has a significant effect on the achievable calibration performance and coasting capability. Performance simulations by covariance analyses with a nominal system configuration are carried out to understand the characteristics of the hybrid navigation system. A very detailed hybrid system sensitivity analysis to the system parameters is also explored for two main reasons: one is that the results can be an useful reference for the future research with different system configurations or applications, another is that these results provide an foundation to quantify the requirements on IMU and gravity model quality to meet LAAS CAT I/III fault-free integrity requirements.

4.1 Performance Analysis of Hybrid Navigation System

The complete system model for Kalman filter implementation has been discussed in Chapter 3. Covariance analysis is the main tool used throughout this chapter to simulate the system performance from different aspects. A few system assumptions have to be made in the analysis and a nominal scenario is introduced to make the performance results comparable.

Nominal parameters for DGPS measurements are 0.3 meter one sigma (standard deviation) for SD code measurement, 1 cm one sigma for SD carrier measurement, and

the multipath time constants for both code and carrier are 100 seconds. The troposphere height and the standard deviation of refractivity for the tropospheric decorrelation model (equation 2.17) are assumed as: h_0 = 15000 m and $\sigma_{\Delta n}$ = 10. The ionospheric shell height and the standard deviation of vertical ionospheric gradient for the ionospheric decorrelation model (equation 2.18) are assumed as: h_I = 350 km and σ_{VIG} = 2 mm/km. The VPL and LPL for the hybrid navigation system coasting performance in this preliminary analysis are generally computed in compliance with the stringent LAAS CAT III SIS integrity risk 1×10^{-9} since there is no GPS signal involved during coasting.

4.1.1 Nominal Approach. A nominal LAAS precision approach flight path is defined to provide a common stage for system performance comparison. Figure 4.1 illustrates this nominal flight path, and the nominal location is chosen at Chicago O'Hare international airport.

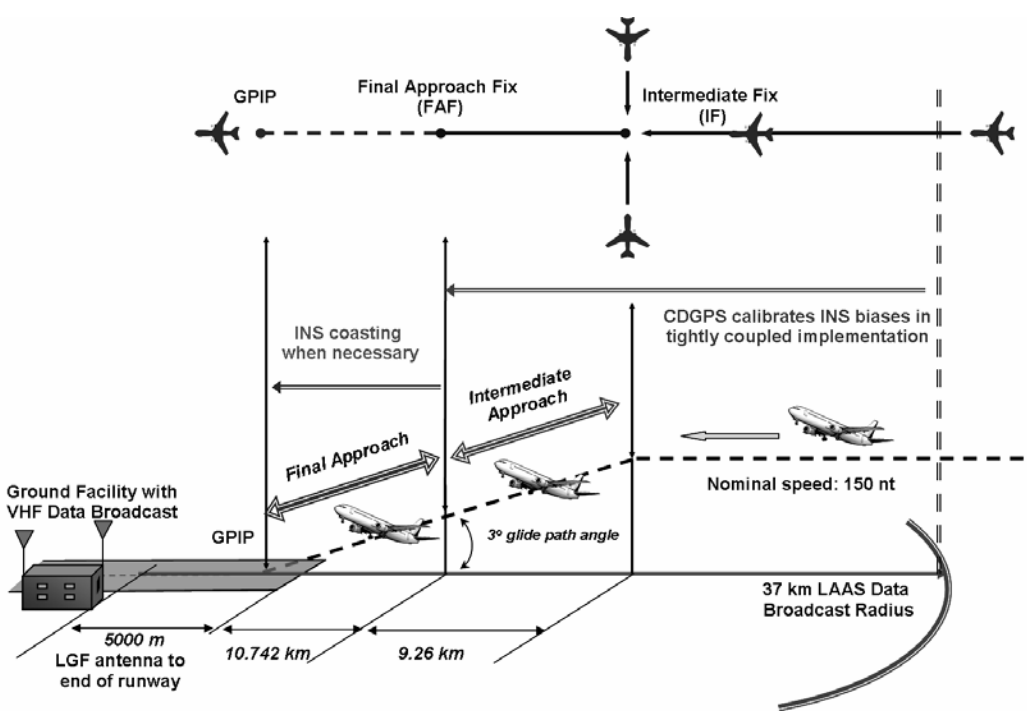

Figure 4.1. Nominal Flight Path Illustration

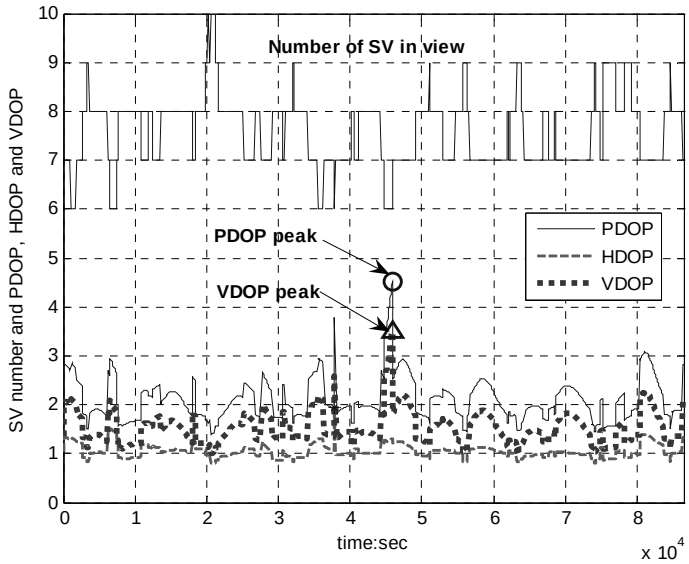

Figure 4.2. 24 Hours Delusion of Precision from GPS Satellite Geometry

The reference antenna is conservatively set at five kilometers away from the runway end to avoid taking advantage of very short distance between reference station and aircraft users, which may result overly optimistic positioning performance. The nominal flight speed is set at 150 knots throughout the approach, which is approximately 77 m/sec. A straight-in flight path is adopted as the nominal approach, which is composed of two segments: a straight and level flight before the intermediate fix point and a descending flight with a constant rate afterward until touchdown. The most demanding system requirements (CAT III) are applied during the system performance simulations unless otherwise specified.

Another important factor which affects the system performance is the GPS satellite geometry. A valuable tool to indicate the contribution to the estimated position error from satellite geometry is Dilution of Precision (DOP). There are Position DOP (PDOP), Vertical DOP (VDOP), Horizontal DOP (HDOP) and others (TDOP, GDOP etc.), which are defined based on the satellites' line-of-sight vectors in position estimation

Table 4.1. Specifications of Nominal IMU

standard devication	Gyroscope	Accelerometer
Scale Factor Error (σ_{sf})	15 ppm	30 ppm
Misalignment (σ_{mis})	10 μrad	10 μrad
Bias Stability (σ_{bg} / σ_{ba})	0.01 deg/hr	10 μg
Measurement noise (σ_{vg} / σ_{va})	0.001 deg/hr$^{\wedge 1/2}$ (ARW)	10 μg

equations [Misra01]. Estimated vertical position errors can be obtained simply by multiplying the range measurement errors with VDOP. The worst geometry obtained using the DO-229D constellation at the nominal location has been selected as the nominal geometry for all analyses to maintain conservativeness. The criterion of selecting the worst geometry is the highest VDOP from a 24 hour satellite geometry simulation shown in Figure 4.2 at the site of O'Hare airport.

4.1.2 INS Coasting Performance. The coasting performance after a period of INS in-flight calibration process, during which fault-free GPS measurements are assumed, will vary depending on the quality of the IMU. The nominal IMU model parameters for the nominal performance simulation are listed in Table 4.1. The popular LN-100 navigation grade IMU has similar quality. A nominal gravity model is also needed in order to perform the hybrid navigation system coasting performance simulation. Table 4.2 has the

Table 4.2. Nominal Gravity Model

	standard deviation	correlation distance (τ_{gm})
δξ (DOV in NS)	5 arcsecond (σ_{ξ})	20 nmi
δη (DOV in EW)	5 arcsecond (σ_{η})	20 nmi
$\delta\Delta g_0$ (Vertical Gravity Error)	2.5 μg ($\sigma_{\Delta g_0}$)	20 nmi

detailed numbers applied in the simulation. While the nominal DOV quality is available from NIMA's (currently NGA) 2 arcminute database globally [Grejner03], better accuracy can be achieved from local airborne gravimetric measurements for local gravity field survey [Marti02].

All the INS calibration performance in this chapter is presented with the in-flight INS calibration process working throughout the whole approach, while the coasting performance is actually evaluated by starting coasting at the FAF point (the starting point of an final approach). All the coasting position errors shown in Sections 4.1 and 4.2 only account for the errors contributed from INS system. The GPS positioning errors at the coasting started point (FAF) are taken into account to compute the total navigation errors when the IMU and gravity model quality are quantified to meet the LAAS requirements in Section 4.3.

Figure 4.3 shows the coasting distance vs. position propagation errors with 10^{-9} fault-free integrity risk. The lateral position error is horizontal position error projected on

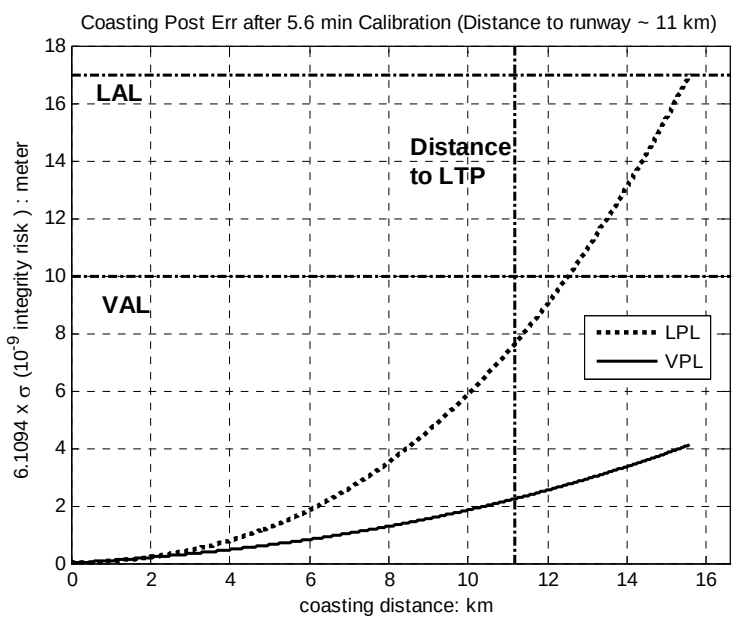

Figure 4.3. Nominal INS Coasting Performance

the horizontal off-track direction (ie. the horizontal direction orthogonal to the aircraft approach direction). The nominal approach (98° azimuth angle) is chosen to maximize the lateral position error (for the worst case satellite geometry scenario selected). Due to the lack of observability on vehicle heading angle in the nominal approach, the estimation error on yaw angle is the worst attitude error in Figure 4.4. The standard deviation of the yaw angle only converges to the 0.1 degree level when initialized with 1 degree attitude error. This lack of observation on yaw angle can be explained by looking into the coefficients in the velocity error propagation equation 3.45. Expanding the elements inside the matrix multiplied by the attitude errors, equation 3.45 is express below:

$$\begin{bmatrix} \delta^n \dot{v}_N(t) \\ \delta^n \dot{v}_E(t) \\ \delta^n \dot{v}_D(t) \end{bmatrix}_e^n = \begin{bmatrix} 0 & -f_z^n(t) & f_y^n(t) \\ f_z^n(t) & 0 & -f_x^n(t) \\ -f_y^n(t) & f_x^n(t) & 0 \end{bmatrix} \begin{bmatrix} \delta\phi(t) \\ \delta\theta(t) \\ \delta\psi(t) \end{bmatrix} + C_b^n(t)\delta\vec{f}^b(t) + \delta\vec{g}_l^n(t) \quad (4.1)$$

where the elements f_x^n, f_y^n and f_z^n are the true specific forces expressed in the navigation frame coordinates. For the nominal approach, aircraft is assumed to have no

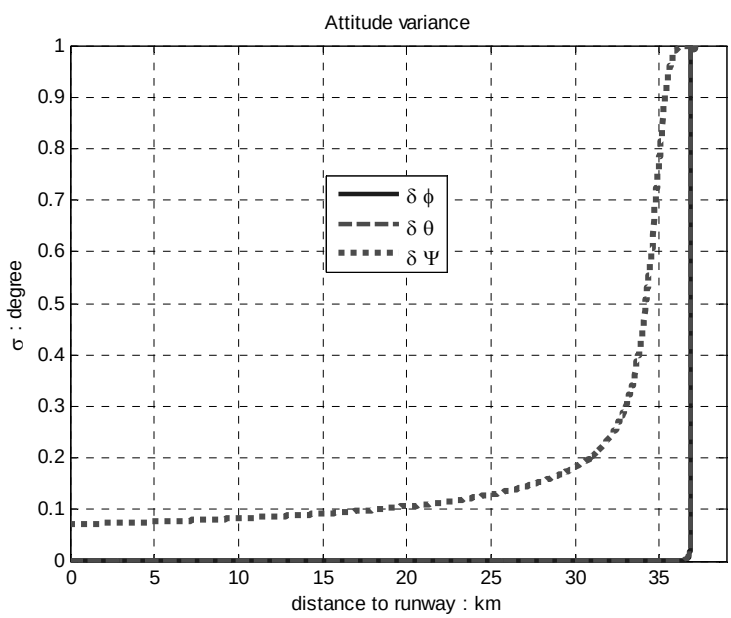

Figure 4.4. Attitude Errors of Nominal INS Coasting Performance

acceleration during the whole approach. Therefore, f_x^n and f_y^n are zero constants, and f_z^n is equal to the negative value of the true vertical gravity. With these coefficient values arranged in the above equation, roll and pitch angle errors will be propagated into north and east velocity errors constantly due to vertical gravity, then propagated into position errors, which can be calibrated when GPS measurements are available. In contrast, yaw angle is disconnected form the velocity error for any direction. This makes the calibration on the yaw angle error only possible through the correlations between yaw angle and other states and results in much worse calibration performance shown in Figure 4.4.

Figure 4.3 demonstrates that the system performance exceeds the requirements. It shows that when aircraft coasts on INS to reach the Landing Threshold Point (LTP), Vertical Protection Level (VPL) and Lateral Protection Level (LPL) both are still safely under the Vertical Alert Limit (VAL), which is 10 meters for CAT III., and the Lateral Alert Limit (LAL), which is 17 meters. The covariance simulation stops when either LPL or VPL hits its respective alert limit. For the nominal case, the lateral position error is the most stringent constraint on the system performance.

4.1.3 GPS Aided INS Coasting Performance. A less than four satellite vehicles (SV) in view scenario is very likely to happen if unintentional jamming occurs in the final approach stage. In the case of hostile interference from a nearby jammer on the ground, the possibility that only some of GPS satellite signals are jammed still exists. Although a quantitative analysis of the jamming scenario is beyond of the scope of this research, the system performance is simulated qualitatively to emphasize how well the system coasting range can be improved with partial GPS aiding (ie. with one to three SVs available).

Two SV and three SV cases analyzed are selected to provide the worst geometries during the final approach. Coasting starts when aircraft pass FAF point which is around 11 km away from the end of runway, and the number of satellite in view drops to two or three and remains at that level throughout the coasting. The number of satellites in view is shown in grey lines in Figure 4.6. The aided coasting results are shown in Figure 4.5, it can be seen that the healthy 2-SV-aided coasting range is about 3.5 km longer than no-aiding, and 3-SV-aided case increases 9.5 km dramatically. It also shows that the lateral position error can be effectively reduced with the aiding of two or more SVs. As a consequence, the vertical error becomes the performance limiter with aided coasting performance when there are three or more SVs available for aiding. Figure 4.6 shows the velocity coasting performance for the two SV aiding and three SV aiding cases. In this figure, the vertical components in both cases are overlapping with each other along the

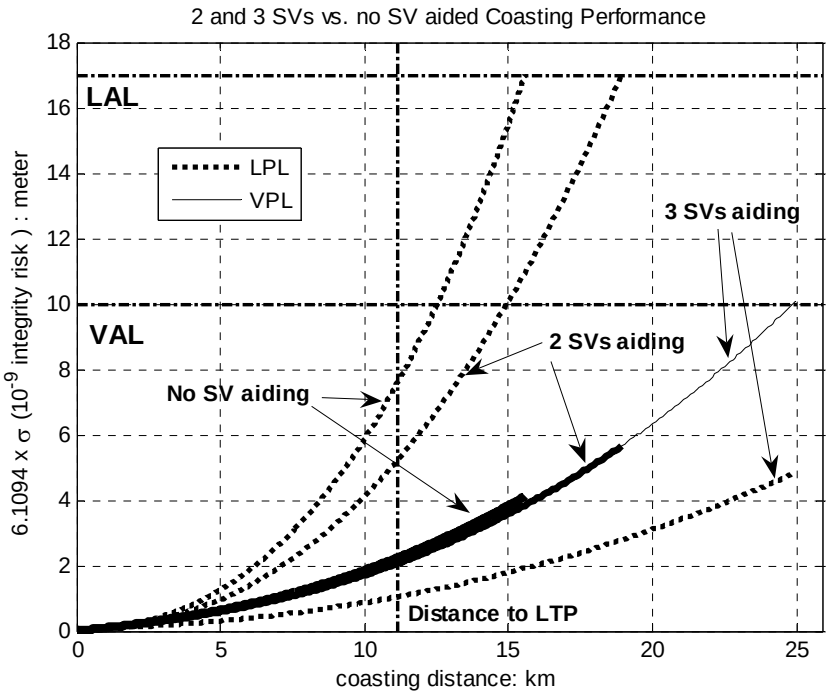

Figure 4.5. Partial GPS Aided INS Coasting Performance

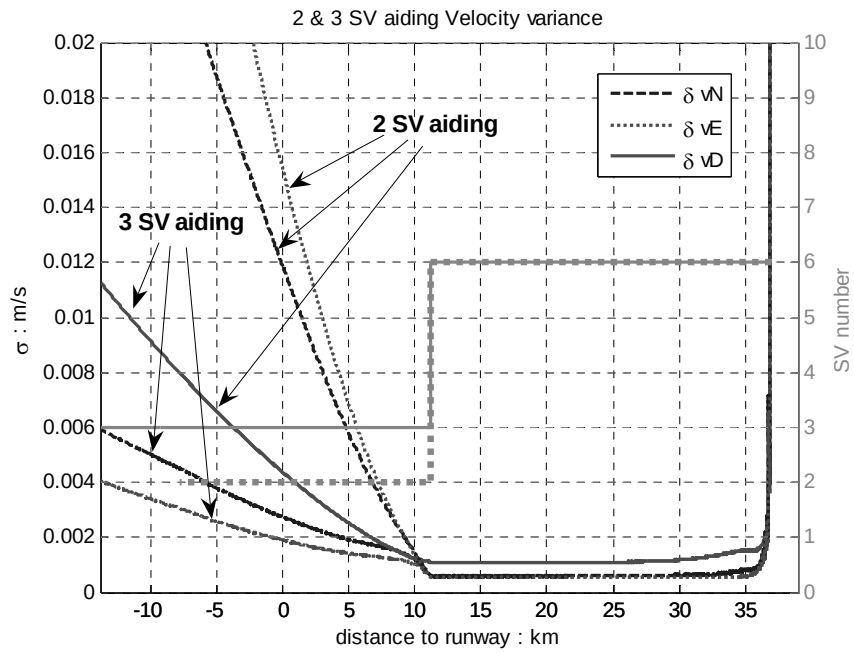

Figure 4.6. Coasting Velocity Performance with Partial GPS Aiding

flight path, but the northern and eastern velocity errors are much smaller in 3 SV aiding case, which explains the reduced lateral position errors in Figure 4.5.

Coasting performance with two and three SVs aiding represents a transition from pure INS coasting to full GPS positioning. The enhanced coasting performance shown by these two illustrative cases demonstrates the potential to improve the fault-free availability for LAAS CAT I/III applications.

4.2 Hybrid Navigation System Sensitivity Analysis

To better understand the variability in the hybrid system performance, coasting performance sensitivity with respect to the system parameters and heading information augmentation are simulated. Two most significant factors influencing the coasting performance are the IMU measurement quality and the INS calibration period. The gravity model has a direct relationship to the IMU gravity compensation process, so it is

also expected that the quality of the gravity model will be highly influential. A sensitivity analysis will be performed in this regard. The sensitivity to aircraft flight path must also be explored due to the nonlinearity of the navigation equations. Horizontal accelerations during the final coasting stage, which can propagate azimuth errors into the lateral velocity, can cause unexpected lateral coasting error. This issue, as well as the heading information augmentation introduced to mitigate azimuth errors, is also analyzed. Lever arm effects, due to the physical displacement between the GPS antenna phase center and the origin of the IMU triad, are also analyzed to understand the impact of the residual displacement error on the coasting performance.

4.2.1 Lever Arm Effect. The typical equipment setup makes it impossible to have the GPS antenna phase center coincide with the IMU's location. The displacement between these two points is generally called a lever arm. This spatial separation makes the position propagations of these two points different from each other during certain

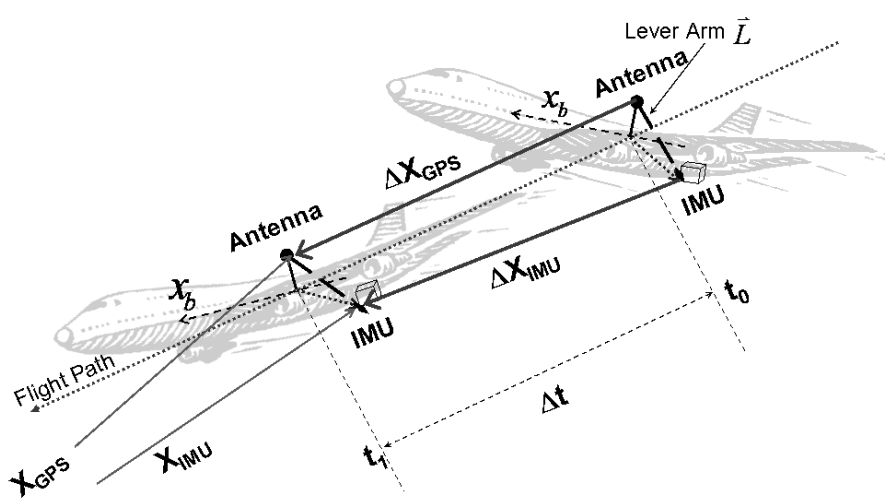

Figure 4.7. Lever Arm Effect Illustration

circumstances. Therefore, a further analysis is necessary to account for this effect.

Figure 4.7 illustrates the physical relationship among the IMU origin position, the GPS antenna phase center position and the lever arm displacement ($\vec{L}^b$: from GPS to IMU in the body frame). It is clear that when aircraft attitude changes with time, GPS propagating positions are different from the propagated position of the IMU origin due to the orientation of the lever arm. Equation 4.2 and 4.3 show this relationship as a function of time:

$$\vec{X}^n_{GPS}(t_0) = \vec{X}^n_{IMU}(t_0) + C^n_b(t_0)(-\vec{L}^b) \tag{4.2}$$

$$\vec{X}^n_{GPS}(t_1) = \vec{X}^n_{IMU}(t_1) + C^n_b(t_1)(-\vec{L}^b) \tag{4.3}$$

After subtracting 4.2 from 4.3, the GPS antenna incremental displacement during a short time period is equal to the IMU origin incremental displacement plus the orientation change of lever arm in this period of time:

$$\Delta\vec{X}^n_{GPS}(\Delta t) = \Delta\vec{X}^n_{IMU}(\Delta t) + [C^n_b(t_1) - C^n_b(t_0)](-\vec{L}^b) \tag{4.4}$$

where $\Delta t = t_1 - t_0$

With the assumption that error is small for a short duration, lever arm error equations can be derived by applying a perturbation method:

$$\delta\Delta\vec{X}^n_{GPS}(\Delta t) = \delta\Delta\vec{X}^n_{IMU}(\Delta t) - [\Psi_{t1}C^n_b(t_1) - \Psi_{t0}C^n_b(t_0)]\vec{L}^b - [C^n_b(t_1) - C^n_b(t_0)]\delta\vec{L}^b \tag{4.5}$$

where $\Psi_{t0} = \begin{bmatrix} 0 & -\delta\psi & \delta\theta \\ \delta\psi & 0 & -\delta\phi \\ -\delta\theta & \delta\phi & 0 \end{bmatrix}_{t0}$, it is the attitude error at t_0 in cross product form.

It is clear from equation 4.5 that the propagation errors for the GPS antenna positions are composed of the INS propagation errors and two other error terms related to the lever

arm. These two terms are consequently called the lever arm effect in this system error analysis.

After further observation on the lever arm effect, two simple conclusions can be made: 1) the first term translates the attitude errors into position errors proportional to the magnitude of lever arm length (if the cross product of the attitude error and the lever arm vector expressed in navigation coordinates, $C_b^n \vec{L}^b$, has noticeable change during the propagation period); 2) the second term will contribute the lever arm survey residual error to the GPS propagation error during a vehicle maneuver.

Using current advanced surveying techniques, the lever arm displacement survey error is unlikely to be large enough to impact the system performance in most of the short coasting time applications. Centimeter level lever arm residual error is assumed in the analysis. The length of lever arm can also be deliberately engineered to be small to avoid translating attitude error into significant position propagation error if the INS coasting duration is long.

The nominal flight scenario is simulated and results are shown in Figure 4.8. There are 3 cases of lever arm configurations; the first lever arm displacement has coordinates in body frame $\vec{L}^b = [-20 \quad 10 \quad 5]$; the second lever arm is $\vec{L}^b = [1 \quad 1 \quad 1]$ and the last case has no lever arm displacement. The results of these three cases are overlapping, which means there is no impact on coasting performance in our nominal flight scenario. These results are understandable because the simulated nominal approach has no aircraft attitude change and no noticeable incremental attitude error during such a short mission period.

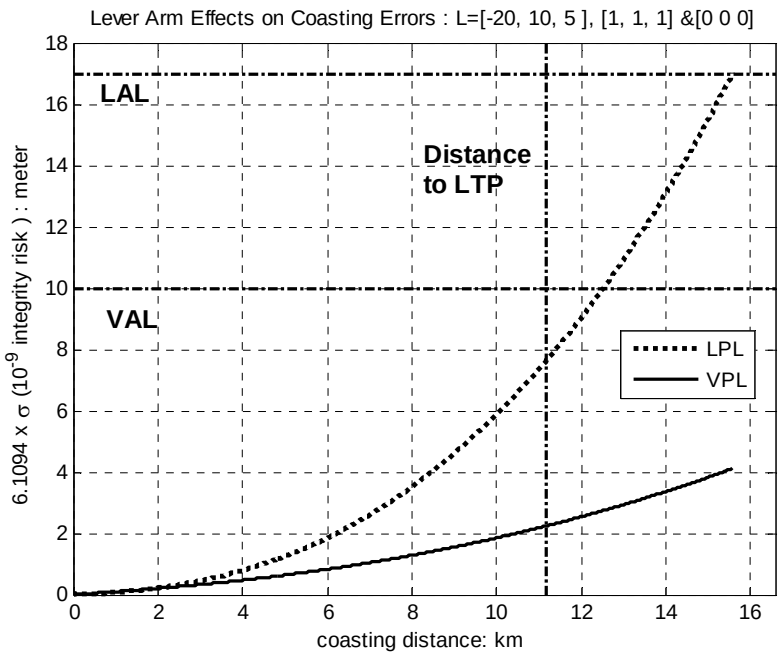

Figure 4.8. Sensitivity Analysis Results of Lever Arm Effect

Even though the results show no impact on coasting performance, it doesn't mean the lever arm has no influence at all. These results just demonstrate that in a level and straight flight path, the lever arm effect can be neglected. A one-turn approach would have aircraft attitude change considerably, therefore the lever arm effect will be re-examined in the multiple parameter variation analysis later on.

4.2.2 Calibration Period. The tightly coupled GPS/INS Kalman filter is implemented as described in Section 3.3 to perform the in-flight INS calibration. The calibration time necessary for the estimated INS state covariance to reach a certain quality for a safe final approach coasting was analyzed.

The nominal flight scenario was applied in the analysis. The only varying parameter was the period of tightly coupled GPS/INS calibration processing, in other words, the tightly coupled Kalman filter estimation time. The simulation started with an initial calibration time of 30 seconds with an incremental time step of 30 seconds, ending

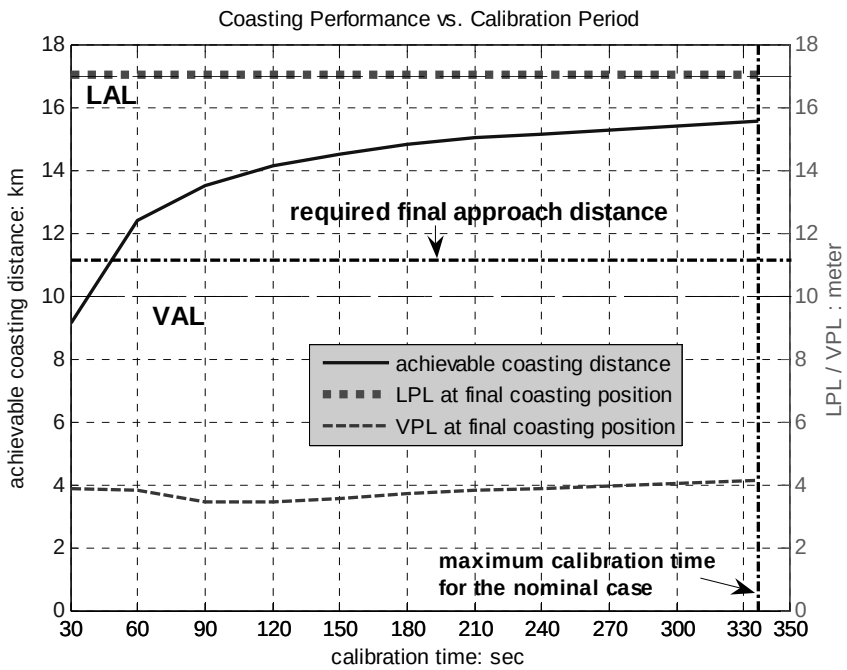

Figure 4.9. Sensitivity Analysis for Calibration Time

with the nominal calibration time (the maximum available calibration period for the nominal approach) of approximately 340 seconds. For each calibration period, the achievable coasting distance was recorded when either the LAL or VAL was exceeded by the LPL or VPL. The results of the calibration time analysis are shown in Figure 4.9. In the figure, LPL is the system coasting constraint. Therefore, the line of the LPL at DH overlaps the LAL line.

As far as achievable coasting distance is concerned, 60 seconds calibration time is necessary in Figure 4.9 (the achievable coasting distance exceeds the required final approach distance). After 150 seconds, the achievable coasting distance increases slowly and approaches to a steady value. If a longer coasting range is required with similar integrity requirements, an additional aiding sensor to help suppress lateral error should be considered.

4.2.3 IMU Measurement Quality. IMU measurement quality has the most direct influence on INS coasting performance. A sensitivity analysis in this regard can provide valuable quantitative information regarding how the coasting performance varies using different grades of IMU quality. The results would be very helpful to define the requirements on IMU sensor quality for any desired system configuration, such as LAAS CAT I or III in this research.

The methodology for exploring the IMU sensitivity to the coasting performance is to change the standard deviations of the gyroscope's and the accelerometer's measurement noise and biases individually for the nominal approach. The worst satellite geometry is used throughout this analysis. In an effort to remain concise, only the relevant trends of the simulation results are given.

Gyroscope influence: Angle Random Walk (ARW) is a popular index for the quality of measurement noise of gyroscopes [Stockwell] and is applied in the analysis.

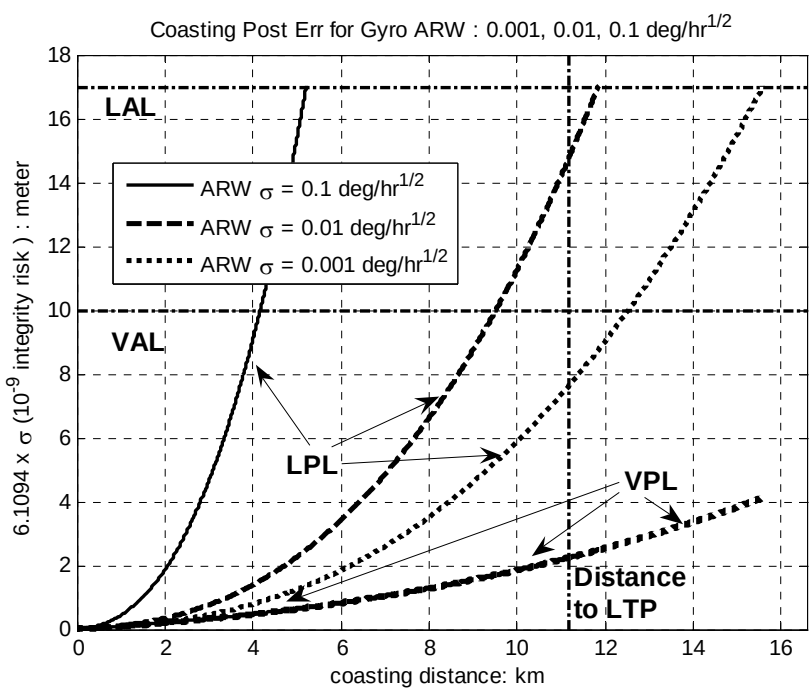

Figure 4.10. Sensitivity Analysis for Gyro ARW (1)

The parameter values of ARW in this analysis are 0.001 deg/hr$^{1/2}$ (nominal value), 0.01 deg/hr$^{1/2}$ and 0.1 deg/hr$^{1/2}$ respectively. The system coasting performance is shown in Figure 4.10.

The dominant error shown in the figure is clearly the lateral position error for all ARW values. Three VPL lines are overlapping. The coasting performance is reduced considerably when ARW is increased. The most dramatic sigma increment on the estimation errors is the attitude yaw angle estimation error, which is equivalent to the heading azimuth angle error in the Euler angle attitude implementation. The lack of observability on the yaw angle makes this angle very susceptible to ARW variation. This effect can be observed more clearly in Figure 4.11. When the azimuth angle uncertainty gets worse, the tilt angles (pitch and roll angles) are also estimated less accurately. As a result, the lateral velocity error degrades greatly when ARW increases and becomes the main constraint for coasting performance. Although the azimuth angle is affected by the ARW degradation significantly, the yaw angle estimation error has no direct impact on

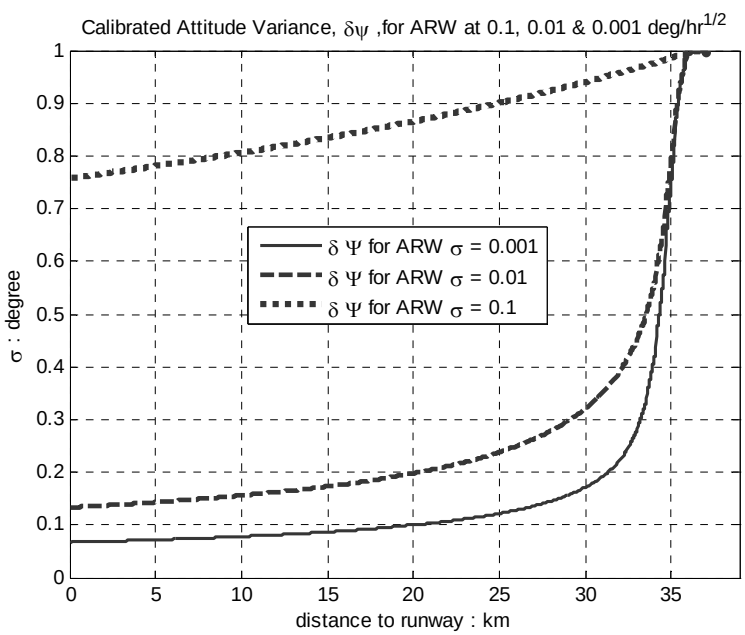

Figure 4.11. Sensitivity Analysis for Gyro ARW (2)

velocity or position errors because the coefficients (the horizontal accelerations f_x^n and f_y^n in equation 4.1) to propagate yaw angle errors to velocity states are zeros during the nominal approach. Only the lateral velocity is affected by the errors propagated from the degraded tilt angles through the gravity (f_z^n). This observation is supported by the overlapping VPL lines in Figure 4.10.

Another effect of a large ARW is that the gyro output noise could shadow the observability on the higher order state, gyro bias. No improvement on the nominal gyro bias estimation was observed for 0.1 ARW while better estimations were achieved for 0.01 and 0.001 ARW cases (reduced to 0.0097 and 0.0087 respectively from the initial sigma of 0.01 deg/hr).

The last result observed from this analysis is revealed in Figure 4.12. It shows that the sigmas of the tilt angle estimation errors increase much quicker for a large ARW value. This observation is consistent with the fast deteriorated lateral coasting errors

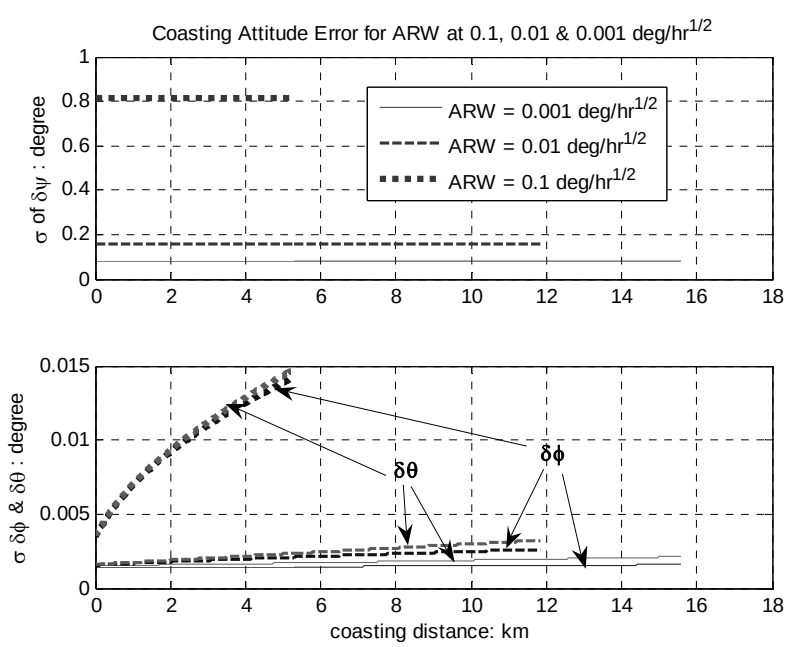

Figure 4.12. Sensitivity Analysis for Gyro ARW (3)

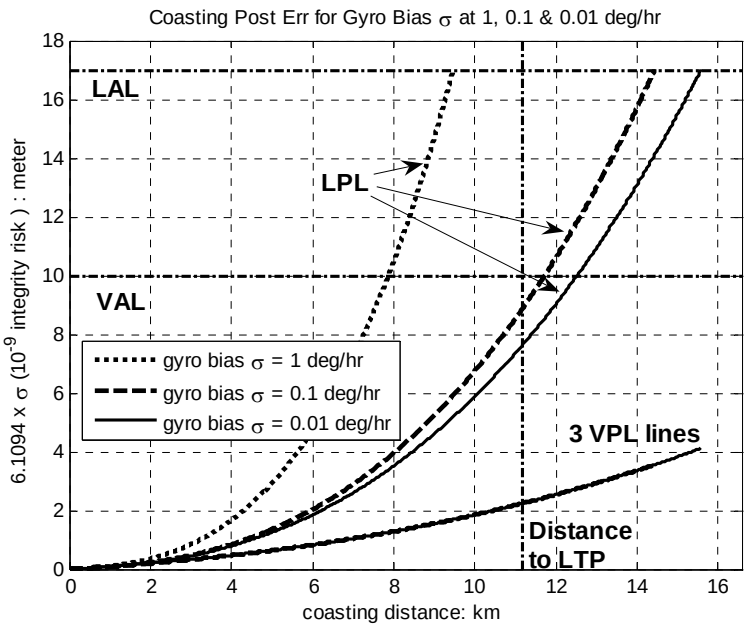

Figure 4.13. Sensitivity Analysis for Gyro Bias (1)

shown in Figure 4.10.

The Gyro bias stability is analyzed similarly by changing one sigma values at 1, 0.1 and 0.01 deg/hr. The coasting performance results are shown in Figure 4.13. The impact on the coasting performance is less severe than ARW degradation. However, the

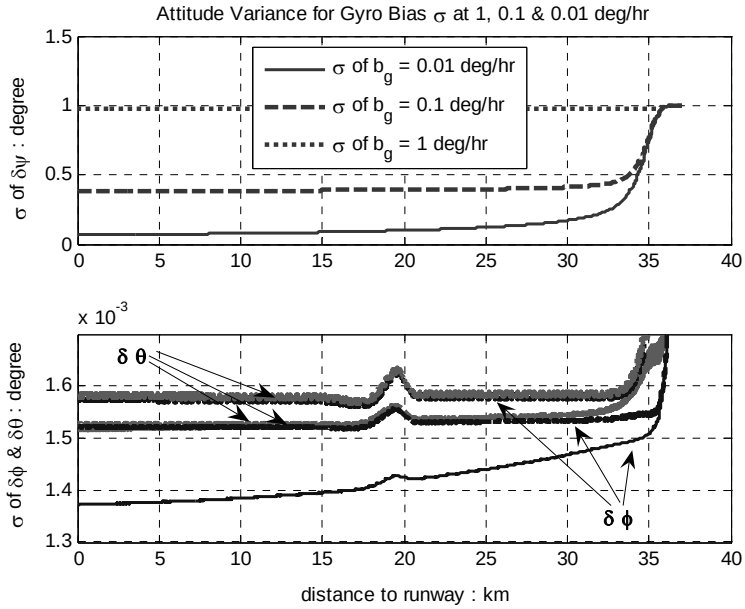

Figure 4.14. Sensitivity Analysis for Gyro Bias (2)

performance limiter is still the lateral position error.

Figure 4.14 shows the attitude estimation errors for different sigmas of gyroscope bias errors. The small peaks at pitch and roll angle errors corresponds to the period that aircraft starts to descend. This shows that the attitude errors are sensitive to acceleration variations. The calibrated azimuth error is correlated with the z axis gyro bias error in body frame since the azimuth angle is mainly propagated from the z axis gyro measurements during the nominal approach. Because there is no horizontal acceleration in the nominal approach, the azimuth angle estimation is poor. In contrast, vertical gravity can effectively calibrate out tilt angle errors (roll and pitch angles). Zero horizontal acceleration in current nominal flight path stops the azimuth angle error from propagating into velocity state, therefore makes it much less observable in the range domain.

In current nominal flight path, the major contribution to the azimuth error comes

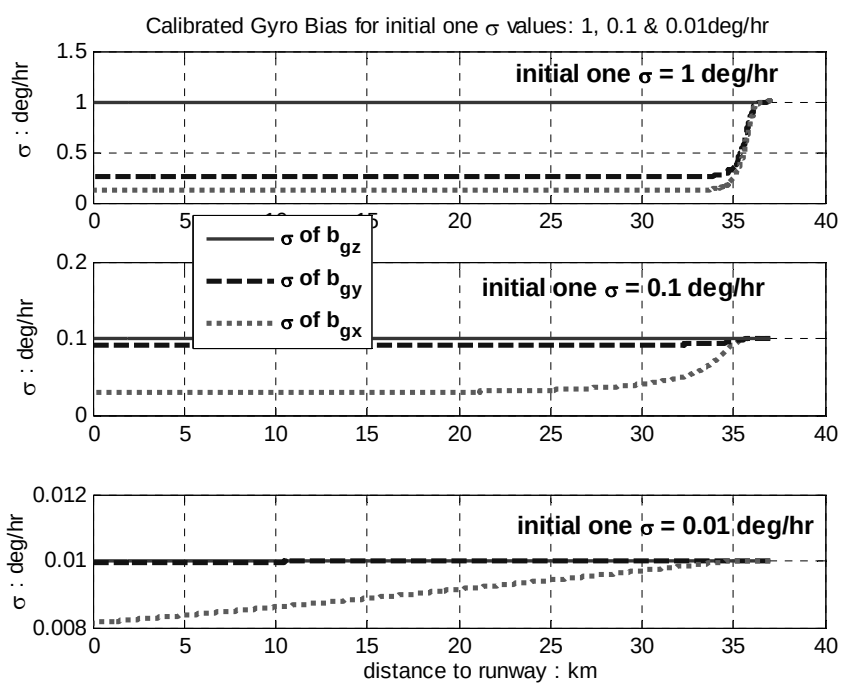

Figure 4.15. Sensitivity Analysis for Gyro Bias (3)

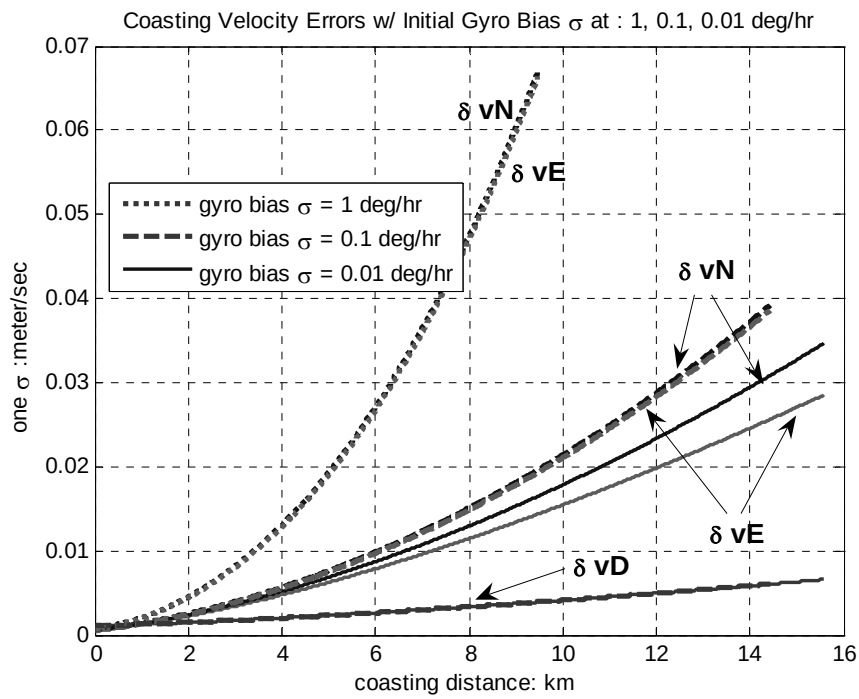

Figure 4.16. Sensitivity Analysis for Gyro Bias (4)

from ARW and gyro bias error along the body frame's z axis. The limited observability on the azimuth angle also results in poor calibration of the z axis gyro bias of the body frame. Figure 4.15 shows the calibrated gyro bias results with different initial attitude errors. While large initial attitude errors on the tilt angles can be reduced by the calibration process, the azimuth angle errors remain constant. Hence, the quality of the azimuth angle estimation is mainly decided by the quality of the gyro z axis output.

A further look at the coasting velocity in Figure 4.16 can provide more understanding about the gyro bias variation effect on the coasting errors. In a straight and level flight, the vertical channel is generally treated as being decoupled from the horizontal channels due to no horizontal accelerations. It is supported by the results shown in Figure 4.16 in which all three vertical velocity errors are uncorrelated with the change in the horizontal velocity errors.

<u>Accelerometer influence</u>: The system sensitivity with respect to accelerometers quality is discussed here. Analogous to the analysis that was done for the gyroscope, the measurement noise of the accelerometer output is analyzed first. The standard deviation of the measurement noise varies by 1, 0.1 and 0.01 mg, in which 0.01 mg is the nominal value.

Figure 4.17 presents the simulated coasting performance. The dominant error is still the lateral position error, but the vertical and lateral coasting position errors degrade in a similar fashion. Degradations on the velocity and attitude errors are expectable and shown in Figures 4.18 and 4.19 as noise magnitude increases. The dramatic performance reduction in the 1 mg case is mainly due to the combined errors from multiple state errors (velocity and attitude errors) with larger degradation. Figure 4.18 shows the influence on calibrated velocity states. The large saw-tooth fluctuations in the bottom plot are caused by the fast error accumulation from the 1 mg noise.

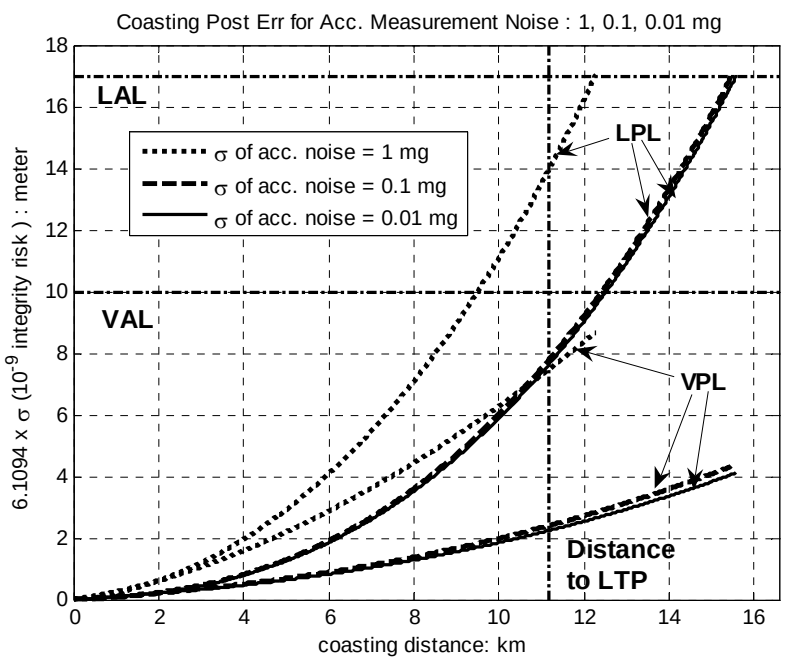

Figure 4.17 Sensitivity Analysis for Accelerometer Noise (1)

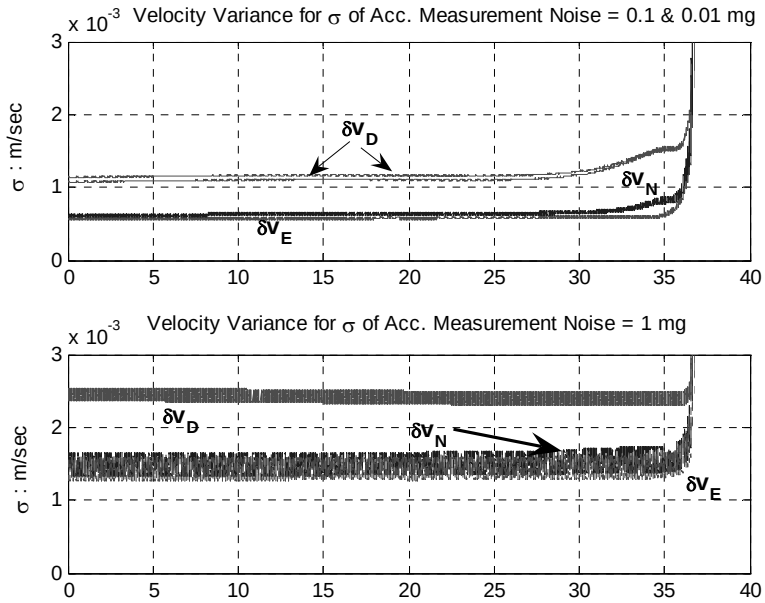

Figure 4.18 Sensitivity Analyses for Accelerometer Noise (2)

The accelerometer measurement noise contributes directly to the velocity errors while the attitude errors are affected indirectly through the degradation on the velocity state estimations. The calibrated attitude errors are presented in Figure 4.19. The similar shadow effect happened on the gyro bias estimation with big ARW also appears on the

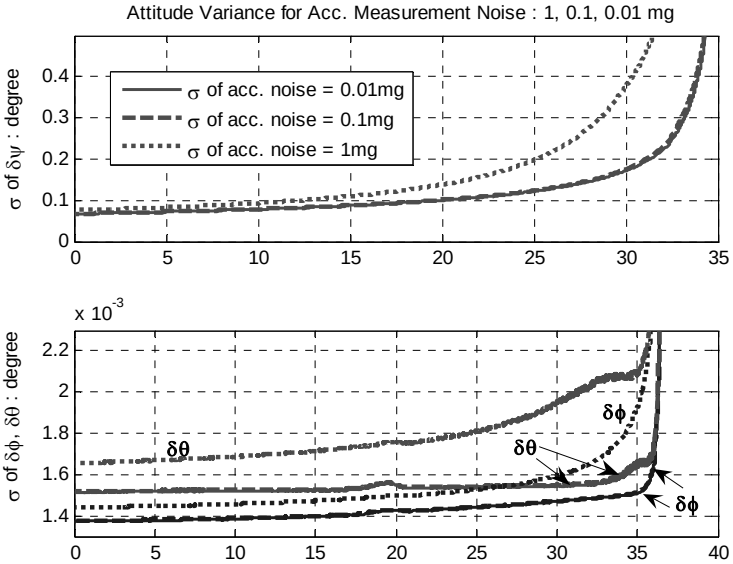

Figure 4.19 Sensitivity Analyses for Accelerometer Noise (3)

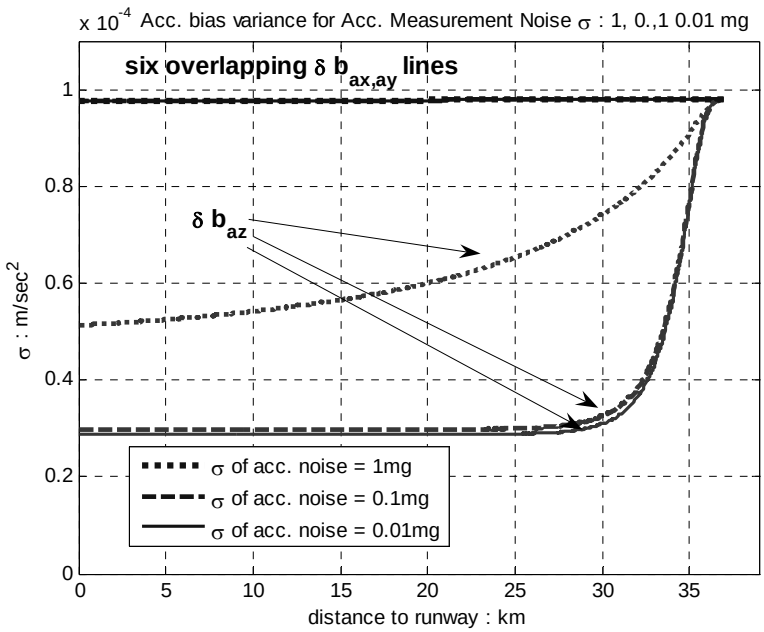

Figure 4.20. Sensitivity Analysis for Accelerometer Noise (4)

accelerometer bias estimation and is shown in Figure 4.20, which makes the bias estimation improvement along the body z axis less.

The accelerometer bias stability was analyzed at 0.01 mg (the nominal value), 0.1 mg and 1 mg. Figure 4.21 shows the system coasting performance for the accelerometer

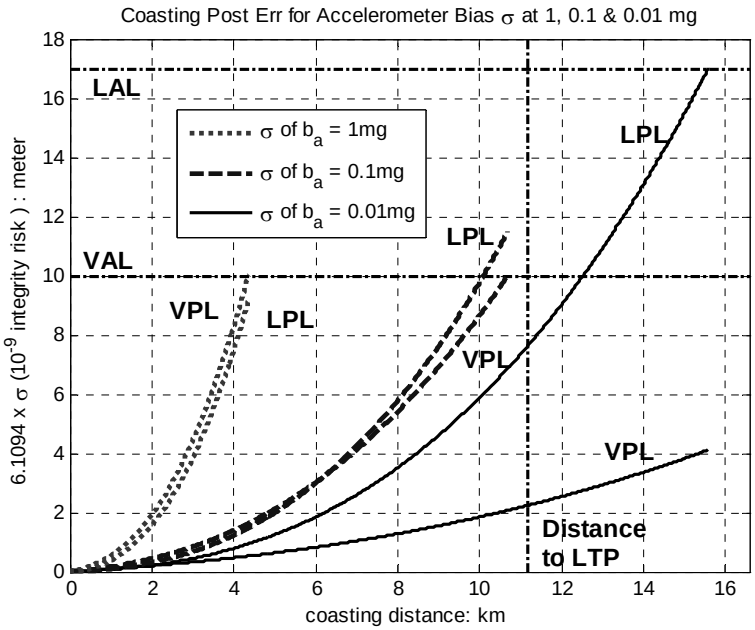

Figure 4.21. Sensitivity Analysis for Accelerometer Bias (1)

bias sensitivity.

The achievable coasting distance decreased much faster than the accelerometer measurement noise case. This observation is consistent with the properties of these two error sources: the measurement noise is random naturally, and its time accumulated errors have randomness as well; the bias error behaves more like an indeterminate constant error over short periods because of the long correlation time constant. There is no averaging effect for a constant error case, which makes the coasting error grow faster. The calibrated velocity shown in Figure 4.22 demonstrates that better estimation of the velocities is achievable with smaller bias error.

The bias error affects the attitude calibration differently from the way noise does. Without aircraft maneuver, it is not possible to distinguish the accelerometer bias offsets along horizontal axis outputs from the sensed partial gravities resulting from tilt angle errors. Consequently, the tilt angle estimations have relatively big and steady errors when the bias error is big. Only a small step-down occurred while the aircraft started

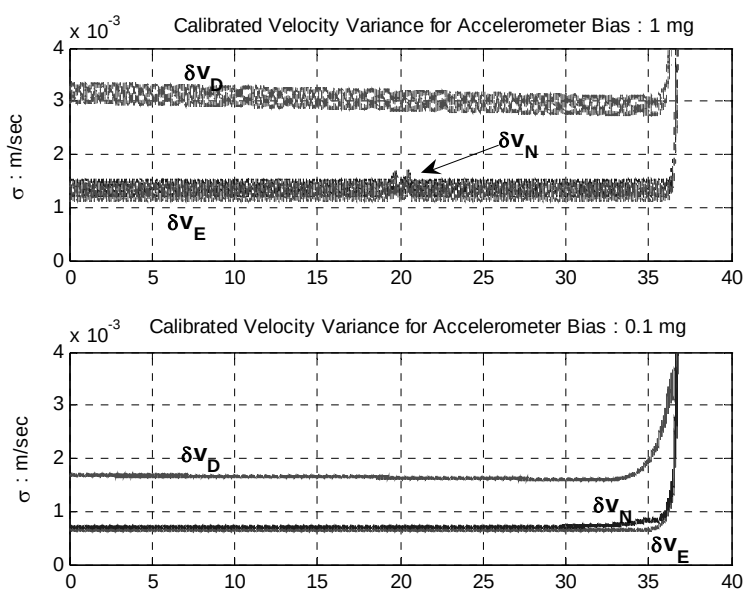

Figure 4.22 Sensitivity Analyses for Accelerometer Bias (2)

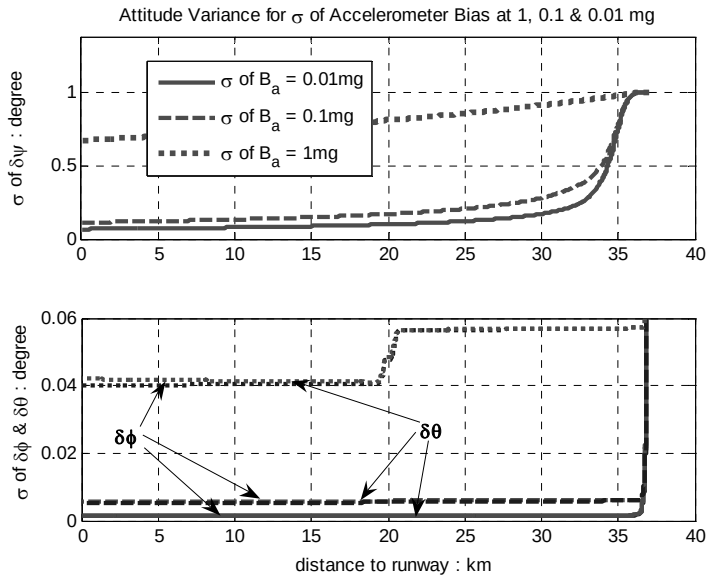

Figure 4.23. Sensitivity Analysis for Accelerometer Bias (3)

descending as shown in Figure 4.23.

The resulted larger uncertainties in the attitude estimations not only impact the calibration of the gyro bias as shown in Figure 4.24, but also circle back to affect the improvement on accelerometer bias itself which is displayed in Figure 4.25.

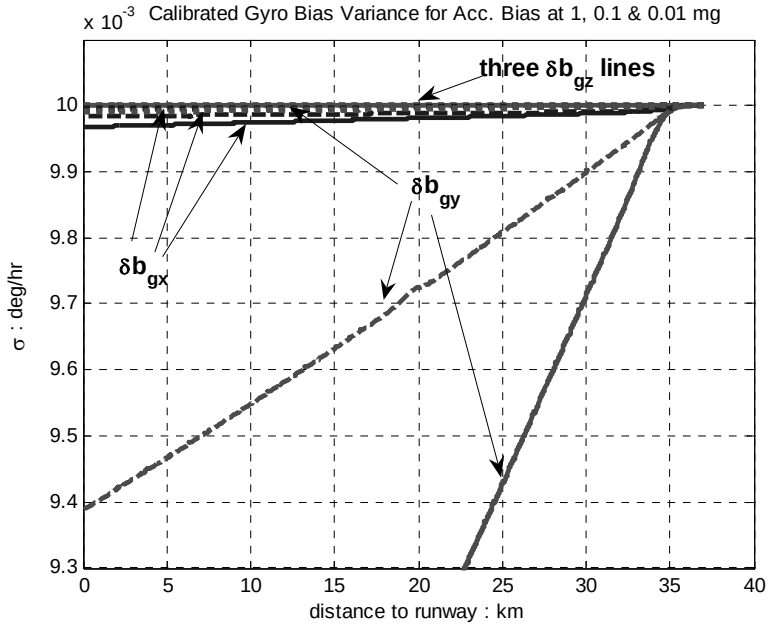

Figure 4.24. Sensitivity Analysis for Accelerometer Bias (4)

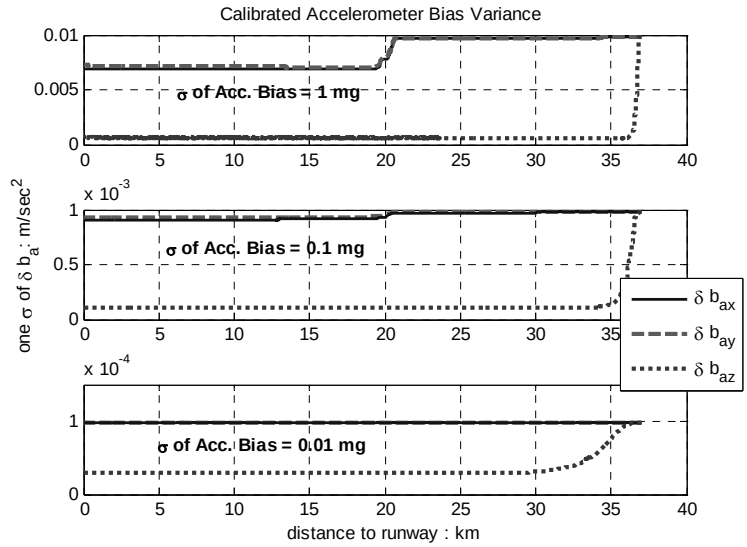

Figure 4.25. Sensitivity Analysis for Accelerometer Bias (5)

4.2.4 Straight and Turned Approach. Through the study of the system dynamic model in Section 3.3.1, vehicle motion related elements in the transition matrix can be found. Therefore, it can be anticipated that the calibration and coasting performance of a tightly coupled GPS/INS system will be dependent on the vehicle motion and that it will be sensitive to different types of approaching paths.

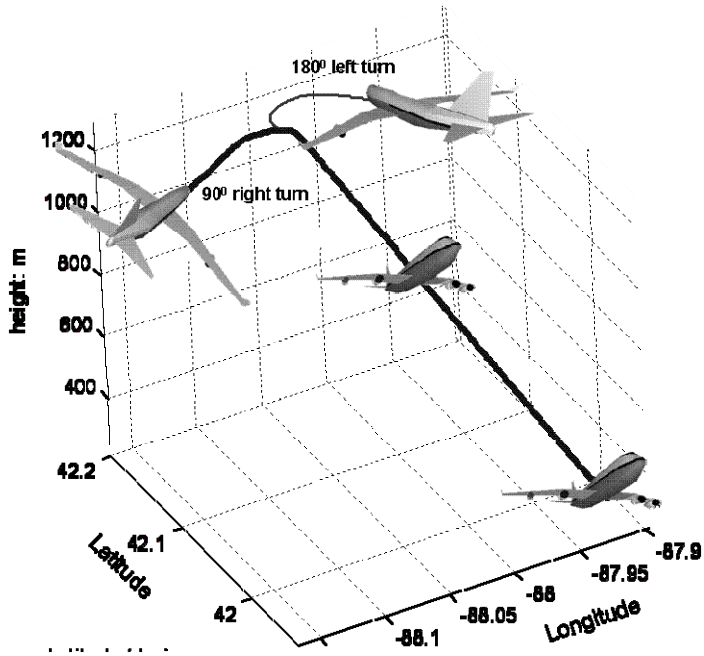

Figure 4.26. One-Turn Flight Path for Sensitivity Analysis

To further comprehend this influence, 90-degree and 180-degree turned approaches were simulated, both turns ending at the IF point. Figure 4.26 is a 3-D graphical presentation of these two turn approaches. Four approaches were actually simulated and the results were compared with each other. These four approaches were 90^0 left and right turns and 180^0 left and right turns. Because the results of left and right turns with the same turning angle were very similar, only one is presented here.

The coasting performance of turn-approaches is shown in Figure 4.27 along with the nominal straight-in approach results for comparison. The vertical channel shows no difference, while the lateral errors for the turn-approaches are smaller than the nominal approach due to better calibration on the attitude angles. The calibrated velocity and attitude are presented in Figure 4.28 and 4.29.

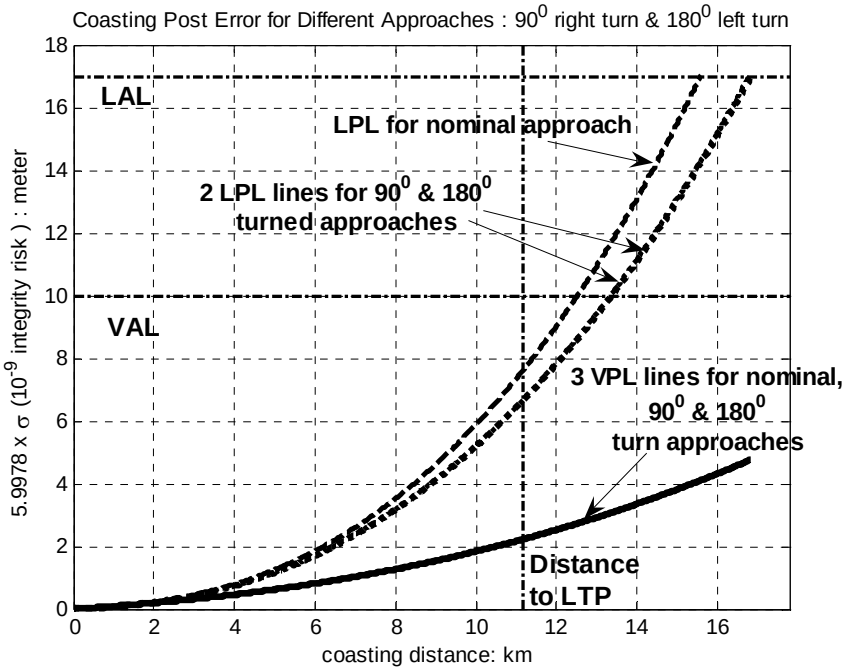

Figure 4.27. Sensitivity Analysis for Flight Path (1)

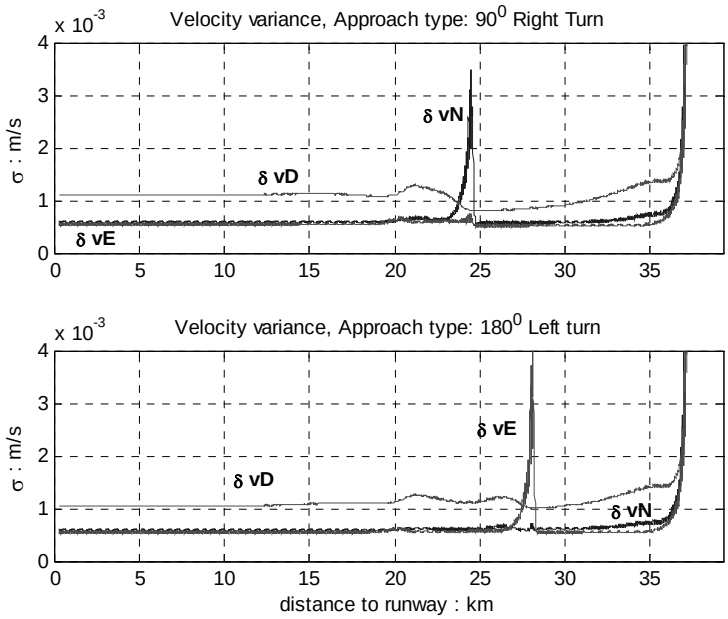

Figure 4.28. Sensitivity Analysis for Flight Path (2)

The peaks on the velocity error shown in Figure 4.28 were caused by the vehicle turns which created horizontal accelerations and enabled the azimuth estimation errors to propagate to the velocity states. The quickly accumulated velocity errors were calibrated

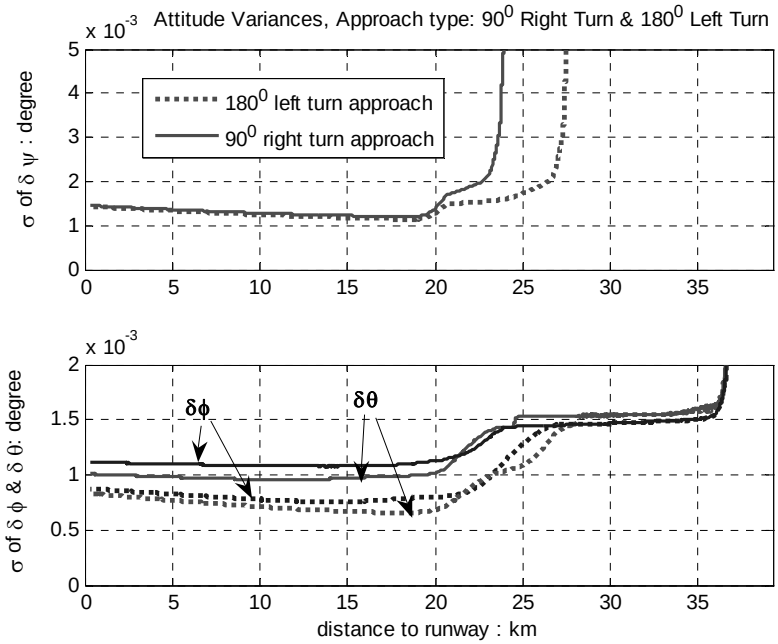

Figure 4.29. Sensitivity Analysis for Flight Path (3)

out rapidly by GPS carrier phase measurements. As a result, a better observation on the azimuth state through the appearance of horizontal accelerations was established. The azimuth angle error was improved significantly through the better observability during the vehicle turns, and the tilt-angle errors were, in turn, improved from the nominal case at the coasting starting location.

The large jumps on the velocity errors at the beginning of the turns expose a potential issue. The worst scenario is that the aircraft maneuvers to adjust the flight course in response to external disturbances (such as strong wind) after coasting started, and then velocity error peaks would appear. However, GPS measurements no longer are available to calibrate out the peaks. The increased coasting errors propagated from the yaw angle error in the worst scenario pose no integrity threat since these additional coasting errors will be accounted for in the covariance propagation. Nevertheless, it is a continuity risk because an on going approach may be interrupted unexpectedly. Theoretically, the azimuth errors would not contribute to the coasting position errors if there was no horizontal acceleration, which is the case for the nominal approach simulation. Nevertheless, this zero horizontal acceleration assumption is very unlikely in reality, especially when there are human control and weather factors involved. Therefore, heading information augmentation is explored and analyzed in the following section to address this concern. In addition, a sensitivity analysis for non-zero horizontal accelerations is carried out to understand the impact on the nominal approach scenario, and then the effect is accounted for the IMU and gravity model quality to meet the LAAS CAT I/III requirements.

4.2.5 Heading Information Augmentation. To address the concern of low observability on the azimuth angle, which is a continuity risk, without increasing too much cost in adding extra sensors, a second GPS antenna is considered to be added to form a short baseline aligned with the *x* axis in the body frame. The short distance between two GPS antennas, roughly between 5 to 15 meters, makes the carrier phase integer resolution achievable before the aircraft enters DGPS service volume. While a floating implementation might be workable, effective techniques which resolve the integers for such a short baseline can be found in literature [Hayward99][Yang01]. This analysis is focused on the possible benefit of the heading information augmentation. Therefore, the integrity of the augmented heading information is not addressed in this research.

Simulations were done with the assumption of correctly resolved carrier phase integers between two GPS antennas. Centimeter level relative positioning is realized in real time to provide the orientation of the vehicle's body *x* axis in ECEF coordinates at 1

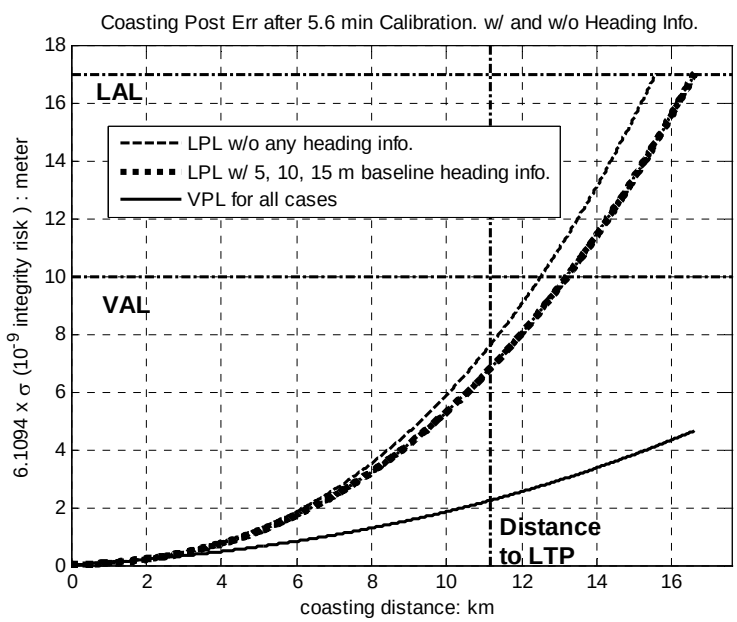

Figure 4.30. Sensitivity Analysis for Heading Information Augmentation (1)

HZ update rate. By applying the nominal scenario, the coasting performance was simulated with 5, 10 and 15 meter baseline lengths and presented in Figure 4.30. The coasting performance among different baseline lengths shows no noticeable difference.

The achievable coasting ranges are different from the nominal case which has no heading information augmentation in Figure 4.30. The improvements in the azimuth angle estimation result in better tilt angle estimations, and then are reflected in smaller lateral position errors observed, while the vertical errors remain identical for all cases. The attitude estimations with heading information augmentations of different baseline lengths are shown in Figure 4.31.

A major improvement is obvious in the azimuth angle estimation, the one sigma error drops considerably from around 0.08 degree without augmentation to below 0.005 degree with 5 meter baseline augmentation at the time when the vehicle reaches FAF point. As the baseline length is increased, the one sigma azimuth angle error reduces

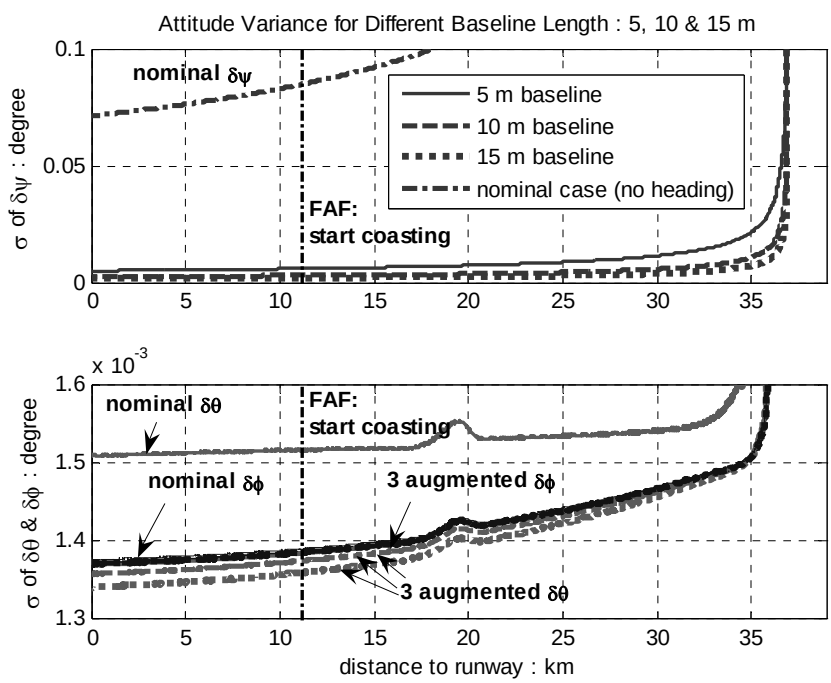

Figure 4.31. Sensitivity Analysis for Heading Information Augmentation (2)

further. The other two attitude estimation errors (pitch and roll angles) are also improved from the nominal case. The magnitudes of the improved tilts angles errors at FAF point are similar no matter which baseline lengths are. Hence, the lateral coasting errors in Figure 4.30 stay closely.

The effect of augmented heading information is explored for one-turn approaches as well. The results in the top plot of Figure 4.32 illustrate the coasting ranges by zooming in the LPL values near the LAL line. Approximately additional one kilometer of coasting range is achieved for the nominal scenario with the augmented heading information. This improvement on the coasting performance is not sensitive to the simulated approach paths nor to the baseline lengths ranged from 5 to 15 meters. The bottom plot in Figure 4.32 shows the calibrated azimuth angles for different baselines and turns.

From the results shown in Figure 4.29 and 4.31, comparing azimuth angle errors

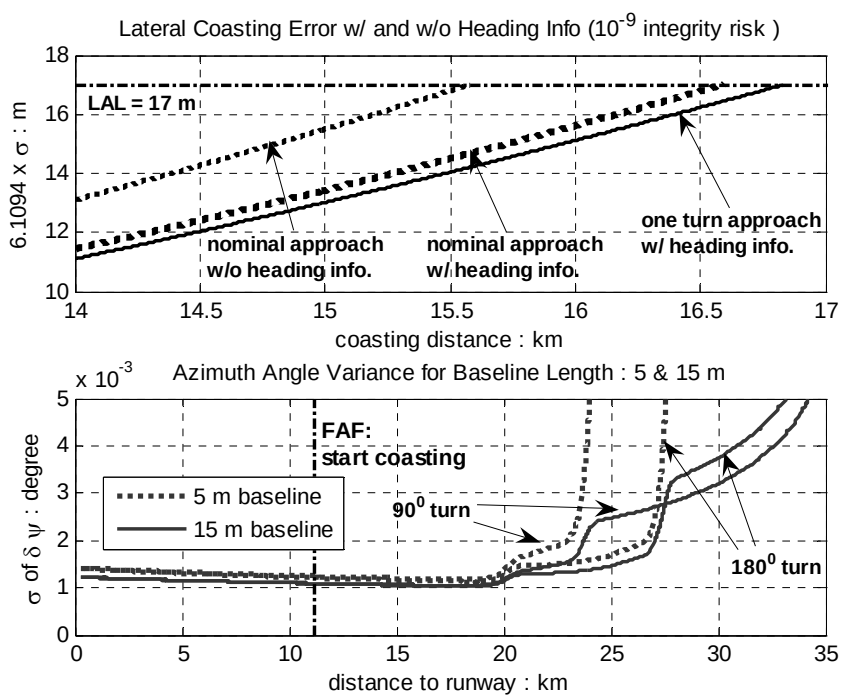

Figure 4.32. Sensitivity Analysis for Heading Information Augmentation (3)

suggests that GPS heading information augmentation with a 15 meter baseline would have the similar benefit on the azimuth angle estimation to the one-turn approach has, except for a slower convergence rate. As explained earlier, azimuth error has no effect on the system coasting performance during the nominal approach because of the lack of horizontal accelerations. However, a better azimuth estimation can result better tilt angle estimations. Consequently, better lateral coasting performance can be achieved.

One advantage of the heading information augmentation over a one-turn approach is a smoother calibration process. Unlike the sharp error peaks appearing in Figure 4.28, the heading information augmentation can reduce the azimuth angle errors from the very beginning of an approach. Hence, the error peaks on the velocity errors are much smaller and smoother when the vehicle starts to turn. From this analysis, it can be concluded that an GPS heading augmentation can benefit the hybrid system performance for the nominal straight-in approach as if a turned approach is conducted.

4.2.6 Gravity Model Accuracy. The nominal parameter values for gravity model were chosen (Table 4.2) to be achievable for local area navigation. However, variations on these values would have impacts on the coasting performance of the hybrid system.

The sensitivity in this regard is evaluated through covariance analysis by varying the standard deviations of DOV, vertical gravity error and the correlation time constant individually. DOV has two independent parameters; one is the north-south direction angle ξ; the other is the east-west direction angle η. The same sigma value is selected to apply on both directions' DOV errors, σ_ξ and σ_η, to keep the analysis simple and general. The simulated coasting performance for the sigma values of DOV error at 2.5, 5 and 10 arcseconds is shown in Figure 4.33. The lateral coasting errors deteriorate with

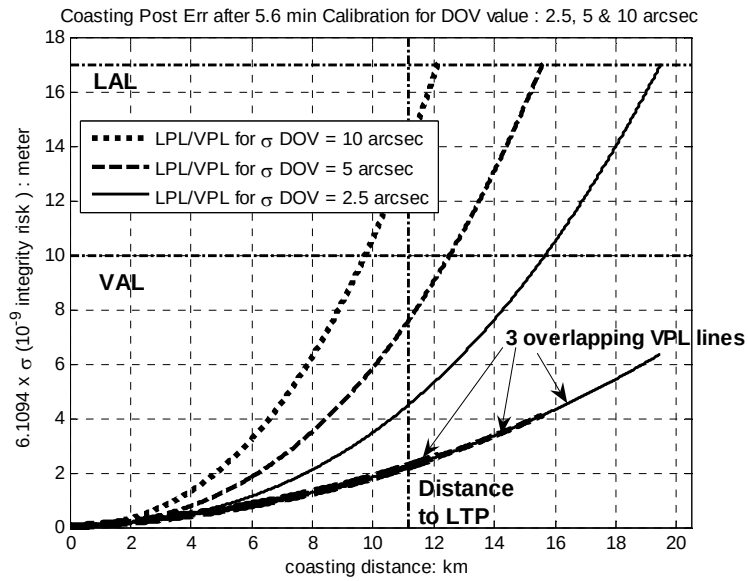

Figure 4.33. Sensitivity Analysis for Gravity Anomalies (1)

increasing DOV sigma as expected. While the magnitude of the deterioration on the lateral error is roughly proportional to the change of the DOV value, the vertical error shows no noticeable change. This can be explained by looking into the attitude estimation errors in Figure 4.34.

Intuitively, the accuracy of DOV would affect the estimation in the local gravity

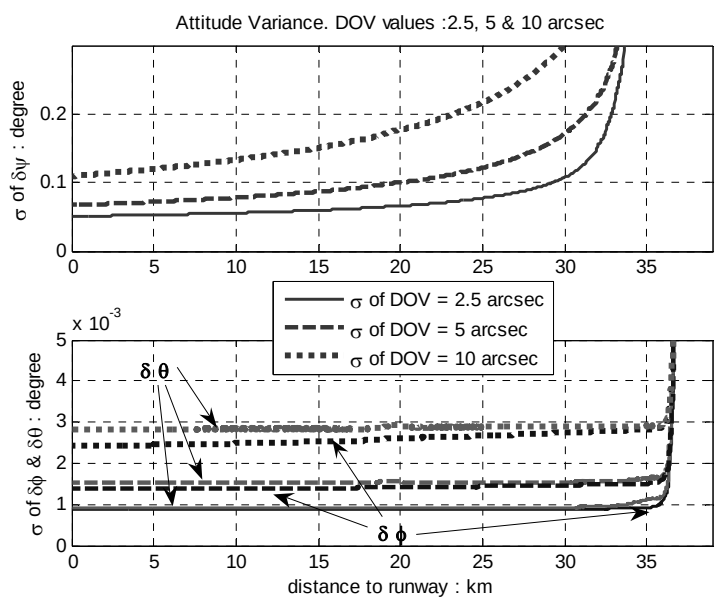

Figure 4.34. Sensitivity Analysis for Gravity Anomalies (2)

direction. This expectation is supported by the quality of the tilt angle estimations shown at the bottom plot in Figure 4.34. The azimuth angle errors are, therefore, affected as well due to the correlation with the tilt angles. Different degradation levels in the tilt angle error result in different lateral coasting error accumulations displayed in Figure 4.33. The vertical errors have no noticeable change to the variations of DOV parameters due to lack of horizontal accelerations. The results are reflected in the three overlapping VPL lines in Figure 4.33.

The vertical gravity error, $\delta\Delta g(0)$, has a direct impact on the vertical channel. Figure 4.35 shows the effects of one sigma vertical gravity errors, $\sigma_{\Delta g(0)}$, at 2.5, 10 and 20 μg. Note that coasting performance declines only when the dominant error switches from the lateral error to the vertical error in the 20 μg case. However, the fault-free CAT III system integrity can still be met.

Figure 4.36 shows that the estimated vertical gravity error could be reduced at both 10 and 20 μg cases. This improvement in the estimation of the vertical gravity

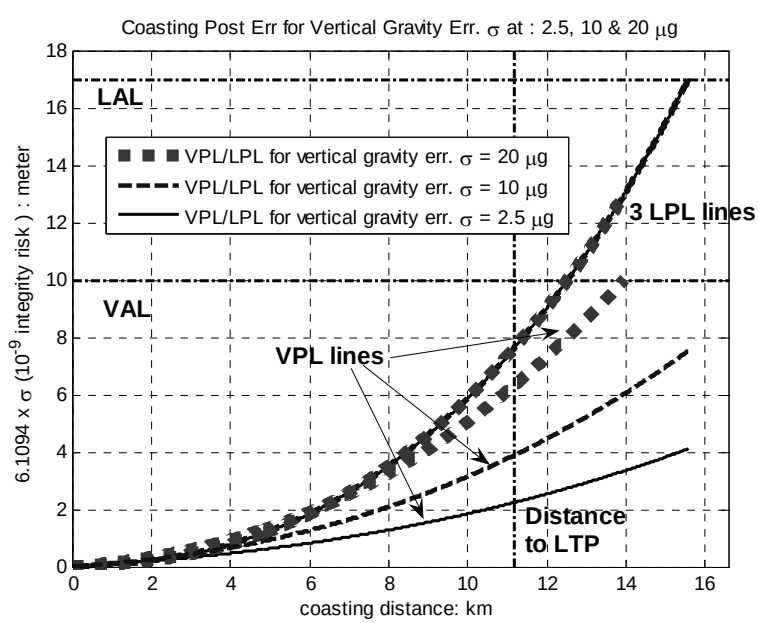

Figure 4.35. Sensitivity Analysis for Gravity Anomalies (3)

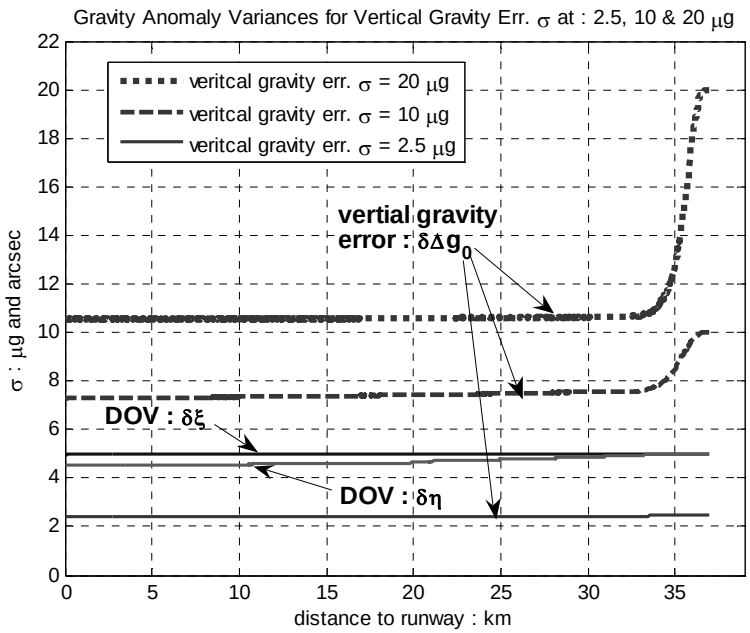

Figure 4.36. Sensitivity Analysis for Gravity Anomalies (4)

anomaly state makes the system coasting performance degrade less than expected. Even with a vertical gravity error sigma eight times larger than the nominal value of 2.5 μg, the CAT III fault-free requirement can still be met. This property might be very helpful when the requirements on the gravity data need to be relaxed in some areas which might have very rugged terrain.

The correlation distance is used in the gravity model as another index for the randomness of gravity anomalies. The smaller the distance is, the more random the gravity anomalies are. Consequently, more process noise will be pumped into the gravity states. The effect of the gravity anomaly randomness on coasting performance is shown in Figure 4.37

From the plot, the lateral coasting errors deviate from the nominal case significantly while the vertical coasting errors remain relatively unchanged. The un-proportional degradations in the lateral and vertical errors are due to the variations on the

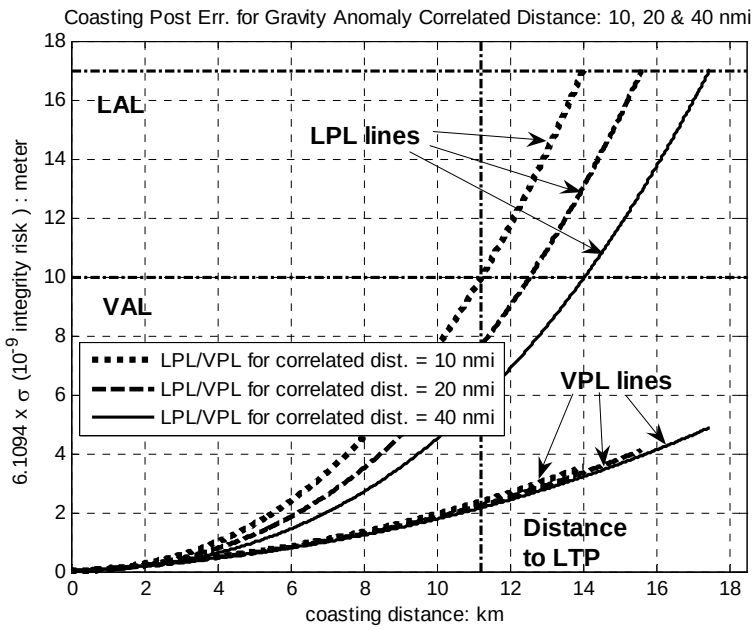

Figure 4.37. Sensitivity Analysis for Gravity Anomalies (5)

attitude calibration performance. This variation can be inspected at the beginning values in the top plot of Figure 4.38, which are the attitude calibration errors at coasting started location (FAF point). The differences on the beginning coasting azimuth angle errors mainly contribute to the lateral coasting position errors. The effect of higher process

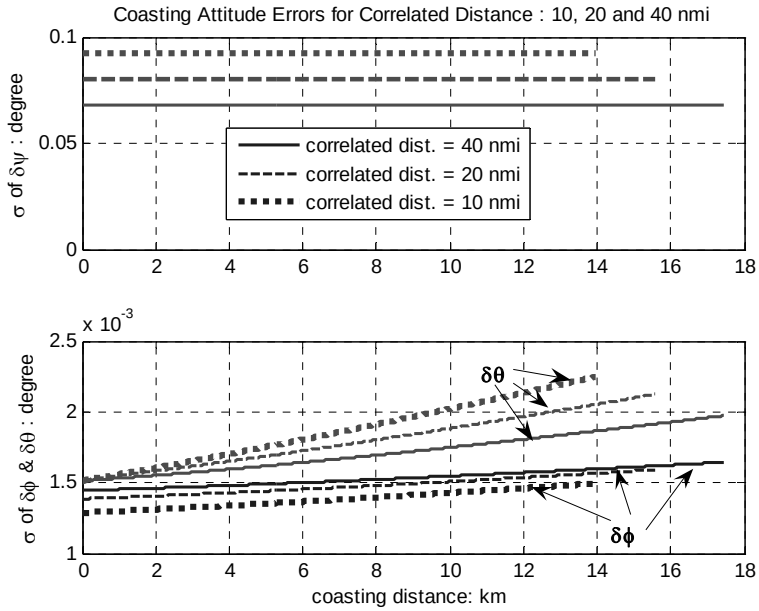

Figure 4.38. Sensitivity Analysis for Gravity Anomalies (6)

noise of the shorter time constant is observable on the tilt angle error accumulations during the coasting stage, which are shown at the bottom plot in Figure 4.38. This tilt angle error accumulation results in the slightly different vertical error propagations as seen in Figure 4.37.

4.2.7 Effect of Non-zero Acceleration During Final Approach. The impact of non-zero acceleration during the final stage of the nominal approach is investigated. From the system error dynamic equation 4.1, the azimuth angle error would not propagate to the velocity unless horizontal accelerations exist, which is not the case for the simulated nominal straight-in approach. The fact that the velocity errors disconnected from the attitude yaw angle error implies that the coasting performance is not sensitive to the yaw angle error. Nevertheless, it also results in the lack of observability on the yaw angle state and makes the uncertainty on the system's yaw angle relatively high, which is a potential threat to the system continuity.

However, having zero horizontal accelerations during the whole coasting period is impossible. Any pilot's adjustment to keep the aircraft close to the nominal flight path or external disturbance caused by an unstable airflow could create accelerations in any direction. Although the horizontal acceleration appears to be non-zero in real approaches all the time, the zero value can be treated as the 'mean' of the horizontal acceleration. Using zero as the nominal value for the standard straight-in approach can make the nominal simulation results more general. The sensitivity to this factor is investigated in this section.

In order to simulate the sensitivity results for a realistic aircraft approach, the acceleration values during the coasting stage are derived from actual flight data which

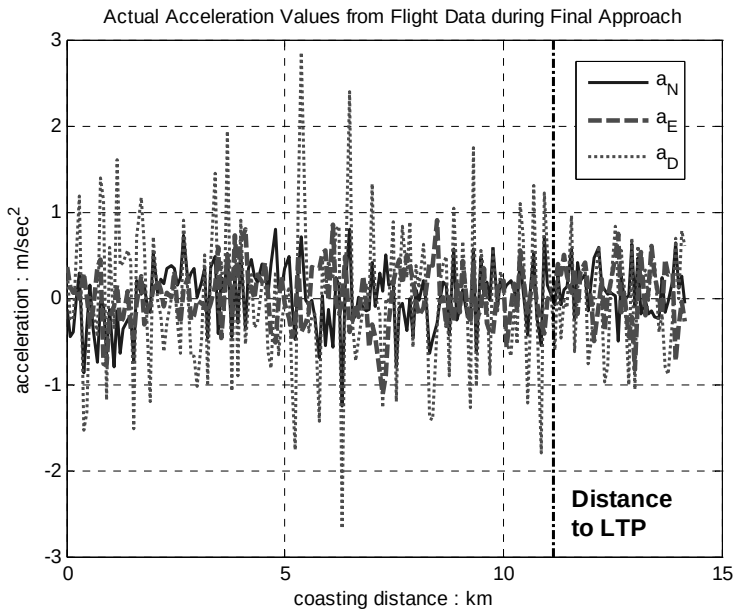

Figure 4.39. Example of Actual Accelerations during a Final Approach

were collected on April 3rd 2002 flight tests directed by the FAA's William J. Hughes Technical Center. Figure 4.39 shows an example of the actual acceleration values derived by taking the velocity differences for each one second interval from Time Space Position Information (TSPI) true system velocity data. TSPI data has position accuracy approximately 10 cm [Warburton98].

The derived acceleration values from four approach TSPI data were applied to simulate the measured specific force values in the navigation frame, and substituted into the system dynamic transition matrix (coefficients f_x^n, f_y^n and f_z^n in equation 4.1) during the final coasting stage to observe the effect in the system coasting performance. Figure 4.40 shows the coasting errors for the four approaches with non-zero horizontal accelerations and the coasting results for the nominal case for comparison. The vertical errors basically have unnoticeable differences between the non-zero acceleration and the nominal case, while the lateral errors have obvious deviations between these two

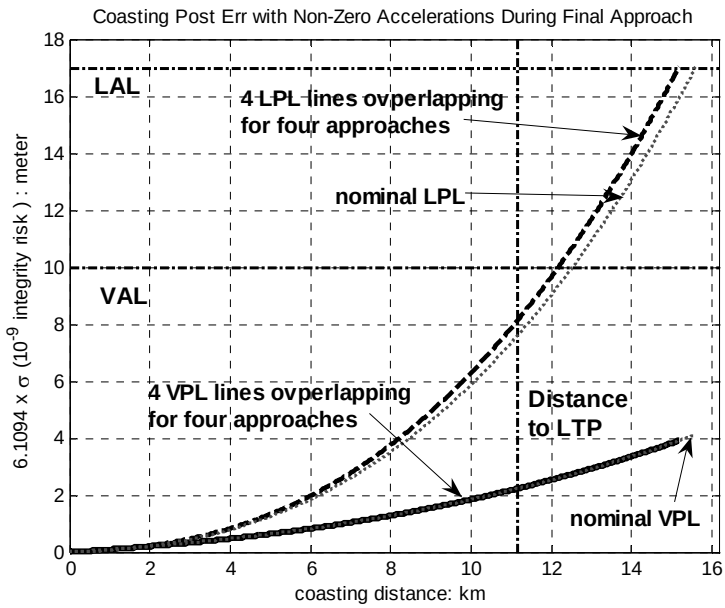

Figure 4.40. Sensitivity Analysis for Non-zero Acceleration

scenarios. The deviations can be understood clearly through the velocity errors in Figure 4.41. The horizontal velocity errors are pumped up higher than the nominal case due to the existence of the non-zero accelerations on horizontal directions. Although the non-zero accelerations enable all attitude angle errors to be propagated into velocity states, very small magnitudes on both tilt angle errors don't contribute significantly to the

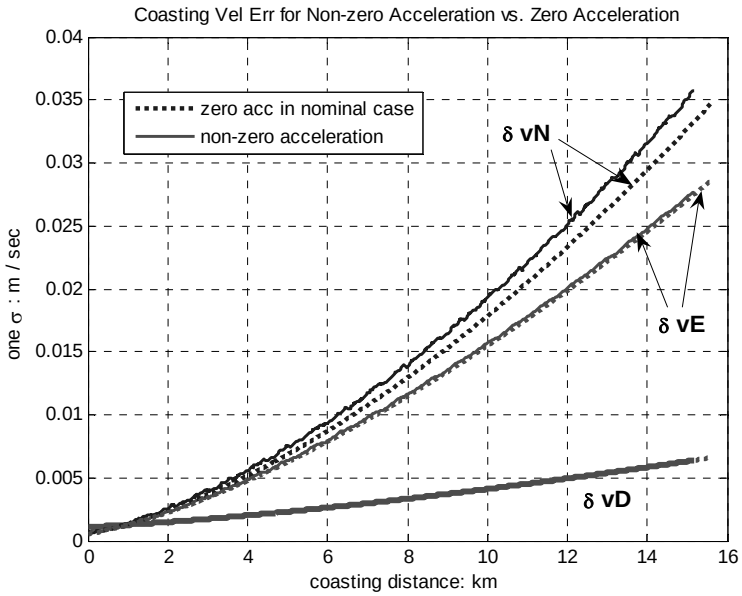

Figure 4.41. Coasting Velocity Error for Non-Zero Acceleration

vertical velocity errors. In contrast, the much larger yaw angle errors are propagated into lateral velocity through the non-zero horizontal accelerations, and consequently degrade the lateral coasting positions. The reduction on the coasting distance is about a half kilometer.

Since the root cause of the system sensitivity to non-zero accelerations is lack of observation on the yaw angle during the nominal in-flight calibration, any augmentation or configuration which can reduce the yaw angle estimation error should be able to make the system more robust to this factor. Heading information augmentation and the one-turn approach are two of them. The simulated results are presented in Figure 4.42. Two nearly-overlapping LPL lines show the cases of the heading information augmentation and the one-turn approach. Both have better coasting performance than the nominal zero-acceleration case, and show no noticeable difference from the previous simulated coasting results in Sections 4.2.5 and 4.2.4 for the nominal zero-acceleration scenario.

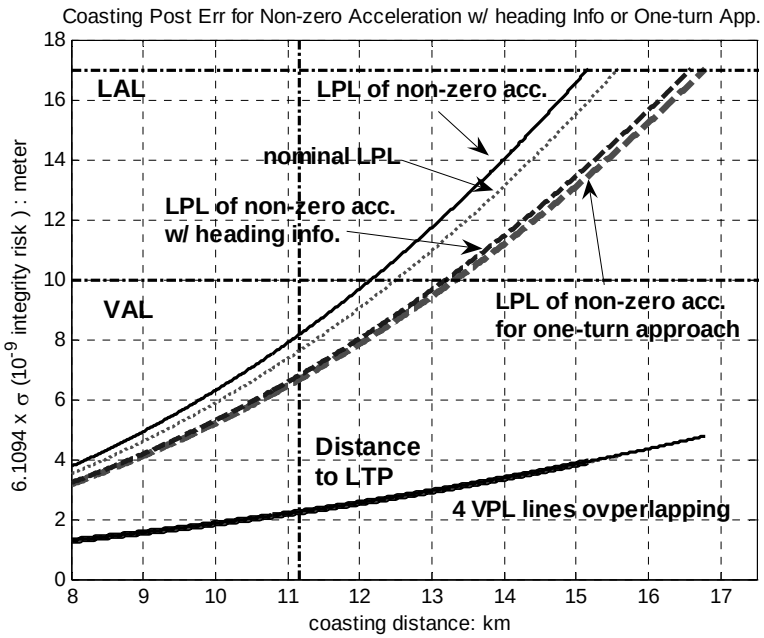

Figure 4.42. Comparison of Coasting Position Error for Non-Zero Acceleration with Heading Information Augmentation and One-turn Approach

This analysis confirms that as long as the attitude errors are small, the system coasting performance will be robust to non-zero accelerations which are often caused by external disturbances.

Applying non-zero accelerations only on the final coasting stage is a conservative way to analyze the coasting performance, because non-zero accelerations can actually be helpful to observe the attitude angle errors during the calibration period if they exist. However, the system sensitivity to non-zero accelerations has to be accounted for when the quality of IMU and gravity models to meet LAAS CAT I/III requirements are quantified in Section 4.32. This conservative approach is adopted during the IMU and gravity model qualification analysis. Hence, the derived non-zero accelerations from flight data during one whole approach are used to demonstrate this effect.

Figure 4.43 presents the actual acceleration values during one whole approach and the resulting calibrated velocity errors. The first group of acceleration peaks, happening around 25 km, was caused by the aircraft making a horizontal turn. The second group of

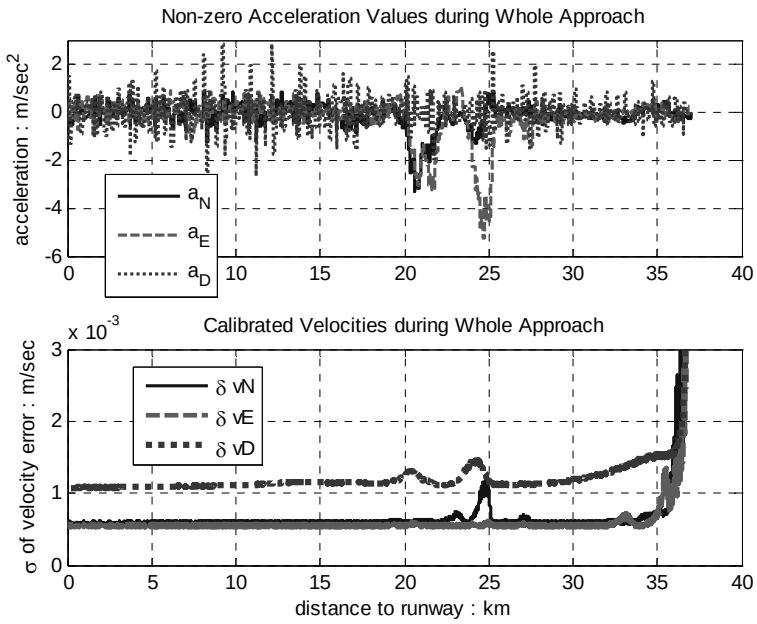

Figure 4.43. Non-Zero Acceleration and Calibrated Velocity Error during One Whole Approach

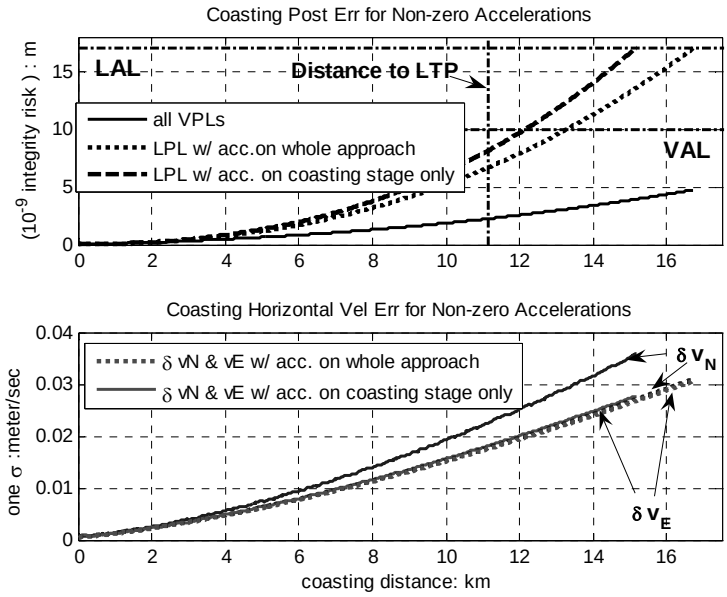

Figure 4.44. Non-zero Accelerations on Coasting Stage Only vs. Whole Approach

acceleration peaks at around 20 km indicates that the aircraft was passing the IF point and starting to descend. The coasting performances are displayed in Figure 4.44 with the position errors in the top plot and the velocity errors in the bottom. These results verify that applying non-zero accelerations on the coasting stage only is conservative.

Up to now, the hybrid system sensitivity to each individual error model parameter was analyzed. The coasting performance with combinations of the system parameter variations will be analyzed in the following section, and the quantified requirements on IMU and gravity models to meet fault-free LAAS CAT I/III requirements will be defined.

4.3 Coasting Performance Simulation with Multiple Parameter Variation.

A number of the system parameters would not by themselves affect the coasting performance, such as the lever arm effect and yaw angle errors, unless other than the nominal (straight-in) flight path applied. Following the parameter setups in the sensitivity analyses performed previously, the combined influence on the system coasting performance due to varying a few system parameters together is studied here. The simulation results of the multiple parameter variation are discussed in the section 4.3.1. After studying the impact from multiple coasting error contributors, attempts to quantify the quality requirements on the IMU and gravity models for LAAS CAT I and III applications are made. The derived IMU and gravity model requirements will be utilized in the availability analysis in the next chapter.

4.3.1 Lever Arm Effect for One Turn Approach With and Without Heading Information Augmentation. Recall from Section 4.2, that there was little coasting performance sensitivities to the lever arm effect and yaw angle error for the nominal approach. To ensure the robustness of the hybrid system to these two factors during other flight paths, they are re-examined by applying the one-turn approach and the heading information augmentation to understand the combined influence.

The parameter variations in this analysis include flight path: 90^0 right turn and 180^0 left turn, lever arm vector: [1 1 1] and [-20 10 5] (following the setups in Section 4.2.1), and the existence or nonexistence of heading information augmentation. After a series of simulations with different combinations of the parameters, the presented results are the coasting performance with the parameter combinations of the 180^0 left turn approach, [-20 10 5] lever-arm vector and heading information augmentation. The rest of

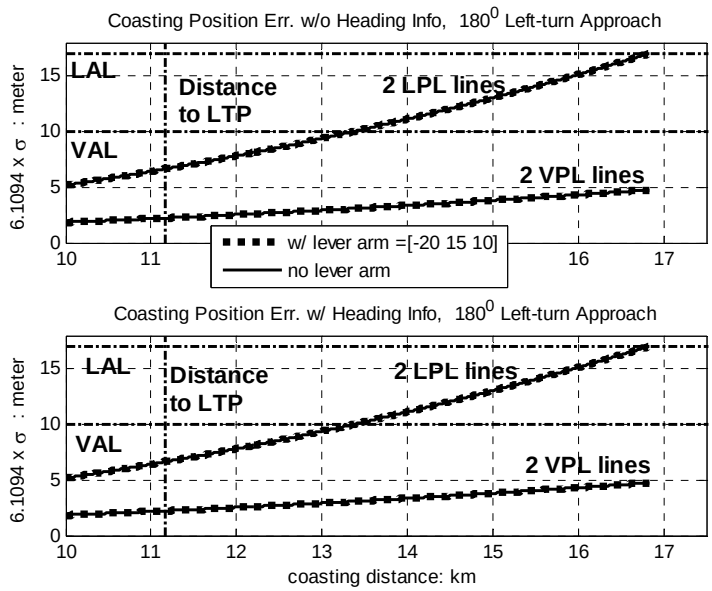

Figure 4.45. Sensitivity Analysis for Multiple Parameter Variation (1)

the results with other combinations are not distinguishable from the ones presented. Lever arm residual errors were also studied by applying different standard deviation values at 0.001, 0.01 and 0.1 meters, but showed no perceptible differentiation on the system coasting performance. Therefore, the nominal one-sigma value of 0.01 meters was applied in this study.

Figure 4.45 shows the coasting performances with and without the lever arm by arranging the results without heading information augmentation in the top plot, and those with heading augmentation in the bottom for the same 180^0 left-turn approach. All the VPL and LPL lines overlap. Thus, it is fair to say that the heading information augmentation and the lever arm have negligible effect on both vertical and lateral coasting errors for the one-turn approach. Equation 4.5 is re-presented here to facilitate the explanation of the simulated results:

$$\delta\Delta\vec{X}^{\,n}_{GPS}(\Delta t) = \delta\Delta\vec{X}^{\,n}_{IMU}(\Delta t) - [\Psi_{t1}C^n_b(t_1) - \Psi_{t0}C^n_b(t_0)]\vec{L}^b - [C^n_b(t_1) - C^n_b(t_0)]\delta\vec{L}^b$$

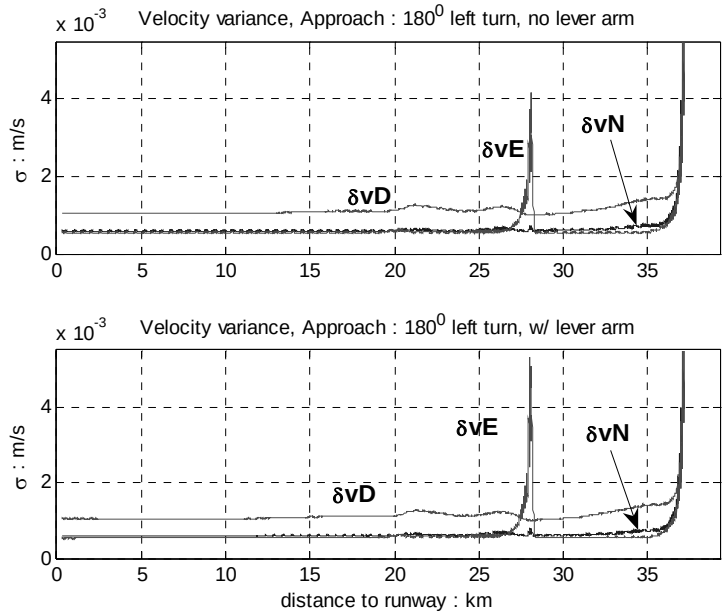

Figure 4.46. Sensitivity Analysis for Multiple Parameter Variation (2)

The errors introduced by the second term of the lever arm effect (the second square brackets) are neglected for now and will be discussed later. The first term of the lever arm effect, induced by the attitude angle errors Ψ, is scaled by the lever arm vector and then contributes to the position error. The amount of velocity error caused by the lever arm effect is small compared with the errors propagated from the attitude errors through horizontal accelerations. As shown in Figure 4.46, no obvious difference exists on the velocity error between the top and bottom plots except in the magnitudes of the peaks. The difference in the peak magnitudes is the result of superposing the lever arm induced errors onto the errors propagated through the horizontal accelerations. When GPS measurements are available, the composite errors can be calibrated out quickly like other errors. Therefore, no coasting performance difference is observed in the top plot of Figure 4.45. The lever arm effect should be minimized by reducing the lever arm length

and a careful installation to avoid the undesired effect during free-INS coasting; especially for the applications that might involve an aircraft maneuver.

Figure 4.45 shows that there is no gain on the coasting performance by having the heading information augmentation for turn approaches. The fundamental advantage of having the heading information augmentation is to make the coasting performance robust to un-expected external disturbances for any approach. With the heading information augmentation, not only it can eliminate the concern about the system continuity risk in Section 4.2.7 and improve the lateral coasting errors for the nominal approach, but it also smoothes the peaks of the velocity state errors for turn approaches as shown in the top plot of Figure 4.47.

The lever arm induced error from the second term in the equation is studied in Figure 4.47. The only difference between the top and the bottom plots is the residual lever arm error; the top plot has 1 cm sigma while the bottom one has 10 cm sigma,

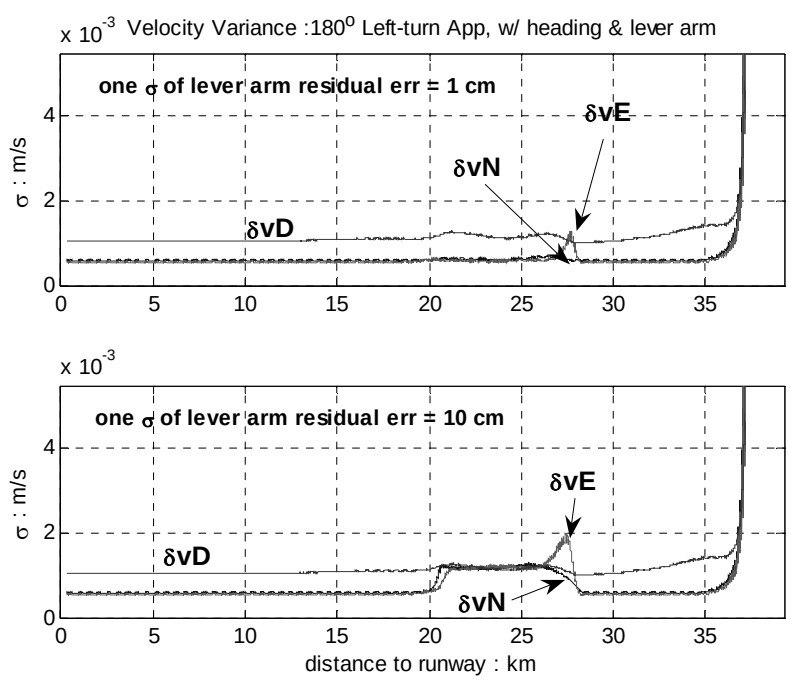

Figure 4.47. Sensitivity Analysis for Multiple Parameter Changes (3)

which is a little exaggerated for comparison. The smoothing effect on the velocity error peak is obvious in the figure. The higher lever arm residual error results in the larger velocity errors during the turning period in the bottom graph, which were then calibrated out quickly once the vehicle exited the turning period. Hence, the variation on the lever arm residual has little influence on the coasting performance even for a turning flight path.

The calibrated attitude errors, which are displayed in Figure 4.48, serve as a more direct view of the influence on the coasting position errors for non straight-in approaches with different system configurations (whether the lever arm and heading information augmentation are existed). From this figure, the attitude state errors in all cases stay very closely to each other except the azimuth error ($\delta\psi$) at the beginning. The same attitude errors at the FAF point for all cases result in that the coasting performance is nearly identical in Figure 4.45. The deviations at the beginning (before 27 km roughly) on the

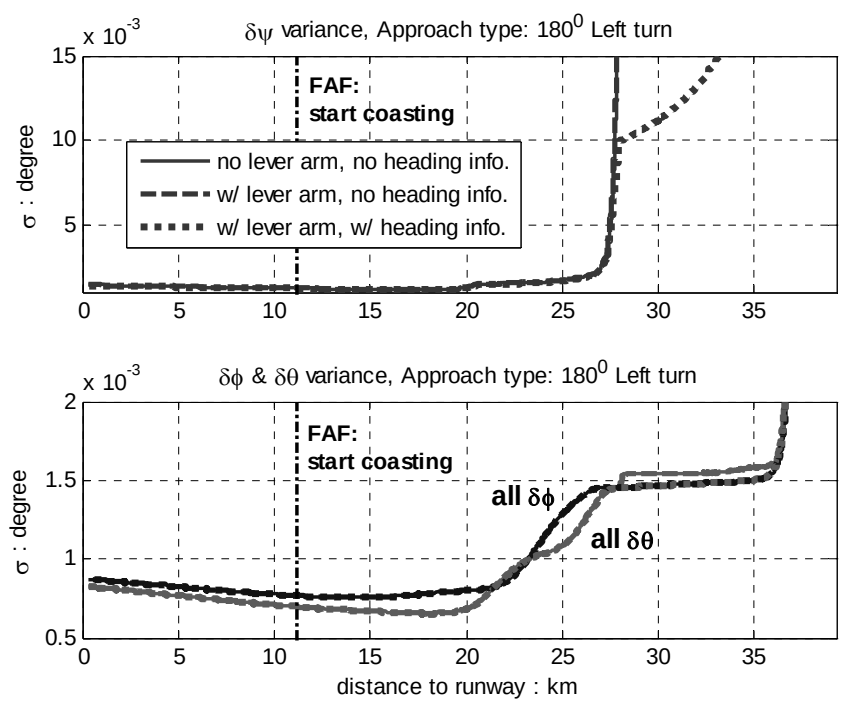

Figure 4.48 Sensitivity Analyses for Multiple Parameter Changes (4)

yaw angle errors demonstrate once again that the heading information augmentation works early and results in the smaller velocity error peaks.

Another way to consider the benefit of the heading information augmentation is from a system continuity perspective. As discussed in Section 4.2.4, unexpected vehicle maneuvers might happen during the coasting stage; this scenario would not be a problem to the system integrity because the VPL and LPL will respond to the maneuver and discontinue the approach if either VAL or LAL was violated. On the other hand, such events will be a threat to the system continuity if unexpected maneuvers happen frequently. Heading information augmentation can effectively reduce this risk by significantly improving the estimated azimuth angle error.

4.3.2 IMU and Gravity Model Quality for LAAS CAT I and CAT III Applications.

Inertial sensor quality varies enormously and generally proportionally to the costs. To be cost effective, it is important to have appropriate requirements on the IMU and gravity model quality. An over-qualified IMU is safe from the system performance's point of view; however, it also burdens the system with the heavy cost. Relieving the economic pressure from the system by employing a marginally qualified IMU might undermine the system's availability, continuity and even integrity. The trade-off between the quality and the cost should be made based on the system performance analysis, which is the subject of this section.

Although the main objective is to quantify the quality of IMU and gravity models that are sufficient for LAAS CAT I/III applications, the approach taken here is a more general way to provide the foundation from which a real implementation of the GPS/INS hybrid navigation system can start. Therefore, the factors which might affect the system

Table 4.3. Minimum Requirements on IMU and Gravity Model Parameters for LAAS CAT III Fault-free Precision Approach

Minimum Requirements on IMU parameters			
standard deviation	gyroscope	accelerometer	correlation time ($\tau_{a/g}$)
bias stability (σ_{bg}/σ_{ba})	0.01 deg/hr	10 μg	1 Hour
measurement noise (σ_{vg}/σ_{va})	0.01 deg/hr$^{1/2}$	100 μg	N/A
Minimum Requirements on Gravity Model parameters			
	DOV in N-S ($\delta\xi$)	DOV in E-W ($\delta\eta$)	vertical gravity Error ($\delta\Delta g(0)$)
standard deviation	5 arcsecond	5 arcsecond	20 μg
correlation distance	20 nmi	20 nmi	20 nmi

coasting performance are considered as generally as possible to avoid quantified results with high dependency on any specific system property.

Given LAAS CAT I and III as the potential system applications, the hybrid navigation system coasting performance was simulated by covariance analysis. Based on the knowledge provided from previously performed sensitivity analyses, the IMU and gravity model parameters were varied from the nominal values, which have been shown to be over-qualified for the most stringent CAT III applications, to meet the LAAS fault-free requirements. Two sets of parameters were evaluated to meet the fault-free requirements with reasonable margins to accommodate various sensitivity effects, especially performance degradation due to the non-zero horizontal acceleration after coasting started.

The IMU and gravity model parameters to meet the fault-free CAT III requirements are listed in Table 4.3, and the coasting performance results, together with the results with each parameter downgraded individually, are shown in Figure 4.49. The minimum requirements on IMU and gravity models in Table 4.3 are justified by

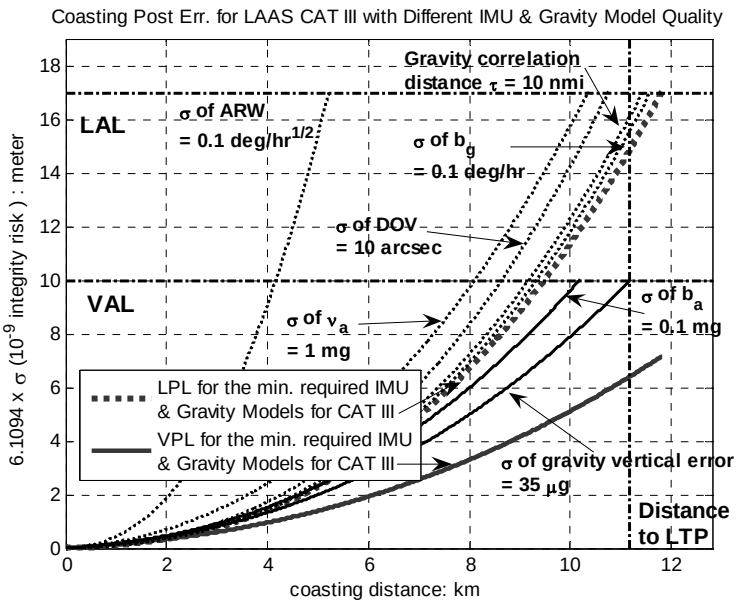

Figure 4.49. Minimum Requirements on IMU and Gravity Models for LAAS CAT III

comparing the coasting performance for individually degraded parameters with the performance generated from the parameters in Table 4.3. Because the requirements are quantified in terms of IMU quality grades rather than fine tuning system performance, the degradation on each parameter was picked intentionally to be about one order worse in the magnitude than the corresponding value in Table 4.3.

The dominant error which constraints the coasting performance in Figure 4.49 is still the lateral error, although the vertical error is also inferior compared with that for the nominal case in Section 4.2.2. The comparison curves for each degraded parameter are shown by either VPL or LPL. The selection depends on which one is the dominating error. Some parameter variations, such as accelerometer bias, might make the dominant system error switch from the lateral error to the vertical error.

Compared with the nominal parameters, this analysis shows that the gyroscope ARW can be relaxed from 0.001 to 0.01 deg/hr$^{1/2}$ and a relaxation on the sigma of the vertical gravity error from 2.5 to 20 μg is allowed. One-turn approaches (90 degree left turn and 180 degree right turn) were simulated with the minimum required IMU and gravity model quality as well. The results of these two one-turn approaches are undistinguishable from each other. Therefore, only the 180 degree left-turn approach results are presented in Figure 4.50. The coasting performance curves for the degraded parameters in Figure 4.50 are focused on those which can meet the LAAS CAT III requirements due to the performance improvement from turned approaches.

There are a few observations worth noting from the two figures above. In Figure 4.49, the coasting curves with 0.1 deg/hr sigma b_g and 10 nmi correlation distance do meet the Cat III requirements through simulations. However, the margins on both curves are too small to be safe from external disturbances (which will be shown in Figure 4.51).

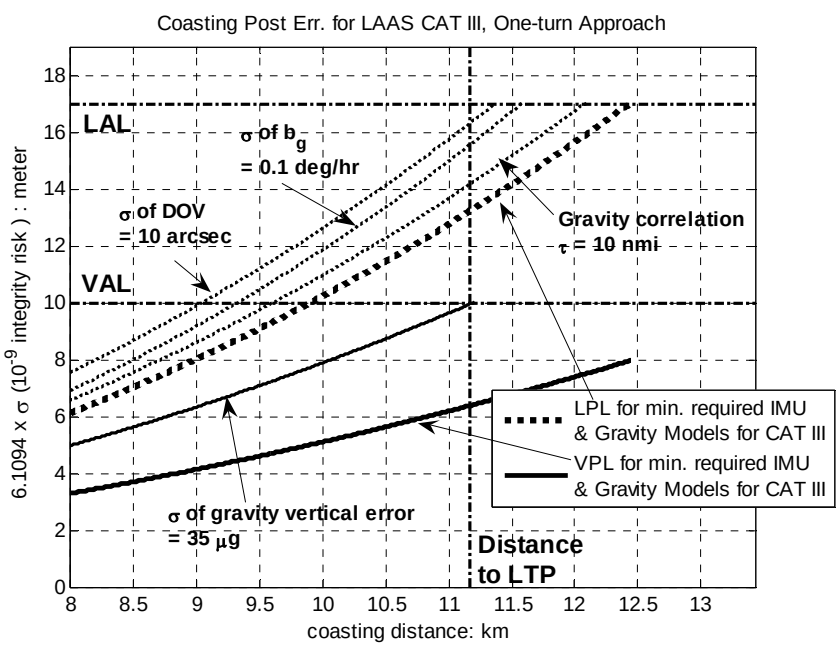

Figure 4.50. One-turn Approach Results with Minimum Required IMU and Gravity Models for LAAS CAT III

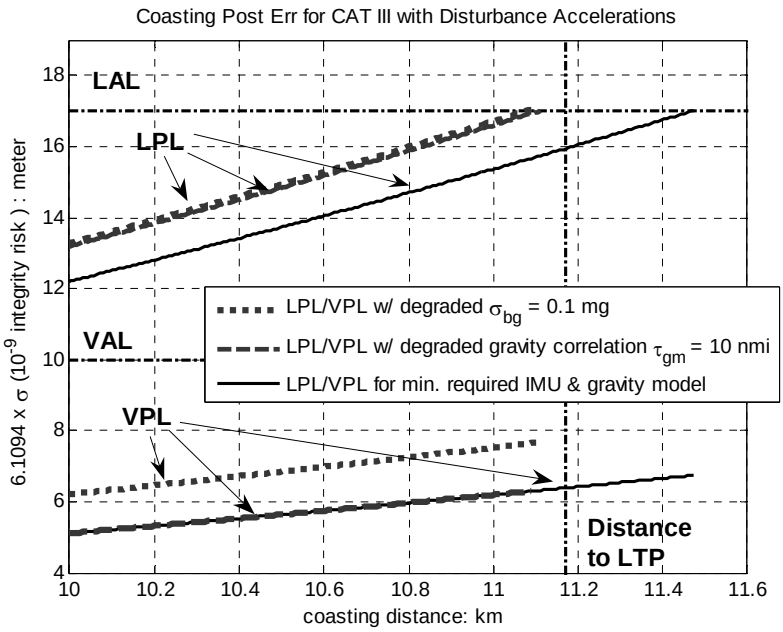

Figure 4.51. Disturbance Acceleration Effect on Coasting Performance with Minimum Required IMU and Gravity Models for LAAS CAT III

Therefore, these two values were not adopted in Table 4.3. Another thing worth noting is that the LPL curve with 10 arcsecond sigma DOV meets the requirements in Figure 4.50, while it does not in the nominal straight-in approach simulation in Figure 4.49. This observation is consistent with the results from the sensitivity analysis in Section 4.2.4; better coasting performance can be achieved with turn approaches.

The effect of disturbance-induced accelerations during the coasting stage has been analyzed in Section 4.2.7 and the results showed minor degradation on the system performance. However, multiple parameters in Table 4.3 are changed from the nominal values for the non-linear hybrid navigation system. The same analysis is, therefore, carried out to ensure that the quantified minimum requirements for the IMU and gravity models have the tolerance to this factor. Figure 4.51 shows the coasting performance of the minimum required IMU and gravity models, and another two sets of parameters which meet the system requirements in Figure 4.49. The coasting performance of the two

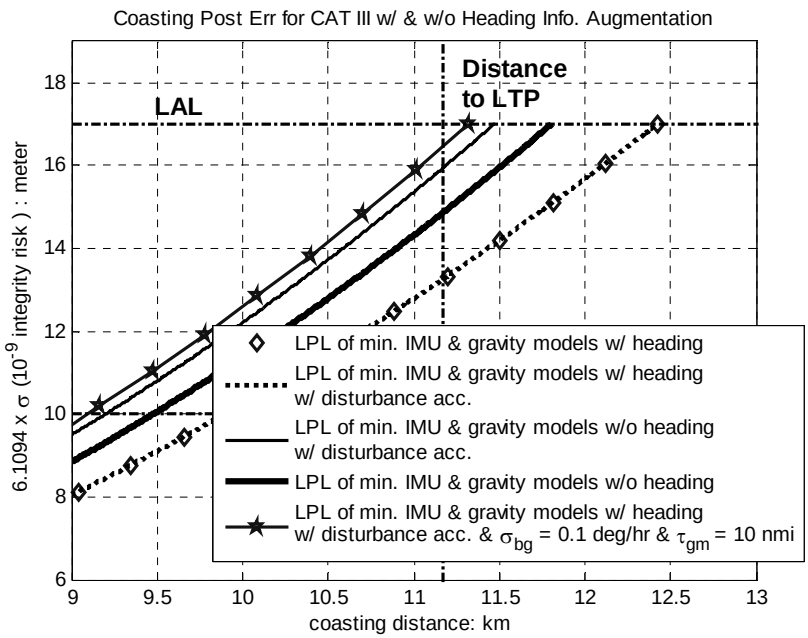

Figure 4.52. Benefit of Heading Information Augmentation with Disturbance Acceleration for Minimum Required IMU and Gravity Models for LAAS CAT III

lower quality cases falls short of the required coasting distance. This analysis excludes the possibility of using 0.1 deg/hr sigma on the gyro bias and 10 nmi on the gravity correlation distance as the minimum requirements on IMU and gravity models, and once again demonstrates the important influence from non-zero accelerations during the coasting stage.

The benefit of implementing heading information augmentation with an additional GPS antenna is clearly demonstrated in Figure 4.52. The heading information augmentation has improved the system sensitivity to not only become robust to disturbance accelerations, but also to increase the coasting performance for the 0.1 deg/hr gyro bias sigma and the 10 nmi gravity correlation distance cases. As a result, it becomes possible to relax the minimum requirements on the IMU and gravity models when the system is augmented with heading information.

Table 4.4. Minimum Requirements on IMU and Gravity Model Parameters for LAAS CAT I Fault-free Precision Approach

Minimum Requirements on IMU parameters			
standard deviation	gyroscope	accelerometer	correlation time ($\tau_{a/g}$)
bias stability (σ_{bg}/σ_{ba})	0.1 deg/hr	10 μg	1 Hour
measurement noise (σ_{vg}/σ_{va})	0.01 deg/hr$^{1/2}$	100 μg	N/A
Minimum Requirements on Gravity Model parameters			
	DOV in N-S ($\delta\xi$)	DOV in E-W ($\delta\eta$)	vertical gravity Error ($\delta\Delta g(0)$)
standard deviation	20 arcsecond	20 arcsecond	25 μg
correlation distance	10 nmi	10 nmi	10 nmi

Another set of IMU and gravity model parameters to meet LAAS CAT I fault-free requirements (without heading information augmentation) are evaluated and listed on Table 4.4. The analysis of the CAT I system coasting performance was performed in a similar fashion to the CAT III case and is presented in Figure 4.53. The coasting performance for each individually degraded parameter is shown to justify the quantified IMU and gravity model parameters in Table 4.4. The dominant error for the CAT I application is the vertical position error instead of the lateral error for the CAT III, mainly due to the significant relaxation on the LAL when the VAL value remains the same. The integrity risk for the CAT I fault-free case is set to be 2×10^{-7} which is about 200 times higher than the CAT III requirement. Comparing the IMU and gravity model parameters with those for the CAT III, the requirement on the gyro bias can be loosened by one order of magnitude; additionally some relaxation on the gravity model parameters is possible. The relatively tight VAL in the CAT I requirements (compare to LAL) makes the

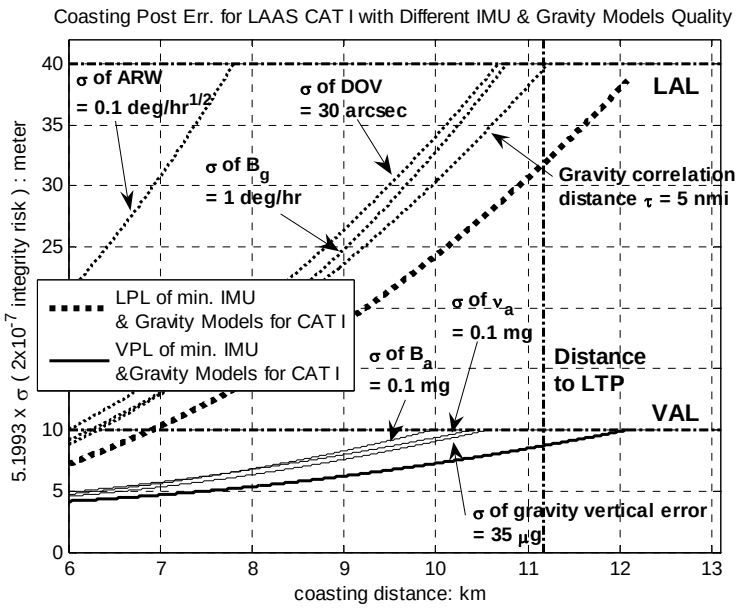

Figure 4.53. Minimum Requirements on IMU and Gravity Models for LAAS CAT I

required quality on the accelerometer sensors the same as the accelerometer quality for CAT III.

Figure 4.54 shows the simulated results of the one-turn approach for LAAS CAT I applications. Similar to the case of CAT III, only 180 left-turn approach simulation

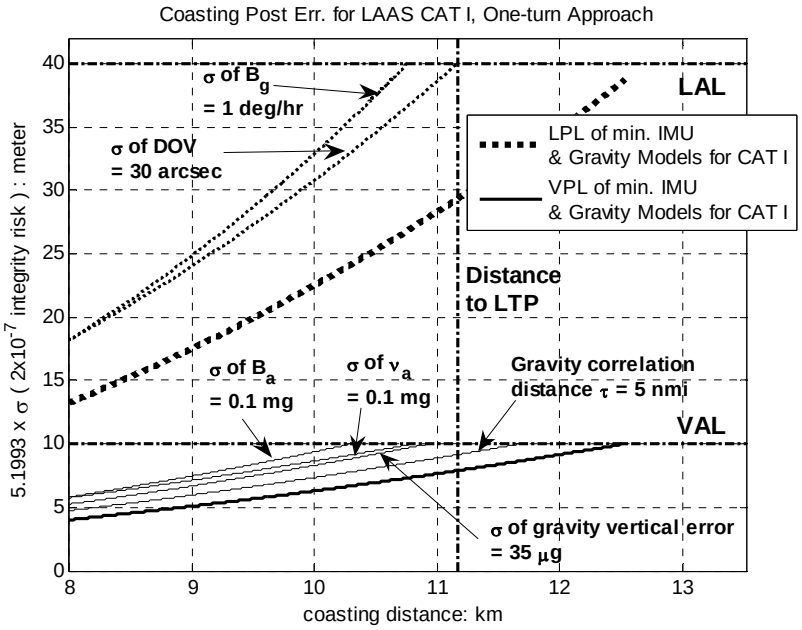

Figure 4.54. One-turn Approach Results of IMU and Gravity Models for LAAS CAT I

results are presented. The coasting performance with 5 nmi gravity correlation distance is shown to meet the CAT I requirements because the dominant error switched from lateral to vertical error. But a necessary margin to tolerate the sensitivity of coasting performance to disturbance accelerations is not acquired. This effect will be shown later in Figure 4.55. The main improvements for the turn approach are on the lateral errors due to a great reduction on the azimuth angle estimation error during the turning period. A careful comparison on the VPL curves between Figure 4.54 and 4.53 observes that they are almost identical.

The effect of disturbance accelerations on the coasting performance during the final coasting stage was simulated and shown in Figure 4.55 for the CAT I minimum required IMU and gravity models. The LPL curves deteriorate slightly while the VPL lines remain almost unchanged. Only three downgraded parameter cases were simulated

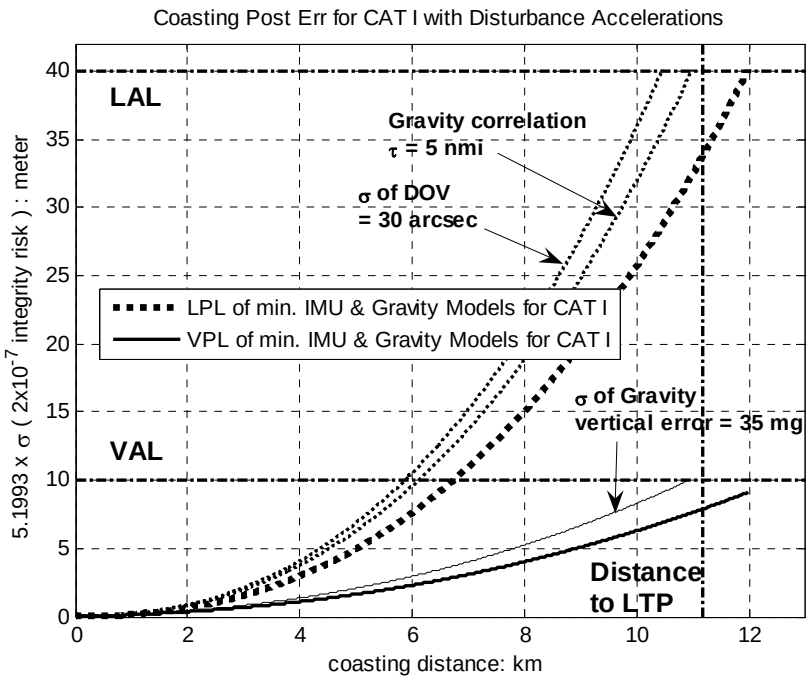

Figure 4.55. Disturbance Acceleration Effect on Coasting Performance of Minimum Required IMU and Gravity Models for LAAS CAT I

and presented in Figure 4.55 for the disturbance acceleration analysis. The results illustrate the necessary margin of the coasting performance to accommodate the system sensitivity to disturbance accelerations. And, therefore, 5 nmi correlation distance is not adopted as the gravity model requirement for CAT I.

Heading information augmentation is also explored to understand the possibility of relaxing the IMU and gravity model requirements for CAT I. All curves in Figure 4.56 are the coasting results with heading information augmentation and the existence of the disturbance acceleration except noted otherwise. The results show that the curve with 5 nmi correlation distance meets the CAT I requirements. This implies either the heading information augmentation or a turning approach would help to relax the gravity model requirements for CAT I precision approach.

Even thought the one-turn approach has similar benefits to those provided by heading augmentation, it is impossible to command all aircraft to perform at least one

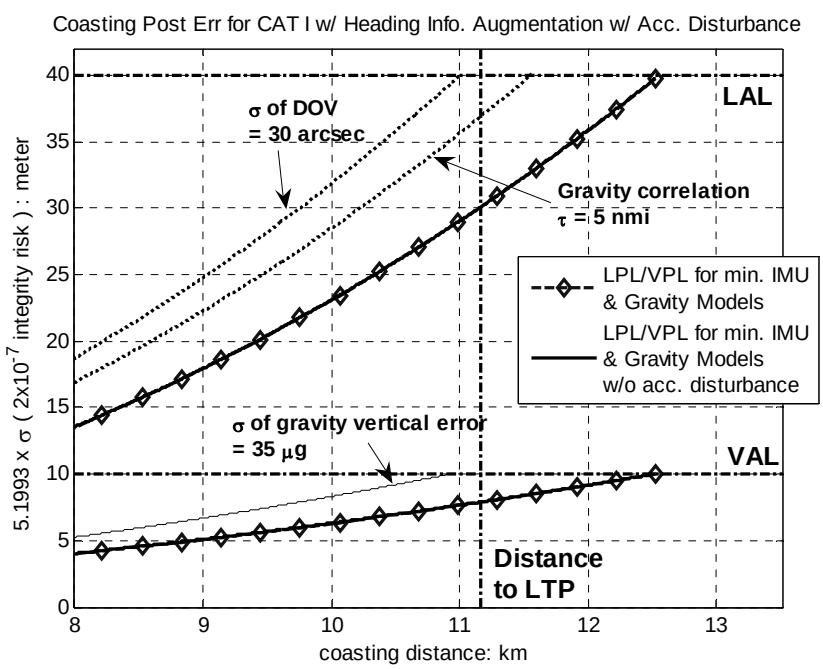

Figure 4.56 Benefit of Heading Information Augmentation with Disturbance Acceleration for Minimum Required IMU and Gravity Models for LAAS CAT I

turn before landing. If the GPS/INS hybrid navigation system is augmented with heading information, not only it can be robust to external acceleration disturbances (thereby reducing continuity risk), but relaxation of the IMU and gravity model parameters are also possible.

CHAPTER 5

SYSTEM VALIDATION AND AVAILABILITY SIMULATION FOR LAAS APPLICATIONS

All the analysis done up to now was aimed at the general system investigation: system coasting performance, INS calibration capability and system sensitivity to different parameters. These properties were explored in a general way to understand the characteristics of the GPS/INS hybrid navigation system. The exception was Section 4.3.2, which was focused on defining IMU and gravity model requirements for LAAS precision approach applications.

To validate the proposed hybrid navigation system architecture and the performance simulated by covariance analysis, in this chapter , flight data from GPS and IMU sensors for LAAS precision approach test flights was collected and processed. The system performance evaluated by post-processing actual flight data will ultimately substantiate all the analyses that have been done and will layout a foundation for the availability analysis in Section 5.2.

5.1 System Architecture and Performance Validation by Flight Data

A set of flight data which include GPS and IMU measurements was recorded during a LAAS flight test at Memphis International Airport on Sep. 28th 2006. This flight data provided by FAA William J. Hughes Technical Center are used to validate the proposed GPS/INS hybrid navigation system performance. Eight approaches were conducted in this flight test. Before using the recorded data for validation, a few corrections for GPS measurements (which will be discussed in the next section) need to be carried out and a set of IMU error model parameters needs to be properly selected to

avoid feeding wrong information into the Kalman filter. All GPS and IMU data was supposed to be recorded without any post-processing to avoid introducing unknown errors. This is the case for GPS data. However, it is not so for IMU measurements in this set of flight data. Details will be addressed in the IMU model evaluation section. All the following corrections applied for GPS measurements are necessary and feasible in a real time positioning process.

5.1.1 GPS Measurement Corrections. Raw GPS measurements usually are corrupted while the signals propagate through the atmosphere. DGPS has the inherent advantage of eliminating errors which are common to the reference station and the users. However, remaining spatially decorrelated errors can still be significant for high accuracy and integrity applications. These DGPS errors are listed and corrected as follows:

Tropospheric delay: GPS code and carrier-phase signals experience the same delay when they propagate through the lower part of the atmosphere, known as the troposphere. This delay results from a composite of different dry gas components and water vapor in the air. Because the troposphere is not a dispersive medium for GPS signals (signal speed does not vary with frequency), this delay can't be estimated from dual frequency GPS measurements. Applying a tropospheric delay model to predict and then remove the delay from GPS measurements is currently the best approach to mitigate this error. Most models are used to predict the zenith delay, and then a mapping function is applied to generate the projected slant delay experienced by GPS signals. The zenith dry delay caused by various components (mainly O_2 and N_2) in dry air can be modeled precisely up to a few millimeters if accurate surface pressure is available. On the contrary, zenith wet delay caused by water vapor varies significantly due to local weather

activity and is more difficult to model accordingly, especially in storm conditions. Strong decorrelations on tropospheric delays in DGPS measurements have been observed during weather storms with error magnitudes of up to 30 centimeters for a short baseline (less than 20 kilometers). This potential integrity threat to navigation will be discussed later in Chapter 6.

There are a number of nominal troposphere models which work well on different types of applications. The two models adopted in this research both are modified Hopfield models. One is published by Goad and Goodman in 1974 [Goad74] and can be found in *GPS Satellite Survey* table 9.3 [Leick94], another is by van Graas from Ohio University [LAASADD06]. Both models work well on flight data. The basic idea and model formulas are briefly introduced here. More details about other tropospheric models can be found on [Misra01] and [SpilkerJr96b].

Given the refractive index profile, $n(l)$, along the signal propagation path, *l*, from a GPS satellite to a receiver, the effective path increase is:

$$T_z = \int_{satellite}^{receiver} [n(l) - 1] dl \tag{5.1}$$

It is convenient to define refractivity *N* as:

$$N = (n - 1) \times 10^6 \tag{5.2}$$

The effective tropospheric delay along the signal propagation path can be expressed:

$$T_z = 10^{-6} \int_{satellite}^{receiver} N(l) dl$$

Two quadratic models for dry and wet refractivity profiles, $N_d(h)$ and $N_w(h)$, which are the functions of altitude *h* relative to the ground and were empirically derived by Hopfield in 1969, are well known as the *Hopfield model* [Hopfield69]:

$$N_d(h) = N_{d0}\left(1 - \frac{h}{h_d}\right)^4 \tag{5.3}$$

$$N_w(h) = N_{w0}\left(1 - \frac{h}{h_w}\right)^4 \tag{5.4}$$

where N_{d0} and N_{w0} are the dry and wet refractivities at the ground surface respectively, and h_d (≈ 43 km) and h_w (≈ 12 km) are the heights above the ground antenna, at which the refractivities are zero.

The total estimated zenith tropospheric delay according to the Hopfield model is:

$$\widetilde{T}_z = 10^{-6}\int [N_d(h) + N_w(h)]dh \tag{5.5}$$

A mapping function or an obliquity factor is then used to project the vertical delay into a slant delay. The Hopfield model can generally predicts the total zenith delay with an error of 1 to 2 cm when accurate meteorological measurements on the surface are applied, and 5 to 10 cm by using an averaged archived meteorological data.

The *Modified Hopfield model* is basically a fine tuned version of the Hopfield model. A numerical summation of nine segments replaces the analytic integration in the Hopfield model. For each segment, a more sophisticated mapping function and refractivity profile formula is used. The coefficients and computational formulas of the modified Hopfield model by Goad and Goodman is given in [Goad74] [Leick94].

Linearization error: The DGPS measurement model (equations 2.4 ~ 2.6) is linearized with respect to a ground reference location by assuming line-of-sight (LOS) vectors are the same for ground and air receivers. The error resulting from this linear approximation for each satellite increases proportionally to the square of the normal distance from the aircraft to the ground station's LOS vector (*dn* in Figure 5.1). For a 5

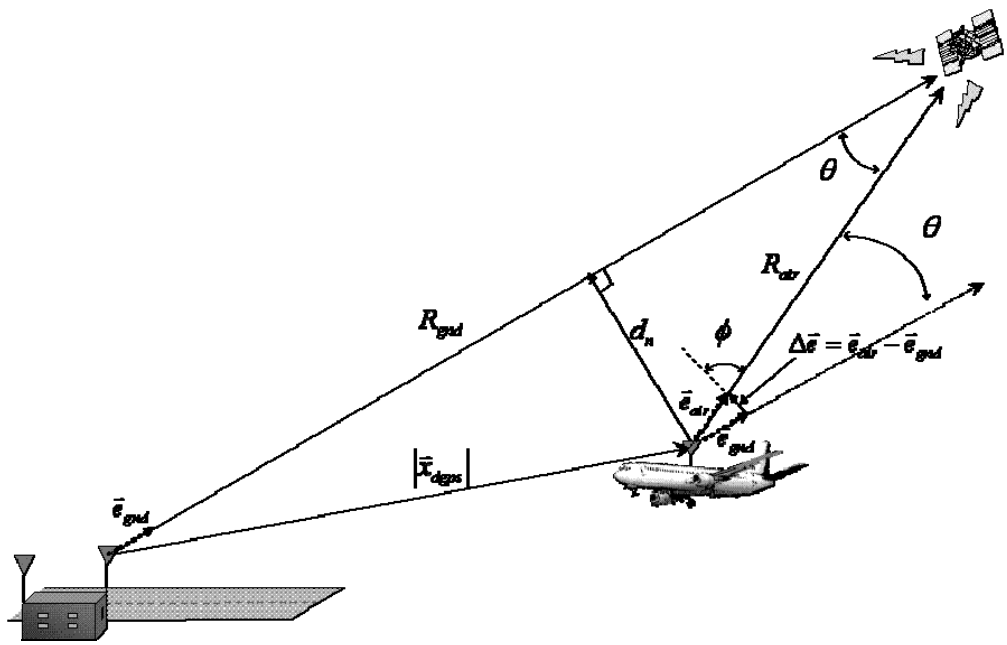

Figure 5.1. DGPS Measurement Model Linearization Error

km baseline (between reference and aircraft), the error may be up to half meter, which is unacceptable for precision demanding applications. Corrections have to be applied to compensate for linearization errors in DGPS measurements. Figure 5.1 is an illustrative plot to explain the mechanism of linearization error. The correction can be mathematically derived as follows:

$$\begin{aligned}
\Delta R^i_{true} &= R^i_{air} - R^i_{gnd} \\
&= \vec{e}^{\,i}_{air} \cdot (\vec{x}^i_{sv} - \vec{x}_{air}) - \vec{e}^{\,i}_{gnd} \cdot (\vec{x}^i_{sv} - \vec{x}_{gnd}) \\
&= \vec{e}^{\,i}_{gnd} \cdot (\vec{x}^i_{sv} - \vec{x}_{air}) - \vec{e}^{\,i}_{gnd} \cdot (\vec{x}^i_{sv} - \vec{x}_{gnd}) + \vec{e}^{\,i}_{air} \cdot (\vec{x}^i_{sv} - \vec{x}_{air}) - \vec{e}^{\,i}_{gnd} \cdot (\vec{x}^i_{sv} - \vec{x}_{air}) \\
&= [-\vec{e}^{\,i}_{gnd} \cdot \vec{x}_{dgps}] + [(\vec{e}^{\,i}_{air} - \vec{e}^{\,i}_{gnd}) \cdot (\vec{x}^i_{sv} - \vec{x}_{air})]
\end{aligned} \tag{5.6}$$

where ΔR^i_{true} is the true geometry range difference between the ground and air receivers for satellite *i*, $\vec{e}^{\,i}_{air}$ and $\vec{e}^{\,i}_{gnd}$ are the line-of-sight vectors, $\vec{x}^i_{sv}$, $\vec{x}_{air}$ and $\vec{x}_{gnd}$ are the absolute positions for the satellite *i*, the aircraft and the ground station and $\vec{x}_{dgps}$ is the differential position of the aircraft relative to the ground station.

The first bracket in the final results in equation 5.6 is the linearization of the geometry range difference by projecting the differential position onto the LOS of the ground station. The second bracket is the exact form of the linearization error. By defining the difference on LOS vectors as:

$$\Delta e^i = (\vec{e}^i_{air} - \vec{e}^i_{gnd}) \tag{5.7}$$

The correction for the linearization error can then be defined as:

$$EC_{lin} = \Delta\vec{e}^{\,i} \cdot (\vec{x}^i_{sv} - \vec{x}_{air}) \tag{5.8}$$

This projection from an aircraft-to-satellite vector onto the difference of LOS vectors is equivalent to:

$$\Delta\vec{e}^{\,i} \cdot (\vec{x}^i_{sv} - \vec{x}_{air}) = |\Delta\vec{e}^{\,i}|\,|\vec{x}^i_{sv} - \vec{x}_{air}|\cos(\phi) \tag{5.9}$$

Each individual term in equation 5.9, can be either measured from the GPS signal or approximated from the geometrical relationship in Figure 5.1:

$$|\Delta\vec{e}^{\,i}| = 2\sin(\theta/2) \approx 2\times\theta/2 = \theta\text{, since } \theta/2 << 1\,\text{deg} \tag{5.10}$$

$$|\vec{x}^i_{sv} - \vec{x}_{air}| = R_{air} \tag{5.11}$$

$$\cos(\phi) = \cos(90^0 - \theta/2) = \sin(\theta/2) \approx \theta/2 \tag{5.12}$$

Using the results above to substitute the corresponding terms in equation 5.9 and noting that $d_n << R_{air}$, the final form of linearization correction is [Lawrence96]:

$$EC_{lin} = R_{air}\frac{\theta^2}{2} \approx \frac{R_{air}}{2}\frac{d_n^{\ 2}}{R_{air}^{\ 2}} = \frac{d_n^{\ 2}}{2R_{air}} \tag{5.13}$$

The residual error after applying the appropriate linearization correction remains at the millimeter level for baselines as big as 40 km with δd_n less than 5 m, which can be evaluated by considering variations on equation 5.13:

$$\delta EC_{lin} = \frac{d_n}{R_{air}} \delta d_n - (\frac{d_n}{R_{air}})^2 \delta R_{air} \approx \frac{d_n}{R_{air}} \delta d_n \tag{5.14}$$

Signal travel time correction: The GPS signal travel time from the satellite to the receiver varies roughly between 65 to 90 milliseconds, depending on the distance between the satellite position and the user location. A correct LOS vector for a satellite should be drawn from the user location where the GPS signal is received to the satellite position where the GPS signal was initially transmitted. Without considering satellite motion during signal travel, the resulting error is equivalent to LOS errors caused by inaccurate satellite position information, which is proportional to the distance between the DGPS user and the reference station. A high elevation angle satellite and a 20 km baseline might result in a 20 cm DGPS measurement error. However, the GPS signal travel time for each satellite is estimated by dividing the received pseudorange measurement by the speed of light. The travel time is used to propagate satellite positions backward from the satellite positions at the signal reception time to estimate the satellite positions at the signal transmission time.

Other residual DGPS measurement errors exist, but they have negligible influence (millimeter level) on precision landing navigation. These effects can be important in certain high precision surveying or geodetic applications and are discussed in [Lawrence96].

5.1.2 Reference Trajectory by Wide-lane GPS positioning. Raw GPS measurements in the archived flight data were recorded with a 5 Hz output rate by two L1/L2 capable NovAtel OEM-4 receivers, one on an N47 aircraft and the other at the ground reference station. After applying the corrections on raw GPS L1 and L2 carrier-phase

measurements, ionosphere-free DD wide-lane integers were estimated and fixed by filtering wide-lane carrier plus narrow-lane code. Wide-lane carrier-phase and narrow-lane code measurements are defined using equations 5.15 and 5.16 accordingly:

$$\Delta\phi_{L1} - \Delta\phi_{L2} = \frac{\lambda_{L2} - \lambda_{L1}}{\lambda_{L1}\lambda_{L2}}(-\vec{e}\cdot\vec{x}^{r} + \Delta\tau + \Delta T) - \frac{\lambda_{L1} - \lambda_{L2}}{\lambda_{L1}^{2}}\Delta I_{L1} \\ (\Delta N_{L1} - \Delta N_{L2}) + b_{L1/L2} + \varepsilon_{wlane} \tag{5.15}$$

$$\frac{\Delta\rho_{L1}}{\lambda_{L1}} + \frac{\Delta\rho_{L2}}{\lambda_{L2}} = \frac{\lambda_{L2} + \lambda_{L1}}{\lambda_{L1}\lambda_{L2}}(-\vec{e}\cdot\vec{x}^{r} + \Delta\tau + \Delta T) + \frac{\lambda_{L1} + \lambda_{L2}}{\lambda_{L1}^{2}}\Delta I_{L1} + \varepsilon_{nlane} \tag{5.16}$$

where ε_{wlane} and ε_{nlane} are the residual errors in wide-lane carrier and narrow-lane code, $b_{L1/L2}$ is an inter-frequency bias which will be canceled in DD carrier-phase measurement

$$\begin{aligned}\Delta\hat{N}_{W} &= ave(\Delta N_{L1} - \Delta N_{L2}) \\ &= ave[(\Delta\phi_{L1} - \Delta\phi_{L1}) + (\frac{\lambda_{L1} - \lambda_{L2}}{\lambda_{L2} + \lambda_{L1}})(\frac{\Delta\rho_{L1}}{\lambda_{L1}} + \frac{\Delta\rho_{L2}}{\lambda_{L2}})]\end{aligned} \tag{5.17}$$

Equation 5.17 describes the process for SD wide-lane integers, from which DD wide-lane integers can be obtained easily once a master satellite is selected.

As long as DD wide-lane integers are fixed correctly, wide-lane carrier-phase positioning is enabled with an error standard deviation of 10 cm level or less by using a least-squares estimation technique. Figure 5.2 shows all eight trajectories using the DD wide-lane GPS positioning method. Because DD wide-lane GPS positions will serve as the role of the "true" trajectory, DD wide-lane carrier-phase measurement residuals are checked to ensure the correctness of reference positions. The residuals are generated by removing the estimated geometric ranges, which are the projections of wide-lane positions on the LOS vectors, and fixed wide-lane integers from the corrected DD wide-lane carrier-phase measurements. As long as the removed position projections and

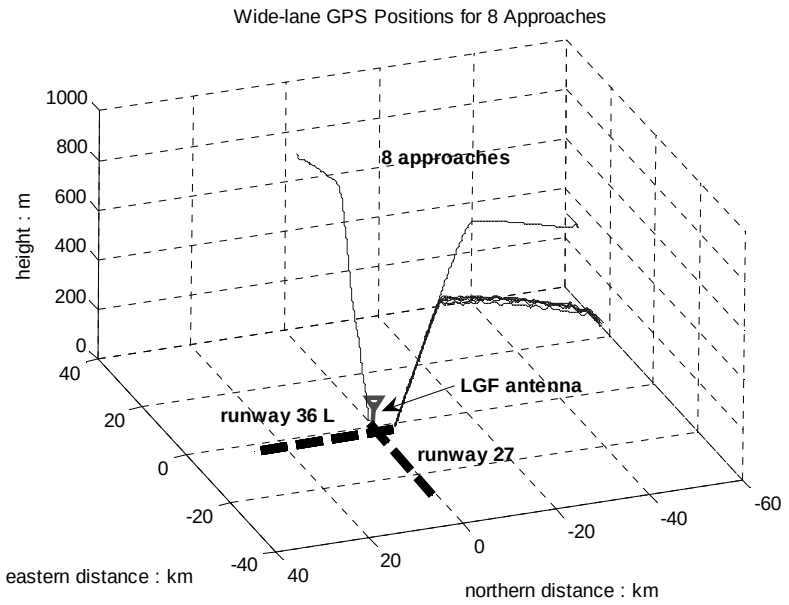

Figure 5.2. 3-D Trajectories of Eight LAAS Precision Approaches in Flight Test

integers are correct, the main components in the DD wide-lane carrier-phase residuals would be DD spatial ionospheric decorrelations and DD wide-lane carrier-phase multipath. The DD ionospheric residual error under normal ionospheric activity is expected to be the dominant error, with one sigma magnitude around 10 cm or less at the beginning of each approach when the aircraft is further from the reference station, then the ionospheric error reduces gradually while the carrier-phase multipath remains with a similar magnitude along the way to the DH location. The one sigma DD wide-lane carrier-phase multipath generally has a magnitude around 2 to 3 cm or less.

Figure 5.3 displays one example of the DD wide-lane carrier-phase residuals. The residuals clearly fit the expectations. The other seven approaches have also passed a similar residual check, therefore we can confidently treat the wide-lane GPS positions as “true” trajectories for future GPS/INS hybrid performance evaluations.

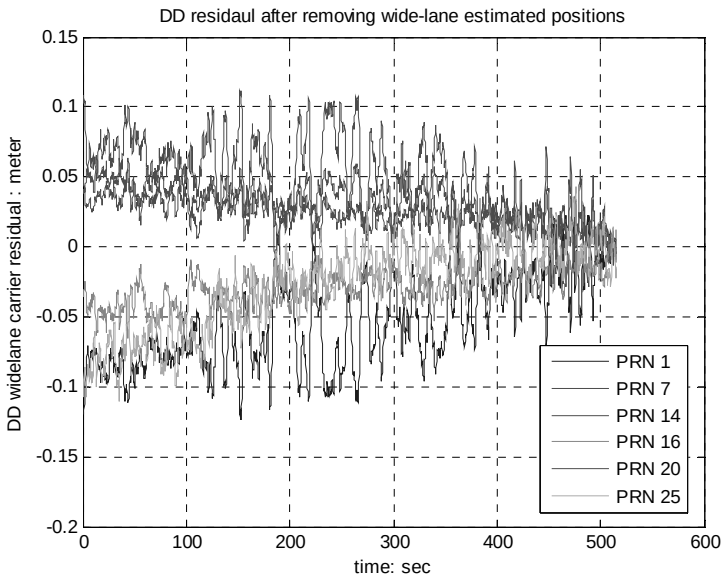

Figure 5.3. DD Wide-lane Carrier-phase Residuals from First Approach Data

5.1.3 IMU Model Evaluation. Due to the proprietary and confidential protections, normally it is difficult to obtain error model parameters for a navigation grade IMU or even raw IMU data which could be used to model IMU errors effectively. Unfortunately, this is also true for the IMU data in this flight test. The IMU data was generated by a Honeywell navigation grade IMU (HG 2001GD) at 50 Hz without any accompanying error model information. It is also unfortunately true that the available inertial data did not include raw IMU outputs; the data was either processed by IMU internal algorithms or post-processed by other software. Without any source of IMU error model information and the IMU raw measurements themselves, free coasting positions and attitudes, which were propagated from the initial positions and velocities obtained from the corresponding "true" trajectories by using equation 3.18 and available archived inertial data without any calibration process (pure INS propagation), were generated to compare with the "true" trajectories and reference attitudes as the first step in evaluating

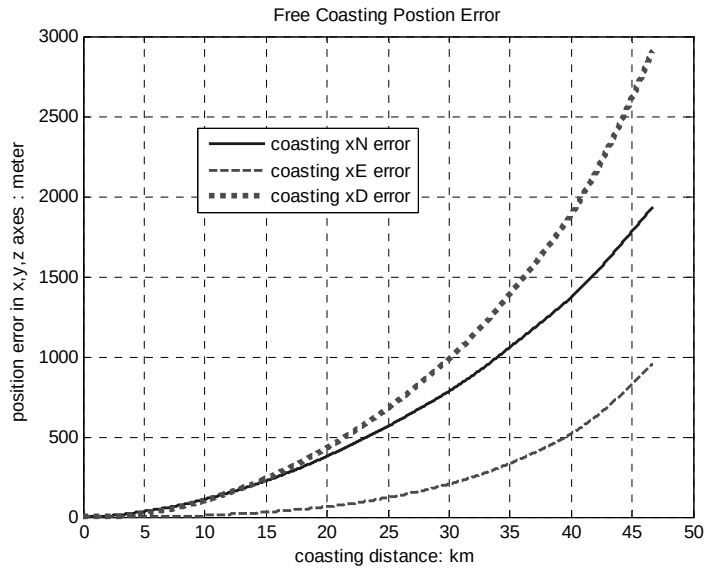

Figure 5.4. Free Coasting Position Errors during First Approach

the IMU data. Since there is no other source that can be validated as "true attitudes", the archived INS attitude outputs were used as the reference for attitude comparison.

The differences between the free coasting positions and the true trajectory generated by DD wide-lane GPS positioning are large. Figure 5.4 shows the results for the first approach and serves as an example of problematic acceleration data. The deviations between the reference attitudes and the propagated attitudes are presented in Figure 5.5, which are also much worse than the expected results from a navigation grade IMU. To handle the problematic data (with the objective of being able to validate the hybrid system architecture), a strategy is laid out, which is to ignore the acceleration data, then simulate accelerometer outputs by interpolating the "true" positions with high frequency in the Latitude, Longitude and Altitude (LLA) domain. And the reference attitudes are treated as the "true" attitudes to convert the simulated accelerations from the navigation frame to the body frame. Following this process, the 'hybrid' version of IMU

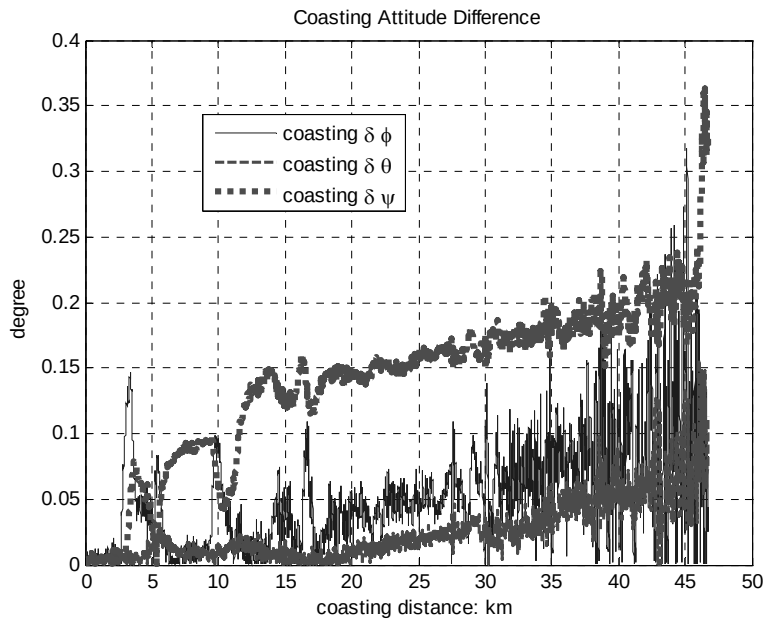

Figure 5.5. Free Coasting Attitude Difference during First Approach

flight data is produced. From now on, whenever the IMU flight data is mentioned, the acceleration data is all obtained in this manner.

The aircraft attitudes were the results of the aircraft fluid dynamics and external forces during the flight tests, which are very difficult to simulate. Theoretically, IMU accelerometer outputs can be simulated according to any arbitrary aircraft attitude. To simulate IMU accelerometer outputs in this way, however, all the connections of the inertial information to the flight test data will be lost. In order to reserve the reality in flight data as much as possible, the available gyro measurements from the archived flight data are treated as raw IMU gyro outputs from low quality gyroscopes. To correctly respond to the attitude propagation errors in Figure 5.5, the gyroscope error model parameters are selected in such a way that the attitude covariance propagation can meet the actual free coasting attitude errors.

Table 5.1 is the HG 2001 error model based on a report presented by Fermi Lab in

Table 5.1 Honeywell HG 2001GD IMU

Navigation Grade IMU parameters			
	Gyroscope	Accelerometer	Correlation Time
Bias Stability (one σ)	0.003 deg/hr	25 μg	N/A
Measurement noise (one σ)	0.001 deg/hr$^{1/2}$	N/A	N/A

a geodetic research report [Bocean99]. This model could not be validated owing to the quality of current flight data. It is listed only as a reference of a navigation grade IMU specification. In order to serve the purpose of validating the system architecture, it is necessary to adjust the gyro error model parameters to reasonably reflect the results in Figure 5.5.

Complete parameter values for the IMU and gravity error models are listed in Table 5.2. The simulated accelerometer data and gravity anomalies follow the IMU requirements for CAT III in previous analysis. The lever arm effect is not included in the simulated accelerometer measurements.

Table 5.2. IMU and Gravity Model Parameters for System Validation by Flight Data

IMU model parameters			
standard deviation	gyroscope	accelerometer	correlation time ($\tau_{a/g}$)
bias stability (σ_{bg}/σ_{ba})	1 deg/hr	10 μg	1 Hour
measurement noise (σ_{vg}/σ_{va})	0.5 deg/hr$^{1/2}$	100 μg	N/A
Gravity Model parameters			
	DOV in N-S (δξ)	DOV in E-W (δη)	vertical gravity Error (δΔg(0))
standard deviation	5 arcsecond	5 arcsecond	20 μg
correlation distance	20 nmi	20 nmi	20 nmi

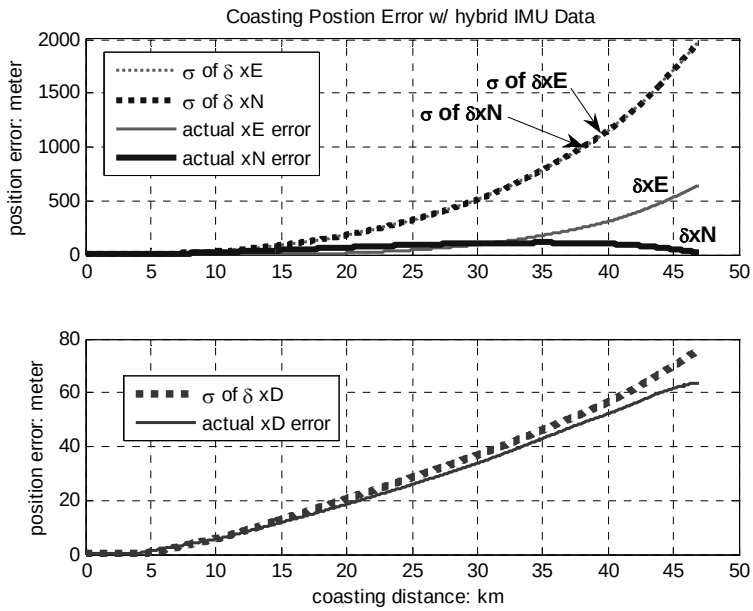

Figure 5.6. Free Coasting Position Err with IMU Error Model during First Approach

Figure 5.6 and 5.7 demonstrate the free coasting position and attitude errors in the first approach with the error model parameters applied from Table 5.2. The predicted one sigma error envelopes have growing magnitudes that are reasonably comparable to the actual propagating errors. Similar results appear on the remaining seven approaches.

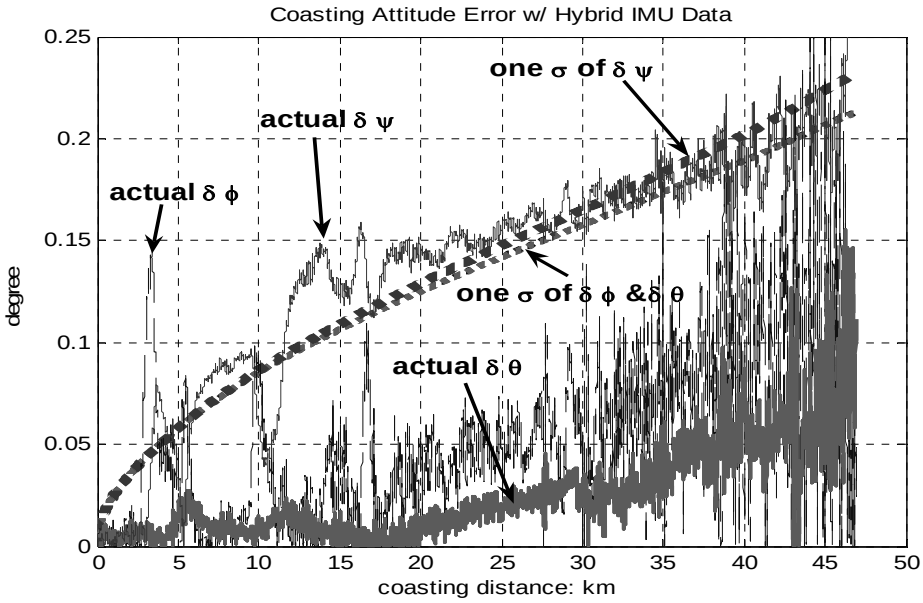

Figure 5.7. Free Coasting Attitude Err with IMU Error Model during First Approach

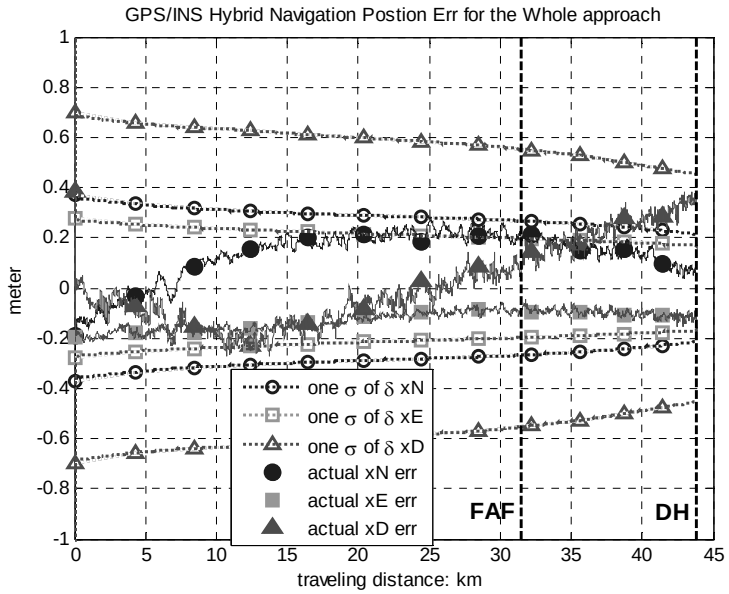

Figure 5.8. Position Errors of GPS/INS Hybrid System during Approach Two

5.1.4 Validated System Performance Results by Flight Data. With the pre-evaluated IMU data and reference GPS trajectories, the hybrid navigation system coasting performance for the eight approaches in the flight test are evaluated by feeding in the flight data into the Kalman filter implemented upon the novel hybrid system architecture described in Chapter 3.

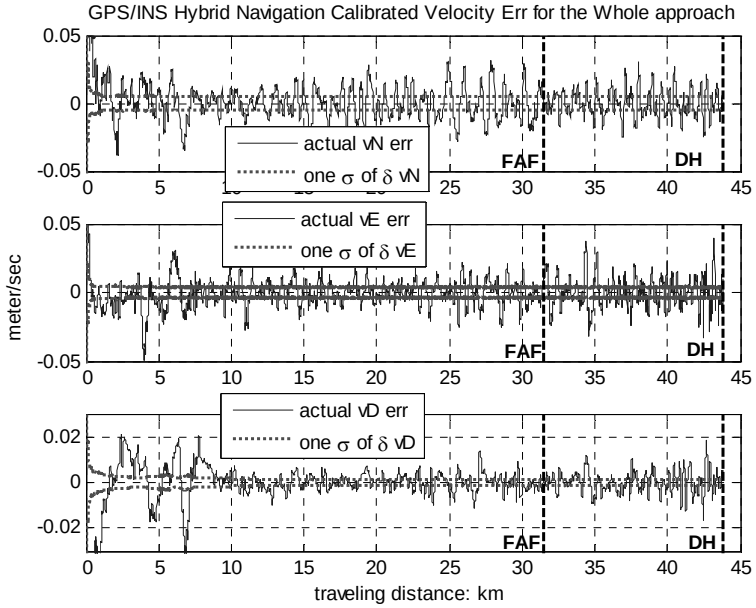

Figure 5.9. Velocity Errors of GPS/INS Hybrid System during Approach Two

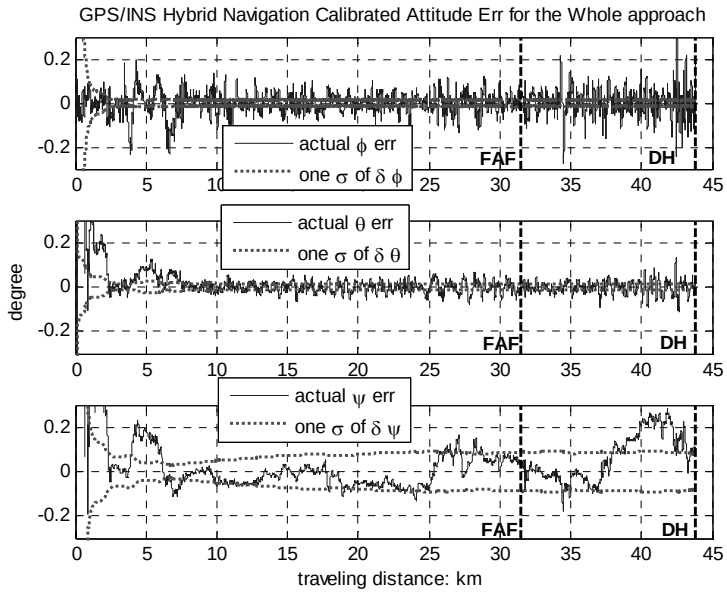

Figure 5.10. Attitude Errors of GPS/INS Hybrid System during Approach Two

Carrier-smoothed code is generated and employed for positioning according to LAAS specifications. The correlation between SD carrier-smoothed code and SD raw carrier-phase measurements will be analyzed in Section 5.2.1. However, the results are implemented in the flight data validation.

Results from the second approach are shown here as an example of the quality of the estimated position, velocity and attitude in Figures 5.8, 5.9 and 5.10. The calibration process was working during the whole approach in these figures. The standard deviation envelopes of the estimated states stay reasonably close to the estimated errors. Therefore, the calibration process of the hybrid system architecture is validated with the support of these results. The confidence on the covariance analysis is established as well.

For better understanding the coasting position errors, a three dimensional coasting trajectory for the second approach is shown in Figure 5.11. The lateral error is the dominant error in this example and it is also true for the rest of the approaches due to the low quality on the gyro data.

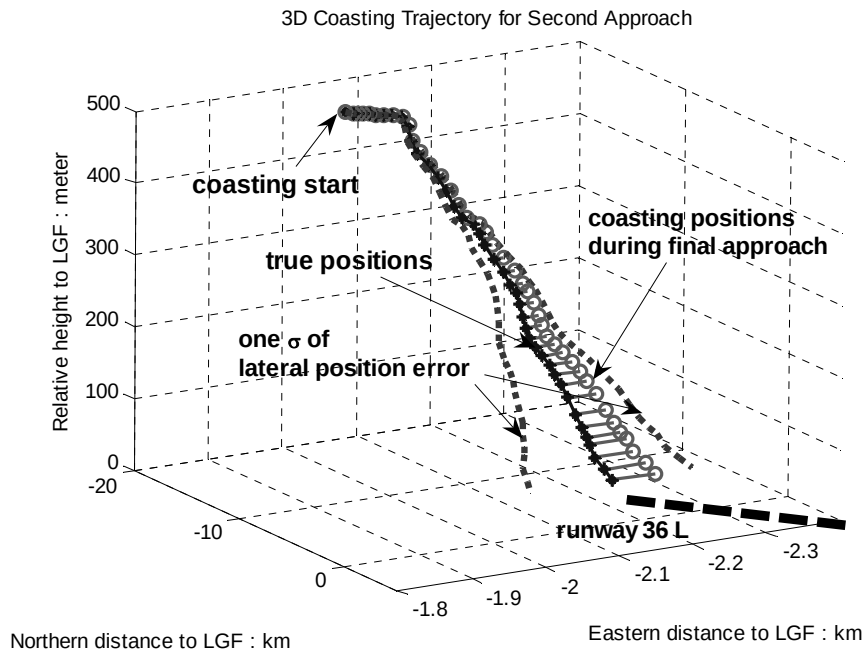

Figure 5.11. Coasting Trajectory of GPS/INS Hybrid System from Approach Two

With the visual help of this 3D example, the complete set of lateral and vertical coasting position errors for the eight approaches are displayed in Figure 5.12 and 5.13. Final coasting position errors at DH are shown in Figure 5.14. The GPS measurement output rate in this set of flight data is 5 Hz, which is different from the 2 Hz required by

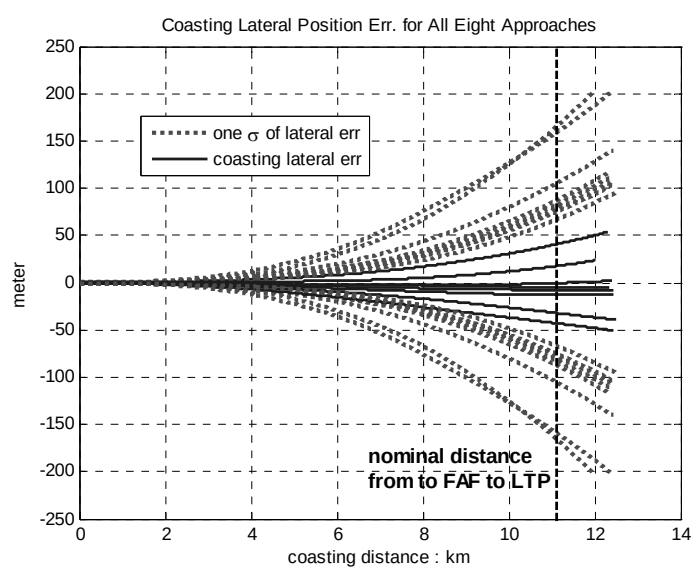

Figure 5.12. Lateral Coasting Errors of All Approaches

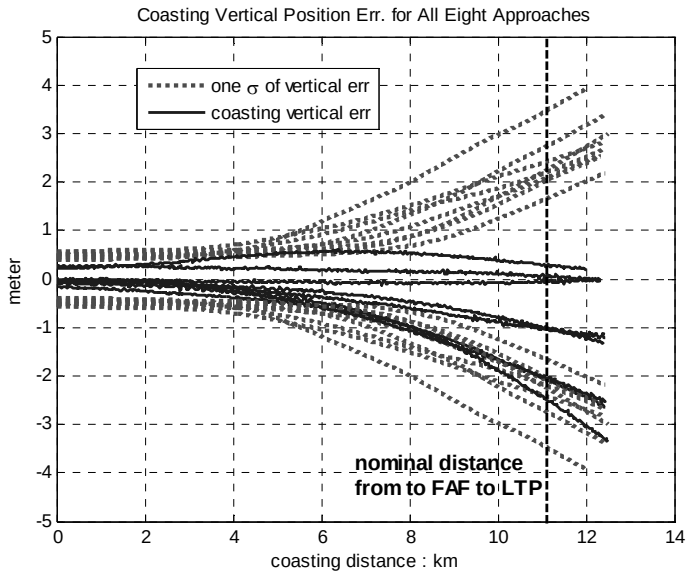

Figure 5.13. Vertical Coasting Errors of All Approaches

LAAS. Nevertheless, all required processes on GPS measurements from LAAS specifications are applied in the system validation, such as 100 second code smoothing time. The unspecified multipath time constant for carrier-phase measurements is assumed to be 10 sec, which as shown in the next section is the worst case for CAT I.

All displayed results demonstrate that the actual state propagation errors are close

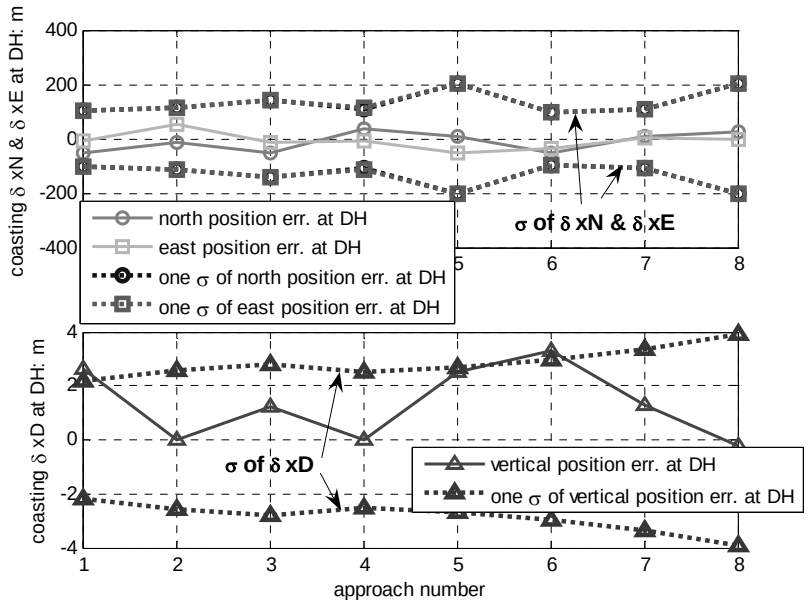

Figure 5.14. Final Coasting Position Errors at DH in All Approaches

to the standard deviation errors predicted by the covariance propagation. Based on the results generated from flight test data, the proposed GPS/INS hybrid system architecture and coasting performance (covariance propagation) are validated with high confidence.

5.2 Fault-free Availability Analysis for LAAS Precision Approach and Landing

A properly working navigation system has to be available most of the time to the system users. LAAS has inherited the stringent requirements from ILS, which include requirements on availability. The required availability for LAAS at the system level should fall between 0.99 and 0.99999. Only the availability of the straight-in approach is evaluated for the hybrid navigation system as the one-turn approach will produce better performance, which has been shown in the sensitivity analysis in Section 4.2.4. All the analyses previously done for the hybrid navigation system are assumed to use raw SD code and carrier measurements to be in general. However, LAAS has adopted carrier-smoothed code as the way to mitigate multipath errors. The measurement noise standard deviation of the SD smoothed code and the SD raw carrier-phase measurements and the correlation between these two are analyzed to ensure the conservativeness of the analysis.

5.2.1 Hybrid System Parameter and Carrier-smoothed Code Analysis for LAAS Availability Simulation. The availability of the proposed GPS/INS hybrid navigation system is basically evaluated by covariance analysis; the parameters for the system IMU and gravity models are the same as in Table 4.3 for CAT III and Table 4.4 for CAT I. Meanwhile, GPS signal quality is assumed to meet the Minimum Operational Performance Standards (MOPS) for GPS Local Area Augmentation System Airborne Equipment [RTCA/DO253B] and LGF specification standards [FAA-E-2937A] for

airborne and ground receivers. Nevertheless, the correlation between the SD carrier-smoothed code measurements and the SD carrier-phase measurements has not been analyzed before, because the SD carrier-phase measurements are not included in the current LAAS broadcast message yet.

The main advantage of using carrier-smoothed code instead of raw code is that code noise and multipath, which are the main error sources for current LAAS system configuration, can be significantly mitigated by this technique. With the new proposed hybrid navigation system configuration, the correlation between the SD smoothed code and the newly required SD carrier needs to be addressed. A correlation analysis to ensure the system integrity from mis-modeling the measurement correlation in the Kalman filter is derived next.

Single difference raw code and carrier measurement equations 2.5 and 2.6 for one satellite are re-displayed below with simpler notation:

$$\Delta\rho_k = -\vec{e}_k \cdot \vec{x}_k^r + \Delta\tau_k + \Delta I_k + \Delta T_k + \Delta m_k^\rho + \Delta v_k^\rho \tag{5.18}$$

$$\lambda_1 \Delta\phi_k = -\vec{e}_k \cdot \vec{x}_k^r + \Delta\tau_k - \Delta I_k + \Delta T_k + \lambda_1 \Delta N + \Delta m_k^\phi + \Delta v_k^\phi \tag{5.19}$$

where the general single difference measurement error term has been broken down into multipath, m_k^ρ and m_k^ϕ, and receiver internal tracking noise, v_k^ρ and v_k^ϕ.

The smoothing filter for carrier-smoothed code adopted in LAAS has a 100 sec smoothing time constant and processes measurements according to equation 5.20 [FAA-E-2937A]:

$$\Delta\overline{\rho}_k = \frac{1}{N_s}\Delta\rho_k + \frac{N_s - 1}{N_s}[\Delta\overline{\rho}_{k-1} + \lambda_1(\Delta\phi_k - \Delta\phi_{k-1})], \Delta\overline{\rho}_0 = \Delta\rho_0 \tag{5.20}$$

where $\Delta\overline{\rho}_k$ is the SD smoothed code measurement at time epoch k, and N_s is the total number of measurements within smoothing time period (not a carrier phase integer).

In the hybrid system Kalman filter, the multipath at each satellite signal is modeled as a state with the properties of a first order GMRP for both code and carrier. Therefore, the receiver tracking noise, which is treated as white noise, will be the measurement noise in the Kalman filter. The measurement correlation between the SD smoothed code and SD raw carrier due to receiver tracking noise only can be analyzed as:

$$E[\Delta v_k^{\overline{\rho}} \Delta v_k^{\phi}] = E[(\frac{1}{N_s}\Delta v_k^{\rho} + \frac{N_s - 1}{N_s}\Delta v_{k-1}^{\overline{\rho}} + \frac{N_s - 1}{N_s}\Delta v_k^{\phi} - \frac{N_s - 1}{N_s}\Delta v_{k-1}^{\phi})\Delta v_k^{\phi}] \quad (5.21)$$

The assumptions of independence and whiteness on the receiver code and carrier tracking noises induces zero correlation on $E[\Delta v_k^{\rho}\Delta v_k^{\phi}]$ and $E[\Delta v_k^{\phi}\Delta v_{k-1}^{\phi}]$. Moreover, $\Delta v_{k-1}^{\overline{\rho}}$ has receiver code and carrier white noise components only at time k-1 and earlier, which are all independent from the current receiver carrier tracking white noise, this also results in zero correlation on $E[\Delta v_{k-1}^{\overline{\rho}}\Delta v_k^{\phi}]$. The final result from equation 5.21 becomes:

$$E[\Delta v_k^{\overline{\rho}} \Delta v_k^{\phi}] = \frac{N_s - 1}{N_s} E[\Delta v_k^{\phi}\Delta v_k^{\phi}] = \frac{N_s - 1}{N_s}\sigma_{\Delta\phi}^2 \quad (5.22)$$

With the smoothed code measurement replacing the raw code in the Kalman filter measurement update describe in Section 3.3.2, the magnitude of the smoothed code measurement noise has to be analyzed. The standard deviation of the SD smoothed receiver code tracking noise can be derived as:

$$\begin{aligned} E[\Delta v_k^{\overline{\rho}} \Delta v_k^{\overline{\rho}}] = {} & \frac{1}{N_s^2} E[(\Delta v_k^{\rho})^2] + (\frac{N_s - 1}{N_s})^2 E[(\Delta v_{k-1}^{\overline{\rho}})^2] + (\frac{N_s - 1}{N_s})^2 E[(\Delta v_k^{\phi})^2] \\ & + (\frac{N_s - 1}{N_s})^2 E[(\Delta v_{k-1}^{\phi})^2] - 2(\frac{N_s - 1}{N_s})^2 E[\Delta v_{k-1}^{\overline{\rho}}\Delta v_{k-1}^{\phi}] \end{aligned} \quad (5.23)$$

In steady state, the time tag in equation 5.23 is removed and the correlation derived from equation 5.22 is substituted into the last term. The final result is:

$$E[\Delta v^{\bar{\rho}} \Delta v^{\bar{\rho}}] = \sigma^2_{\Delta\bar{\rho}} = \frac{1}{2N_s - 1}\sigma^2_{\Delta\rho} + \frac{2(N_s - 1)^2}{N(2N_s - 1)}\sigma^2_{\Delta\phi} \tag{5.24}$$

With results from equation 5.22 and 5.24, the Kalman filter measurement model can be implemented accordingly. Actual values adopted for stand-alone code and carrier tracking noises are 0.5 and 0.002 meters respectively [Misra01]. For the LAAS implementation of the hybrid navigation system, the SD raw code measurement has to be replaced by the SD smoothed code as below:

$$\Delta\bar{\rho}_k = -\vec{e}_k \cdot \vec{x}^r_k + \Delta\tau_k + \Delta\bar{I}_k + \Delta T_k + \Delta m^{\bar{\rho}}_k + \Delta v^{\bar{\rho}}_k \tag{5.25}$$

where $\Delta\bar{I}_k$ is the SD carrier-smoothed ionospheric error which has a code-carrier divergence effect, but it can be modeled properly according to Ko's analysis in [Ko00]. $\Delta m^{\bar{\rho}}_k$ is the smoothed-code multipath which has the same time constant as the filter smoothing time (100 sec for LAAS) and a standard deviation specified in LAAS requirements.

Smoothed-code multipath for each satellite measurement is modeled as a first order GMRP independently. As defined in equation 5.22 above for white receiver noise, there is also a certain correlation between the smoothed-code multipath and carrier multipath due to the smoothing filter process. A conservative approach is to ignore this correlation and treat all multipath states as mutually independent. In principle, system performance predictions are more conservative without modeling the correlation between states. Because of the high variation in multipath properties with different environments,

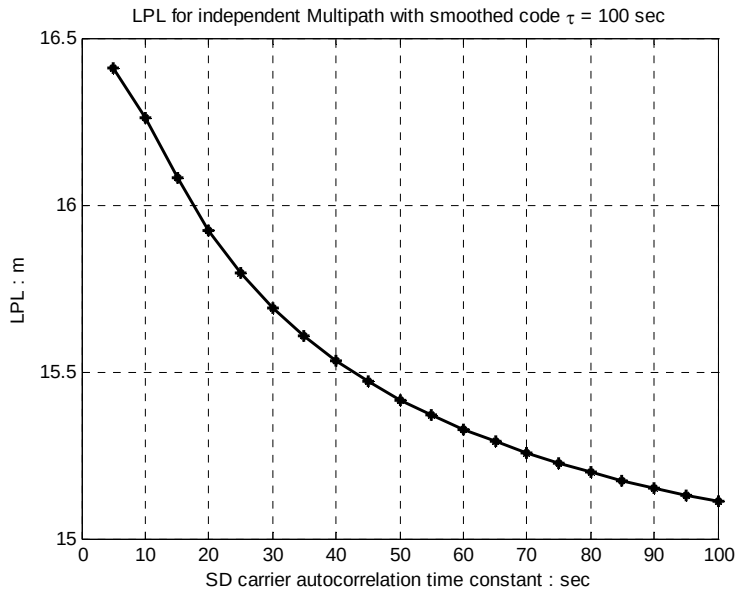

Figure 5.15. Sensitivity of Carrier Multipath Time Constant to Coasting LPL

there is a risk of modeling the correlation incorrectly. Therefore, we will generate the conservative system performance results instead.

The correlation time constant of the first order GMRP model for carrier multipath has to be decided as well. Generally the multipath time constant is a function of the system environment. A sensitivity analysis is performed to understand how the carrier multipath time constant affects coasting performance.

Figure 5.15 shows the results of the sensitivity analysis of the carrier time constant to the coasting LPL at DH by applying CAT III requirements on the IMU model with 5 sec sampling step size. The shorter the time constant is, the worse the coasting LPL becomes. A simple explanation for this result is that the accumulated lateral error from the degraded velocity estimation error is larger than the reduction in position estimation error due to a shorter time constant. To be conservative, a 5 sec carrier multipath time constant is chosen for CAT III availability simulations because the lateral coasting error is the dominant factor.

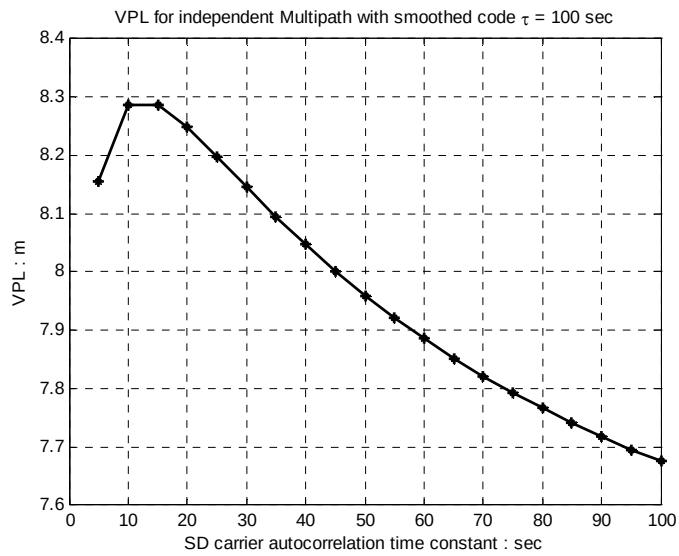

Figure 5.16. Sensitivity of Carrier Multipath Time Constant to Coasting VPL

Results of the sensitivity to VPL are shown in Figure 5.16 with the same scenario. Unlike the simple trend of the LPL line, a worst time constant can be found for the VPL case. Considering the dominant factor for the system coasting performance in CAT I is the vertical coasting error, a 10 second carrier multipath time constant is selected for CAT I availability simulations. In the figure, the vertical positioning error is improved more than the accumulated error from vertical velocity degradation as the time constant approaches zero.

All the system parameters which need to be used in availability analysis have been studied and conservatively selected. Simulated availabilities for LAAS CAT I/III from six selected airports will be displayed in the following two sections.

5.2.2 Availability Simulation for LAAS CAT III Precision Approach and Landing.

LAAS availability usually refers to either long-term service availability or operational availability; the former is a weighed average of the service availability under different assumed states of the satellite constellation, the later mainly considers the impact of long-

term satellite failures on system operation [RTCA/DO245A]. This research is focusing on the feasibility of hybrid navigation system with RFI-robust capability during the final stage of precision approach. Therefore, all the availability analysis is based on the nominal DO-229D full 24 satellites constellation.

Six airports have been chosen to simulate the GPS/INS hybrid navigation system availability for LAAS CAT I/III applications under fault-free assumption with 2×10^{-7} (CAT I) and 1×10^{-9} (CAT III) tolerable integrity risks respectively for this preliminary analysis. The selected airports are New York La Guardia Airport (LGA); Chicago O'Hare Airport (ORD); Miami International Airport (MIA); Dallas/Fort Worth International Airport (DFW); Los Angles International Airport (LAX) and Seattle Boeing Field/King County International Airport (BFI). These airports are picked by geographic distribution with middle to high air traffic volume. Any availability impact relative to the standard LAAS availability on these airports will provide an indication of the insufficiency of the hybrid navigation system.

The required standard deviation of the smoothed code measurement is a function of equipment accuracy designation and satellite elevation angle. Airborne Accuracy Designator B type airborne receiver (AAD B) is used throughout the availability simulation. The standard deviation of the airborne smoothed code for AAD B receiver is specified in [RTCA/DO253B] as:

$$\begin{aligned}
&\sigma_{air}^2(i) = \sigma_{noise}^2 + \sigma_{div}^2 + \sigma(i)_{multipath}^2 \\
&\sigma(i)_{multipath} = 0.13 + 0.53e^{(-\theta_i/10)} \text{ meters} \\
&\sigma_{noise}^2 + \sigma_{div}^2 < 0.15 \text{ meters (using spec. for minimum signal strengh)}
\end{aligned} \tag{5.26}$$

where i is the satellite index, σ_{noise} is the standard deviation of receiver noise, σ_{div} is the

standard deviation of code-carrier divergent error, $\sigma_{multipath}$ is the standard deviation of multipath, θ_i is the elevation angle in degrees.

Receivers at the LGF are assumed to be Ground Accuracy Designator C type receivers. The quantity is assumed to be three (GAD C3, maximum is 4). The standard deviation of the LGF smoothed code for GAD C3 is specified in [FAA-E-2937A] as:

$$\sigma(i)_{pr\_gnd} \leq \sqrt{\frac{(a_0 + a_1 e^{-\theta_i/\theta_0})^2}{M(i)} + a_2{}^2} \tag{5.27}$$

where $M(i)$ is the number of ground receivers and the coefficients a_0, a_1, a_2 are listed in table 5.3.

Because ground and air receiver noise and multipath are independent, the variance for the SD smoothed code is the sum of the variances for air and ground respectively:

$$\sigma(i)^2_{\Delta\bar{\rho}} = \sigma(i)^2_{air} + \sigma(i)^2_{pr\_gnd} \tag{5.28}$$

The SD smoothed code standard deviation from the equation above includes multipath and receiver noise, but it is treated as the standard deviation of SD smoothed code multipath only during availability simulation to simplify the error analysis. Additional receiver noise for SD smoothed code is added as measurement noise according to the derivation from equation 5.24. Therefore, the simulated system performance is conservative in exchange of a simpler simulation model. The sigma of

Table 5.3. Ground Accuracy Designator C Coefficients

Accuracy Designator C	a_0 (meters)	a_1 (meters)	a_2 (meters)	θ_0 (degrees)
$\theta_i \geqq 35^0$	0.15	0.84	0.04	15.5
$\theta_i < 35^0$	0.24	0	0.04	-

the SD carrier multipath is also conservatively yet reasonably chosen as 1 cm for any satellite in view.

The standard deviations of stand-alone raw code and carrier tracking noise magnitudes have been specified at the end of the smoothed code measurement noise analysis in Section 5.2.1 (0.5 and 0.002 meters). However, the SD raw code and carrier sigmas are not computed by multiplying stand-alone raw sigma by the square-root of 2. Equation 5.29 is applied instead due to the averaging process (across multiple reference receivers) on the LGF ground measurements [FAA-E-2937A]:

$$\sigma^2_{\Delta\rho/\Delta\phi} = \sigma^2_{\rho/\phi\_air} + \frac{1}{M(i)}\sigma^2_{\rho/\phi\_gnd} \tag{5.29}$$

Figures 5.17 and 5.18 show the coasting LPL and VPL values at DH over the course of one day with CAT III quality IMU and gravity models at the LGA airport. Availability for this simulation is 100% since no violation of the LAL/VAL requirements for CAT III. The simulation duration is 24 hours with a geometric sampling period of 30

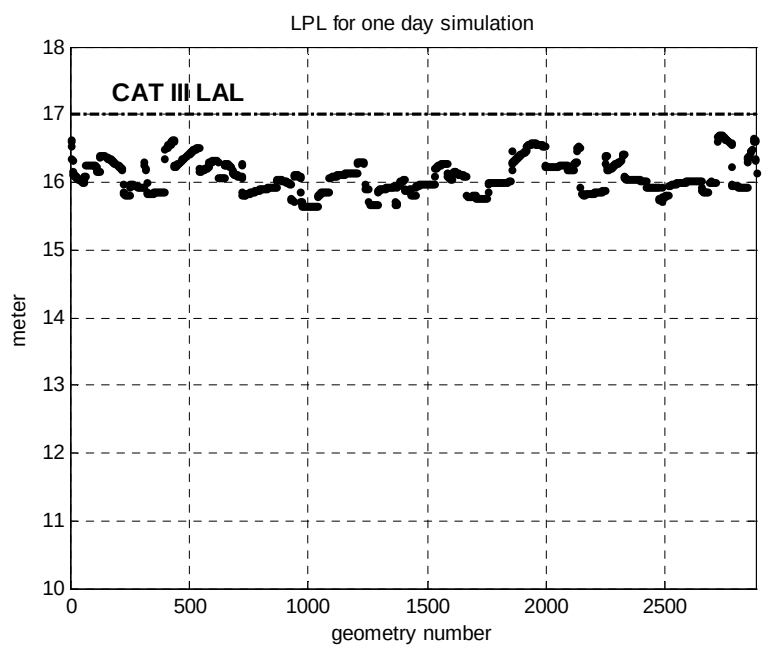

Figure 5.17. Final Coasting LPL at DH for CAT III at LGA Airport

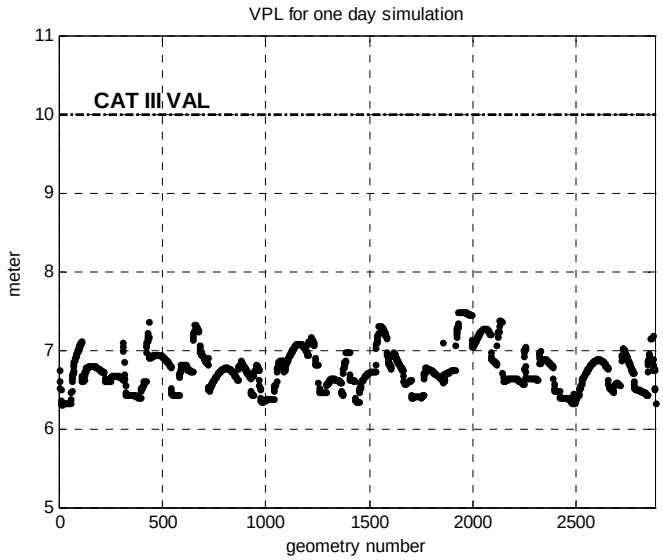

Figure 5.18. Final Coasting VPL at DH for CAT III at LGA Airport

sec. Therefore, in each figure, there are 2880 sample points of coasting position error at DH, which is sufficiently large in terms of satellite geometry change.

Availability simulations at ORD airport are shown in Figure 5.19 and 5.20. 100% availability is reached in this simulation as well. In fact, simulations at all six airports show 100% availability with the full constellation. The results are not surprising because

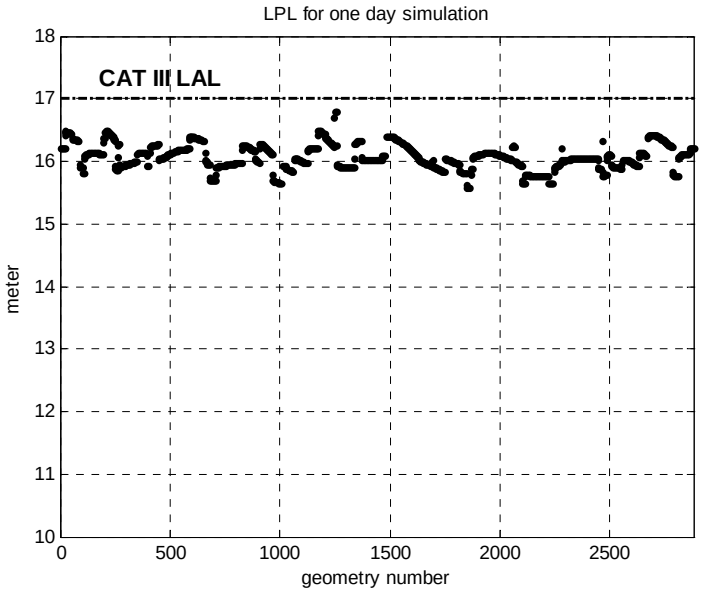

Figure 5.19. Final Coasting LPL at DH for CAT III at ORD Airport

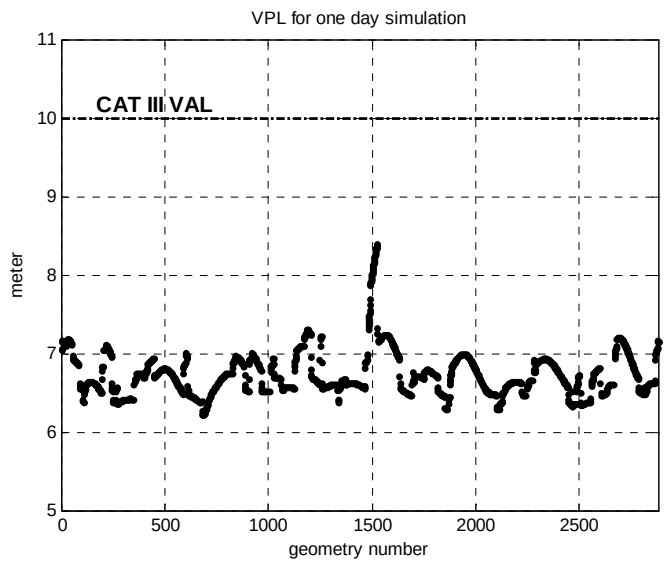

Figure 5.20. Final Coasting VPL at DH for CAT III at ORD Airport

the quality of the IMU and gravity models were considered under a near worst geometry assumption, and with the proper margin to absorb the performance variation due to the system sensitivity to external disturbances. Naturally, depleted GPS constellations may produce lower availabilities.

5.2.3 Availability Simulation for LAAS CAT I Precision Approach and Landing.

The same method and GPS signal quality are applied for availability simulations for CAT I with a 2×10^{-7} tolerable integrity risk at the same six airports, except the IMU and gravity model parameters are adopted from Table 4.4 (previously quantified for CAT I requirements).

Since the vertical error is the dominant factor for CAT I application, only the coasting VPL results for another two airports are displayed. Figure 5.21 is the coasting VPL at DH for BFI airport and Figure 5.22 is for LAX airport. Just like the availability results in CAT III, simulated availabilities for CAT I at all six airports achieve 100% with the full constellation. Furthermore, the derived requirements on IMU quality still have

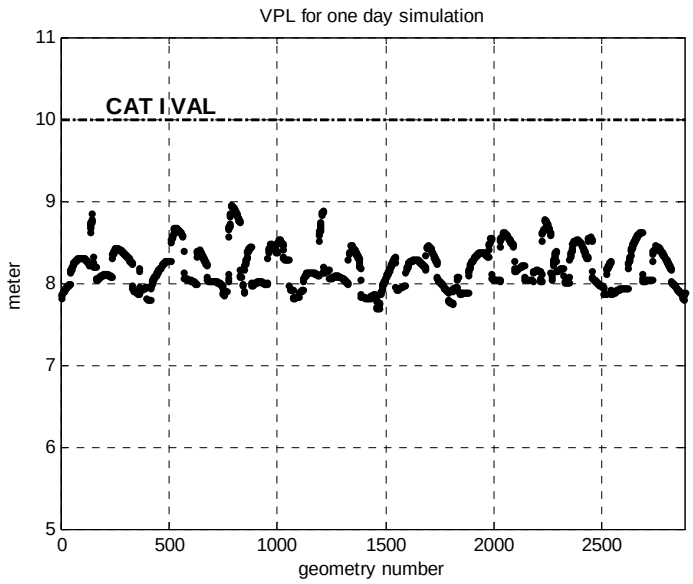

Figure 5.21. Final Coasting VPL at DH for CAT I at BFI Airport

some margin relative to the limit of current inertial sensor technology. Therefore, the system coasting performance can be engineered to meet more stringent requirements, or the same requirements under worse satellite geometries, by upgrading IMU quality to reduce coasting position error. In other words, further performance improvement can be traded at the expense of system cost.

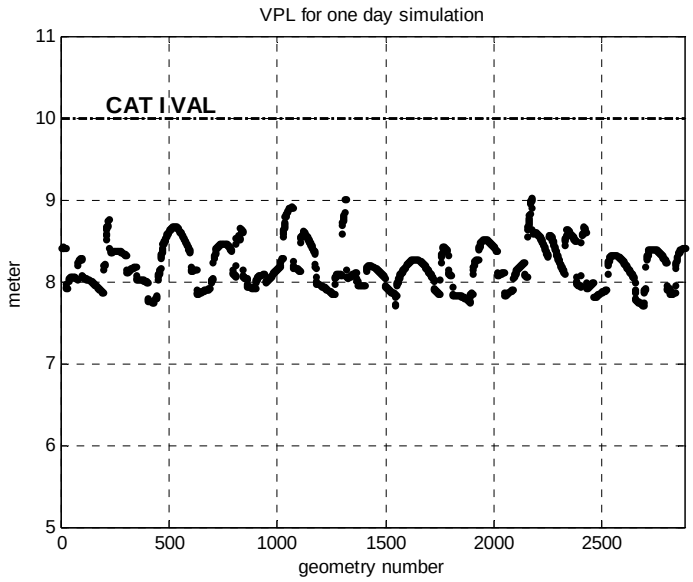

Figure 5.22. Final Coasting VPL at DH for CAT I at LAX Airport

All full constellation availability simulation results are shown in Appendix D. The long term service availability with satellite outage model is not simulated in this research. The main reason is that the driving requirements for the IMU and gravity model quality are not fault-free case. It will be shown in Chapter 6 that better than the fault-free quality IMU and gravity models are necessary to ensure the hybrid system integrity under abnormal GPS signals. Therefore, it has no use to spend enormous computational time to simulate the long term service availability with satellite outage model.

5.3 Comparison of Hybrid Navigation System with Conventional Tightly Coupled GPS/INS and GPS-Only Navigation Systems

The novel GPS/INS hybrid navigation system has a number of advantages over current LAAS GPS-only and conventional tightly coupled GPS/INS navigation systems. The following two sections will try to illuminate the pros and cons of these systems objectively.

5.3.1 Positioning Performance Comparison between Current LAAS GPS-Only and GPS/INS Hybrid Navigation Systems. GPS-only smoothed code positions were generated from flight data to be compared with the GPS/INS hybrid system positions. Superior positioning performance from the hybrid system was expected and it is supported by the results. The position improvement in the hybrid system is primarily due to the additional low-noise carrier-phase measurements. Precise but ambiguous carrier-phase measurements did not only bring down the positioning error, but INS calibration is also made possible because of these measurements.

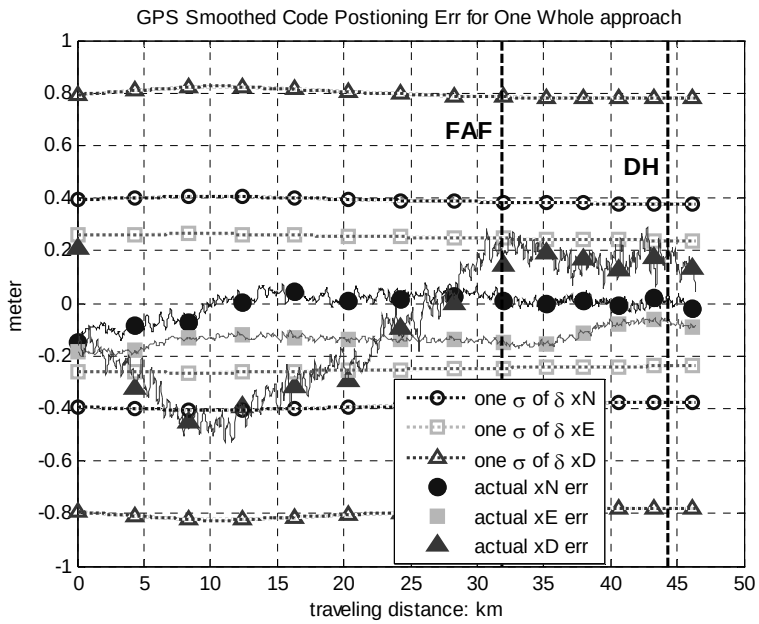

Figure 5.23. GPS-only SD Smoothed Code Positioning Errors

GPS-only smoothed code positioning errors from the third approach fight test data is shown in Figure 5.23 to be compared with Figure 5.24 containing hybrid navigation system positioning errors for the same approach. As anticipated, positioning errors are lower in Figure 5.24 due to the help of additional carrier-phase measurements. The

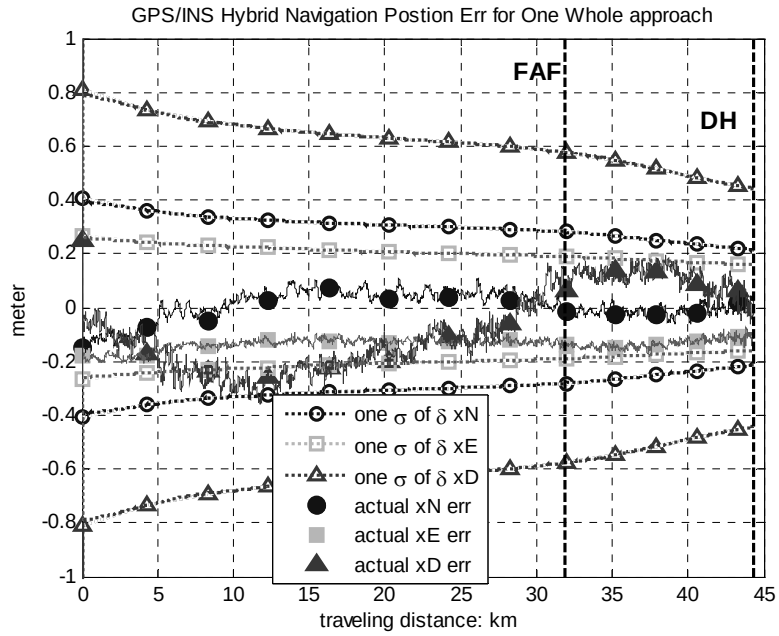

Figure 5.24. Hybrid Navigation System Positioning Errors

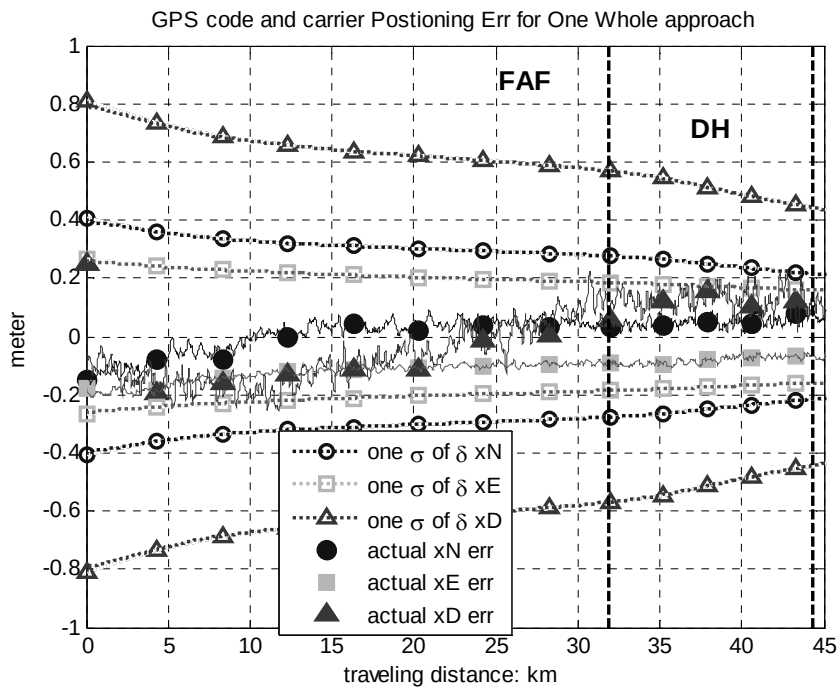

Figure 5.25. GPS-only Positioning Errors with Smoothed Code and Carrier

performance improves with time (distance) travelled because cycle ambiguity estimation continuously improves.

To demonstrate the improvement in positioning errors for the hybrid navigation system is indeed coming from the information provided by the carrier, Figure 5.25 displays the positioning errors by GPS-only with smoothed code and carrier measurements without INS integration, which are the same input measurements for the hybrid system in Figure 5.24. The same level of position error magnitude can be observed in Figures 5.24 and 5.25, although the estimated positions are somewhat different, which is driven by the dynamic information from the IMU. The nearly identical sigma envelopes strongly support the claim. This result also implies that the benefit of GPS/INS integration is not to improve positioning accuracy, but to ensure

continuity in the event that GPS signals are partially or fully blocked or interfered. The threat of GPS signal interference is precisely the motivation of this research.

5.3.2 Mechanization and Advantage Comparison between Conventional Tightly Coupled GPS/INS Systems and the Hybrid Navigation System. INS navigation has a long history, whereas GPS navigation is a fairly new field. Research on tightly coupled GPS with INS, which was inspired by their complimentary properties, has been the subject of a large number of research papers. The mechanizations of conventional tightly coupled GPS/INS systems can be roughly classified into two groups based on the INS calibration schemes: *velocity calibrated* and *range calibrated.*

Velocity calibrated INS uses carrier-phase measurement differences in time to calibrate the INS (mainly the velocity states) [Farrell02] [Moafipoor04]. Generally the position information is obtained from the integration of the calibrated INS velocity over time. A block diagram to illustrate this system scheme is shown in Figure 5.26. The advantage is that the very low noise carrier-phase measurements can be used to estimate

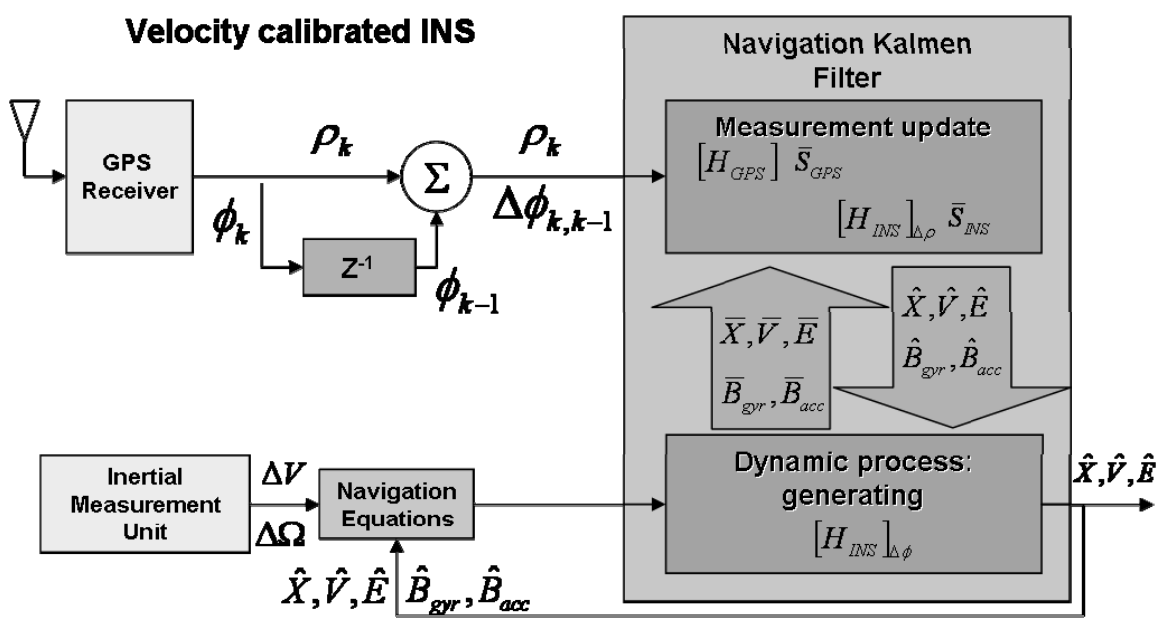

Figure 5.26. System Block Diagram of the Velocity Calibrated INS

the system velocity precisely, with the standard deviation error smaller than 1 cm/sec without the need of solving the cumbersome cycle ambiguity problem. The disadvantages of this approach are very complicated methods to compute the observation matrix for INS calibration and suboptimal use of GPS positioning information. The observation matrix for this calibration scheme has to be generated from the time integration of INS states, which involves matrix inverse operations, in order to get the best performance [Farrell02].

Position information using these methods is normally obtained through the velocity integration from the calibrated INS. If the GPS positioning process were to be combined with the integrated INS position, the correlations between GPS position and INS position as well as the correlations between carrier-phase and time-differential carrier-phase measurements would need to be taken into account carefully, which would further complicate the system. To the author's knowledge, no paper has been published covering this subject. If only code measurements were used for position fusion to avoid correlated carrier measurements, the GPS positioning would not be optimal since the benefit from carrier-phase measurements is lost.

Another minor drawback of the velocity calibrated INS is the need of storing carrier-phase measurement at previous times for time differencing. If either the previous or the current measurement is not available, the corresponding satellite is not available for calibration. This minor drawback might be a significant disadvantage for frequent satellite "in-and-out" scenarios, like an aircraft banking for maneuver or automatic air refueling, in which satellites might be blocked by the fuel tanker aircraft from time to time.

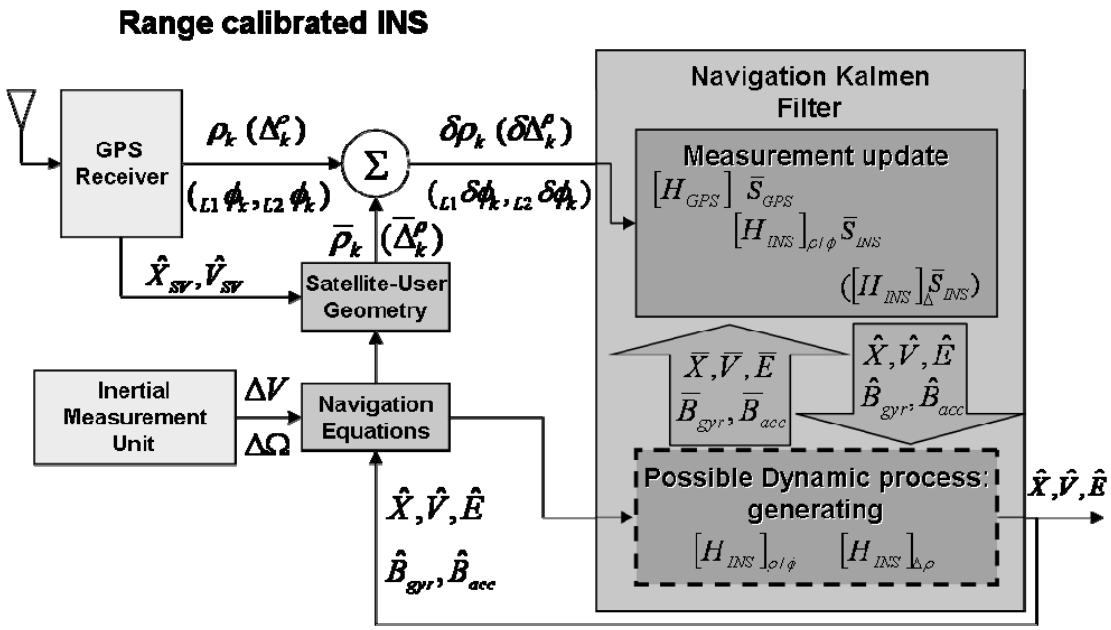

Figure 5.27. System Block Diagram of the Range Calibrated INS

The second group of systems is classified as range calibrated INS, because they use the difference between computed INS range measurements and measured GPS range measurements to calibrate INS errors through a complementary filter [Ko00] [Scherzinger00] [Lee99] [Moafipoor04]. Some systems also include the delta-pseudorange (Δ_k^ρ) measurement comparison [Johnson90]. Figure 5.27 is a general description of this calibration scheme. Like velocity calibrated systems, position information is normally also generated from the integration of the calibrated INS velocity, except that in this scheme the positions are calibrated by GPS measurements. The advantage is the direct and easy access to the observation matrix. The disadvantage is that the INS calibration performance is not exceptional. If high accuracy INS calibration performance is desired, then using low-noise dual frequency carrier-phase measurements to acquire better integer resolution is necessary [Scherzinger00] [Moafipoor04], which impose a great challenge on a single frequency kinematic DGPS system.

This mechanization has the same problems as the previous one when it comes to the positioning process. Correlations among the Kalman filter inputs, the range differences (and the delta-pseudorange differences if applied) are mixed with GPS and INS errors, have to be accounted for properly.

The main advantage of the new GPS/INS hybrid navigation algorithm is that it can calibrate the INS with a method as simple as the range calibrated INS, but also exploit the precise but ambiguous carrier-phase measurements like the velocity calibrated INS implementation without the need of storing previous measurements. GPS and INS positions are completely fused into one set of position states, and the seamless transition from full GPS positioning to free INS coasting only depends on available GPS measurements. An additional advantage is that a carrier cycle-slip detection mechanism is built in; this is achieved by checking the Kalman filter innovations and will be addressed in detail in the next chapter.

One potential negative of the proposed hybrid system is that the centralized state implementation might be too big for certain system computational power to handle. Segmentation of the centralized state matrix by dividing into a number of manageable sub-matrixes is possible. However special attention to the correlation terms is extremely important; it is precisely the accounting for these correlations that enables the Kalman filter to calibrate INS errors properly.

CHAPTER 6

FAULT DETECTION FOR TIGHTLY COUPLED GPS/INS HYBRID NAVIGATIION SYSTEM

Given that precision approach is the primary application for the proposed GPS/INS hybrid navigation system, the system integrity needs to be ensured to meet the service requirements. Integrity is a measure of the assurance that the information is safely provided by a navigation system. Navigation system errors greater than the alert limit without being detected or with detection times greater than the required time to alert are considered Hazardous Misleading Information (HMI) which is unsafe for a CAT I approach and catastrophic for CAT III.

The fault-free hybrid navigation system integrity has been evaluated through the coasting performance simulations with the IMU and gravity models quantified in section 5.2. To maintain the system integrity under abnormal circumstances, one or more fault detection algorithms are necessary. The objective is to detect the erroneous GPS signals which may lead to hazardous misleading information to the hybrid navigation system. Reference receiver faults are already monitored by the LAAS architecture and, therefore, will not be considered here.

The LAAS system design is meant to replace the current ILS for precision approach. The system integrity requirements adopted from ILS will be introduced in the next section along with the integrity monitoring functions.

Possible error sources which might affect in-flight calibration of the GPS/INS hybrid navigation system and how they impact the coasting performance are analyzed. A new detection algorithm which can protect the system integrity from a great variety of threats is proposed. The detection performance of the proposed detection algorithm

along with other popular detection methods are simulated and compared. In the end, the hybrid navigation system is demonstrated to meet the LAAS CAT I/III integrity requirements and an example of the fault detection availability is presented.

6.1 LAAS System Integrity Introduction

LAAS system integrity basically inherits system requirements from ILS. The total system level integrity is allocated into the airborne subsystem and SIS integrity requirements. While the LAAS airborne subsystem integrity remains the same as ILS airborne subsystem, the LAAS SIS integrity is adopted from the requirements and recommendations for ILS in ICAO Annex 10 with the consideration that error sources for LAAS SIS are different from ILS. The methodology of allocating the integrity requirements for LAAS SIS is described in the following section.

6.1.1 Integrity Allocation for LAAS SIS. The total SIS integrity requirement for LAAS CAT I is 2×10^{-7} for any 150 second period during a precision approach. 25% of the total integrity risk is allocated to fault-free (H_0) and single reference receiver fault (H_1) conditions. The rest of the integrity risk is allocated to failures other than H_0 and H_1 (designated as H_2 in this research).

The way to ensure the integrity of H_0 and H_1 hypotheses is to compute the protection levels from the assumed error-free airborne subsystem according to the allocated integrity risk, which is 5×10^{-8} for CAT I, and compare them with predefined alert limit values. As long as computed protection levels are smaller than the alert limits, the integrity under H_0 and H_1 assumptions is secured.

Other failures which are not covered by H_0 and H_1 comprise 75% of the total SIS integrity risk, which is 1.5×10^{-7} for CAT I. LAAS Ground Facility (LGF) is responsible for running a number of integrity monitoring functions to detect potential signal failures. The probability of undetected misleading information for each failure type has to be smaller than the corresponding tolerable integrity risk. The details of the integrity allocations to different error sources can be found in the specification of CAT I LAAS Ground Facility [FAA-E-2937A].

For LAAS CAT III precision approach, a complete integrity allocation has not been fully established yet. Allowable integrity risk for SIS is currently 1×10^{-9} for the vertical error in any 15 second period and for the lateral error in any 30 seconds. The proposed GPS/INS hybrid navigation system follows the LAAS integrity risk analysis methodology.

6.1.2 Integrity Monitoring for LAAS CAT I. GPS system failures categorized in H_2 are supposed to be protected by LGF integrity monitors. A number of ground monitoring functions are required to monitor the ranging signals, ground broadcasting corrections and anomalous atmosphere errors to keep H_2 integrity risks within the requirements. A brief introduction to various threats to the LAAS user, which are monitored by the LGF, is presented in the following:

<u>Signal deformation</u>: A satellite payload failure can cause a deformation of the GPS signal. Such a deformation on broadcasted GPS signals may induce correlation peak distortion in GPS receivers and cause range measurement errors.

Ephemeris error: An ephemeris failure which results in a computed satellite position error that is orthogonal to the line-of-sight vector will cause an effective differential ranging error between LGF and aircraft.

Code and carrier divergence (CCD) error: Carrier smoothed pseudorange measurements are used at both LGF and aircraft; different aircraft and ground filter responses to CCD would cause an effective differential ranging error.

Excessive pseudorange acceleration threat: The pseudorange changing rate is included in the broadcast correction message to compensate for the delay in range correction. A step or abnormal rapid change on ranging measurement is a failure to the system integrity.

VHF Data Broadcast (VDB) monitor: Ensures that all broadcasting correction messages are not corrupted before airborne reception.

Anomalous ionosphere threat: Abnormal ionospheric activities have been observed in the past. These rarely occurring activities are threats to the LAAS system because they can cause enormous navigation system errors due to the large spatial decorrelation between LGF and aircraft.

A complete list of the system failures and the corresponding course of actions to be implemented at the LGF for CAT I service can be found in the LGF specifications [FAA-E-2937A] Table 3-1. Nevertheless, the lack of monitoring on carrier-phase measurements in current LAAS architecture has made the LGF integrity monitoring functions insufficient to ensure the hybrid navigation system integrity.

6.2 Possible Measurement Errors Affecting In-flight INS Calibration and System Impacts

All possible threats to the LAAS system safety have been considered, and the FAA provides guidelines to address these concerns by system design, analysis and monitoring. However, the fundamental difference in the system architecture between the proposed GPS/INS hybrid navigation system and current LAAS system has made the LGF integrity monitors insufficient to protect the hybrid system from all possible threats. One obvious deficiency is that no current LGF monitor is working specifically on protecting carrier-phase measurements since these measurements (LAAS message Type 6) are not currently broadcast. The system integrity of the carrier-phase measurement users will be in danger if the message Type 6 is implemented without any monitoring. Furthermore, the hybrid navigation system has the capability of estimating atmosphere states. However, since the delay models are based on the normal atmospheric activity, the hybrid system architecture simultaneously opens a door to the possibility of incorrect state estimation in the event of abnormal atmosphere activity.

In WAAS MOPS Appendix R [RTCA/DO229D], the assumptions, requirements and verification procedures for equipment that utilizes tightly coupled GPS/INS integration for en route through approach phases of flight are provided. It is a good source for the system design for similar non-precision applications, such as Lateral NAVigation (LNAV). However, for more demanding applications such as LAAS precision approach, the integrity requirements are much stricter than those in WAAS MOPS Appendix R.

Therefore, a comprehensive research is needed to study the new hybrid navigation system integrity in terms of INS calibration error and resulting coasting position error. In

response, possible threats that can affect in-flight INS calibration and the state estimations need to be explored. Fault detection algorithms responding to the possible threats are studied in the next section. In this research, the potential treats having high likelihood to cause decorrelation errors between ground and air, which include ionospheric storms, strong tropospheric activities and receiver cycle slips, are the focus. All the simulations are done by applying the most stringent CAT III requirements and the IMU and gravity models quantified for CAT III in Table 4.3 unless noted otherwise.

6.2.1 Ionospheric Error and the Impact on System State Estimation. A standard ionosphere model has been soundly established and is applicable to normal ionospheric activities [Misra01]. LAAS users, or similar DGPS users, will experience ionospheric delays less than 2 cm for one sigma when aircraft reaches the decision height (DH) location with the normal 2 to 5 mm/km ionospheric spatial decorrelation.

However, very large ionosphere temporal and spatial gradients have been observed in CONUS during ionosphere storms on April 6-7 in 2000, October 29-30 and November 20 in 2003. Figure 6.1 provides a simple illustration of an ionospheric storm's

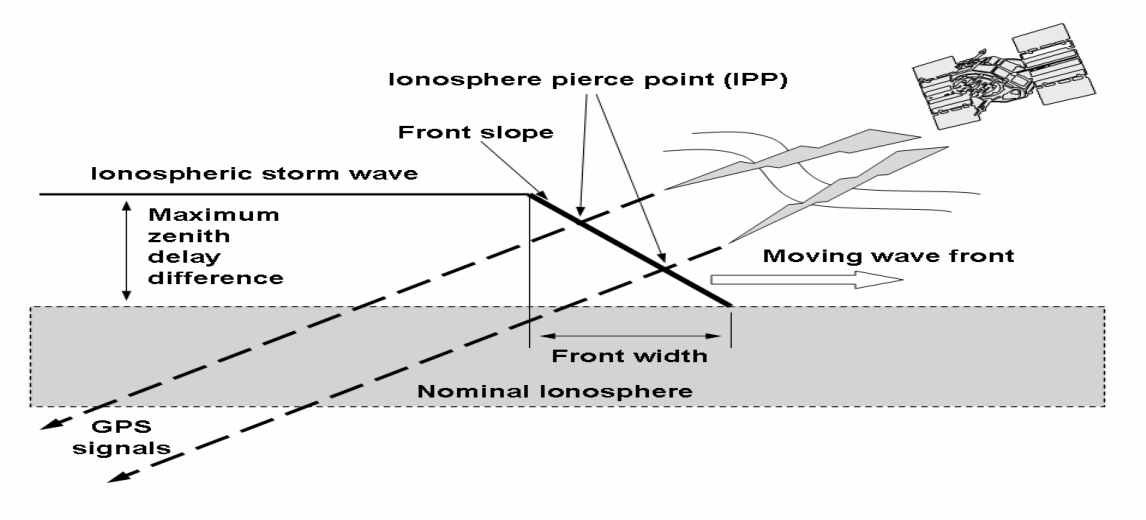

Figure 6.1. Ionosphere Strom Model

moving wave front. During the storms, the spatial gradients of ionospheric vertical delays were estimated up to several hundreds of mm per kilometer. Most of the observed spatial gradients moved rapidly at several hundreds of meters per second with respect to the Earth surface. But in a few cases, the gradients appeared to remain stationary or near stationary for a certain time. For fast moving gradients (ionospheric storm fronts), the LAAS LGF CCD monitor can detect and send out an alarm for affected satellite to aircraft users. The most problematic storm fronts are those that are nearly stationary with respect to the Earth's surface. The worst scenario is that the GPS measurements received by the LGF have not been affected while aircraft's measurements are already corrupted by the storm front. Some efforts have been made to detect the abnormal storm fronts that are most threatening to LAAS airborne users [Gratton06] [Lee06]. However, those efforts focused on detecting ionospheric errors which affected positioning when aircraft are close to DH point. No analysis has been done to understand the impact on INS calibration when aircraft are still far away, especially on the velocity estimation.

The simulated impact on the hybrid navigation system from the ionospheric storm will focus on the slow-moving storm front which is hard to detect at the LGF. Based on the ionospheric threat space derived from the observations from WAAS and National Geodetic Survey Continuously Operation Reference Stations (NGS-CORS or just CORS)

Table 6.1. Ionospheric Storm Threat Space Parameters

Slow-Moving Ionospheric Storm Front Parameters				
	Speed	Width	*VIG* (Vertical Iono Gradient)	Max. Err.
Slow-Moving Front	0~90 m/sec	25~200 km	30~125 mm/km	25 meter
Equivalent Static Front	0 m/sec	11~inf. km	5~275 mm/km	25 meter

up to date [Luo04], the threat space parameters are displayed in Table 6.1.

The front velocity parameter in the derived threat space (first row in Table 6.1) can be eliminated by converting the observed ionospheric delays of a moving front during an approach equivalent to that of a static front. The bottom row in Table 6.1 shows the converted parameters. Basically, an equivalent static wave front is a stretched or squeezed version of a moving wave front depended on the relative motion.

Possible SD zenith errors caused by LGF-undetectable ionosphere storms are simulated and sampled as shown in Figure 6.2. All simulated front end before the physical distance between LGF and aircraft user antennas is zero (condition for undetectability at the LGF). Constant error is possible if the distance between two receivers' ionosphere pierce points (IPP) is larger than the front width during an approach. Four *VIG* values (5, 50, 150 and maximum 275 mm/km) are sampled for various front

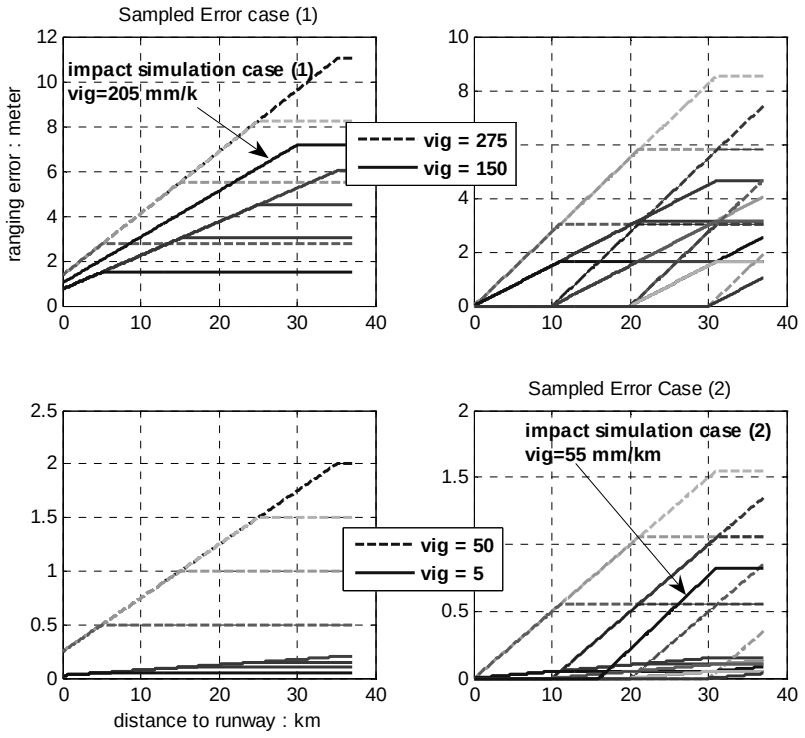

Figure 6.2. Simulated Ionosphere Storm Zenith Error Examples

widths and shown in the figure. SD slant delays were simulated by using LAAS ionospheric decorrelation model (equation 2.18) and the static threat space parameters in Table 6.1. The *VIG* value was sampled at 10 mm/km increment and the front width was sample at 2 km increment. The wave front starting and ending locations were also varied at 4 and 5 km increments respectively.

The technique of simulating the impact on the system is to feed in the hybrid system's Kalman filter with all zero measurements except the corresponding satellite measurements affected by ionosphere storm, which has the simulated SD slant ranging errors as the measurements. The Kalman filter will distribute the simulated erroneous measurements to the estimated states with different weighting according to the filter gains. The resulting deterministic errors in the estimated states reflect the impact on the state estimations from the ionosphere storm.

Figures 6.3 and 6.4 show the system impact from the simulated ionosphere storm

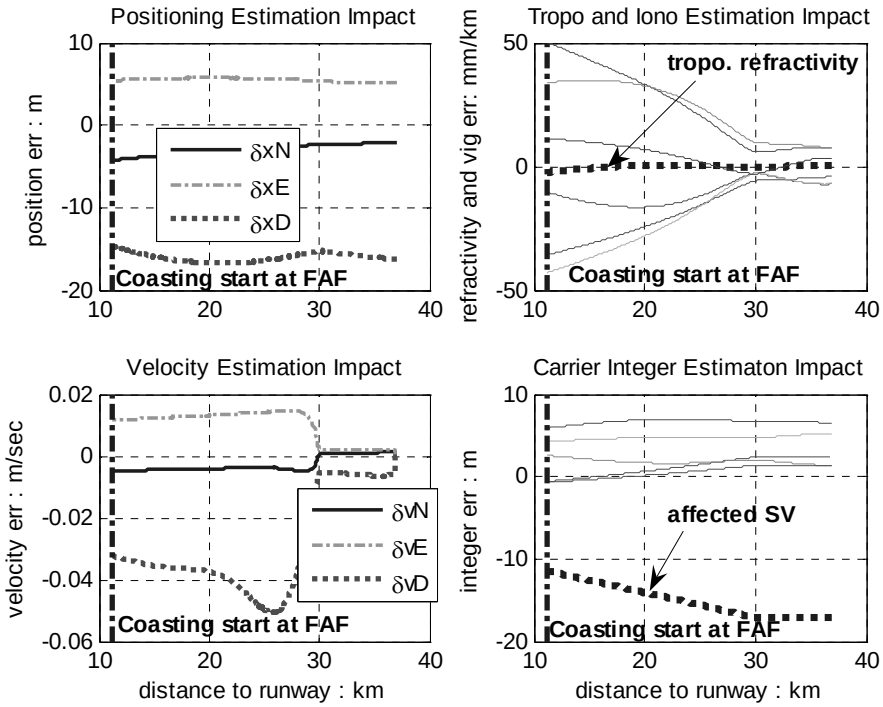

Figure 6.3. System Impact Due to Ionosphere Storm (1)

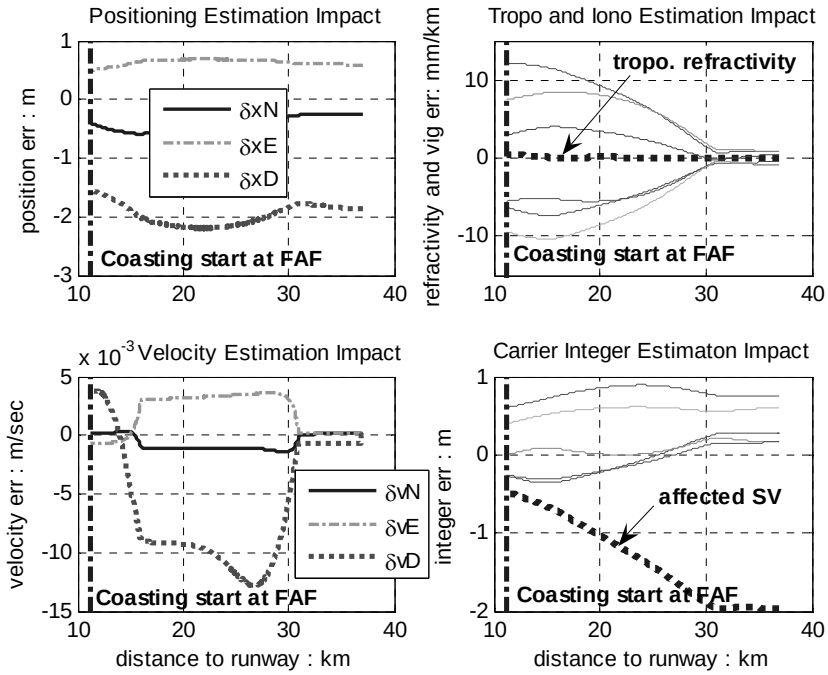

Figure 6.4. System Impact Due to Ionosphere Storm (2)

error cases (1) and (2) in Figure 6.2. These figures serve as qualitative descriptions of how the system is affected by different ionosphere storm scenarios. Because the hybrid navigation system is a complicated filter, it is difficult to be analyzed analytically. Therefore, a quantitative simulation approach is adopted to simulate the responses of detection algorithms to the studied threats in Section 6.3. Even though Figures 6.3 and 6.4 are only illustrative examples, some insightful information can still be observed:

- Velocity estimation will be affected most if the error is ramp-like; the size of the velocity estimation error is proportional to the magnitude of the ramp (which is equivalent to the vertical ionospheric gradient).
- Bias-like measurement errors impact the GPS states significantly; positioning errors will sustain even after the measurement error disappears due to the already corrupted GPS states.

Although the simulated errors were only applied to the measurements from one affected satellite, the Kalman filter (because the covariance information was modeled under the normal condition) recognized the errors as the result of system motion and distributed the errors into all estimated states.

6.2.2 Tropospheric Error and the Impact on System State Estimation. Nominal tropospheric decorrelation has been taken into account in LAAS measurement error models. However, rare severe weather conditions (weather storms), which may cause tropospheric decorrelation 10 times larger than normal, need to be considered as well [Huang06][Lawrence06].

SD ranging errors due to weather storms are seriously considered based on the observed tropospheric errors across short baselines [Huang06]. Figure 6.5 presents the worst SD slant ranging errors ever observed up to date due to severe troposphere activity.

The difficulty of modeling a severe weather condition comes from the nature of this phenomenon, which is normally a strong thermal activity in a small range. This

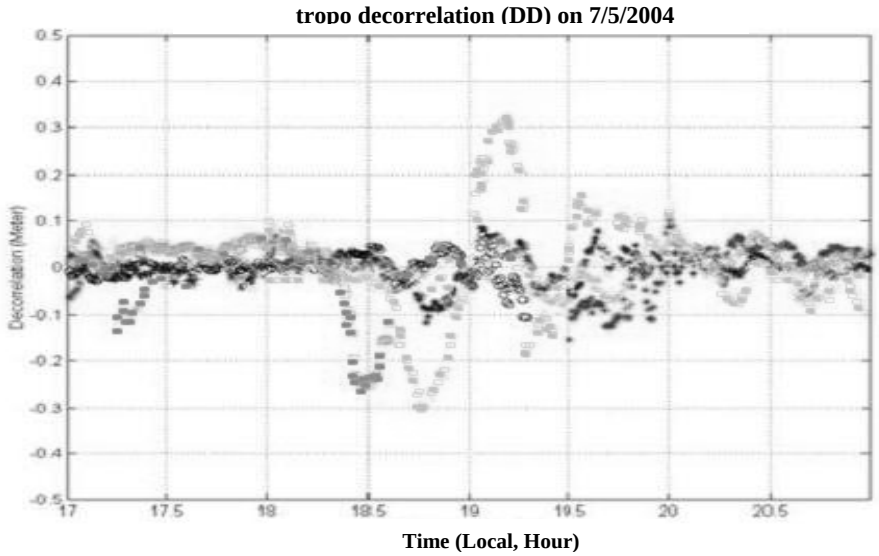

Figure 6.5. Worst Observed SD Tropospheric Decorrelations Over a Short Baseline Courtesy of Ohio Univ. [Huang06]

property makes the vapor distribution become inconsistent and unpredictable within a weather storm. What complicates things more is that different parameters of a weather storm model may result in similar errors in the SD GPS ranging signal. Therefore, analyzing the possible SD ranging errors based on the observed data is the adopted approach to avoid the complexity of weather storm modeling.

From the worst ever-observed SD tropospheric errors in Figure 6.5 and recorded errors in other papers [Gregorius98] [Lawrence06], three types of possible SD zenith ranging errors are assumed; type one and type two are symmetric and asymmetric triangular shapes, type three is the combinations of ramp and bias-like errors which have no triangular resemblance. The maximum zenith decorrelation slope is conservatively assumed as 0.5/16 m/km, which is derived by using the observed peak slant error 0.4 m as zenith delay and taking 10 m/sec storm moving speed (approximate average speed) into account. The maximum zenith delay is also conservatively assumed as 0.5 m. Figures 6.6 through 6.8 are the sampled examples of the three types of SD zenith ranging error patterns.

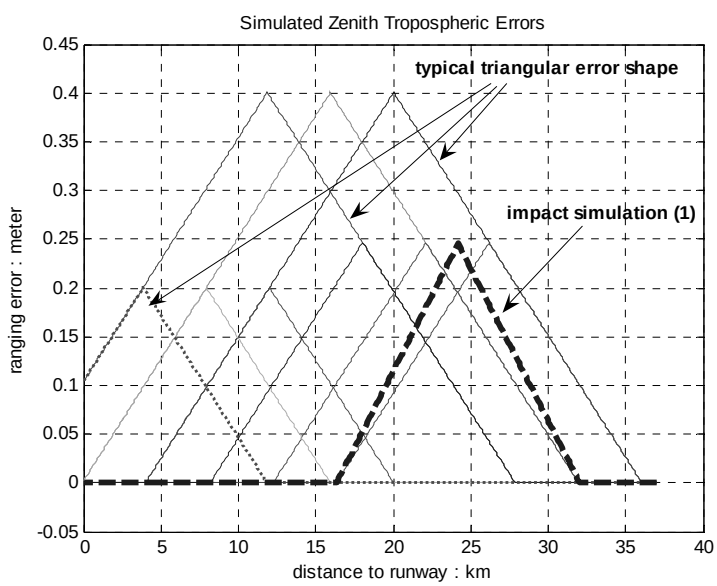

Figure 6.6. Type One Troposphere Storm SD Ranging Errors

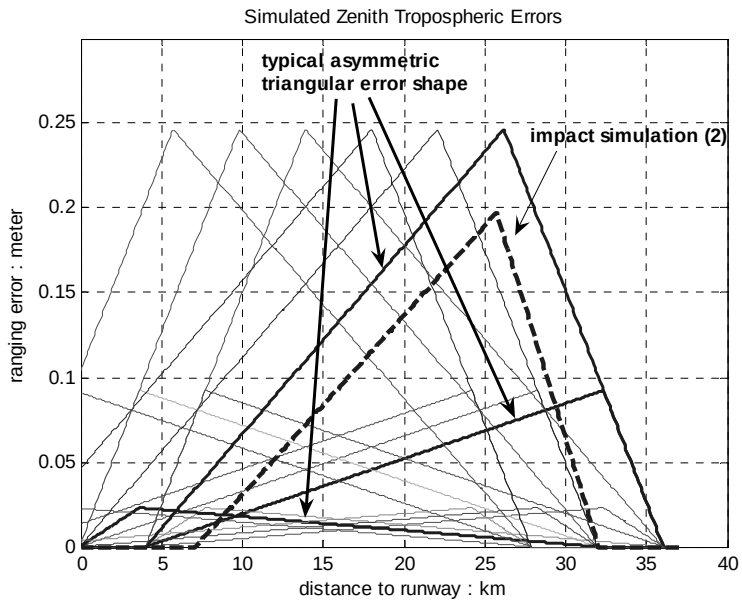

Figure 6.7. Type Two Troposphere Storm Ranging Errors

The simulations of the system impact from the troposphere storm were processed in the same manner as the ionosphere storm impact simulations. Three SD tropospheric zenith ranging error examples selected in Figures 6.6 through 6.8 were simulated to observe the influence on the system. The assumption on the number of affected satellite from a troposphere storm is different from the ionospheric case. A troposphere storm

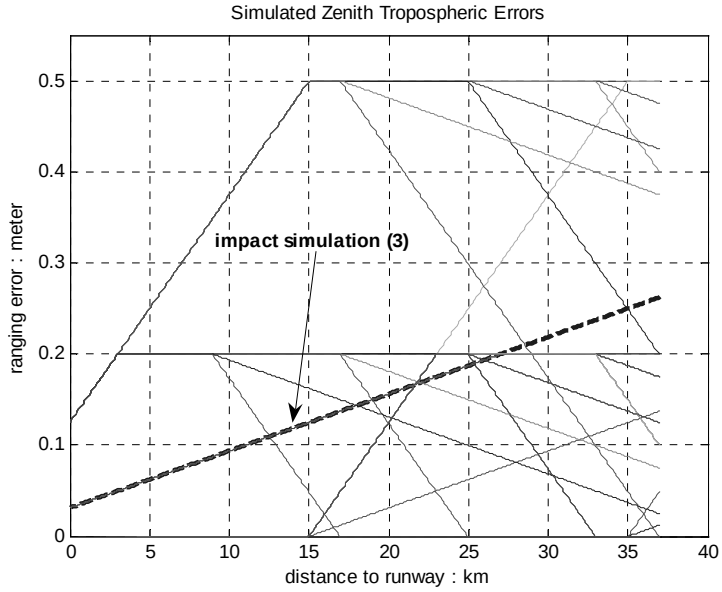

Figure 6.8. Type Three Troposphere Storm SD Ranging Errors

may affect more than one satellite in view while an ionosphere storm has one satellite involved only. Based on the observed data, it is not unreasonable to assume that the maximum affected satellite number for a troposphere storm can be up to half of the satellites in view.

Figures 6.9 through 6.12 present the impact on the hybrid system state estimations while various strong tropospheric decorrelations exist in one or more satellite measurements. One major concern about the simulated tropospheric errors is that they are only based on the observation data, which does not cover other unrecorded error cases. This concern is addressed by the following reasoning: unobserved weather conditions which cause more severe tropospheric errors have lower likelihood of occurrence. In addition, any detection algorithm which can protect the hybrid system from current simulated troposphere storms will also detect larger troposphere induced SD errors. The larger troposphere induced SD errors will generally cause bigger position errors. From the system integrity point of view, the integrity is secure as long as the detection

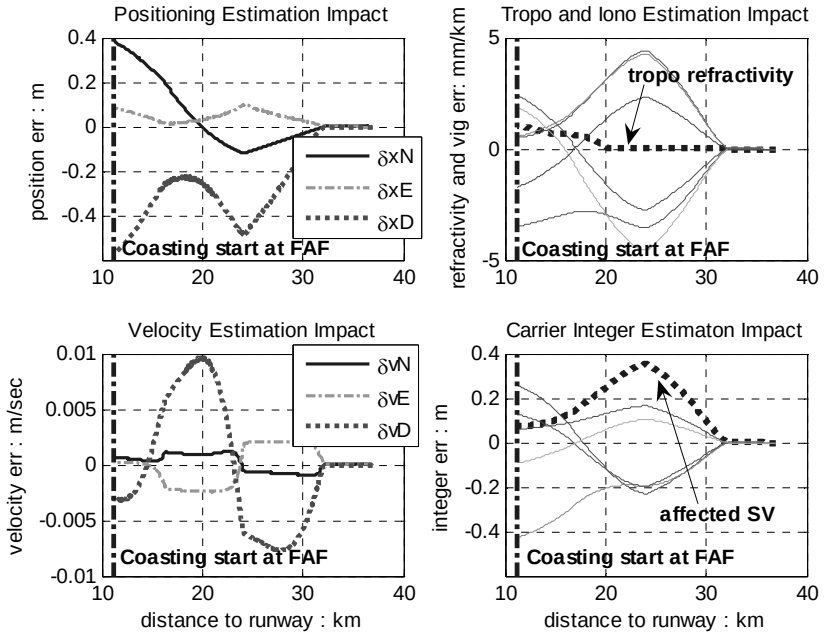

Figure 6.9. System Impacts Due to Troposphere Storm (1) with One SV Affected

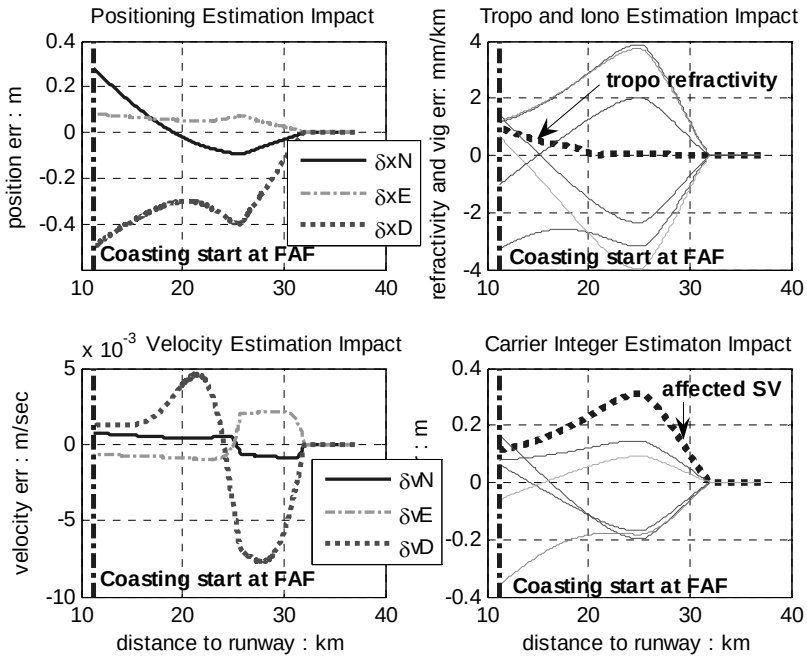

Figure 6.10. System Impacts Due to Troposphere Storm (2) with One SV Affected

mechanism can detect them (then, the detected threat would become a continuity issue). The same logic can apply to the ionosphere storm threats as well.

The system impact on the in-flight calibration differs among simulated

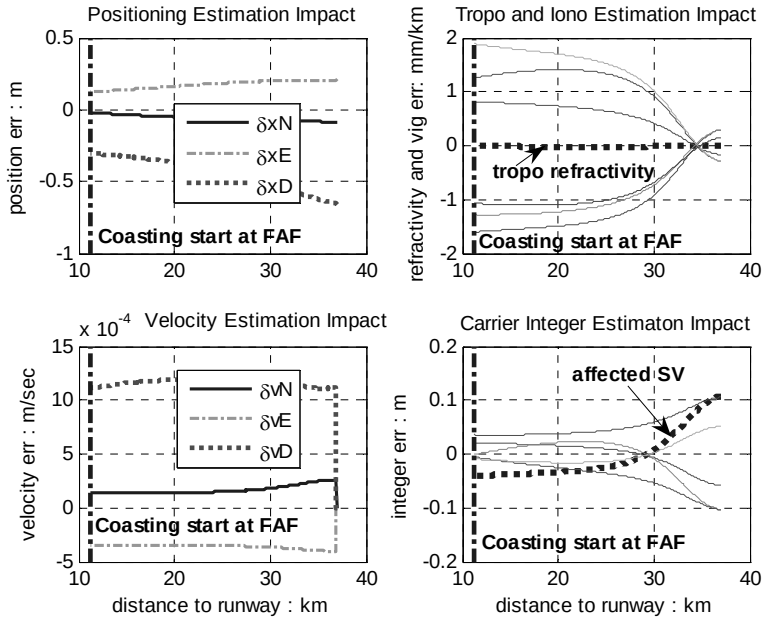

Figure 6.11. System Impacts Due to Troposphere Storm (3) with One SV Affected

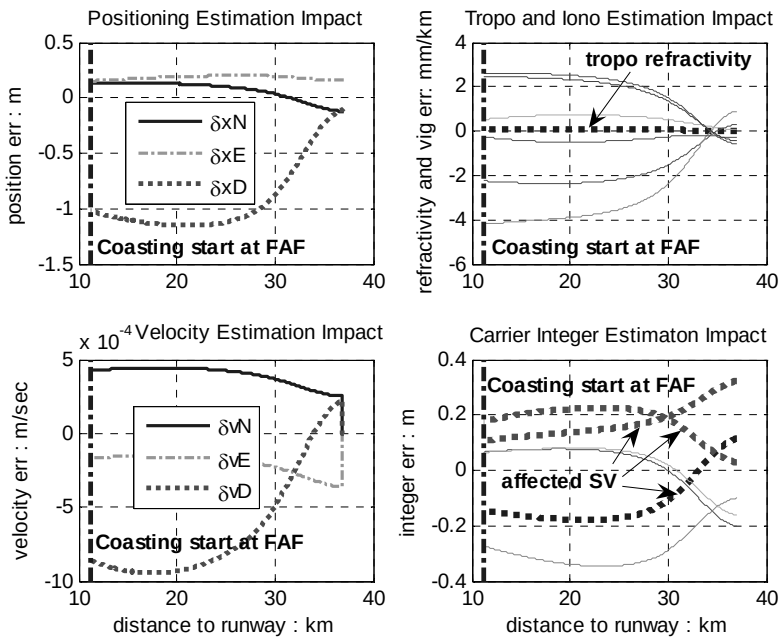

Figure 6.12. System Impacts Due to Troposphere Storm (3) with Three SVs Affected

tropospheric storm cases very much, not only because of the faster variation on SD ranging errors, but also the difference on the affected satellite number. Analogous to ionosphere storms, the velocity estimation error mainly responds to ramp-like ranging errors, whereas position estimation errors are dominated by bias-like ranging errors. In all sampled cases, the estimation errors are smaller than ionospheric storm cases due to the smaller SD measurement errors from the troposphere storms.

The tropospheric refractivity state which had small responses in the ionosphere storm cases starts to react in Figures 6.9 and 6.10. Because the simulated anomalous tropospheric SD ranging errors did not fit the nominal (simple gradient) ionospheric error model, the tropospheric state estimation errors started to increase when the aircraft began to descend, which resulted a better observation on the tropospheric delay due to altitude change. Nevertheless, the ranging errors in the simulation case three have a great

resemblance to the ionospheric error signature (a simple slope); this explains the flat response of the tropospheric refractivity state in this case.

6.2.3 Receiver Cycle Slip and the Impact on System State Estimation. Cycle slips cannot be ignored by any system utilizing carrier-phase measurements, especially high integrity systems such as the proposed hybrid navigation system. Half cycle and one whole cycle slips happening in the middle of an in-flight calibration were simulated, and the impact on the system is shown in Figures 6.13 and 6.14. Only one cycle slip is assumed to occur on one channel during an approach. For avionic grade GPS receivers, this assumption is reasonable and achievable. High end receivers usually have internal cycle slip screening mechanism; however there is no reliable requirement in this regard.

Two cases of cycle slip mentioned above were simulated on the same channel and at the same occurring time for easy comparison. The magnitudes of the system impact in the full cycle slip case are twice of that in the half cycle slip case. If a half cycle slip is

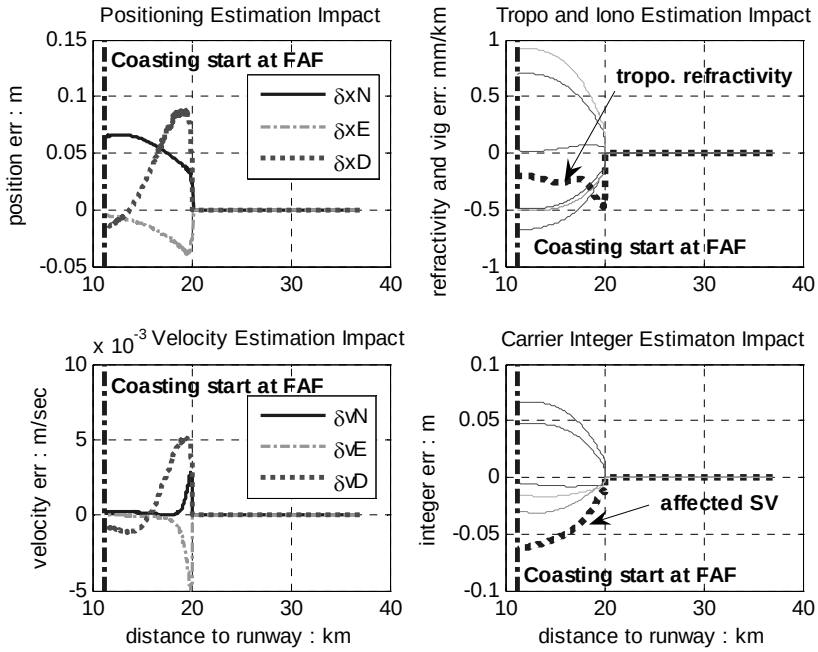

Figure 6.13. System Impacts Due to Half Cycle Slip on One Receiver Channel

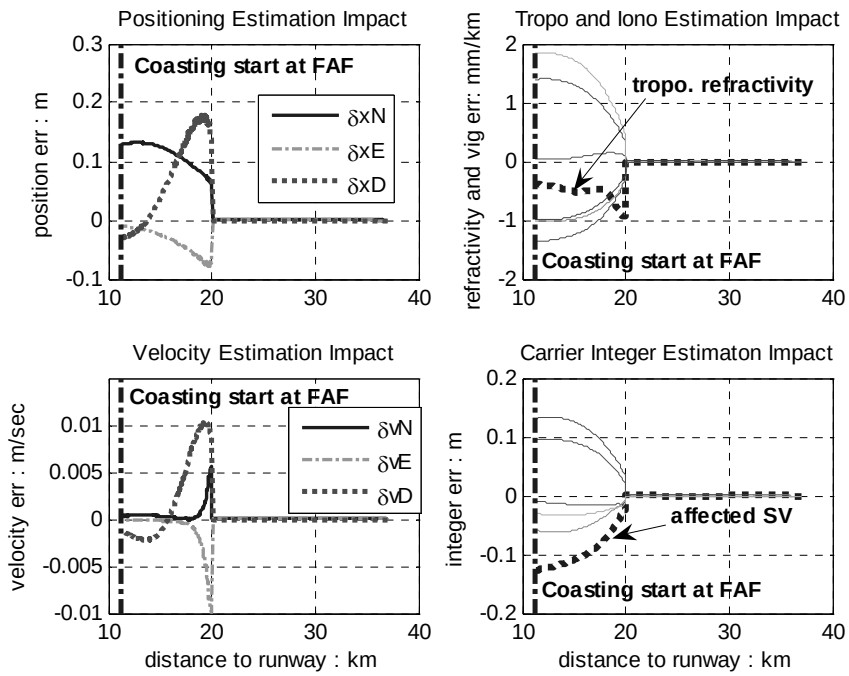

Figure 6.14. System Impacts Due to a Whole Cycle Slip on One Receiver Channel

detectable by any detection algorithm without considering any other factor (such as prior probability, probabilities of final coasting errors exceeding alert limits), so is a full cycle slip and other cycle slip cases with magnitudes larger than one cycle.

6.3 GPS/INS Hybrid Navigation System Integrity Protection.

The analysis above has shown that the GPS/INS navigation system would be affected significantly when abnormal GPS measurement errors occur during the in-flight calibration process. Moreover, incorrectly estimated states would keep generating corrupted position outputs even after the measurement errors are gone. In response, one or more detection algorithms are needed to detect potential threats which would otherwise breach the system integrity.

Since an analytical method to examine the impact on the hybrid system estimation errors from GPS measurement errors is almost impossible to be found, numerical

simulation is resorted to evaluate the detection performance of fault detection algorithms. For a complex navigation filter, it would be idealistic to expect a single perfect detection algorithm can capture all threats. Therefore, a number of well known detection algorithms and a new proposed detection method are analyzed, and the detection performance of these algorithms is simulated and compared.

6.3.1 Fault Detection Algorithm and Test Statistic. Four detection algorithms which are recommended in WAAS MOPS Appendix R and suitable for LAAS high integrity applications are investigated. Additionally a high integrity radar altimeter detection method for the system integrity protection is analyzed. A new detection scheme, innovation integration fault detection, is also proposed and the detection performance is simulated and compared with the others. The detection algorithms can be divided according to the time of applicability: early stage detection and coasting stage detection. An early stage detection indicates a detection mechanism working in the region before FAF point, while a coasting stage detection is the opposite. Five detection algorithms belong to the early stage detection; only the radar altimeter detection method is coasting stage detection method. The six detection algorithms and test statistics are introduced below:

RAIM detection: For GPS navigation systems, the Receiver Autonomous Integrity Monitoring (RAIM) method is widely considered as one very effective way to detect measurement errors when the redundant satellite measurements are available. RAIM-based fault detection is based on checking the consistency of redundant GPS measurements. There are a number of different ways to implement RAIM related detection methods [Brown88] [Brown92]. The most direct implementation is the norm of

the least squares residual vector, which is employed here as one detection mechanism. A general linear observation equation is considered below:

$$z = (H - \delta H)x + v \tag{6.1}$$

where z is the $n \times 1$ measurement vector; H and δH are the observation matrix and its error matrix; x is the $m \times 1$ state vector intended to be estimated ($n>m$) and v is the $n \times 1$ measurement error vector.

Under normal conditions, δH is small and negligible; and v is Gaussian and i.i.d. with zero mean and standard deviation σ. The i.i.d case RAIM residual derivation can be found in related books or papers [Pervan96a] [Heo04]. In the situation where the measurement errors are correlated (non-i.i.d.) with a covariance matrix W, a decorrelation process can be applied by using a 'whitening' matrix $W^{-1/2}$. The weighed residual vector r^w can be derived as:

$$r^w = W^{-1/2}(I - HH^{w+})(v - \delta Hx) \text{, where } H^{w+} \equiv (H^T W^{-1} H) H^T W^{-1} \tag{6.2}$$

Now the weighed residual vector can be treated as i.i.d. and Gaussian with $\sigma = 1$. The magnitude of the residual vector $\|r^w\|$ is used as the indicator of possible system failure. Under fault free conditions, the squared magnitude of the weighted residual vector is a chi-square distribution random variable with n-m (n measurements with m states and $n>m$) Degrees Of Freedom (DOF) [Pervan96a]:

$$\|r^w\|^2 \sim \chi^2(n-m) \tag{6.3}$$

In this research, a SD smoothed code RAIM algorithm is implemented. The normal measurement errors include tropospheric and ionospheric spatial decorrelations

and multipath. The SD smoothed code measurements, the observation matrix and measurement covariance can be expressed as:

$$z_{\Delta\bar{\rho}} = \Delta\bar{\rho} = -H\vec{x} + \Delta\tau_{clk} + \varepsilon_{\bar{\rho}}, \text{ where } \varepsilon_{\bar{\rho}} = \Delta M_p^{\bar{\rho}} + \Delta v_{\bar{\rho}} + \Delta T + \Delta I$$

$$H = \begin{bmatrix} -\vec{e} & 1 \\ \vdots & \vdots \end{bmatrix}_{n\times 2}, \; W_{\Delta\bar{\rho}} = E[\varepsilon_{\bar{\rho}}\varepsilon_{\bar{\rho}}^T] \tag{6.4}$$

The standard deviations of ΔT and ΔI are the same as the nominal assumptions in Section 4.1, and the standard deviations of smoothed code multipath $\Delta M_p^{\bar{\rho}}$ and receiver tracking noise $\Delta v_{\bar{\rho}}$ follow the analysis in Section 5.2.

<u>*Carrier-phase Relative RAIM detection*</u>: Carrier-phase measurements are precise but ambiguous in terms of the number of cycles. A time difference between two sequential carrier-phase measurements will eliminate the cycle ambiguity problem. Thus the time differential carrier can be used to extract precise position information relative to a starting point. The information provided by the time differential carrier is essentially equivalent to what a high quality inertial system delivers in a short time. This is also the implicit mechanism which enables the in-flight INS calibration in the proposed hybrid navigation system. The implementation in equation 6.5 is very much like general RAIM, except the additional measurement difference in time:

$$z_{\Delta^2\phi}^k = \Delta\phi_k - \Delta\phi_0 - (\vec{e}_0 - \vec{e}_k)\cdot\hat{x}_0 = -\vec{e}_k\cdot\Delta\vec{x}_k + \Delta^2\tau_{clk} + \Delta\varepsilon_k^{\phi}$$

$$\text{where } \Delta x_k = x_k - x_0, \; \varepsilon_k^{\phi} = \Delta^2 m_p^k + \Delta^2 v_{\phi}^k + \Delta^2 T_k - \Delta^2 I_k + (\vec{e}_0 - \vec{e}_k)\cdot\delta\hat{x}_0 \tag{6.5}$$

$$H = \begin{bmatrix} -\vec{e}_k & 1 \\ \vdots & \vdots \end{bmatrix}_{n\times 2}, \; W_{\Delta^2\phi} = E[\Delta\varepsilon_k^{\phi}\Delta\varepsilon_k^{\phi T}]$$

With time sequence involved in the process, the notation k is used here to clarify the sequence in time. The standard deviations of SD carrier-phase multipath Δm_p and receiver tracking noise Δv_ϕ also follow the analysis in Section 5.2. The Any double difference operation on the measurements, Δ^2, indicates one difference between the ground and air receivers and another difference in time. In the top equation in equation set 6.5, Δx_k is the relative carrier-phase position at time k with respect to the starting point x_0. The term $(\vec{e}_0 - \vec{e}_k) \cdot \hat{x}_0$ is present to compensate for the satellite line-of-sight vector change during the time difference interval.

<u>*Carrier-phase Relative RAIM detection with free-INS coasting augmentation*</u>: Since the time differential carrier-phase measurement conveys the similar information provided by INS, augmenting a carrier-phase relative RAIM with free-INS coasting positions can include INS information within the RAIM consistency check. The idea is to capture any inconsistency between the relative carrier-phase measurements and INS coasting positions. The implementing equations are listed below:

$$z_{aug}^k = \begin{bmatrix} z_{\Delta^2\phi}^k \\ \Delta x_{INS}^k \end{bmatrix}, H = \begin{bmatrix} -\vec{e}_k & 1 \\ \vdots & \vdots \\ I & 0 \end{bmatrix}_{(n+3)\times 4}, W_{aug} = \begin{bmatrix} W_{\Delta^2\phi} & 0 \\ 0 & P_{\Delta xINS} \end{bmatrix} \tag{6.6}$$

where Δx_{INS}^k is the free-INS coasting position at time k relative to the starting point x_0 and $P_{\Delta xINS}$ is the coasting position covariance.

<u>*Innovation detection*</u>: Innovations are the measurement residuals in a Kalman filter resulting from the removal of the predictable part in the measurements before updating the state estimates. In principle, a measurement error which is not consistent

with the prediction from the system dynamics will generate a bigger than expected residual magnitude. It is very sensitive to an abrupt or step change in the measurements. The general form of an innovation vector r_{Inn} and its covariance are shown as:

$$r_{Inn} = z - H\overline{x}\,,\ P_{Inn} = W_z + H\overline{P}_x H^T \tag{6.7}$$

Under normal conditions, the un-predicted part in measurements should behave like white noise. The innovation vector is similar to the RAIM residual vector in that the squared magnitude of the normalized innovation vector, $\left\| r_{Inno} \right\|_{norm}^2$, is a chi-square random variable with *n* DOF (when *n* measurements are available). The implementation is expressed as:

$$\left\| r_{Inno} \right\|_{norm}^2 = r_{Inn}^T P_{Inn}^{-1} r_{Inn}\text{, and } \left\| r_{Inn} \right\|_{norm}^2 \sim \chi^2(n) \tag{6.8}$$

Generating an innovation vector is a process naturally embedded in the Kalman filter right before doing a measurement update. Therefore, this detection can be executed very easily by tapping out the innovation vector from the Kalman filter. Considering the lack of monitoring on the carrier-phase measurement in current LAAS system configuration and very small noise in carrier, the carrier-phase innovation is a good candidate for fault detection. Therefore, it is investigated in this research.

Innovation Integration detection: Innovation detection has been used as a way to check for system failures before, but it has no shown promise in detecting slow growing errors. To overcome this drawback, the integration of innovation as a failure indicator is proposed as a new detection algorithm for the GPS/INS hybrid navigation system. Although innovation detection has been considered in other work, to the author's

knowledge, the innovation integration detection has not been seen in any navigation research.

One of the difficulties for any effective detection scheme using an integration or averaging discriminator is that the individual test statistic has to be strictly bounded by the statistical assumption, which is "Gaussian" in our case. The integrated innovation test statistics for the hybrid navigation system satisfy the requirement because the innovation vector is very effectively "white" due to the unique system architecture and quality INS information. The equation for the test statistic, $T_S(k)$, of the innovation integration mechanism is expressed below:

$$T_S(k) \equiv \sum_{i=1}^{k} \left\| r_{Inno} \right\|_{norm}^2 (i) \text{, and } T_S(k) \sim \chi^2 (\sum_{i=1}^{k} n_i) \tag{6.9}$$

The DOF of the innovation integration is an accumulated DOF of each snap shot innovations, n_i. Compared with an averaging method, which normally has the same effectiveness in detection, integration is much easier to implement when satellites are lost or new ones are acquired.

Radar Altimeter detection: Modern commercial airliners are generally equipped with quality radar altimeters. For aircraft with the capability to fulfill critical CAT III requirements, triple redundant radar altimeters are typically installed to provide fault tolerance for continuous operation. For CAT I/II non-critical approaches, the radar altimeter is usually used to provide information for pilots to determine the decision height (DH). Since radar altimeters are widely available on commercial airliners to provide direct measurements at Above Ground Level (AGL) heights and capable of meeting the critical CAT III requirements by redundant installations, they are explored in this

research as another means to detect the integrity threats to the hybrid navigation system at the DH location.

The nominal measurement accuracy model is adopted from Honeywell HG8505DA01 radar altimeter [Campbell01] with slight adjustment:

$$\sigma_{al}\ (\text{ft}) = (1 + 0.01 \times h_{AGL}) / 1.955 \tag{6.10}$$

where σ_{al} is the standard deviation of radar measurement error, h_{AGL} is the true height above ground level and 1.955 is the 95 % accuracy multiplier. The adjustment is made by reducing a 3 ft minimum one-sigma accuracy to 1 ft.

Another factor which affects the radar altimeter detection performance is the accuracy of the Digital Elevation Model (DEM). Currently, NIMA's (now NGA) Digital Terrain Elevation Data (DTED) is the most widely used DEM available to civil applications. DTED level one (level one to five, level one has the lowest resolution but widest coverage) has the coverage of 65% earth's land mass, and +/- 30 meter 90% vertical accuracy with approximate 100 meter grid spacing. NASA has an on-going Shuttle Radar Topography Mission (SRTM) collecting data with 1 meter 50% vertical accuracy at 4 meter grid spacing. Although the accuracies of these DEMs cannot meet the requirements for high integrity applications like LAAS precision approach, they have shown the potential for more accurate global DEM.

In contrast to a worldwide DEM, only a local elevation profile underneath the flight path is needed for the radar altimeter detection at the DH. With recent developments in laser altimeter technology, commercial instruments integrated with airborne radar altimeter/INS/GPS can generate a local DEM with standard deviation of 15 cm absolute vertical error and 5 cm relative vertical error at 1 meter grid spacing or

less [Flood99]. The 15 cm sigma of nominal local DEM error, σ_{DEM} , is used in the radar detection simulation. With the assumption that all errors are zero mean and Gaussian, the test statistic is implemented as:

$$T_S(DH)_{radar} = [z_{radar}(DH) - h_{INS}(DH)] / \sqrt{\sigma_{al}^2 + \sigma_{DEM}^2 + \sigma_{h\_ins}^2} \tag{6.11}$$

where $z_{radar}(DH)$ is the radar measurement at the DH location, $h_{INS}(DH)$ is the coasting vertical position at DH and σ_{h_ins} is the associated vertical sigma.

Airborne laser mapping can be the solution for high-accuracy and high-density elevation data to meet the high integrity radar detection requirements. At the same time, it has speed and cost-effectiveness advantages over traditional survey methods.

6.3.2 Detection Threshold Setting and Missed Detection Probability. All detection algorithms specified previously have to meet the continuity requirements after an approach has been initialed. Two types of test statistics are implemented for fault detection: the radar detection test statistic is a normally distributed random variable; the other five test statistics are chi-square distributed random variables. The general methods to setup the detection thresholds (T_H) with *n* available measurements and *m* estimated states for the chi-square detection and Gaussian (normal) detection schemes are discussed, and the missed detection probability for each method is derived as well.

<u>*Chi-square detection*</u>: For the general chi-square random variable in equation 6.3, a false alarm (*FA*) probability under normal error conditions (*NC*) can be derived as:

$$P(FA \mid NC) = P(\left\| r^w \right\|^2 > T_H \mid NC) = \frac{1}{2^{n-m}\Gamma((n-m)/2)} \int_{T_H}^{\infty} s^{\frac{n-m}{2}-1} e^{-\frac{s}{2}} ds \tag{6.12}$$

where the integration is the *incomplete gamma function*, and *P(FA|NC)* is defined by the system continuity requirement:

$$P(FA \mid NC) \leq 1 - contiuity\ risk \tag{6.13}$$

In the event that the coasting position error, δx_c, exceeds a predefined protection radius, *a*, but the test statistic remains below the threshold, a missed detection (*MD*) has occurred. Thus the probability of missed detection can be defined as:

$$P(MD) = P(\left\| r^w \right\|^2 < T_H, \left\| \delta x_c \right\| > a) \tag{6.14}$$

The system integrity risk due to a hazardous event (*HE*), given the occurrence probability of the event *P(HE)*, is computed as:

$$Integrity\ risk = P(MD)P(HE) \tag{6.15}$$

The derivations for the detection threshold and the probability of missed detection can be applied to general chi-square detection schemes. Nevertheless, it will be easier for the fault detection implementations to express the missed detection probability specifically to the LAAS final coasting application. The probability of missed detection in Equation 6.15 can be re-expressed as:

$$P(MD) = \max[P(\left\| r^w \right\|^2 < T_H, \left| \delta x_{c\_lat} \right| > LAL), P(\left\| r^w \right\|^2 < T_H, \left| \delta x_{c\_ver} \right| > VAL)] \tag{6.16}$$

where δx_{c_lat} and δx_{c_ver} are the lateral and vertical coasting errors respectively.

<u>*Gaussian detection*</u>: Only the radar detection test statistic is applicable, and a false alarm (*FA*) probability under normal error conditions (*NC*) can be derived as:

$$P(FA \mid NC) = P(\left| T_S \right| > T_H \mid NC) = \frac{2}{\sqrt{2\pi}} \int_{T_H}^{\infty} e^{-\frac{s^2}{2}} ds \tag{6.17}$$

The probability of missed detection is derived similarly to equation 6.16:

$$P(MD) = \max[P(|T_S| < T_H\ ,\ |\delta x_{c\_lat}| > LAL)\ ,\ P(|T_S| < T_H\ ,\ |\delta x_{c\_ver}| > VAL)] \qquad (6.18)$$

Note that equations 6.13 and 6.15 are applicable to general Gaussian detections as well.

Because the new proposed innovation integration detection algorithm has not yet been tested in any prior research, a Monte Carlo simulation of 1000 aircraft approaches under normal error conditions was performed to validate the underlying assumption on the test statistic. The results are shown in Figure 6.15.

For each individual detection algorithm, the probability of no alarm (*NA*) to one simulated threat at epoch *k* is computed as follows:

$$P(NA)_k = P(|T_S| < T_H \mid b_{Ts}(k)) \qquad (6.19)$$

where a series of detection responses, $[b_{Ts}(1), \cdots, b_{Ts}(k)]$, to the feed-in-measurement threat are obtained from the detection algorithm output during an approach. The coasting lateral and vertical position error biases, $[b_L, b_V]$, due to the threat and the corresponding standard deviations, $[\sigma_L, \sigma_V]$, are obtained at DH. The probability of the vertical

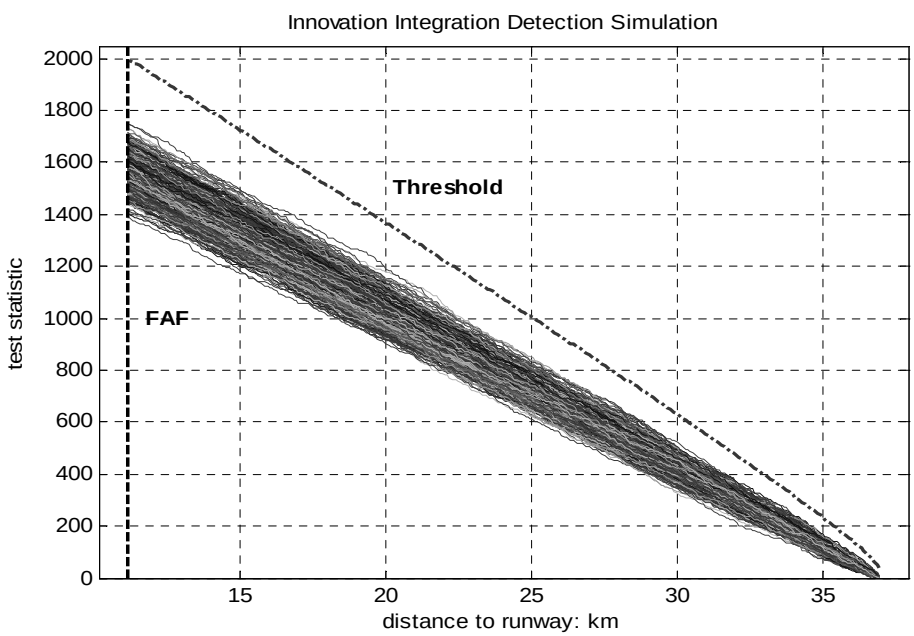

Figure 6.15. A Thousand Times Monte Carlo Simulation of Innovation Integration Test

coasting error at DH, $Err_V(DH)$, exceeds VAL can be computed by equation 6.20:

$$\begin{aligned} b_V \geq 0, P(Err_V(DH) > VAL) &= \frac{1}{\sqrt{2\pi}\sigma_V}\left(\int_{-\infty}^{-(VAL+b_V)} e^{-\frac{(s-b_V)^2}{2\sigma_V^2}} ds + \int_{|VAL-b_V|}^{\infty} e^{-\frac{(s-b_V)^2}{2\sigma_V^2}} ds \right) \\ b_V < 0, P(Err_V(DH) > VAL) &= \frac{1}{\sqrt{2\pi}\sigma_V}\left(\int_{-\infty}^{-|VAL+b_V|} e^{-\frac{(s-b_V)^2}{2\sigma_V^2}} ds + \int_{VAL-b_V}^{\infty} e^{-\frac{(s-b_V)^2}{2\sigma_V^2}} ds \right) \end{aligned} \tag{6.20}$$

The probability of the lateral coasting error at DH, $Err_L(DH)$, exceeds LAL can be computed by substituting (b_V, σ_V) with (b_L, σ_L) in the above equations.

After generating the probabilities of NC and the probabilities of coasting position errors exceeding alert limits during one approach, the probability of missed detection from equation 6.18 for each individual detection algorithm and for a particular threat is evaluated by:

$$\begin{aligned} P(MD) = &\min[P(NA)_1, P(NA)_2 \cdots P(NA)_k \cdots] \\ &\times \max[P(Err_V(DH) > VAL), P(Err_L(DH) > LAL)] \end{aligned} \tag{6.21}$$

The probability of missed detection for each detection method is computed from equation 6.21 (which is taking the smallest no-alarm probability during the detection algorithm active period and multiplied by the probability of coasting errors exceeding alert limits at DH). The prior probability of hazardous event occurrence is treated as a parameter in the analysis, because quantifying the fundamental probability of ionosphere and troposphere storms is still in progress.

6.3.3 Detection Performance on Ionosphere Storm. The simulation method for the detection performance follows the technique for the impact simulation described in section 6.2.1. The response of the test statistic to the simulated error is the bias in the Gaussian detection scheme and the non-centrality parameter in the chi-square detection.

The detection performance was simulated for one approach at ORD airport using the DO-229D full constellation, and the starting time was the same as the worst geometry in Figure 5.20 in order to ensure conservative coasting performance.

The detection performance is evaluated here in terms of the "HMI number" which is the total number of simulated threats that have generated integrity risks from equation 6.15 greater than the required integrity risk:

$$HMI \equiv \{P(MD) \times P(HE) > \text{ requriedintegrityrisk}\} \tag{6.22}$$

The prior probability of event occurrence is treated as a parameter in the analysis. The results of ionosphere storm detection performance are displayed in Figure 6.16 with the six fault detection algorithms working together at three prior probabilities values: 10^{-3}, 10^{-4}, 10^{-5}. Even if the threats occur at a low probability (10^{-5}), some remain as HMI events. The method to address the concern for remaining HMI will be discussed in Section 6.4.

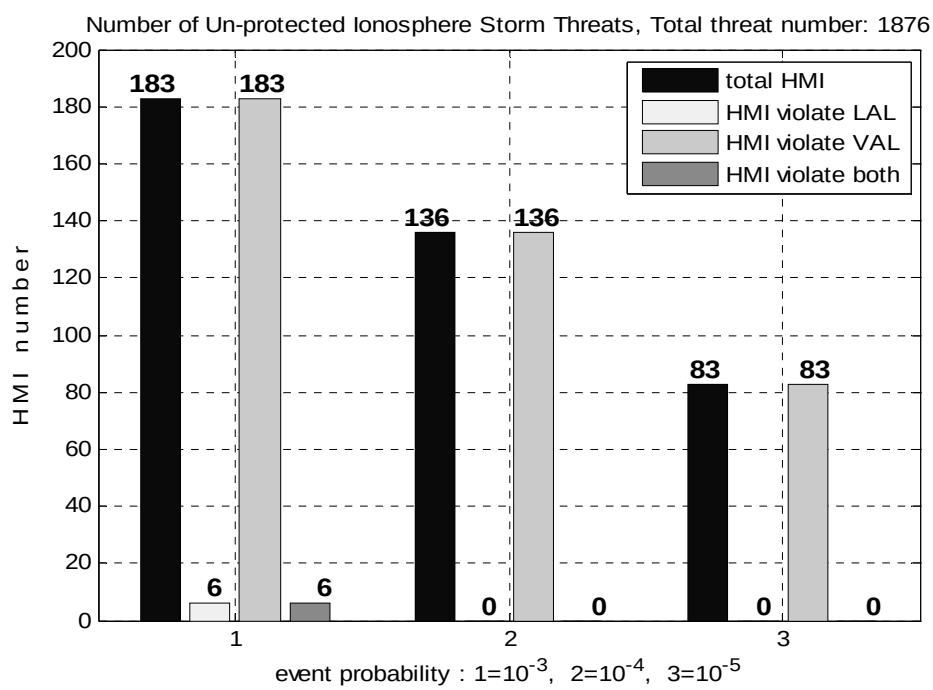

Figure 6.16. CAT III Detection Performance under Ionosphere Storm Threats

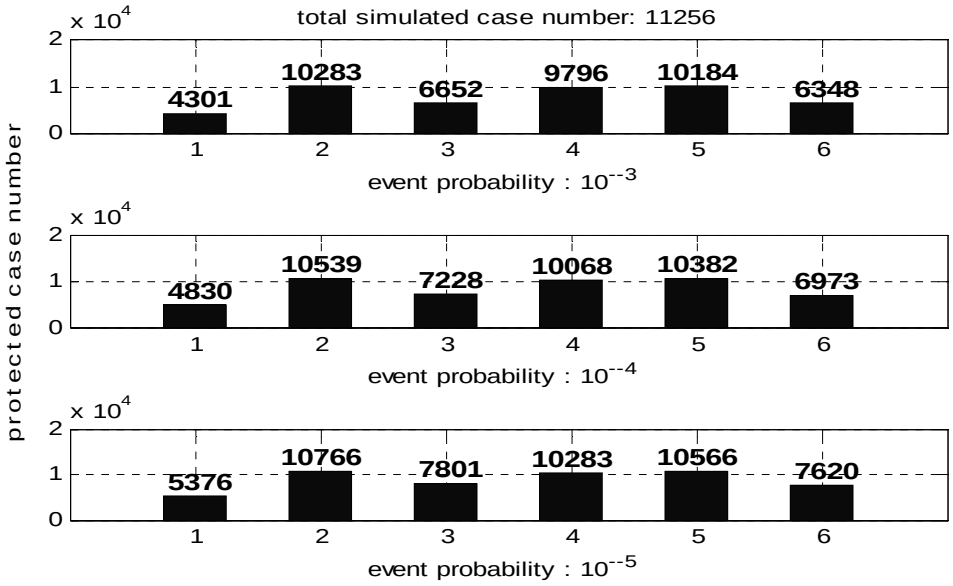

Figure 6.17. Individual Detection Performance under Ionosphere Storm Threats

Detection performance comparisons among six detection algorithms are shown in Figures 6.17, 6.18. The numbers on the *x* axis represent different detection methods; 1: innovation detection; 2: innovation integration detection; 3: smoothed code RAIM

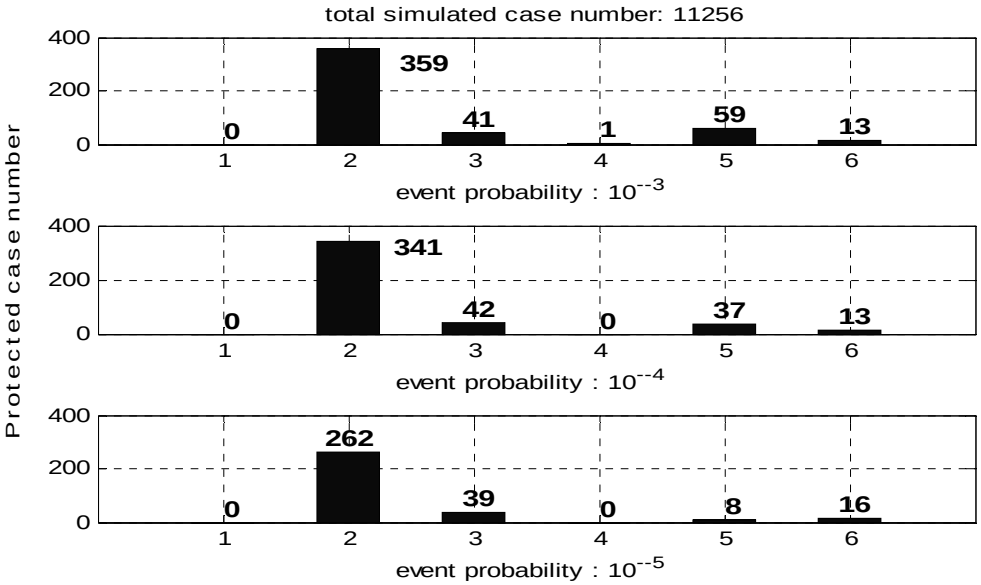

Figure 6.18. Number of Ionosphere Storm Threats Detectable by A Single Algorithm

detection; 4: carrier-phase relative RAIM detection; 5: carrier-phase relative RAIM detection with INS augmentation; 6: radar altimeter detection. The y axis is the number of simulated error cases, which is the number of simulated threat cases multiplied by the number of satellite combinations affected by one threat.

From Figure 6.17, the proposed innovation integration method has superior detection performance. The carrier-phase relative RAIM detection with INS augmentation is the second best. The real value of each detection method is shown in Figure 6.18, in which the numbers of HMI cases that can be protected by one and only one detection algorithm are presented. The innovation integration detection algorithm once again demonstrates its value by the ability to protect the system integrity from potential threats that go unnoticed by other algorithms.

6.3.4 Detection Performance on Severe Weather Activity. The same methodology applies to the simulations of troposphere storm detection with prior event probabilities at 10^{-2}, 10^{-3}, 10^{-4}. The total protection provided by six detection algorithms are shown in Figures 6.19, 6.20 and 6.21 for type I, II and III troposphere storms respectively. HMI numbers are high for any storm type; it indicates that the current system configuration is not safe from the troposphere storm threats. Solutions to resolve this issue will be addressed in Section 6.4, and a demonstration will show that the hybrid navigation system can achieve the integrity requirements.

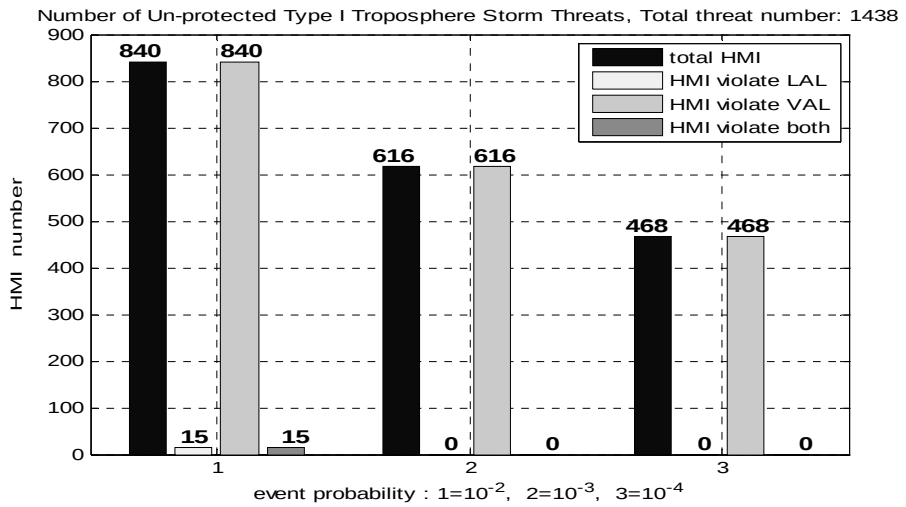

Figure 6.19. CAT III Detection Performance under Type I Troposphere Storm Threats

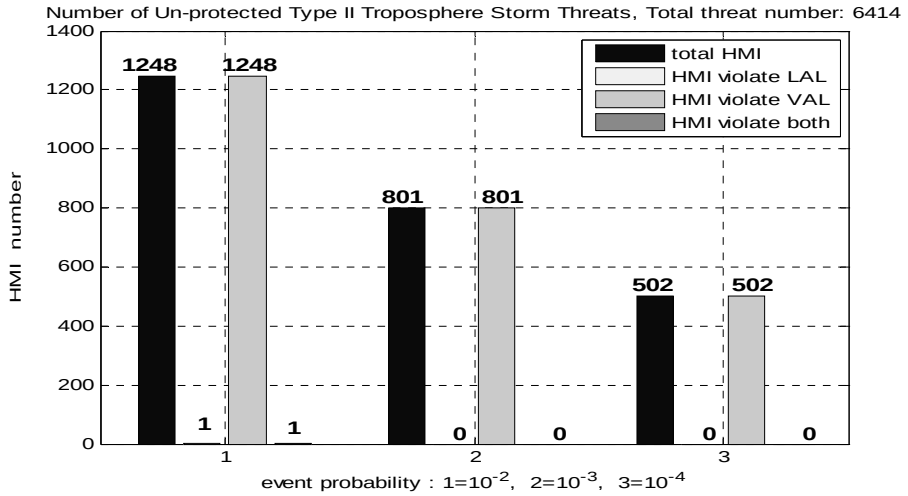

Figure 6.20. CAT III Detection Performance under Type II Troposphere Storm Threats

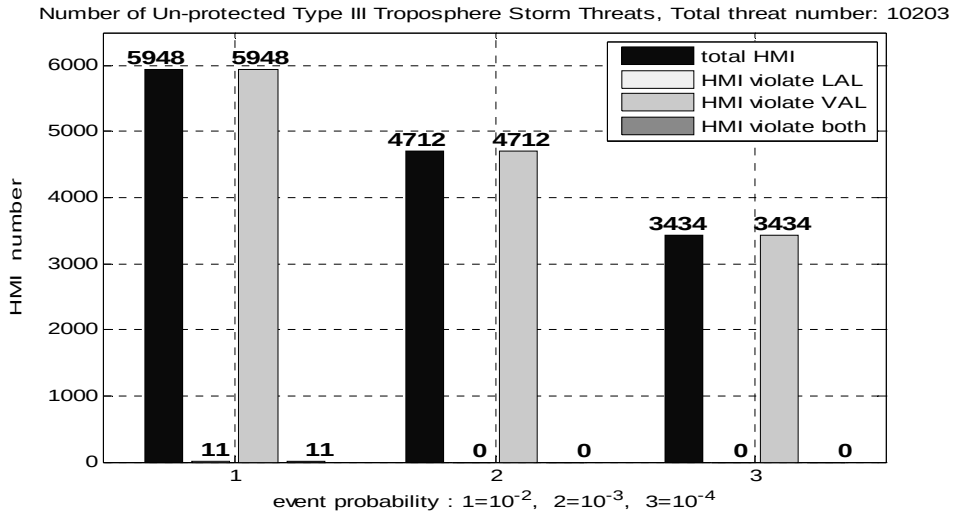

Figure 6.21. CAT III Detection Performance under Type III Troposphere Storm Threats

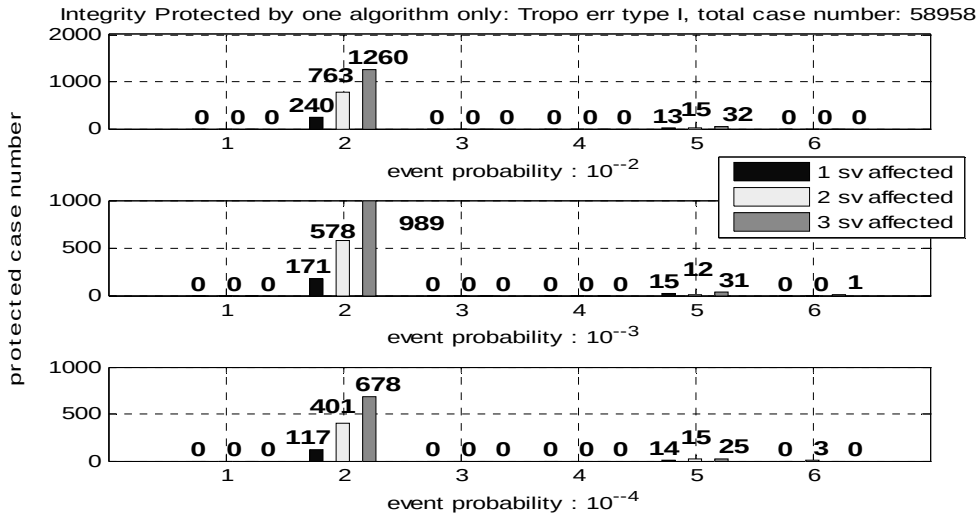

Figure 6.22. Number of Type I Troposphere Storm Threats Detectable by A Single Algorithm

Difficulties in detecting troposphere storm threats are highly related to the storm properties. The magnitude of a troposphere storm error is generally smaller in comparison with that of an ionosphere storm. However, it varies rapidly in both directions (up and down) in a short period of time. Moreover, up to half of the satellites in view (three in simulations) can be affected. These unique properties make all RAIM-based detection methods perform poorly. Even so, the proposed innovation integration

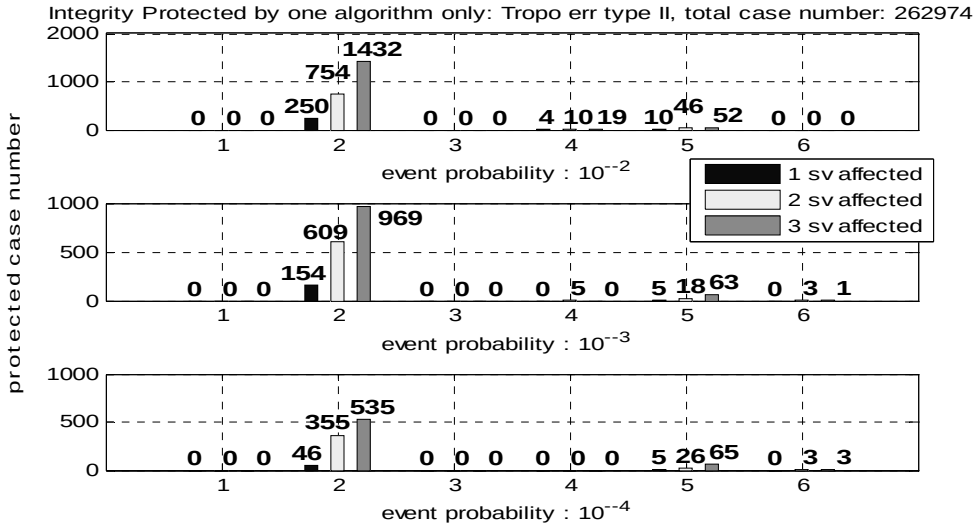

Figure 6.23. Number of Type II Troposphere Storm Threats Detectable by A Single Algorithm

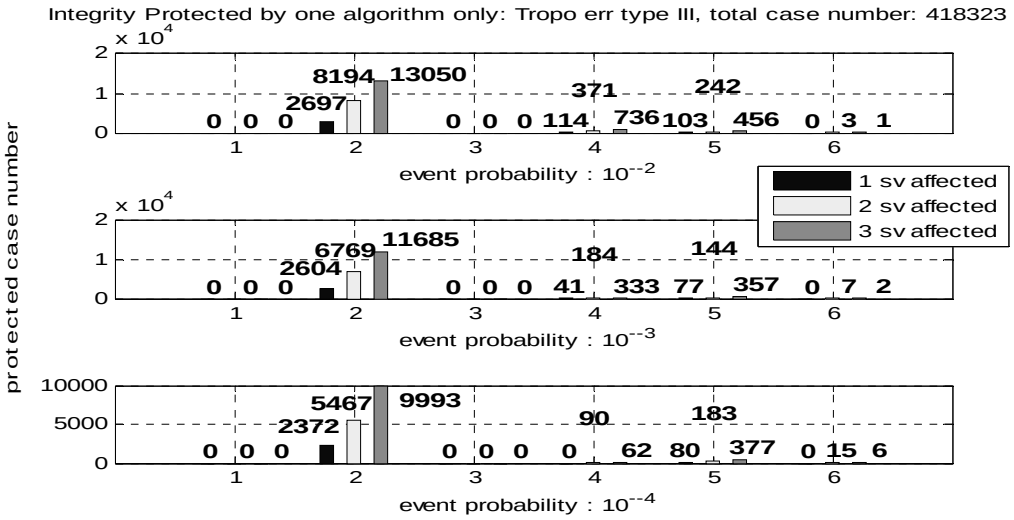

Figure 6.24. Number of Type III Troposphere Storm Threats Detectable by A Single Algorithm

detection shows its impressive capability once again to catch a great number of threats when the other monitors cannot. Figures 6.22, 6.23 and 6.24 demonstrate the potential of the new proposed innovation integration detection.

6.3.5 Cycle Slip Detection. Cycle slip error is distinct from signal propagation errors. It is an internal receiver carrier tracking error which has slid through the receiver internal screening mechanism. The impact simulation has shown the influence on system estimation errors is roughly proportional to the magnitude of cycle slip step. Therefore, the detection capability (probability of *NA*) is simulated for the half cycle slip case which is the smallest and most difficult one to detect.

Typical time responses of the RAIM-based methods and the innovation detection are displayed in Figure 6.25 with the error occurring in the middle of an approach. While others had very small responses to the half cycle slip error, the innovation test statistic reacted immediately and sharply. As for the innovation integration method, it actually has the second best detection performance. To show the time responses of the innovation

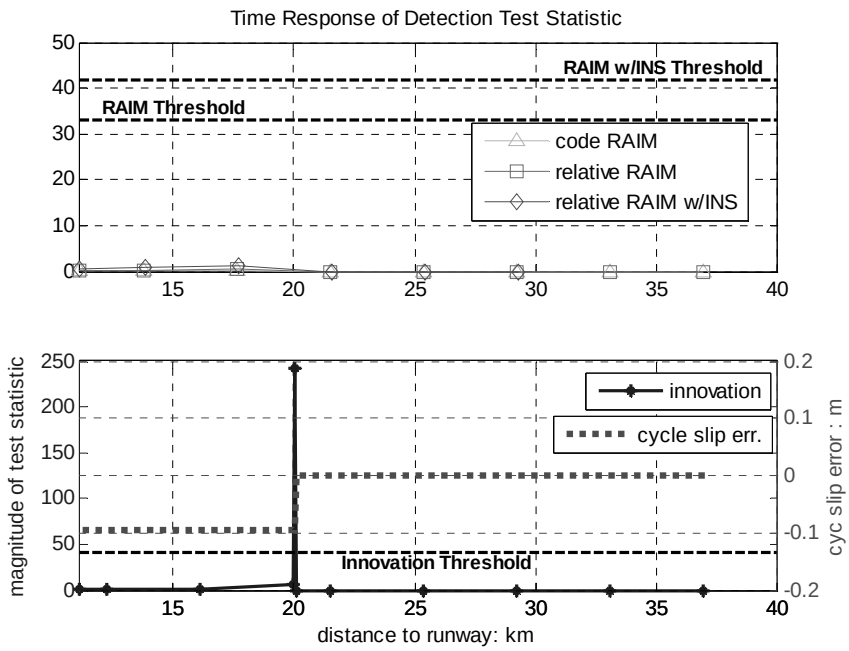

Figure 6.25. Typical Time Response of Test Statistics to Cycle Slip Error

integration test statistic side by side with others is not easy because of its constantly growing magnitude (recall from Figure 6.15). Therefore, it is not shown in this figure but will be shown in the next detection performance result.

The detection capabilities of six fault detection methods are shown in Figure 6.26

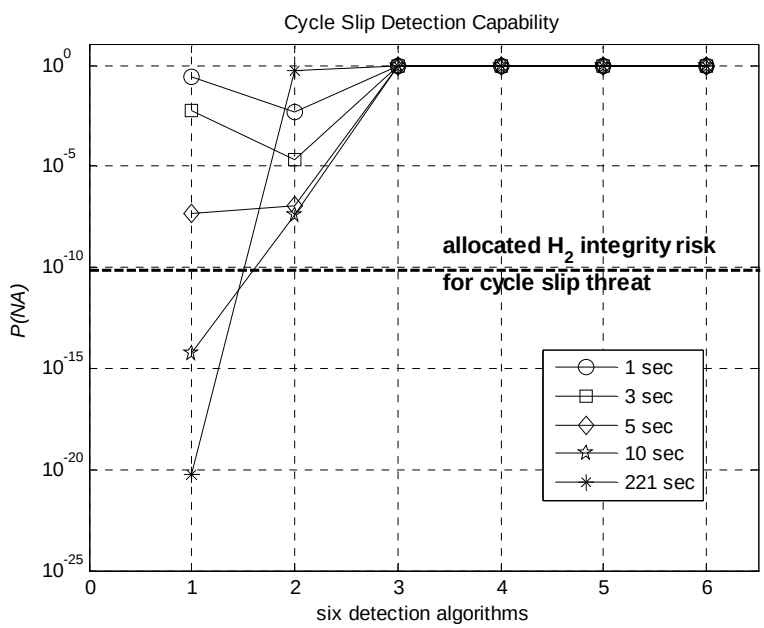

Figure 6.26. Detection Capability for Half Cycle Slip Error Case

in terms of the probability of no alarm. There are 5 curves representing different error occurrence times, which are 1, 3, 5, 10 and 221 seconds after system initialization. The last one is the case corresponding to the time response in the previous figure, which is around 20 km away from the runway end. From Figure 6.26, the innovation integration detection performed better than the innovation-only detection initially, but for the 5 second case and afterward the innovation-only detection scheme is superior. This observation describes a drawback for general averaging or integration type detection methods; a single sharp response can be diluted in the large number of elements constituting the test statistic. A moving average or limited number of integration may be able to reduce this effect to a certain degree.

The nonlinear response of the innovation integration detection requires further analysis on the cycle slip occurrence time. Figure 6.27 shows the probabilities of missed detection from the innovation and innovation integration algorithms with a half cycle slip occurring at all possible times. The missed detection curve from the innovation detection

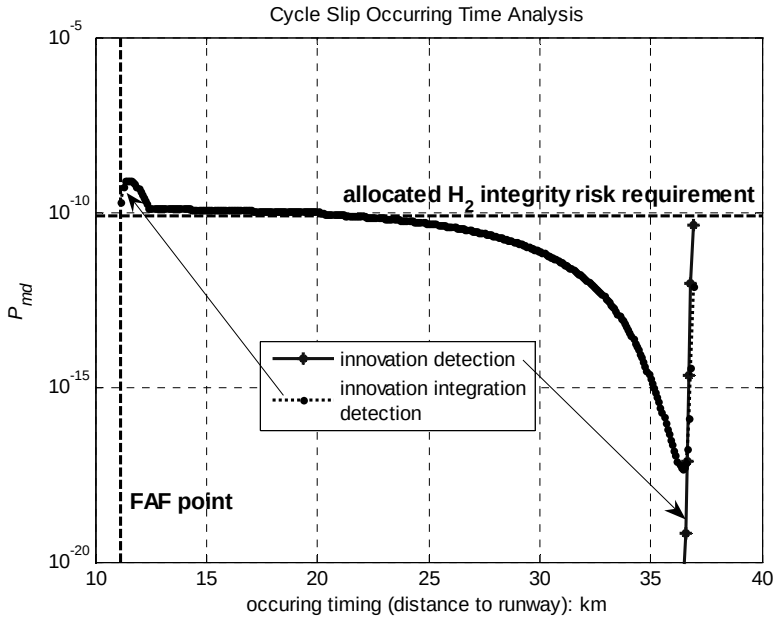

Figure 6.27. Integrity Protection vs. Cycle Slip Occurring Time

method plunged down quickly. Without considering the prior probability of cycle slip occurrence yet, the system integrity is already protected by the innovation detection algorithm alone. The innovation integration detection method works great during the first half of the approach (before 20 km distance to runway), then the magnitude of the detector response is diluted by large numbers of accumulated test statistics and does not meet the H_2 integrity risk requirement (without considering the event occurrence probability). The actual detection performance of the innovation integration detection algorithm for cycle slip threat can be re-evaluated when a prior probability of cycle slip occurrence is established. Based on the excellent detection performance shown from the innovation detection, it is likely that fault isolation and exclusion capability is possible for the innovation detection on cycle slip threats. However, this topic is out of current research scope and will be left for future work.

6.4 Solution Analysis on Fault Detection

According to the detection performance shown in section 6.3.3 and 6.3.4, the six tested detection algorithms are not sufficient to protect the hybrid navigation system from all ionosphere and troposphere storms. The present focus is to make the system safe from those unprotected HMI events. The approach taken here is not to add another more sophisticated detection algorithm, nor to find a way of reasoning out these HMI events. Instead, to avoid further complicating the system, we analyze the adjustments on IMU quality and radar detection parameters necessary to mitigate the HMI events using the current system architecture. This approach also has benefits of easy realization and greater flexibility for modifications to meet other requirements.

To facilitate the analysis, in the next section we identify the most dangerous threats from the system integrity point of view. We will then focus our analysis on these threats.

6.4.1 Identification of Most Dangerous Integrity Threats. The difficulty in protecting the system integrity is quantified as the probability of missed detection, *P(MD)*. The prior probability of an event further lowers the overall integrity risks due to the threats. Therefore, taking the threats that are still HMI events even when the lowest prior probability is applied, which is 10^{-5} for ionosphere storm and 10^{-4} for troposphere storm, as the most dangerous threats (in other words, the highest *P(MD)* among others) is a logical approach. Using the threats with high *P(MD)* as the samples to evaluate the detection performance of previous defined detection algorithms can avoid the necessity of running the whole simulated threats again. Because a detection method can protect a system from a threat with high *P(MD)*, it will have no problem to protect the system from

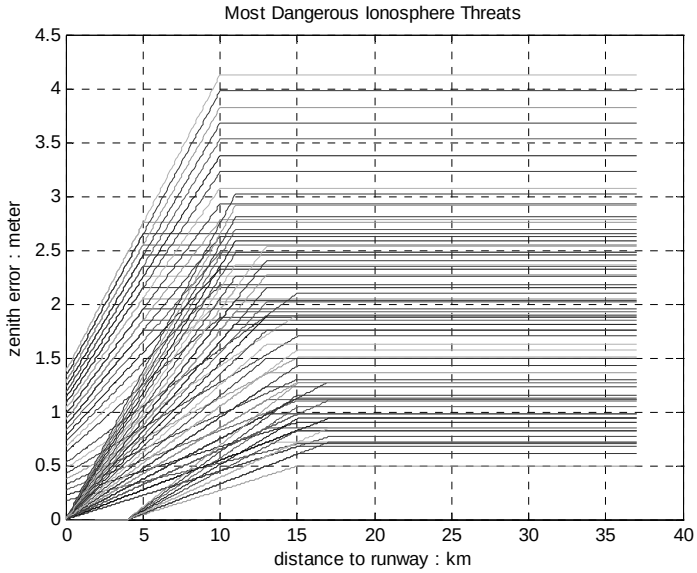

Figure 6.28. Most Dangerous Threats from Ionosphere Storms

threats with lower *P(MD)* under the same conditions.

The threats which are difficult to detect from the ionosphere storms are identified and shown in Figure 6.28. The number of threat cases that need to be simulated to evaluate the detection performance is reduced from 1876 to 83, about 4.4 % of the original threat number. After identifying dangerous threats from all types of the troposphere storms, the number of threat cases is decreased from 18055 to 4404, which is about a 75% reduction. The identified troposphere threats are displayed in Figure 6.29. Even though the final dangerous threat number is still high, it can be further reduced after the analyses in the next section.

6.4.2 Higher Quality IMU and Gravity Model to Reduce Coasting Errors. After reviewing the detection performance results shown in Sections 6.3.3 and 6.3.4, it becomes apparent that the coasting vertical position error is the cause of system integrity violations. Therefore, adjusting the quality of IMU and gravity models toward lowering

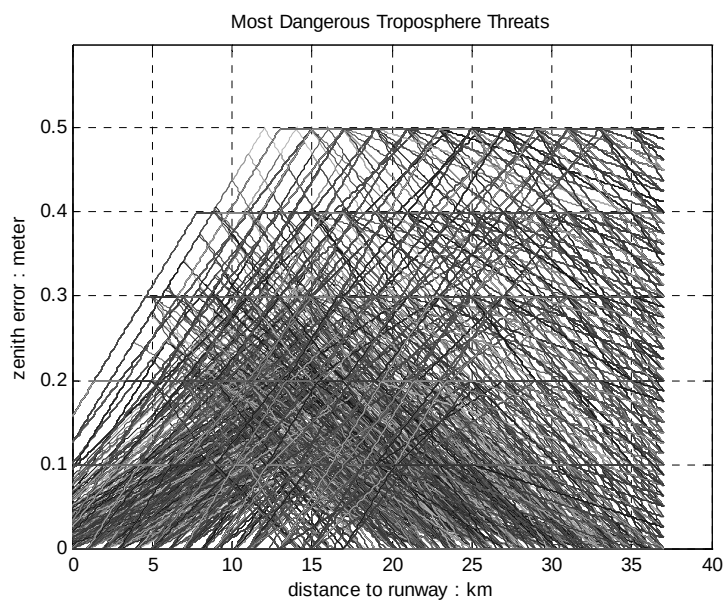

Figure 6.29. Most Dangerous Threats from Troposphere Storms

coasting vertical errors is the reasonable approach to improve the system integrity.

Better quality IMUs and gravity models can help the system integrity in two ways: it can boost the magnitudes of certain test statistics to improve the detection performance by reducing the magnitudes of covariance elements which are used to normalize residuals; meanwhile, a smaller coasting error can also reduce the probability of violating alert limits.

After adjusting the IMU gyroscope random walk value from 0.01 to 0.005 deg/hr$^{1/2}$, accelerometer measurement noise sigma from 0.1 mg to 0.01 mg and gravity anomaly value from 20 μg to 5 μg, the integrity detection results from the most dangerous threats from ionosphere and troposphere storms are encouraging. The hybrid system is protected completely from the ionosphere storm threats at all prior probability levels. However, there are still integrity threats from the troposphere storms at a prior probability of 10^{-2}.

Further refinement on the gravity anomaly can make the hybrid navigation system totally free from previously remaining threats. By applying 2.5 μg anomaly standard deviation, the hybrid navigation system is completely protected from simulated ionosphere storms, troposphere storms, and any cycle slip error by six selected detection algorithms. A conclusive list of the requirements for the IMU and gravity models to meet LAAS CAT III integrity requirements for one poor satellite geometry is made available in Table 6.2.

By checking the exclusive detection performance for each monitor in Figures 6.30 and 6.31 after applying the final adjusted IMU and gravity models, the impressive number of the threats solely detectable by the radar altimeter detection reveals the radar

Table 6.2. Minimum Requirements on IMU and Gravity Model Parameters for LAAS CAT III H_2 Integrity Requirements for One Poor Geometry (* indicates modification)

Minimum Requirements on IMU parameters			
standard deviation	gyroscope	accelerometer	correlation time ($\tau_{a/g}$)
bias stability (σ_{bg}/σ_{ba})	**0.005*** deg/hr	10 μg	1 Hour
measurement noise (σ_{vg}/σ_{va})	0.01 deg/hr$^{1/2}$	**10*** μg	N/A

Minimum Requirements on Gravity Model parameters			
	DOV in N-S ($\delta\xi$)	DOV in E-W ($\delta\eta$)	vertical gravity Error ($\delta\Delta g(0)$)
standard deviation	5 arcsecond	5 arcsecond	**2.5*** μg
correlation distance	20 nmi	20 nmi	20 nmi

altimeter's potential to protect the system integrity. Therefore, a complete analysis on the radar altimeter detection performance is conducted in the next section.

If the radar detection were removed from the system fault detection mechanism, there would be some remaining threats from both ionosphere and troposphere storms even at the smallest prior probabilities. This indicates that the five early stage detection

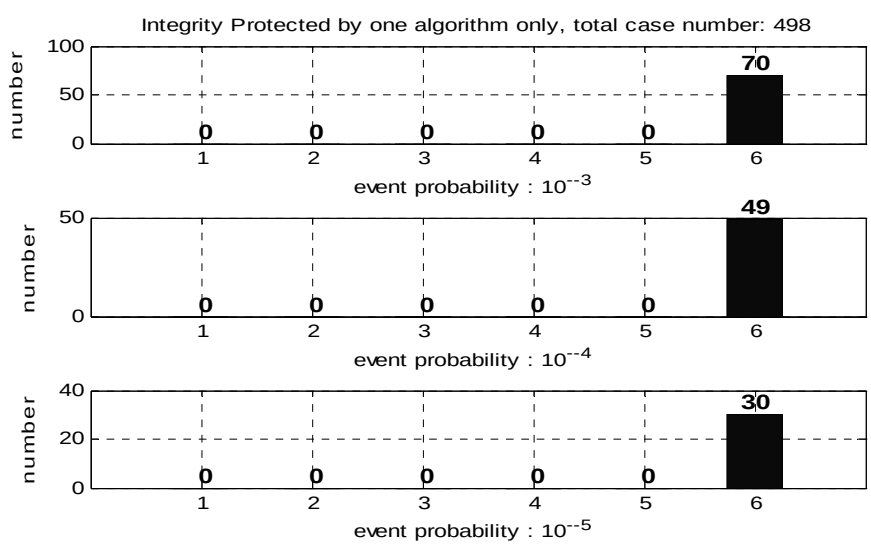

Figure 6.30. Number of Most Dangerous Ionosphere Storm Threats Detectable by A Single Algorithm.

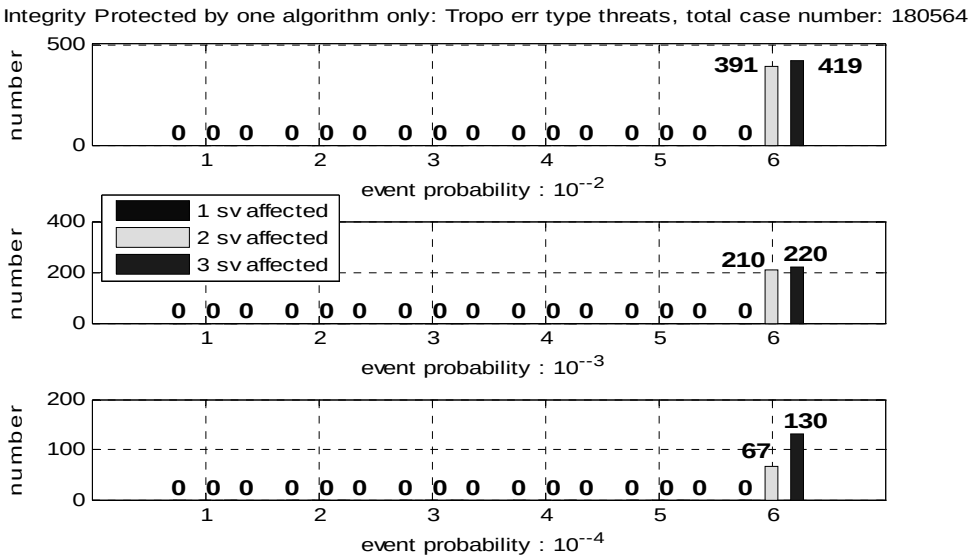

Figure 6.31. Number of Most Dangerous Troposphere Storm Threats Detectable by A Single Algorithm

methods are not sufficient to protect the hybrid navigation from all simulated threats even with refined IMU and gravity models. The remaining threats are certainly the most dangerous threats to the system integrity. Hence, these most dangerous threats are shown in Figures 6.32 and 6.33.

Recall that the new proposed innovation integration detection algorithm has

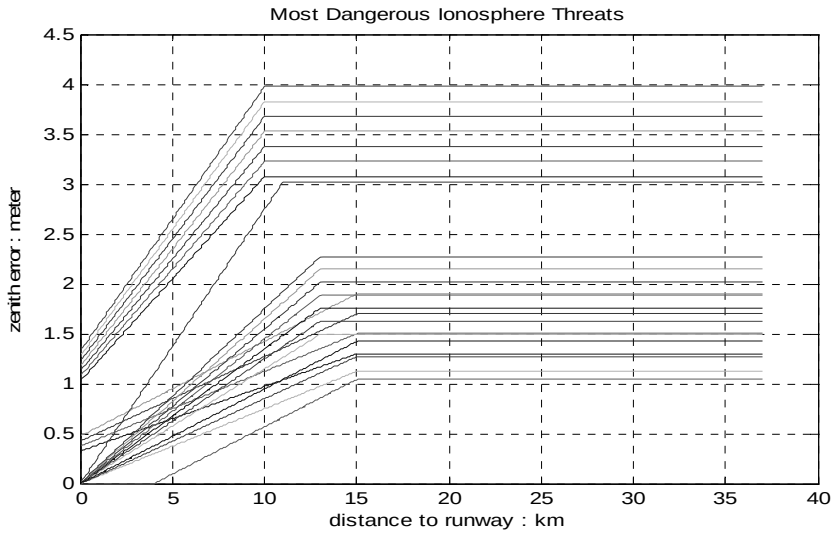

Figure 6.32. The Refined Most Dangerous Ionosphere Storm Threats

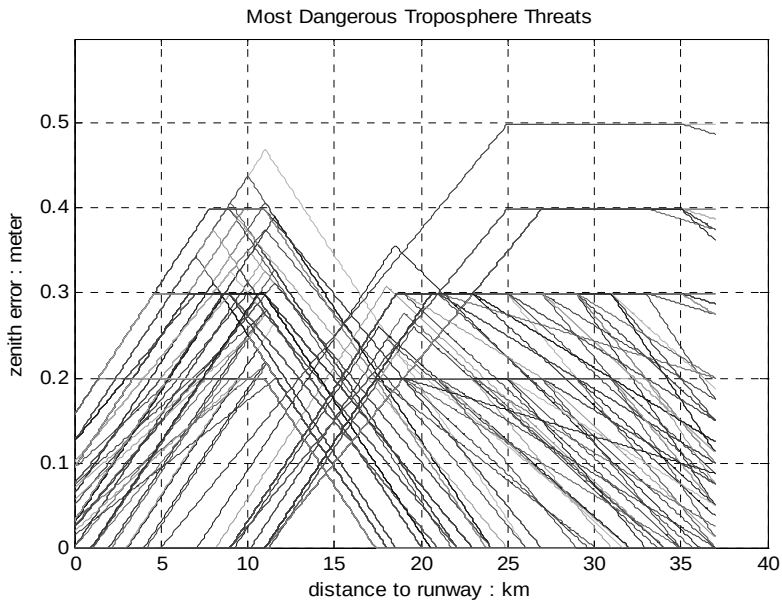

Figure 6.33. The Refined Most Dangerous Troposphere Storm Threats

consistently shown its outstanding detection capability. It is especially effective in detecting slow growing errors which are generally difficult to detect with other mechanisms. The radar altimeter detection scheme didn't work well initially, until the coasting vertical error was improved. Since the importance of the radar detection method has now been revealed, a quantification of the requirements for the radar altimeter detection scheme would be beneficial for future implementations.

6.4.3 High Integrity Radar Altimeter Detection Performance Analysis. A radar altimeter can provide a direct measurement to verify the coasting vertical position at the DH location, which is the most critical error affecting the hybrid navigation integrity. The potential benefit in using a radar altimeter in one of the detection methods to protect the hybrid navigation system integrity is high. Therefore, a generalized analysis to quantify the requirements for the radar altimeter integrity detection is prepared as follows.

To be as general as possible, a few parameters are considered as independent: the vertical position error bias b_V due to a failure, the standard deviation of vertical position error σ_V, and the standard deviation of DEM error σ_{DEM}. Two accuracy models of radar altimeters, which are described earlier in Section 6.3.1, are 1 ft plus 1 % ranging distance and 3 ft plus 1% ranging distance. These two models represent radar altimeter model type one and type two, and the standard deviation of radar measurement error, σ_{al}, for each model can be computed by using equation 6.13 (replace 1 by 3 for type two model). All parameter values are evaluated at the DH location.

For a specific set of σ_{DEM}, b_V and a prior probability, the allowed probabilities of no-alarm (*NA*) without violating an integrity requirement is a function of σ_V:

$$P(NA)_{allow} = (\text{required integrity risk}) / [P(Err_V(DH) > VAL \mid b_V) \times P(HE)] \tag{6.23}$$

where $P(Err_V(DH) > VAL \mid b_V) \sim f(\sigma_V)$. The actual achieved no-alarm probability by radar altimeter, $P(NA)_{ach}$, with the same parameter set can be computed as following:

$$P(NA)_{ach} = P(|T_S| < T_H \mid b_V, \sigma_{DEM}) = \frac{1}{\sqrt{2\pi}} \int_{-(T_H + |b_{Ts}|)}^{T_H - |b_{Ts}|} e^{-\frac{s^2}{2}} ds \tag{6.24}$$

where b_{Ts} is the expect value of radar detection test statistic:

$$b_{Ts} \equiv E[T_s(DH)_{radar}] = E[z_{radar}(DH) - h_{INS}(DH)] / \sqrt{\sigma_{al}^2 + \sigma_{DEM}^2 + \sigma_V^2}\ .$$

Under fault conditions, $E[z_{radar}(DH) - h_{INS}(DH)] = b_V$. Therefore, b_{Ts} is the bias type response of the radar detection test statistic to failures. For a given set of σ_{DEM} and b_V, b_{Ts} is also a function of σ_V:

$$b_{Ts} = b_V / \sqrt{\sigma_{al}^2 + \sigma_{DEM}^2 + \sigma_V^2} \tag{6.25}$$

Therefore, $P(NA)_{ach}$ is also a function of σ_V.

The system integrity is secured if the allowed no-alarm probability is larger than the achieved probability. Both allowed and achieved no-alarm probabilities are functions of the vertical position error σ_V with different trends. The allowed no-alarm probability curve tends to decrease when σ_V increases, while the achieved no-alarm probability curve goes the opposite way. Therefore, a maximum allowable σ_V to ensure integrity can be found for each set of parameters. A typical search process is shown in the left plot of Figure 6.34.

Going through finding the maximum σ_V for different bias errors (b_V) and DEM sigmas (σ_{DEM}), a curve which defines the protected bias error b_V vs. the vertical σ_V at the nominal DEM sigma value 0.15 m is plotted in the right graph of Figure 6.34. The

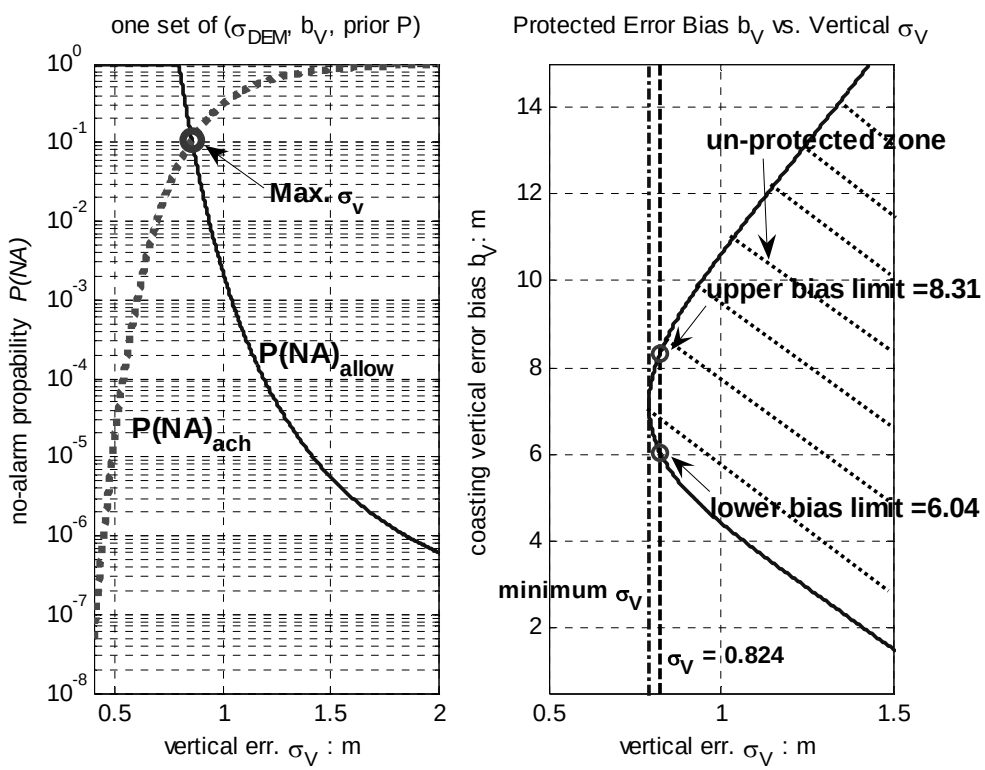

Figure 6.34. Type one Radar Altimeter Detection Performance Analysis

cross-line area on the right side of the curve is the un-protected bias zone. For example, the first adjustment on IMU and gravity models (at the beginning of Section 6.4.2, gravity anomaly was adjusted to 5 μg) has made the coasting vertical sigma at DH reduce to 0.824 meters; a vertical line at this vertical sigma value has two intersections with the protection curve at bias values 8.31 and 6.04. These two bias values define an un-protected band region; any simulated error which results in a vertical error bias at DH falling into the band region is an integrity threat to the radar altimeter detection. For each protection curve, a minimum σ_V which is tangential to the cure can be found. A system which has the coasting vertical position error σ_V at DH smaller than the minimum σ_V is protected from any threat by radar altimeter detection.

The analysis is verified by extracting the coasting vertical error bias values at DH from those unprotected-by-radar HMI cases which were simulated from the example in Figure 6.34 with coasting vertical σ_V at 0.824 meters. The right plot in Figure 6.35

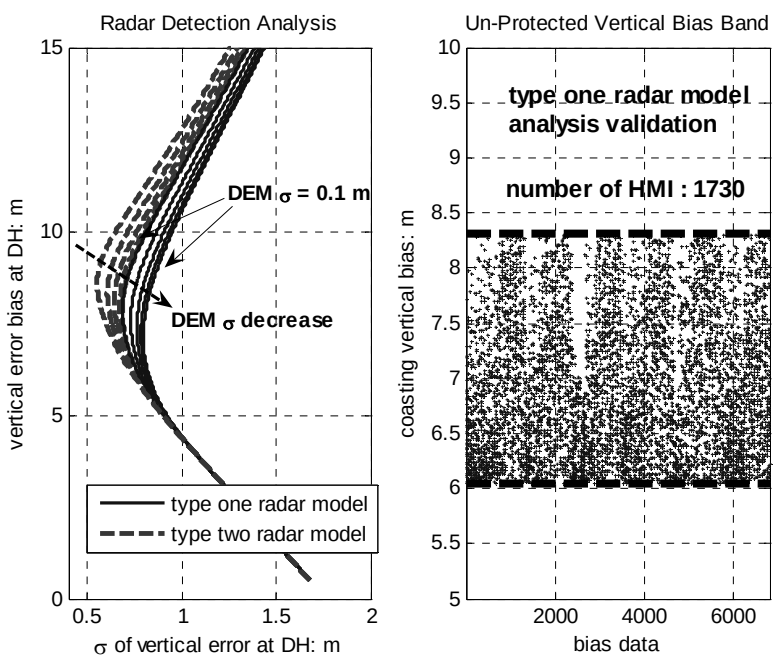

Figure 6.35. Verification of Radar Detection Analysis

clearly shows that all HMI's vertical error biases fall between the upper and lower bias limits which were derived from the analysis curve. The left plot displays the moving trend of the protection curves with different DEM standard deviations.

For easier utilization of the results of this analysis, the same process was repeated with different prior probabilities. The minimum σ_V which can ensure CAT III integrity from any threat at each DEM standard deviation has been obtained. Combining the protect-all σ_V for each DEM standard deviation with different prior probability, two radar detection requirement plots for CAT III integrity for two types of radar altimeter models are shown in Figure 6.36. From the type one plot (left hand side of the figure), the requirement curve with 10^{-2} prior probability for troposphere storms is below the coasting σ_V after the first IMU and gravity models adjustments. This indicates the insufficient integrity protection provided by radar altimeter detection in the event of

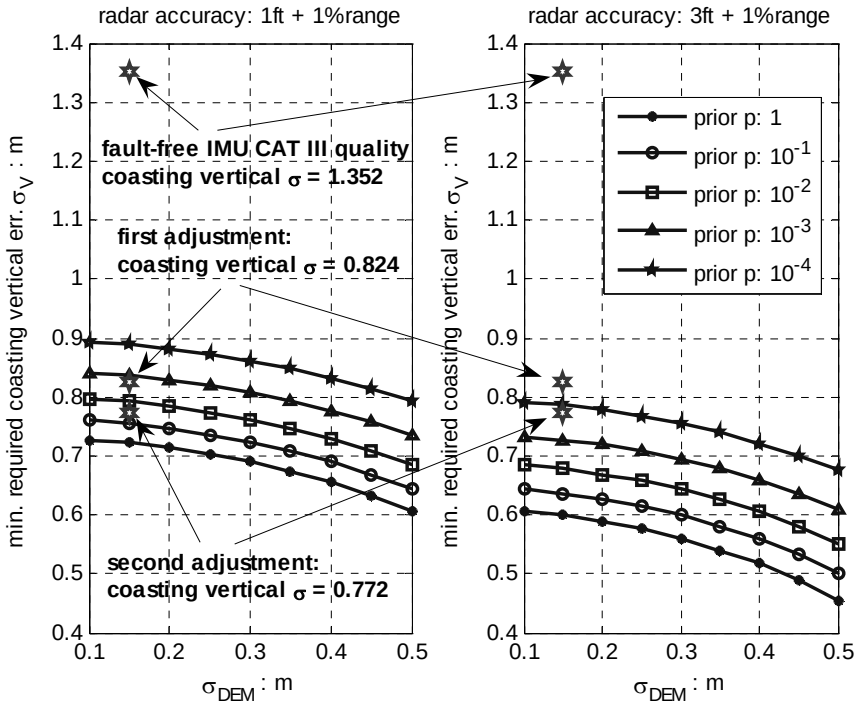

Figure 6.36. Requirements of Radar Altimeter Detection for LAAS CAT III Integrity

troposphere storms. After the second adjustment, the coasting σ_V drops below the 10^{-2} prior probability requirement curve. Therefore, the system integrity is protected from any threat with 10^{-2} or lower prior probability, and this conclusion matches the simulation results previously shown in Section 6.4.2. On the contrary, type two radar altimeter accuracy model, as shown in the right hand side plot, is not sufficient to protect CAT III system integrity from those threats with prior probability higher than 10^{-4}.

The same analysis is repeated for LAAS CAT I requirements. Figure 6.37 shows the radar detection requirements to meet the LASS CAT I integrity. The figure clearly shows that the quality of IMU and gravity models for CAT I fault-free integrity requirements is far from meeting the integrity requirements under fault conditions. With the help from Figure 6.37, a quick adjustment on the IMU accelerometer and gravity model parameters is made to bring the coasting vertical sigma at DH (200 ft) down to

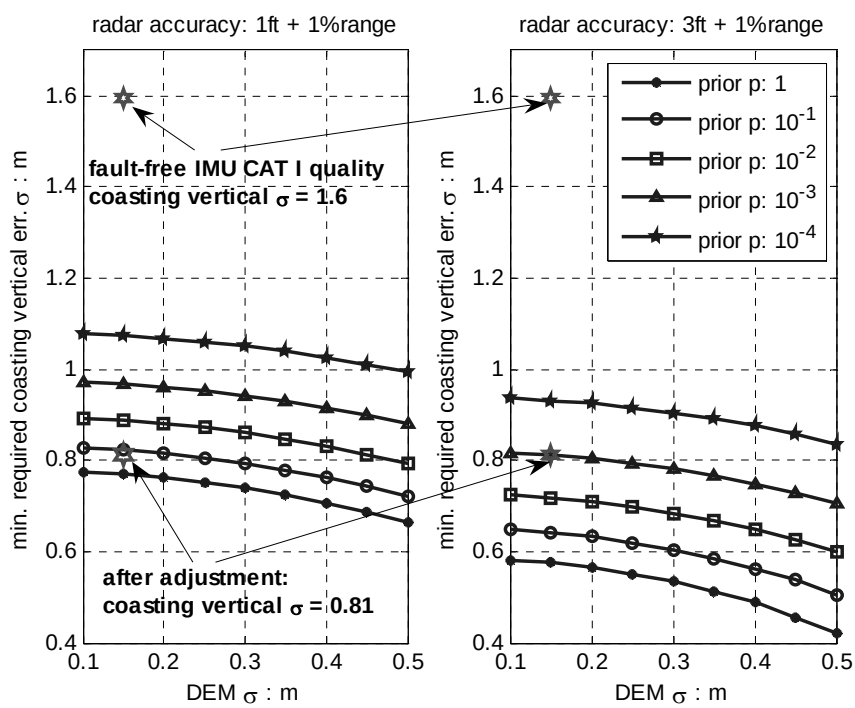

Figure 6.37. Requirements of Radar Altimeter Detection for LAAS CAT I Integrity

0.81 m. The type one radar requirement curve indicates that CAT I system integrity is protected by the adjustment and radar detection with 15 cm DEM standard deviation from any threat with 10^{-1} or lower prior probability. Re-run simulations (no shown) with the ionosphere and troposphere storm threats agree with this analytical conclusion. The DEM requirement can be further relaxed to 40 cm sigma for CAT I if all the threats are considered to have less than 10^{-2} prior probability. Similar to the CAT III case, the type two radar altimeter accuracy model can barely meet CAT I integrity requirements with the adjusted IMU quality and prior probability 10^{-3}.

Table 6.3 shows the IMU and gravity model requirements to meet the CAT I integrity requirements for one poor satellite geometry under fault conditions.

6.5 H_2 System Availability with High Integrity Fault Detection

The hybrid navigation system with fault detection has demonstrated its ability to meet the most stringent LAAS CAT III integrity and continuity requirements at the expense of better quality IMU sensors and local gravity models. The accuracy

Table 6.3. Minimum Requirements on IMU and Gravity Model Parameters for LAAS CAT I H_2 Integrity Requirements for One Poor Geometry (* indicates modification)

Minimum Requirements on IMU parameters			
standard deviation	gyroscope	accelerometer	correlation time ($\tau_{a/g}$)
bias stability (σ_{bg}/σ_{ba})	0.1 deg/hr	10 μg	1 Hour
measurement noise (σ_{vg}/σ_{va})	0.01 deg/hr$^{1/2}$	**10*** μg	N/A
Minimum Requirements on Gravity Model parameters			
	DOV in N-S ($\delta\xi$)	DOV in E-W ($\delta\eta$)	vertical gravity Error ($\delta\Delta g(0)$)
standard deviation	20 arcsecond	20 arcsecond	**5*** μg
correlation distance	10 nmi	10 nmi	10 nmi

requirement is automatically fulfilled when the fault-free integrity requirement is met. Although the full constellation fault-free system availabilities were simulated based on the un-adjusted IMU and gravity models in Sections 5.2.2 and 5.2.3, these fault-free availability results are still applicable since all adjustments were done to reduce the coasting errors.

H_2 availability can be defined as the percentage of the time that the system integrity is protected by the integrity monitoring mechanism. Generally speaking, the integrity can be improved at the cost of the availability (an extreme example: when no approach is allowed, the integrity risk is zero). Geometries that are confirmed by the integrity monitoring mechanism will be available for precision approach navigation. For general GPS-only navigation systems protected by RAIM-based detection methods, the highest missed detection probability for each geometry (i.e, failure on the worst case satellite) is computed and the geometries which cannot meet the integrity requirements are declared unavailable.

However, the general screening process is more complicated for integrated GPS/INS systems which include the coasting positions as part of the navigation solutions. System errors that are not detectable by integrity monitors during the in-flight calibration might increase along with the coasting distance and become integrity threats at the DH location. This 'error propagation' character does not exist in general GPS-only navigation systems, but needs to be predicted in our hybrid system to declare an approach to be available.

Therefore, a well defined threat space is necessary to evaluate the detection performance for the tightly coupled GPS/INS navigation system. WAAS MOPS

Appendix R [RTCA/DO229D] is a great example, in which the possible errors with prior probabilities are defined, and procedures and requirements to simulate the fault detection are listed.

Sections 6.4.2 and 6.4.3 show that the hybrid navigation system is capable of meeting the LAAS CAT I/III integrity requirements with very conservative prior probabilities of threat occurrences under a single poor satellite geometry. However, further validation of prior probability and threat spaces may show that the assumptions used in the hybrid navigation simulations are in fact overly conservative. Therefore, a quantitative evaluation for the current hybrid system H_2 availability would have questionable value without prior probability validation. Instead, important procedures for the hybrid navigation system H_2 availability evaluation and a method for integrity prediction in real time operations are proposed. Finally, an example of the H_2 availability evaluation and improvement using the most dangerous ionosphere threats is shown.

1) *Early stage detection selection*: with the suggested hybrid navigation system configuration, any threat that would lead to HMI will be detected by the radar altimeter detection alone at the DH location. However, this result does not allow us to abandon other detection methods because the high integrity radar detection is only available at the DH location. Threats that can cause large system errors earlier need to be detected soon to avoid disasters before the aircraft reaches the DH location. Not all five simulated early detection algorithms need to be implemented. The decision relies on the detection performance analysis for the considered threat space and prior probability. However, three early stage detection algorithms are strongly recommended for their excellent

detection performance demonstrated earlier: *innovation detection* for cycle slip detection, *innovation integration detection* and *carrier-phase relative RAIM with free-INS coasting augmentation* for ionosphere and troposphere storms.

2) *Approach integrity evaluation*: Similar to the concept of integrity coasting in the WAAS MOPS Appendix R, the integrity risk of the coasting error exceeding VAL/LAL profile is evaluated for the most dangerous threats for 24 hours of satellite geometries. Geometries are declared unavailable when VAL/LAL profile is breached at any location during the coasting. Long-term service availability can be simulated by using weighed constellations with assumed constellation state probabilities in MASPS Appendix F [RTCA/DO245A].

3) *Approach integrity prediction*: General availability evaluations are done by applying a standard constellation, such as DO-229D in this research. Nevertheless, it is not feasible to exhaust all the possible geometries that a navigation system would encounter during the real operation. A real time "approach integrity prediction" is needed to predict the system integrity risk before launching an approach. The process is the same as the described "approach integrity evaluation", but applied to the current geometry during a real time operation. This suggestion is similar to the concept of PVPL and PLPL in MASPS. [RTCA/DO245A]

An example of the H_2 availability using the most dangerous ionospheric storm threats identified in Section 6.4.2 is evaluated for 24 hours at O'Hare international airport with a 24 satellite constellation. A conservative 10^{-3} prior probability for ionosphere threats is applied in the simulation. The three recommended early stage detection

algorithms along with radar detection, and IMU and gravity models from Table 6.2 are applied in the H_2 availability simulation example.

The availability results are shown in Figure 6.38. Instead of reading probability numbers, vertical position error under H_2 conditions (VPE_{H2}) is defined to have a better visualization of the system integrity. VPE_{H2} is the same as VPL_{H2} values, except for some cases which have coasting bias values, b_V, very large and can be detected by monitors. The VPE_{H2} values for these extreme cases are trimmed to be the same as VAL to avoid being mistaken for HMI events. The probability multiplier to compute VPE_{H2} is a function of the required integrity risk, the no-alarm probability from a detection method, and the threat prior probability. It indicates the coasting vertical error bound with the allowed probability under the protections of the implemented fault detection algorithms. VPE_{H2} can be computed using the following equations:

$$\begin{aligned} &IF\ (\text{required integrity risk}) < [P(NA)_{MIN} \times P(HE)] \\ &P(\left|\delta x_{c\_ver}\right| > VPE_{H_2} \mid b_V, \sigma_V) = (\text{required integrity risk}) / [P(NA)_{MIN} \times P(HE)] \end{aligned} \tag{6.26}$$

$$VPE_{H_2} = b_V + M_{H2} \cdot \sigma_V, \text{ where } \frac{P(\left|\delta x_{c\_ver}\right| > VPE_{H_2} \mid b_V, \sigma_V)}{2} = \frac{1}{\sqrt{2\pi}} \int_{-\infty}^{-M_{H2}} e^{-\frac{s^2}{2}} ds$$

$$\begin{aligned} &IF\ (\text{required integrity risk}) \geq [P(NA)_{MIN} \times P(HE)] \\ &VPE_{H_2} = VAL \end{aligned} \tag{6.27}$$

If any VPE_{H2} value exceeds the VAL profile during the coasting stage, that geometry is not available for the system. Even though the VPE_{H2} is convenient to visualize the integrity checks, the actual integrity risk for each detection method are evaluated by equation 6.22. The one sigma envelope of the coasting vertical error at DH is shown in the H_2 availability results figures to ensure the satisfaction of the radar detection requirement. In an approach, if no VPE_{H2} values violate the VAL profile, then the

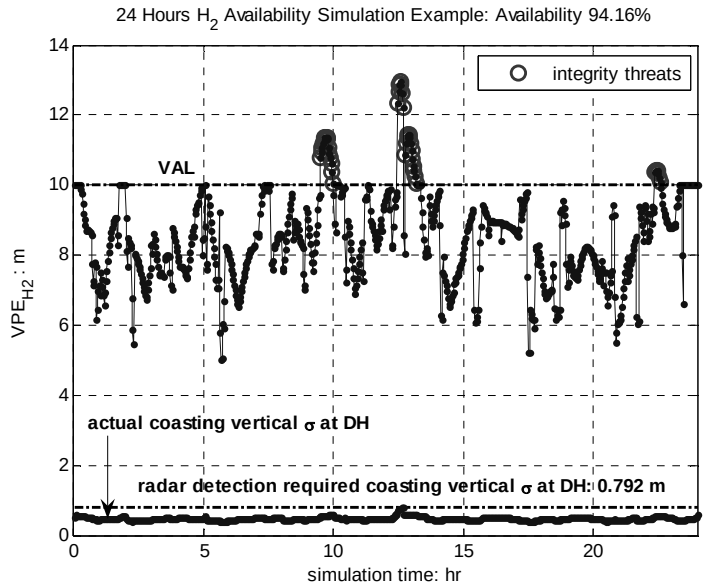

Figure 6.38. H_2 Availability Simulation with 2 min Geometry Interval for CAT III

coasting errors are either detected by radar altimeter (trimmed to be the same as the VAL) or are very small to have no threat to the system integrity.

The example results in Figure 6.38 are far below the LAAS availability requirement. To improve the H_2 availability, examples of coasting errors for one good and one bad geometry are displayed in Figure 6.39. In the bad geometry, some threats

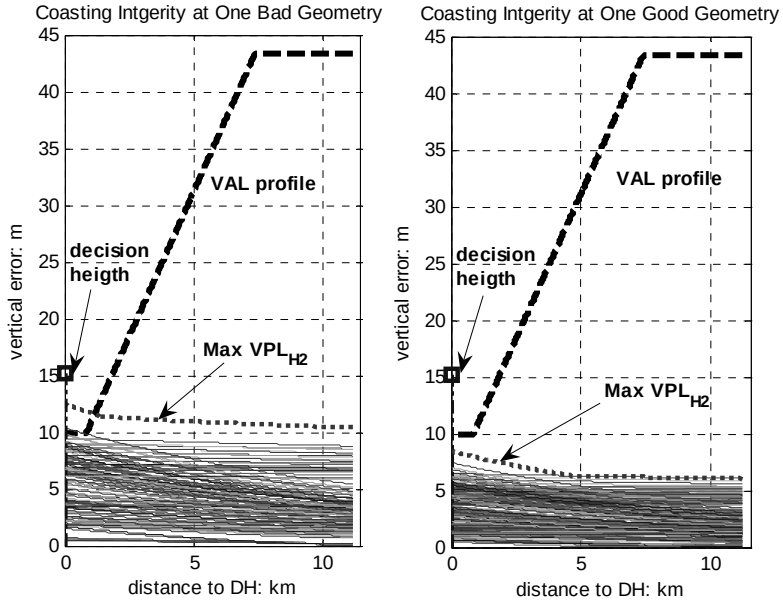

Figure 6.39. Coasting Integrity Simulation Example

clearly break the VAL profile before the radar detection has a chance to work. These rare but extremely dangerous scenarios are the causes of the low availability results in Figure 6.38. The integrity risk can be avoided by running the approach integrity prediction as suggested previously. However, the system availability is sacrificed for the sake of integrity. A solution to improve the H_2 availability without jeopardizing the integrity is to setup a few radar pre-screening points before the DH location.

The improvement in availability for the same bad geometry in Figure 6.39 is shown in Figure 6.40 by setting three prescreening radar detections. The cascaded prescreening setup has made this bad geometry available. The maximum VPE_{H2} values are reduced stepwise by each prescreening check point to avoid the VAL profile violation. The advance screening points are setup at 1.5 km and 1 km ahead of the DH location for P1 and P2 points and at 100 feet height for P3 in Figure 6.40. With this prescreening configuration, The H_2 availability from Figure 6.38 can be improved as shown in Figure 6.41.

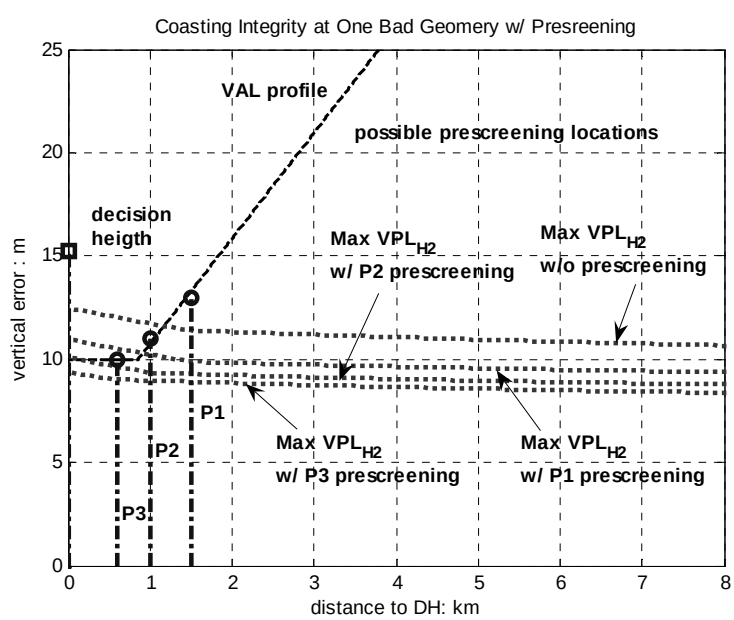

Figure 6.40. Coasting Integrity Simulation Example with Prescreening Detection for CAT III

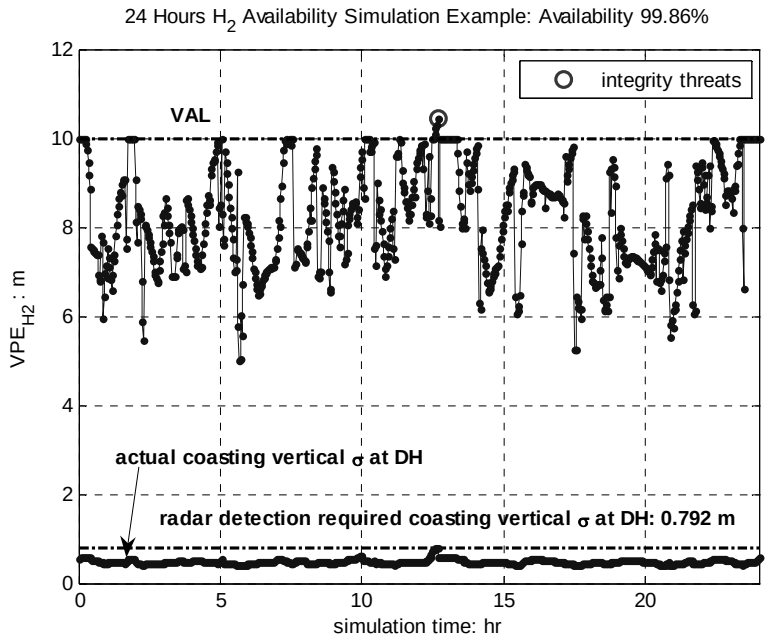

Figure 6.41. H_2 Availability Simulation with Three Steps Advance Radar Detection for CAT III

The availability with three advance radar detection configuration is improved from 94.17% to 99.86%. More precisely, there is only one approach that is not available in the total 720 simulated approaches.

The same system configuration with a CAT I quality IMU and gravity model from Table 6.3 was simulated and 100% availability results are shown in Figure 6.42. The hybrid system for CAT I does not have a similar availability problem to CAT III because of the less stringent integrity requirements and no "bottle neck" part at the end of VAL profile. If extremely caution needs to be taken, the prescreening at locations P1 and P2 for CAT III configuration can be implemented for CAT I as well.

With proper trade-offs on the INS quality and appropriate selections of fault detection methods, the proposed GPS/INS hybrid navigation system has demonstrated its capability to meet LAAS CAT I/III system requirements. It was shown in this chapter that the ultimate driving force for the INS quality is H_2 (rather than fault-free) integrity

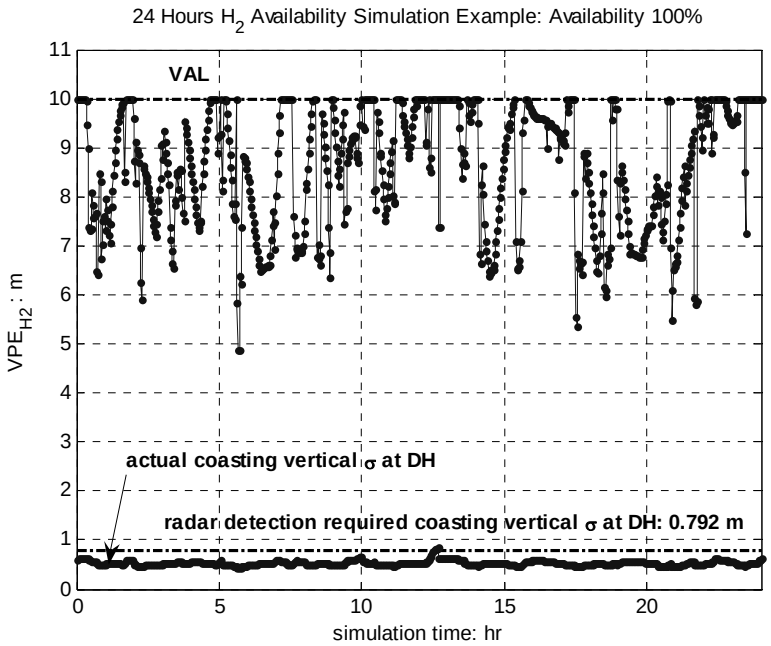

Figure 6.42. H_2 Availability Simulation Example for CAT I

for both CAT I and CAT III applications. In addition a newly proposed innovation integration detection algorithm has been proved to have extraordinary detection performance among early stage detection algorithms. Through the analysis and simulations, radar altimeter detection is also recognized to have a great potential to protect navigation systems from any kind of threats at the DH location. Finally, a simple three-step advance radar detection configuration has shown the advantage on improving H_2 system availability.

CHAPTER 7

CONCLUSION

GPS navigation systems have found wide-spread use in many diverse applications in the past decade. The achievements of GPS navigation systems in positioning and navigation services have been nothing short of extraordinary. However, there is many remains some apprehension about extensive dependence on GPS. For example, the "Vulnerability Assessment of the Transportation Infrastructure Relying on the Global Positioning System" report discloses the concerns about the vulnerability of transportation infrastructure reliance on GPS. In this research, the performance of the high integrity navigation systems were studied, and concerns about the vulnerability of GPS signals was addressed.

A new dual-frequency CDGPS architecture has been developed in this research and its performance was evaluated relative to the requirements for the unique shipboard landing application. This research also addressed the vulnerability concern by incorporating a single frequency system as a back-up in the event of hostile jamming on one frequency. For critical civil aviation applications without the luxury of accessing dual frequency GPS signals, a novel GPS/INS tight-coupling hybrid navigation system was proposed in response to the GPS signal vulnerability issue, and it was validated by flight data. The hybrid navigation system availability which complies with the LAAS CAT I/III fault-free integrity requirements has been evaluated. A new proposed detection algorithm, together with radar altimeter detection method and other existing fault detection schemes, has demonstrated the capability to ensure the hybrid navigation system integrity under the considered threats through fault detection analysis.

7.1 Accomplishments

This research focuses on one topic, the performance of a high integrity navigation system, with two distinct applications. Military-based SRGPS fully explores the performance of the high integrity CDGPS system by applying extremely precise GPS carrier-phase measurements. The tightly coupled GPS/INS hybrid navigation system with high integrity coating capability is studied in response to the RFI threats during the critical approaching stage for precision approach and landing in civil aviation applications. Sections 7.1.1 through 7.1.4 summarize the major accomplishments of this research.

7.1.1 Algorithm and Performance Analysis of High Integrity CDGPS Navigation System. A high accuracy and high integrity CDGPS navigation system for shipboard landing applications has been developed and proven to be a viable architecture that can achieve the required integrities on positioning and carrier cycle resolution. The high integrity cycle resolution for real time applications is made possible by incorporating Teunissen's 'Integer Bootstrapping' algorithm with 'Least-square AMBiguity Decorrelation Adjustment' (LAMBDA) for cycle ambiguity decorrelation. This algorithm can compute the probabilities of correct cycle resolution; it is this quantity that is evaluated to ensure system integrity.

The influence of system parameters, such as the quality of the raw code and carrier measurements, satellite geometry and filter duration, was carefully explored by sensitivity analysis. Both single frequency and dual frequency system architectures were investigated using covariance analysis, including cases of satellite outage in response to the need of redundancy in the event of hostile jamming or interference on one frequency.

7.1.2 Novel GPS/INS Hybrid Navigation System for Precision Approach and Landing Application. A novel GPS/INS hybrid navigation architecture was constructed from an SRGPS-based single frequency GPS system innovatively integrated with an INS in the dynamic model. The in-flight INS calibration process was implicitly accomplished in a tightly coupled fashion, which worked by fusing the INS dynamic information with the GPS states in one centralized Kalman filter. The linearized GPS measurement model was employed to estimate the GPS states in the same way as an ordinary GPS-only navigation system, and the INS was simultaneously calibrated through the correlations between GPS and INS states. Another advantage of the hybrid navigation system is a built-in innovation detection mechanism which shows excellent performance in cycle slip detection.

Validation of the novel hybrid navigation system was done by post-processing flight data from the FAA Technical Center to verify the accuracy of all covariance analyses performed.

7.1.3 The Hybrid Navigation System Sensitivity Analysis and Fault-free Availability Analysis. The hybrid navigation system coasting performance was analyzed by covariance analysis. Sensitivities of the system coasting performance with respect to calibration period, IMU and gravity model quality, straight and curved approach, heading information augmentation and disturbance acceleration during coasting were studied thoroughly. INS free coasting and partial GPS aided coasting were both analyzed. The quality of IMU sensors and gravity model was quantified to meet the requirements of LAAS Cat I and III precision approach and landing under the fault-free assumption.

Fault-free system availability was also evaluated at 6 selected airports spread around CONUS with a constellation of 24 satellites.

7.1.4 New High Integrity Fault Detection Algorithm and Detection Performance Analysis for GPS/INS Hybrid Navigation System. A new fault detection algorithm for GPS navigation using the integration of the innovation residuals was developed and compared with other detection methods. The major threats to the hybrid navigation system during ionosphere and troposphere storms and cycle slip were simulated and the performance of fault detection algorithms was analyzed. The results showed that the new developed innovation integration detection method has superior detection performance over others to most threats.

The most dangerous threats to the hybrid navigation system were identified and addressed by the proposed solutions (better IMU and gravity model quality and radar detection at pre-screening points). The final system integrity and availability were evaluated to demonstrate the feasibility of the hybrid navigation to meet the LAAS CAT I/III requirements under the considered threats.

7.2 Recommendations for Future Work

A few recommendations for the GPS/INS hybrid navigation system research are given below:

System performance sensitivity to the carrier-phase GSP measurement quality. The current LAAS system has well defined requirements on smoothed code measurement quality to ensure system performance. The requirements on carrier-phase measurements should be evaluated and defined in a similar fashion for the

GPS/INS hybrid navigation system within the LAAS system configuration. A sensitivity analysis similar to the one performed for SRGPS system is preferable if the computational resources are available.

Long term service availability simulation. After the ionosphere and troposphere threat spaces and prior probabilities for LAAS applications are validated, INS quality for the hybrid system can be analyzed, and fault detection algorithms can be selected to meet the H_2 system integrity requirements through the fault detection analysis in Chapter 6. The long term fault-free and H_2 system availabilities should be evaluated for the hybrid navigation system by applying the constellation state probability model (for satellite outages).

Augmentation with radar altimeter in final coasting stage. Through a proper system design (satisfy a radar protection curve and pre-screening point setups), high integrity radar altimeter detection has demonstrated its potential to protect any system from any threat to meet LAAS CAT I/III integrity requirements. Extending the usage of the radar altimeter further to become an aiding senor during the high integrity final coasting stage is possible. Additional research and development is required in the areas of radar altimeter error modeling and DEM. In particular, the digital elevation models beneath all possible flight paths in the LAAS service volume have be validated with the necessary integrity.

Fault isolation and exclusion. The innovation detection algorithm has shown superior detection performance on cycle slip errors. It has great potential to be able to detect and isolate an abrupt or step change in the GPS measurements. A successful error detection and exclusion algorithm can improve the system

integrity and continuity at the same time. However, further analysis on the probability of correct isolation and exclusion is required.

APPENDIX A

INS VELOCITY AND ATTITUDE ERROR DYNAMICS DERIVATION

The attitude error dynamic equations for an inertial navigation system are derived first, because some results are going to be used when deriving the velocity error dynamic equations. The Euler angle propagation for attitude information is a non-linear process which can be seen in equations 3.14 and 3.15. An estimated body-to-navigation (b2n) transformation can be broken down into two consecutive transformations: the first is the true b2n transformation, the second is the transformation using the three erroneous Euler angles:

$$\hat{C}_b^n = R_3(-\delta\psi)R_2(-\delta\theta)R_1(-\delta\phi)C_b^n = R_3(\delta\psi)^T R_2(\delta\theta)^T R_1(\delta\phi)^T C_b^n \tag{A.1}$$

The second transformation can be expressed as a mis-orientation matrix $B = [R_1(\delta\phi)R_2(\delta\theta)R_3(\delta\psi)]^T$. By expanding *B*, a matrix similar to C_b^n is expressed using the three Euler angle errors:

$$B = \begin{bmatrix} c(\delta\theta)c(\delta\psi) & -c(\delta\phi)s(\delta\psi)+s(\delta\phi)s(\delta\theta)c(\delta\psi) & s(\delta\phi)s(\delta\psi)+c(\delta\phi)c(\delta\psi)s(\delta\theta) \\ c(\delta\theta)s(\delta\psi) & c(\delta\phi)c(\delta\psi)+s(\delta\phi)s(\delta\theta)s(\delta\psi) & -s(\delta\phi)c(\delta\psi)+c(\delta\phi)s(\delta\psi)s(\delta\theta) \\ -s(\delta\theta) & s(\delta\phi)c(\delta\theta) & c(\delta\phi)c(\delta\theta) \end{bmatrix} \tag{A.2}$$

The tree Euler angle errors can be reasonably assumed to be small, so that the linearized attitude error transformation matrix is:

$$B \approx \begin{bmatrix} 1 & -\delta\psi & \delta\theta \\ \delta\psi & 1 & -\delta\phi \\ -\delta\theta & \delta\phi & 1 \end{bmatrix} \Rightarrow (I+\Psi), \Psi = \begin{bmatrix} 0 & -\delta\psi & \delta\theta \\ \delta\psi & 0 & -\delta\phi \\ -\delta\theta & \delta\phi & 0 \end{bmatrix} \tag{A.3}$$

Representing the three small Euler angle errors in a vector form as the attitude errors, Ψ is the matrix representation of the cross product form the Euler angle error vector:

$$\delta E = \begin{bmatrix} \delta\phi \\ \delta\theta \\ \delta\psi \end{bmatrix}, \Rightarrow \Psi = [\delta E \times] \tag{A.4}$$

The linearized equation A.1 is re-written:

$$\hat{C}_b^n = (I + \Psi) C_b^n \tag{A.5}$$

$$\Rightarrow \Psi + I = \hat{C}_b^n C_b^{n^T} \tag{A.6}$$

Taking the derivative on equation A.6:

$$\dot{\Psi} = \dot{\hat{C}}_b^n C_b^{n^T} + \hat{C}_b^n \dot{C}_b^{n^T} \tag{A.7}$$

The rate of change of C_b^n needs to be derived. Because the direct measurement taken from the gyro sensors is in the body frame, the derivation of $\dot{C}_b^n$ will start from a small transformation from the body frame at time $t + \Delta t$ to the body frame at the time t. In this way, the connection to the instantaneous body rotational rate can be established logically. Analogous to equation A.1, the transformation matrix $C_b^n(t + \Delta t)$ can be resolved into the product of transformation $C_b^n(t)$ and another transformation of three small Euler angles during Δt, which transforms a vector from the body frame at the time $t + \Delta t$ to the body frame at the time t: (note: the three small Euler angles are unrelated to the current three Euler attitude angles)

$$C_b^n(t + \Delta t) = C_b^n(t)(I + \Phi), \ \Phi = \begin{bmatrix} 0 & -\Delta\psi & \Delta\theta \\ \Delta\psi & 0 & -\Delta\phi \\ -\Delta\theta & \Delta\phi & 0 \end{bmatrix}$$

Applying the definition of derivative, the matrix time derivative can be derived as:

$$\dot{C}_b^n = \lim_{\Delta t \to 0} \frac{C_b^n(t + \Delta t) - C_b^n(t)}{\Delta t} \Rightarrow \lim_{\Delta t \to 0} \frac{C_b^n(t) + C_b^n(t)\Phi - C_b^n(t)}{\Delta t} = C_b^n \lim_{\Delta t \to 0} \frac{\Phi}{\Delta t}$$

$$\dot{C}_b^n = C_b^n \lim_{\Delta t \to 0} \begin{bmatrix} 0 & -\frac{\Delta\psi}{\Delta t} & \frac{\Delta\theta}{\Delta t} \\ \frac{\Delta\psi}{\Delta t} & 0 & -\frac{\Delta\phi}{\Delta t} \\ -\frac{\Delta\theta}{\Delta t} & \frac{\Delta\phi}{\Delta t} & 0 \end{bmatrix} = C_b^n \begin{bmatrix} 0 & -w_z & w_y \\ w_z & 0 & -w_x \\ -w_y & w_x & 0 \end{bmatrix}_{nb} = C_b^n \Omega_{nb}^b \tag{A.8}$$

Taking the transpose of both sides of equation A.8, and then changing the order between the differentiation and the transpose:

$$\frac{dC_b^{n^T}}{dt} = \dot{C}_n^b = (C_b^n \Omega_{nb}^b)^T = \Omega_{bn}^b C_n^b \tag{A.9}$$

The rotation rate Ω_{nb}^b can be further decomposed as $\Omega_{nb}^b = \Omega_{ib}^b - \Omega_{in}^b$, and substituting back to equation A.9:

$$\dot{C}_b^n = C_b^n \Omega_{ib}^b - C_b^n \Omega_{in}^b, \ \because \Omega_{in}^b = C_n^b \Omega_{in}^n C_n^{b^T} \text{ by similarity transformation}$$

$$\therefore \dot{C}_b^n = C_b^n \Omega_{ib}^b - C_b^n C_n^b \Omega_{in}^n C_b^n = C_b^n \Omega_{ib}^b - \Omega_{in}^n C_b^n \tag{A.10}$$

The derivative of the estimated transformation matrix can be expressed similarly:

$$\therefore \dot{\hat{C}}_b^n = \hat{C}_b^n \hat{\Omega}_{ib}^b - \hat{\Omega}_{in}^n \hat{C}_b^n \tag{A.11}$$

Equation A.7 can be re-written by substituting in equations A.10 and A.11, and expanding the results:

$$\begin{aligned} \dot{\Psi} &= (\hat{C}_b^n \hat{\Omega}_{ib}^b - \hat{\Omega}_{in}^n \hat{C}_b^n) C_b^{n^T} + \hat{C}_b^n (C_b^n \Omega_{ib}^b - \Omega_{in}^n C_b^n)^T \\ &= \hat{C}_b^n \hat{\Omega}_{ib}^b C_b^{n^T} - \hat{\Omega}_{in}^n \hat{C}_b^n C_b^{n^T} + \hat{C}_b^n \Omega_{ib}^{b\,T} C_b^{n^T} - \hat{C}_b^n C_b^{n^T} \Omega_{in}^{n\,T} \\ &= \hat{C}_b^n (\hat{\Omega}_{ib}^b - \Omega_{ib}^b) C_b^{n^T} - \hat{\Omega}_{in}^n \hat{C}_b^n C_b^{n^T} + \hat{C}_b^n C_b^{n^T} \Omega_{in}^n \end{aligned}$$

where the skew-symmetry matrix property, $\Omega_{ib}^{b\,T} = -\Omega_{ib}^b$ and $\Omega_{in}^{n\,T} = -\Omega_{in}^n$, has been applied. The estimated transformation matrix $\hat{C}_b^n$ can be replaced by equation A.5:

$$\begin{aligned}\dot{\Psi} &= (I+\Psi)C_b^n(\hat{\Omega}_{ib}^b - \Omega_{ib}^b)C_b^{n^T} - \hat{\Omega}_{in}^n(I+\Psi)C_b^nC_b^{n^T} + (I+\Psi)C_b^nC_b^{n^T}\Omega_{in}^n \\ &= (I+\Psi)C_b^n(\hat{\Omega}_{ib}^b - \Omega_{ib}^b)C_b^{n^T} - \hat{\Omega}_{in}^n(I+\Psi) + (I+\Psi)\Omega_{in}^n\end{aligned}$$

Use the definitions of $\delta\Omega_{ib}^b = \Omega_{ib}^b - \hat{\Omega}_{ib}^b$ and $\delta\Omega_{in}^n = \Omega_{in}^n - \hat{\Omega}_{in}^n$:

$$\begin{aligned}\dot{\Psi} &= -(I+\Psi)C_b^n\delta\Omega_{ib}^bC_b^{n^T} - (\Omega_{in}^n - \delta\Omega_{in}^n)(I+\Psi) + (I+\Psi)\Omega_{in}^n \\ &= -C_b^n\delta\Omega_{ib}^bC_b^{n^T} - \Psi C_b^n\delta\Omega_{ib}^bC_b^{n^T} - \Omega_{in}^n\Psi + \delta\Omega_{in}^n + \delta\Omega_{in}^n\Psi + \Psi\Omega_{in}^n \\ &\approx -C_b^n\delta\Omega_{ib}^bC_b^{n^T} - \Omega_{in}^n\Psi + \delta\Omega_{in}^n + \Psi\Omega_{in}^n\end{aligned} \tag{A.12}$$

where any term has the second or higher order errors is neglected.

The final results of the attitude error dynamic equations are expressed by converting equation A.12 from a matrix form into a vector form through the relation in equation A.4:

$$\begin{aligned}&\left[\delta\dot{E}\times\right] = \left[\delta E\times\right]\left[\vec{w}_{in}^n\times\right] - \left[\vec{w}_{in}^n\times\right]\left[\delta E\times\right] - C_b^n\left[\delta\vec{w}_{ib}^b\times\right]C_b^{n^T} + \left[\delta\vec{w}_{in}^n\times\right] \\ &\Rightarrow \delta\dot{E} = -\vec{w}_{in}^n\times\delta E - C_b^n\delta\vec{w}_{ib}^b + \delta\vec{w}_{in}^n\end{aligned} \tag{A.13}$$

The velocity error dynamic equations for an inertial navigation system are derived next. The navigation equation from Chapter 3 equation 3.10 is:

$$\dot{\vec{v}}_e^n = C_b^n\vec{f}^b - (2\vec{w}_{ie}^n + \vec{w}_{en}^n)\times\vec{v}_e^n + \vec{g}_l^n \tag{A.14}$$

$$\dot{\hat{v}}_e^n = \hat{C}_b^n\hat{f}^n - (2\hat{w}_{ie}^n + \hat{w}_{en}^n)\times\hat{v}_e^n + \hat{g}_l^n \tag{A.15}$$

Equation A.14 is the true navigation equation, while A.15 is the estimated version. The errors can be derived by the definition:

$$\begin{aligned}\delta\dot{\vec{v}}_e^n &= \dot{\vec{v}}_e^n - \dot{\hat{v}}_e^n \\ &= (C_b^n\vec{f}^b - \hat{C}_b^n\hat{f}^b) - [(2\vec{w}_{ie}^n + \vec{w}_{en}^n)\times\vec{v}_e^n - (2\hat{w}_{ie}^n + \hat{w}_{en}^n)\times\hat{v}_e^n] + (\vec{g}_l^n - \hat{g}_l^n)\end{aligned} \tag{A.16}$$

Substituting equation A.5 for $\hat{C}_b^n$, and applying $\hat{f}^b = \vec{f}^b - \delta\vec{f}^b$, $\hat{v}_e^n = \vec{v}_e^n - \delta\vec{v}_e^n$, $\hat{w}_{ie}^n = \vec{w}_{ie}^n - \delta\vec{w}_{ie}^n$, $\hat{w}_{en}^n = \vec{w}_{en}^n - \delta\vec{w}_{en}^n$, $\hat{g}_l^n = \vec{g}_l^n - \delta\vec{g}_l^n$ in the equation above:

$$\begin{aligned}\delta\dot{\vec{v}}_e^n &= [C_b^n \vec{f}^b - (I+\Psi)C_b^n(\vec{f}^b - \delta\vec{f}^b)] \\ &\quad - \{(2\vec{w}_{ie}^n + \vec{w}_{en}^n)\times\vec{v}_e^n - [2(\vec{w}_{ie}^n - \delta\vec{w}_{ie}^n) + (\vec{w}_{en}^n - \delta\vec{w}_{en}^n)]\times(\vec{v}_e^n - \delta\vec{v}_e^n)\} + \delta\vec{g}_l^n\end{aligned}$$

$$\Rightarrow \delta\dot{\vec{v}}_e^n \approx -\Psi C_b^n \vec{f}^b + C_b^n \delta\vec{f}^b - [(2\delta\vec{w}_{ie}^n + \delta\vec{w}_{en}^n)\times\vec{v}_e^n + (2\vec{w}_{ie}^n + \vec{w}_{en}^n)\times\delta\vec{v}_e^n] + \delta\vec{g}_l^n \quad \text{(A.17)}$$

The results are the first order approximation. The Coriolis effect errors are small generally compared with other error terms. Therefore, the error terms caused by the Coriolis effect are negligible in equation A.17. The final results for the navigation error dynamic equations are then:

$$\begin{aligned}\delta\dot{\vec{v}}_e^n &= -\Psi C_b^n \vec{f}^b + C_b^n \delta\vec{f}^b + \delta\vec{g}_l^n = -[\delta E\times]\vec{f}^n + C_b^n \delta\vec{f}^b + \delta\vec{g}_l^n \\ &= [\vec{f}^n\times]\delta E + C_b^n \delta\vec{f}^b + \delta\vec{g}_l^n\end{aligned} \quad \text{(A.18)}$$

APPENDIX B

COORDINATE TRANSFORMATION

Most of the coordinate transformations used can be easily found in navigation or dynamic systems related books. Hence, the transformation which is derived here is specific to the needs of this research. Considering the future extended applications for the hybrid navigation system, the local-level coordinates at a reference station might have a significant orientation difference from the user's navigation frame when the distance between them becomes bigger. A transformation matrix to precisely transfer a user local-level coordinates to a reference station's local frame can be obtained through a three rotation Euler angle transformation. Figure C.1 shows the geographical relation between the *n* frame (user's local-level frame or navigation frame) and *r* frame (reference station's local-level frame).

The first step is to rotate the *n* frame to an intermediate local-level frame which is located at the same longitude as the *n* frame but zero latitude, this intermediate frame is

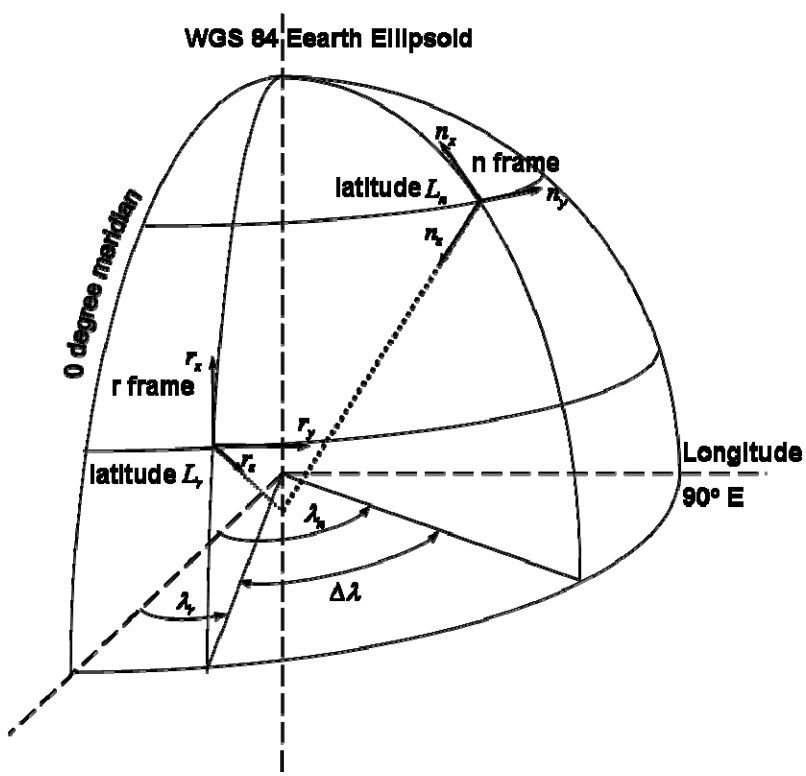

Figure B.1 WGS 84 Ellipsoid and Local-level Frames

noted as $m1$ frame. This transformation is done through a rotation about the n_y axis by the angle L_n:

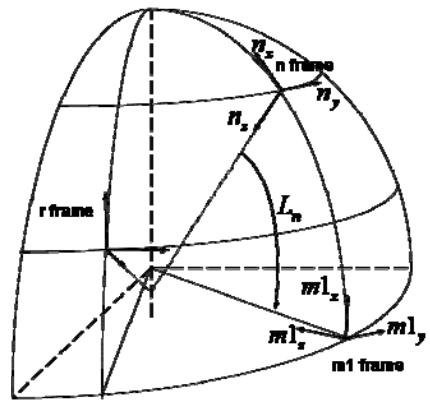

$$C_n^{m1} = R_2(L_n) = \begin{bmatrix} \cos(L_n) & 0 & -\sin(L_n) \\ 0 & 1 & 0 \\ \sin(L_n) & 0 & \cos(L_n) \end{bmatrix},$$

The second step is to rotate the $m1$ frame about its x axis by $-\Delta\lambda$ (the longitude difference between the n and r frame) to reach another intermediate frame $m2$ which has the same longitude as the reference frame,

where $\Delta\lambda = \lambda_n - \lambda_r$:

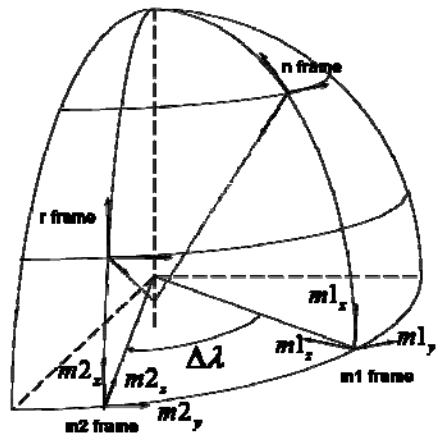

$$C_{m1}^{m2} = R_1(-\Delta\lambda) = \begin{bmatrix} 1 & 0 & 0 \\ 0 & \cos(\Delta\lambda) & -\sin(\Delta\lambda) \\ 0 & \sin(\Delta\lambda) & \cos(\Delta\lambda) \end{bmatrix},$$

The last step is to rotate the $m2$ frame about its y axis by $-L_r$ to reach the destination r frame:

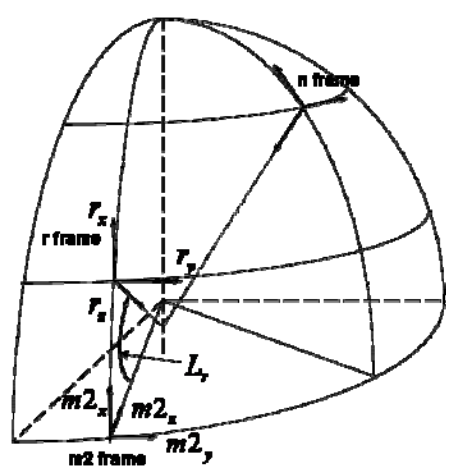

$$C_{m2}^{r} = R_2(-L_r) = \begin{bmatrix} \cos(L_r) & 0 & \sin(L_r) \\ 0 & 1 & 0 \\ -\sin(L_r) & 0 & \cos(L_r) \end{bmatrix},$$

The complete transformation matrix is:

$$C_n^r = C_{m2}^r C_{m1}^{m2} C_n^{m1} \quad ,$$

APPENDIX C

DISCRETE TIME PROCESS NOISE IN KALMAN FILTER

The Kalman filter is the most important element of the navigation system, and it is the core process in this research because of its capability in handling the time-varying linear system. To ensure the filter will work properly, two key points need to be satisfied: one is to establish the correct (or conservative) process noise for the system time propagation, another is to properly model measurement noise.

A well-defined system process noise can account for the mis-modeling or simplified model errors. It is especially important for the inertial navigation system because that all IMU related errors will be fed into the system dynamic equations directly. From equations 3.50, 3.58 and 3.60, the hybrid navigation system process noise is defined as:

$$\begin{aligned}\vec{W} &= \begin{bmatrix} \vec{W}_I \\ 0 \\ \vec{n}_{Mp} \\ \vec{n}_{mp} \end{bmatrix}_{(15+4+4\cdot sn)\times 1} \\ &= \begin{bmatrix} (C_b^n \vec{W}_a)^T & (C_b^n \vec{W}_g)^T & \vec{n}_g{}^T & \vec{n}_a{}^T & \vec{n}_{gm}{}^T & 0_{1\times(4+2\cdot sn)} & \vec{n}_{Mp}^T & \vec{n}_{mp}^T \end{bmatrix}^T \end{aligned} \tag{C.1}$$

where sn is the number of satellite in view and $\vec{W}_a = \delta S_f^a \vec{f}^b + \delta M_{is}^a \vec{f}^b + \vec{v}_a$, $\vec{W}_g = \delta S_f^g \vec{w}_{ib}^b + \delta M_{is}^g \vec{w}_{ib}^b + \vec{v}_g$. The signs of all errors are set to be positive because the contributions to the state errors are added up in the statistic sense (the positive or negative sign actually doesn't matter in a covariance analysis).

The covariance of the process noise can be obtained by:

$$
\begin{aligned}
\Sigma^W &= E[\vec{W}\vec{W}^T] \\
&= diag(\ E\left[C_b^n \vec{W}_a \vec{W}_a{}^T C_b^{nT}\right]\ E\left[C_b^n \vec{W}_g \vec{W}_g{}^T C_b^{nT}\right]\ E\left[\vec{n}_g \vec{n}_g{}^T\right]\ E\left[\vec{n}_a \vec{n}_a{}^T\right]\ E\left[\vec{n}_{gm} \vec{n}_{gm}{}^T\right] \\
&\quad 0_{1\times(4+2\cdot ns)}\ \ E\left[\vec{n}_{Mp} \vec{n}_{Mp}{}^T\right]\ E\left[\vec{n}_{mp} \vec{n}_{mp}{}^T\right]) \\
&= diag(\ C_b^n E\left[\vec{W}_a \vec{W}_a{}^T\right] C_b^{nT}\ \ C_b^n E\left[\vec{W}_g \vec{W}_g{}^T\right] C_b^{nT}\ \ E\left[\vec{n}_g \vec{n}_g{}^T\right]\ E\left[\vec{n}_a \vec{n}_a{}^T\right]\ E\left[\vec{n}_{gm} \vec{n}_{gm}{}^T\right] \\
&\quad 0_{1\times(4+2\cdot ns)}\ \ E\left[\vec{n}_{Mp} \vec{n}_{Mp}{}^T\right]\ E\left[\vec{n}_{mp} \vec{n}_{mp}{}^T\right])
\end{aligned}
\tag{C.2}
$$

where $diag(\,)$ means a block diagonal matrix with the diagonal blocks equal to those elements or matrixes inside the brackets. There are seven diagonal blocks inside the process noise covariance matrix, Σ^W, the first block can be expanded as:

$$
C_b^n E\left[\vec{W}_a \vec{W}_a{}^T\right] C_b^{nT} = C_b^n E[(\delta S_f^a \vec{f}^b + \delta M_{is}^a \vec{f}^b + \vec{v}_a)(\delta S_f^a \vec{f}^b + \delta M_{is}^a \vec{f}^b + \vec{v}_a)^T] C_b^{nT} \tag{C.3}
$$

The focus is on the expectation term:

$$
\begin{aligned}
&E[(\delta S_f^a \vec{f}^b + \delta M_{is}^a \vec{f}^b + \vec{v}_a)(\delta S_f^a \vec{f}^b + \delta M_{is}^a \vec{f}^b + \vec{v}_a)^T] \\
&= E[\delta S_f^a \vec{f}^b (\delta S_f^a \vec{f}^b)^T] + E[\delta M_{is}^a \vec{f}^b (\delta M_{is}^a \vec{f}^b)^T] + E[\vec{v}_a (\vec{v}_a)^T]
\end{aligned}
\tag{C.4}
$$

The assumption of no correlation among the scale factor error, misalignment error and accelerometer measurement noise is applied in equation C.4. By recalling the IMU sensor model from equation 3.33 [IONtutorial02], a detailed derivation for equation C.4 proceeds as following:

$$
\begin{bmatrix} \tilde{f}_x(t) \\ \tilde{f}_y(t) \\ \tilde{f}_z(t) \end{bmatrix} = \left(I + \begin{bmatrix} s_x & 0 & 0 \\ 0 & s_y & 0 \\ 0 & 0 & s_z \end{bmatrix} \right) \begin{bmatrix} f_x(t) \\ f_y(t) \\ f_z(t) \end{bmatrix} + \begin{bmatrix} 0 & m_{xy} & m_{xz} \\ m_{yx} & 0 & m_{yz} \\ m_{zx} & m_{zy} & 0 \end{bmatrix} \begin{bmatrix} f_x(t) \\ f_y(t) \\ f_z(t) \end{bmatrix} + \begin{bmatrix} b_x^{all}(t) \\ b_y^{all}(t) \\ b_z^{all}(t) \end{bmatrix} + \begin{bmatrix} v_x(t) \\ v_y(t) \\ v_z(t) \end{bmatrix}
$$

For $E[\delta S_f \vec{f}^b (\delta S_f \vec{f}^b)^T]$ term:

$$
\delta S_f \vec{f}^b = \begin{bmatrix} \delta s_x & 0 & 0 \\ 0 & \delta s_y & 0 \\ 0 & 0 & \delta s_z \end{bmatrix} \begin{bmatrix} f_x \\ f_y \\ f_z \end{bmatrix} = \begin{bmatrix} \delta s_x f_x \\ \delta s_y f_y \\ \delta s_z f_z \end{bmatrix}
$$

$$E[\delta S_f^a \vec{f}^b (\delta S_f^a \vec{f}^b)^T] = E(\begin{bmatrix} \delta s_x f_x \\ \delta s_y f_y \\ \delta s_z f_z \end{bmatrix} \begin{bmatrix} \delta s_x f_x & \delta s_y f_y & \delta s_z f_z \end{bmatrix})$$

$$= E\begin{bmatrix} (\delta s_x f_x)^2 & \delta s_x f_x \delta s_y f_y & \delta s_x f_x \delta s_z f_z \\ \delta s_x f_x \delta s_y f_y & (\delta s_y f_y)^2 & \delta s_y f_y \delta s_z f_z \\ \delta s_x f_x \delta s_z f_z & \delta s_y f_y \delta s_z f_z & (\delta s_z f_z)^2 \end{bmatrix}$$

Assuming that there is no correlation among the scale factor errors across the individual axis, and all scale factor errors are distributed as $N(0, \sigma_s^2)$:

$$E[\delta S_f^a \vec{f}^b (\delta S_f^a \vec{f}^b)^T] = \begin{bmatrix} E(\delta s_x{}^2) f_x{}^2 & 0 & 0 \\ 0 & E(\delta s_y{}^2) f_y{}^2 & 0 \\ 0 & 0 & E(\delta s_z{}^2) f_z{}^2 \end{bmatrix}$$

$$= \begin{bmatrix} (\sigma_s f_x)^2 & 0 & 0 \\ 0 & (\sigma_s f_y)^2 & 0 \\ 0 & 0 & (\sigma_s f_z)^2 \end{bmatrix} \tag{C.5}$$

$$= \begin{bmatrix} f_x{}^2 & 0 & 0 \\ 0 & f_y{}^2 & 0 \\ 0 & 0 & f_z{}^2 \end{bmatrix} \sigma_s^2$$

For $E[\delta M_{is}^a \vec{f}^b (\delta M_{is}^a \vec{f}^b)^T]$ term, the IMU misalignment results from the imperfection in mounting of the sensors. This manufacturing error makes the actual triad of the IMU sensors (accelerometers and gyroscopes) deviate from the ideal triad which is assumed to be perfectly orthogonal. An assumed assembly process for the general IMU is that an ideal triad is targeted as the base to be aligned with by the accelerometer and gyroscope sensors. Therefore, the misalignment of each individual axis is modeled as independent. As a result, the measurement along each axis is affected by the true acceleration or rotation about the other two axes. The misalignment error for a single axis is illustrated by using accelerometers as an example:

In Figure C.1, the actual $\tilde{z}_b$ axis is misaligned with true z_b axis in the sensor body frame by an orientation angle, ψ_h and a deviation angle ψ_v; where ψ_h is the angle between the true x_b axis and the projection of $\tilde{z}_b$ onto the horizontal plan, and ψ_v is the angle between $\tilde{z}_b$ and the true z_b axis.

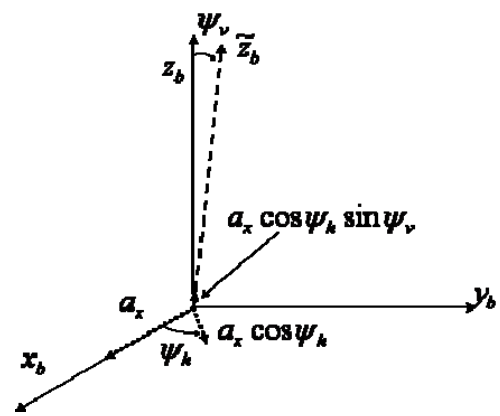

Figure C.1 Misalignment of Z axis of IMU body frame

If there is an acceleration, a_x, along the x_b axis, the accelerometer aligned with $\tilde{z}_b$ axis will inevitably sense a small portion of this acceleration, which can be calculated by the geometry relationship. Another similar mis-sensing can be induced by the acceleration along the y_b axis. Hence, the total measurement error due to misalignment for the specific force along the *z* axis is:

$$\begin{aligned}\Delta f_z &= \cos\psi_h \sin\psi_v a_x + \sin\psi_h \sin\psi_v a_y \\ &\approx \psi_v \cos\psi_h a_x + \psi_v \sin\psi_h a_y\end{aligned} \tag{C.6}$$

The approximation is reasonable because the magnitude of the deviation angle is small in general. Equation C.6 can be further analyzed in two ways, depending on where a further calibration on the deviation angle is possible or not. For the case of a high quality IMU, the angle ψ_v is already too small to be calibrated, and equation C.6 can be used directly to define the residual errors due to misalignment by replacing $\psi_v \Rightarrow \delta\psi_v$:

$$\delta f_z = \delta\psi_v \cos\psi_h a_x + \delta\psi_v \sin\psi_h a_y \tag{C.7}$$

If a further calibration on the deviation angle ψ_v is possible (various calibration techniques can be applied to remove a significant amount of ψ_v [Titterton04][Hou04]), the residual error of the specific force due to the residual misalignment angles can be shown by taking perturbations on both sides of equation C.6:

$$\begin{aligned} \delta f_z &= (\delta\psi_v \cos\psi_h + \psi_v \delta\psi_h \sin\psi_h) a_x + (\delta\psi_v \sin\psi_h - \psi_v \delta\psi_h \sin\psi_h) a_y \\ &\approx \delta\psi_v \cos\psi_h a_x + \delta\psi_v \sin\psi_h a_y \end{aligned} \tag{C.8}$$

where an approximation on $\delta\psi_h \cdot \psi_v \approx 0$ is applied because that both are small.

Equations C.7 and C.8 are the same equation, which can be expressed in a general form by substituting the accelerations, $\vec{a}$,with the equivalent specific forces, $\vec{f}$:

$$\begin{aligned} \delta f_z &= \delta\psi_v \cos\psi_h f_x + \delta\psi_v \sin\psi_h f_y \\ &= \delta m_{zx} f_x + \delta m_{zy} f_y \end{aligned} \tag{C.9}$$

Extending the result in equation C.9 to the misalignment residual errors for the other two axes, the results for all three axes can be expressed in a matrix form:

$$\delta M_{is}^{a} \vec{f}^{b} = \begin{bmatrix} 0 & \delta m_{xy} & \delta m_{xz} \\ \delta m_{yx} & 0 & \delta m_{yz} \\ \delta m_{zx} & \delta m_{zy} & 0 \end{bmatrix} \begin{bmatrix} f_x \\ f_y \\ f_z \end{bmatrix} = \begin{bmatrix} \delta m_{xy} f_y + \delta m_{xz} f_z \\ \delta m_{yx} f_x + \delta m_{yz} f_z \\ \delta m_{zx} f_x + \delta m_{zy} f_y \end{bmatrix} \tag{C.10}$$

Because the majority of misalignment errors have been eliminated by the great effort either from the manufacturing process or through the internal calibration algorithm, the residual misalignment angles, therefore, can be treated as random variables. A few assumptions on the statistical properties of the misalignment angles are stated: the residual deviation angle has a zero mean normal distribution probability density function with standard deviation σ_M : $\delta\psi_v \approx N(0, \sigma_M^2)$; the orientation angle, ψ_h, has an uniform distribution probability density function with magnitude of $1/2\pi$ in the range $0 \sim 2\pi$.

The last assumption is that these two angles are independent of each other, and so are all six misalignment angles when a three axis IMU misalignment model is considered.

The mean and variance of the trigonometric functions of the orientation angle can be derived as:

$$E[\cos\psi_h] = \int_0^{2\pi} \cos\psi_h / 2\pi \cdot d\psi_h = 0 = E[\sin\psi_h] \tag{C.11}$$

$$E[(\cos\psi_h)^2] = \int_0^{2\pi} (\cos\psi_h)^2 / 2\pi \cdot d\psi_h = 1/2 = E[(\sin\psi_h)^2] \tag{C.12}$$

The mean and variance of any single element inside the misalignment error model matrix δM_{is}^{a} can be deduced by applying the results from equations C.11 and D12:

$$E[\delta m_{zx}] = E[\delta\psi_v \cos\psi_h] = E[\delta\psi_v]E[\cos\psi_h] = 0 \tag{C.13}$$

$$E[(\delta m_{zx})^2] = E[\delta\psi_v{}^2 \cos^2\psi_h] = E[\delta\psi_v{}^2]E[\cos^2\psi_h] = \sigma_M^2 / 2 \tag{C.14}$$

The results from equations C.13 and C.14 can be applied to the other elements in δM_{is}^{a}.

Based on previous results, the covariance matrix for the residual misalignment errors can be obtained:

$$E[\delta M_{is}^{a} \vec{f}^{b} (\delta M_{is}^{a} \vec{f}^{b})^T]$$
$$= E\left(\begin{bmatrix} \delta m_{xy} f_y + \delta m_{xz} f_z \\ \delta m_{yx} f_x + \delta m_{yz} f_z \\ \delta m_{zx} f_x + \delta m_{zy} f_y \end{bmatrix} \begin{bmatrix} \delta m_{xy} f_y + \delta m_{xz} f_z & \delta m_{yx} f_x + \delta m_{yz} f_z & \delta m_{zx} f_x + \delta m_{zy} f_y \end{bmatrix} \right)$$

After expansion, the equation above becomes:

$$E[\delta M_{is}\vec{f}^{\,b}(\delta M_{is}\vec{f}^{\,b})^T]$$

$$= E\begin{bmatrix} (\delta m_{xy} f_y + \delta m_{xz} f_z)^2 & (\delta m_{xy} f_y + \delta m_{xz} f_z)(\delta m_{yx} f_x + \delta m_{yz} f_z) & (\delta m_{xy} f_y + \delta m_{xz} f_z)(\delta m_{zx} f_x + \delta m_{zy} f_y) \\ (\delta m_{yx} f_x + \delta m_{yz} f_z)(\delta m_{xy} f_y + \delta m_{xz} f_z) & (\delta m_{yx} f_x + \delta m_{yz} f_z)^2 & (\delta m_{yx} f_x + \delta m_{yz} f_z)(\delta m_{zx} f_x + \delta m_{zy} f_y) \\ (\delta m_{zx} f_x + \delta m_{zy} f_y)(\delta m_{xy} f_y + \delta m_{xz} f_z) & (\delta m_{zx} f_x + \delta m_{zy} f_y)(\delta m_{yx} f_x + \delta m_{yz} f_z) & (\delta m_{zx} f_x + \delta m_{zy} f_y)^2 \end{bmatrix}$$

Since the correlation among the six elements in δM_{is}^{a} is zero:

$$E[\delta M_{is}\vec{f}^{b}(\delta M_{is}\vec{f}^{b})^T] = \begin{bmatrix} E(\delta m_{xy} f_y)^2 + E(\delta m_{xz} f)^2 & 0 & 0 \\ 0 & E(\delta m_{yx} f_x)^2 + E(\delta m_{yz} f_z)^2 & 0 \\ 0 & 0 & E(\delta m_{zx} f_x)^2 + E(\delta m_{zy} f_y)^2 \end{bmatrix}$$

$$= \begin{bmatrix} f_y^{\,2} + f_z^{\,2} & 0 & 0 \\ 0 & f_x^{\,2} + f_z^{\,2} & 0 \\ 0 & 0 & f_x^{\,2} + f_y^{\,2} \end{bmatrix} \frac{\sigma_M^2}{2} \tag{C.15}$$

For the $E[\vec{v}_a \vec{v}_a^{\,T}]$ term:

$$E[\vec{v}_a \vec{v}_a^{\,T}] = E[\begin{bmatrix} v_{ax} \\ v_{ay} \\ v_{az} \end{bmatrix} \begin{bmatrix} v_{ax} & v_{ay} & v_{az} \end{bmatrix}] = E\begin{bmatrix} v_{ax}^{\,2} & v_{ax}v_{ay} & v_{ax}v_{az} \\ v_{ay}v_{ax} & v_{ay}^{\,2} & v_{ay}v_{az} \\ v_{az}v_{ax} & v_{az}v_{ay} & v_{az}^{\,2} \end{bmatrix}$$

Since the noise is white, there is no correlation between any two axes, and all noises are distributed as $N(0, \sigma_{va}^2)$:

$$E[\vec{v}_a \vec{v}_a^{\,T}] = \begin{bmatrix} E(v_{ax}^{\,2}) & 0 & 0 \\ 0 & E(v_{ay}^{\,2}) & 0 \\ 0 & 0 & E(v_{az}^{\,2}) \end{bmatrix} = I\sigma_{va}^2 \tag{C.16}$$

Applying all the derived results into equation C.4, the process noise for accelerometer errors is presented:

$$E\left[\vec{W}_a\vec{W}_a^{\,T}\right]=\begin{bmatrix} f_x^{\,2} & 0 & 0 \\ 0 & f_y^{\,2} & 0 \\ 0 & 0 & f_z^{\,2} \end{bmatrix}\sigma_s^2+\begin{bmatrix} f_y^{\,2}+f_z^{\,2} & 0 & 0 \\ 0 & f_x^{\,2}+f_z^{\,2} & 0 \\ 0 & 0 & f_x^{\,2}+f_y^{\,2} \end{bmatrix}\frac{\sigma_M^2}{2}+I\sigma_{va}^2 \qquad \text{(C.17)}$$

By handling the gyro process noise term similarly to the accelerometer, the results can be derived as:

$$E\left[\vec{W}_g\vec{W}_g^{\,T}\right]=\begin{bmatrix} w_x^{\,2} & 0 & 0 \\ 0 & w_y^{\,2} & 0 \\ 0 & 0 & w_z^{\,2} \end{bmatrix}\sigma_s^2+\begin{bmatrix} w_y^{\,2}+w_z^{\,2} & 0 & 0 \\ 0 & w_x^{\,2}+w_z^{\,2} & 0 \\ 0 & 0 & w_x^{\,2}+w_y^{\,2} \end{bmatrix}\frac{\sigma_M^2}{2}+I\sigma_{vg}^2 \qquad \text{(C.18)}$$

where $\vec{w}_{ib}^{\,b}=[w_x \quad w_y \quad w_z]^T$

The rest of the non-zero terms in equation C.1 share the common properties since they are driving white noise of the first order GMRPs. Therefore, the results are similar to equation C.16 with different magnitudes:

$$E[\vec{n}_a\vec{n}_a^{\,T}]=\begin{bmatrix} E(n_{ax}^{\,2}) & 0 & 0 \\ 0 & E(n_{ay}^{\,2}) & 0 \\ 0 & 0 & E(n_{az}^{\,2}) \end{bmatrix}=I\sigma_{na}^2 \qquad \text{(C.19)}$$

$$E[\vec{n}_g\vec{n}_g^{\,T}]=\begin{bmatrix} E(n_{gx}^{\,2}) & 0 & 0 \\ 0 & E(n_{gy}^{\,2}) & 0 \\ 0 & 0 & E(n_{gz}^{\,2}) \end{bmatrix}=I\sigma_{ng}^2 \qquad \text{(C.20)}$$

$$E[\vec{n}_{gm}\vec{n}_{gm}^{\,T}]=\begin{bmatrix} E(n_{\xi}^{\,2}) & 0 & 0 \\ 0 & E(n_{\varsigma}^{\,2}) & 0 \\ 0 & 0 & E(n_d^{\,2}) \end{bmatrix}=\begin{bmatrix} \sigma_{\delta\xi}^{\,2} & 0 & 0 \\ 0 & \sigma_{\delta\varsigma}^{\,2} & 0 \\ 0 & 0 & \sigma_{\delta\Delta g(0)}^{\,2} \end{bmatrix} \qquad \text{(C.21)}$$

$$E[\vec{n}_{Mp}\vec{n}_{Mp}^{\,T}]=\begin{bmatrix} E(n_{Mp}^{1\,2}) & \cdots & 0 \\ \vdots & \ddots & \vdots \\ 0 & \cdots & E(n_{Mp}^{sn\,2}) \end{bmatrix}_{sn\times sn}=\begin{bmatrix} \sigma_{Mp}^{1\,2} & \cdots & 0 \\ \vdots & \ddots & \vdots \\ 0 & \cdots & \sigma_{Mp}^{sn\,2} \end{bmatrix}_{sn\times sn} \qquad \text{(C.22)}$$

$$E[\vec{n}_{mp}\vec{n}_{mp}{}^{T}] = \begin{bmatrix} E(n_{mp}^{1}{}^{2}) & \cdots & 0 \\ \vdots & \ddots & \vdots \\ 0 & \cdots & E(n_{mp}^{sn}{}^{2}) \end{bmatrix}_{sn\times sn} = \begin{bmatrix} \sigma_{mp}^{1}{}^{2} & \cdots & 0 \\ \vdots & \ddots & \vdots \\ 0 & \cdots & \sigma_{mp}^{sn}{}^{2} \end{bmatrix}_{sn\times sn} \tag{C.23}$$

APPENDIX D

MORE RESULTS

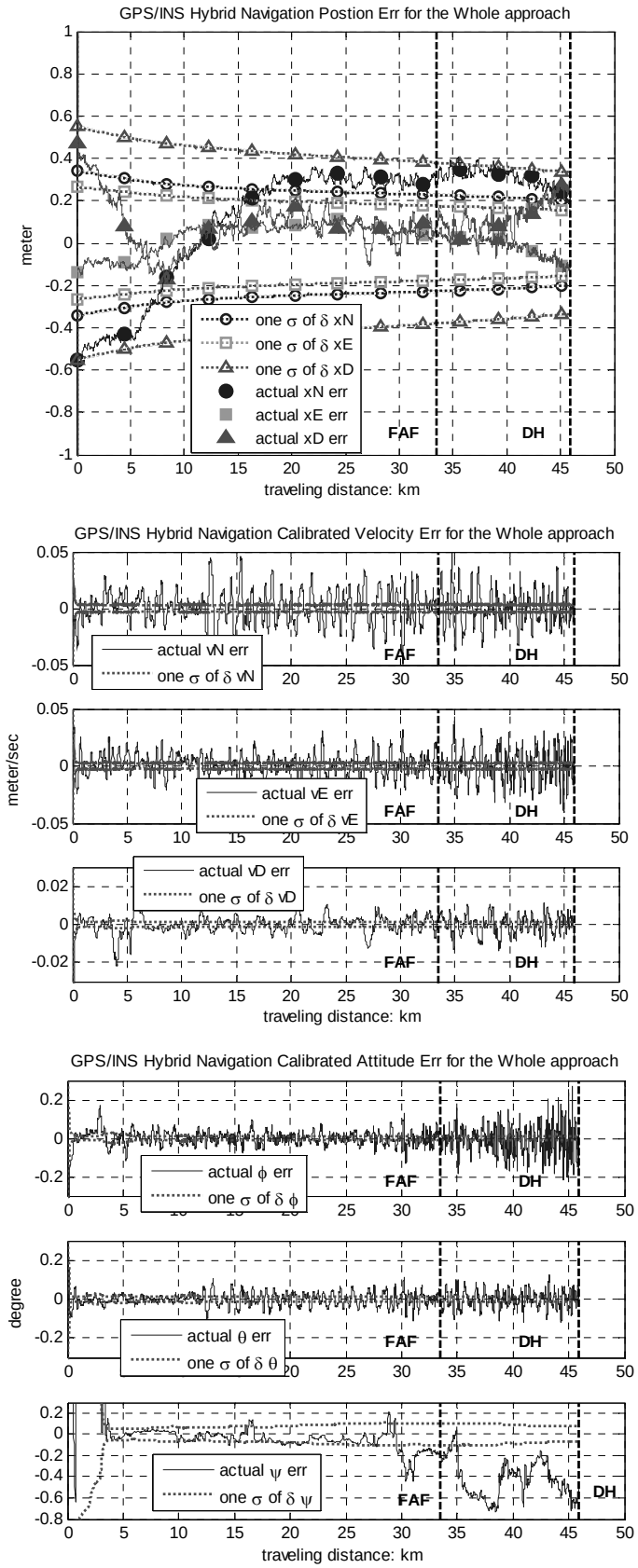

Figure D.1. GPS/INS Hybrid Navigation System Validation by Flight Data: Approach One.

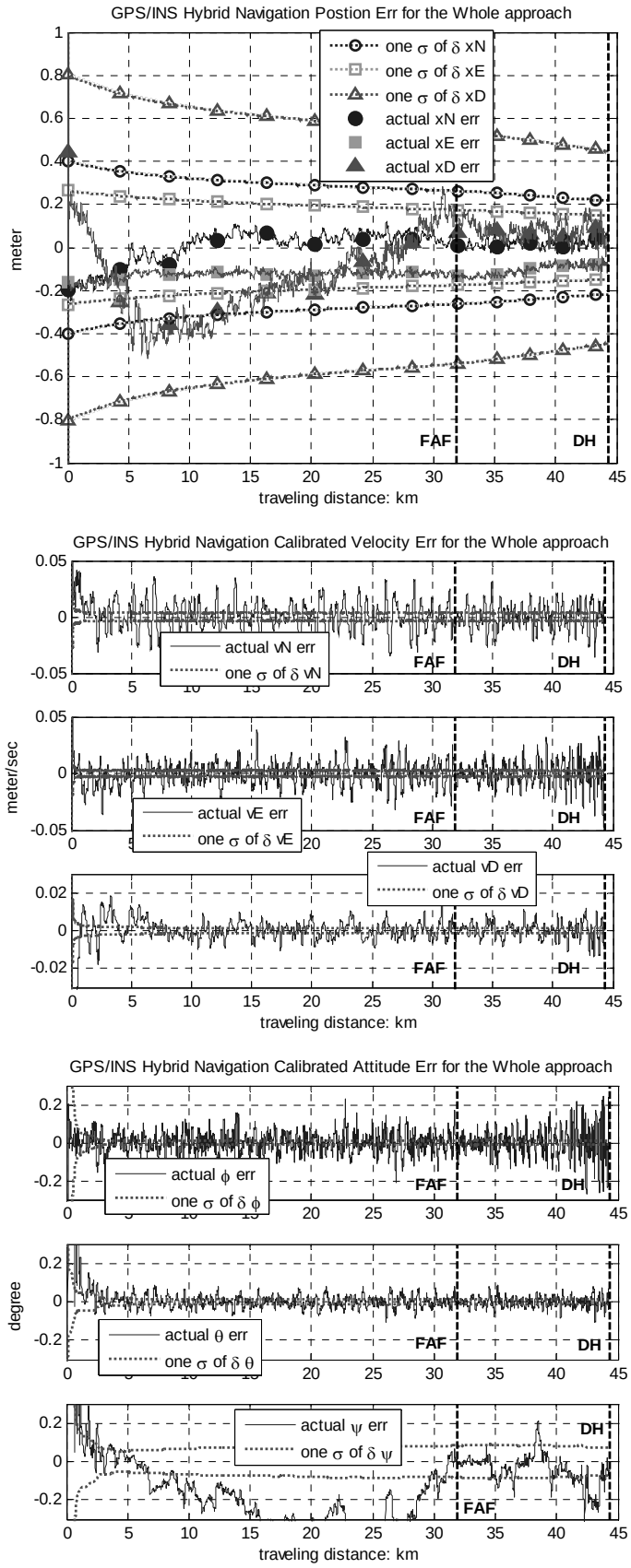

Figure D.2. GPS/INS Hybrid Navigation System Validation by Flight Data: Approach Three.

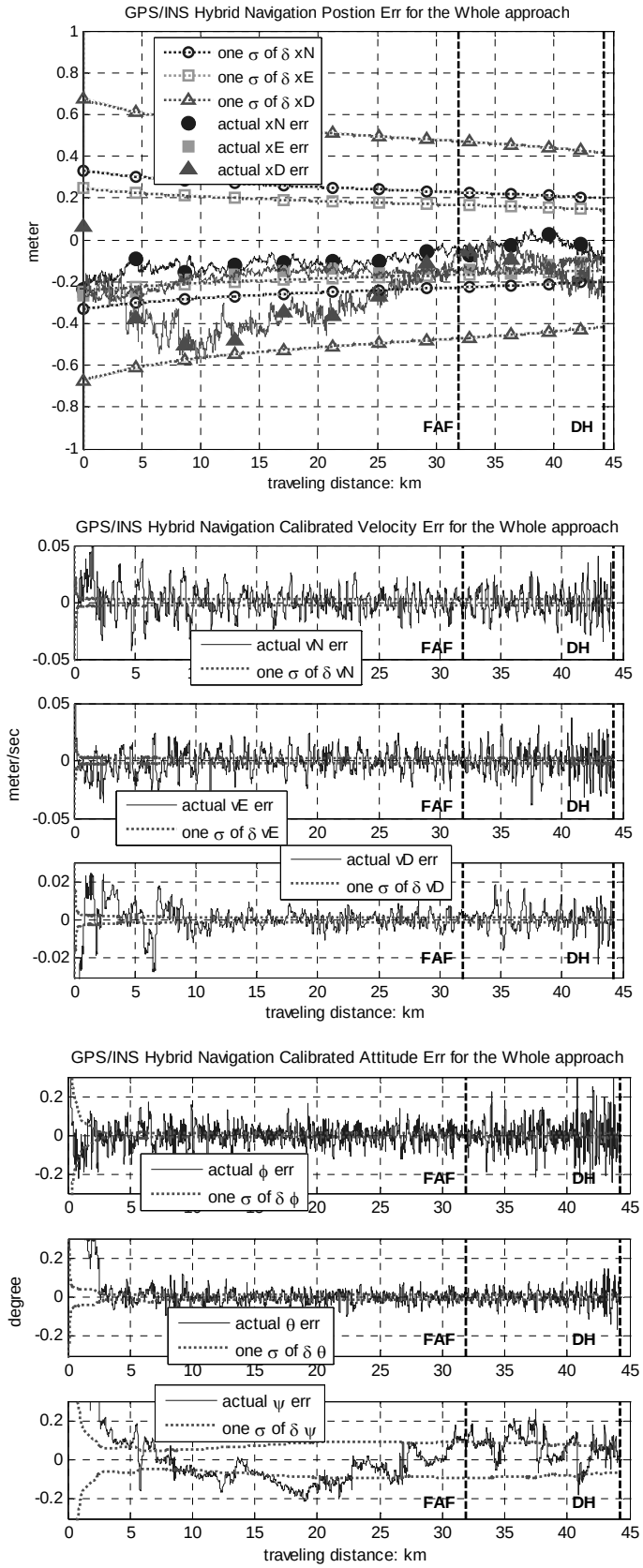

Figure D.3. GPS/INS Hybrid Navigation System Validation by Flight Data: Approach Four.

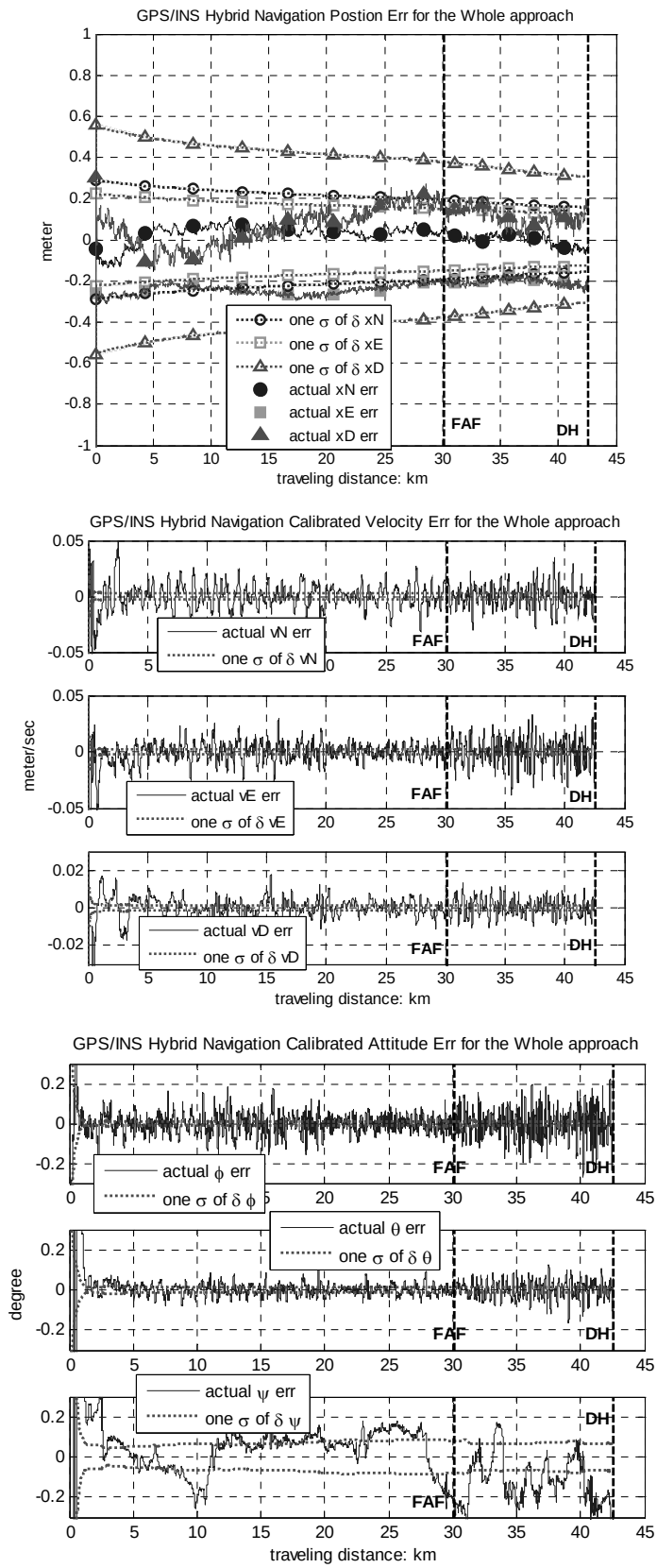

Figure D.4. GPS/INS Hybrid Navigation System Validation by Flight Data: Approach Five.

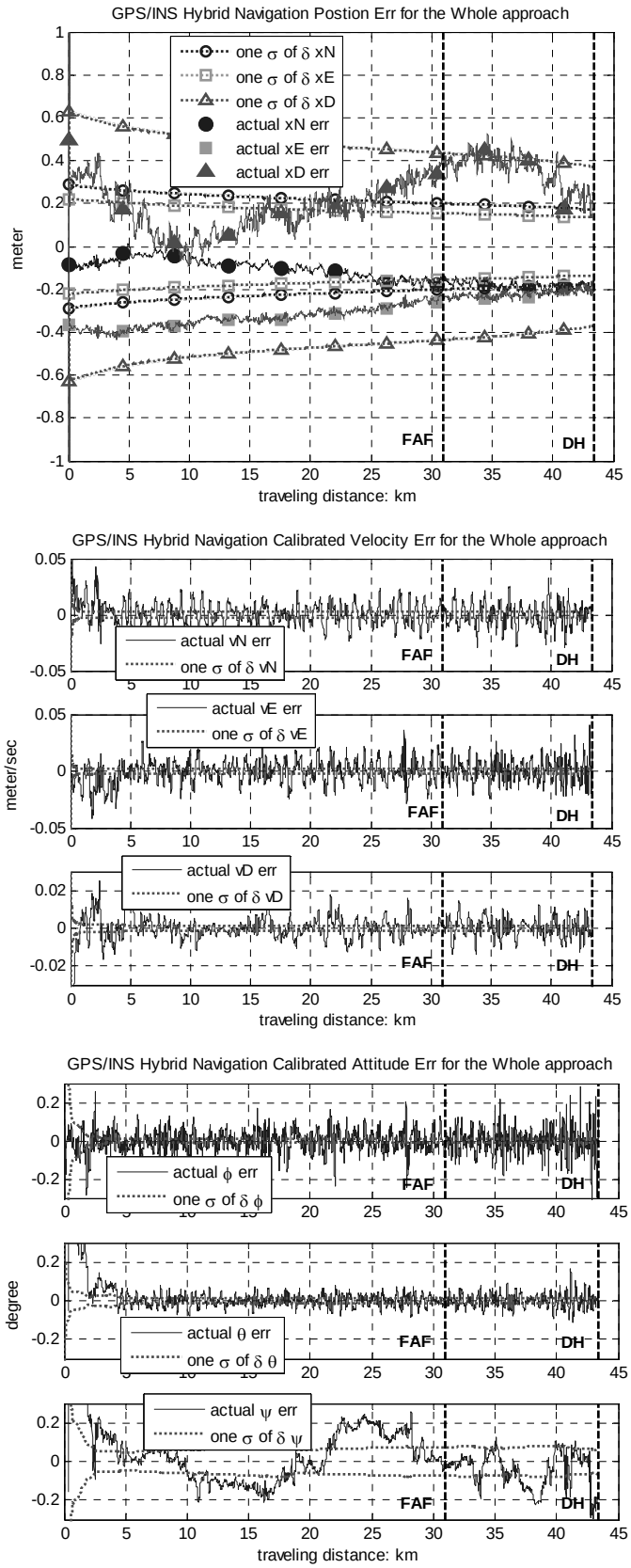

Figure D.5. GPS/INS Hybrid Navigation System Validation by Flight Data: Approach Six.

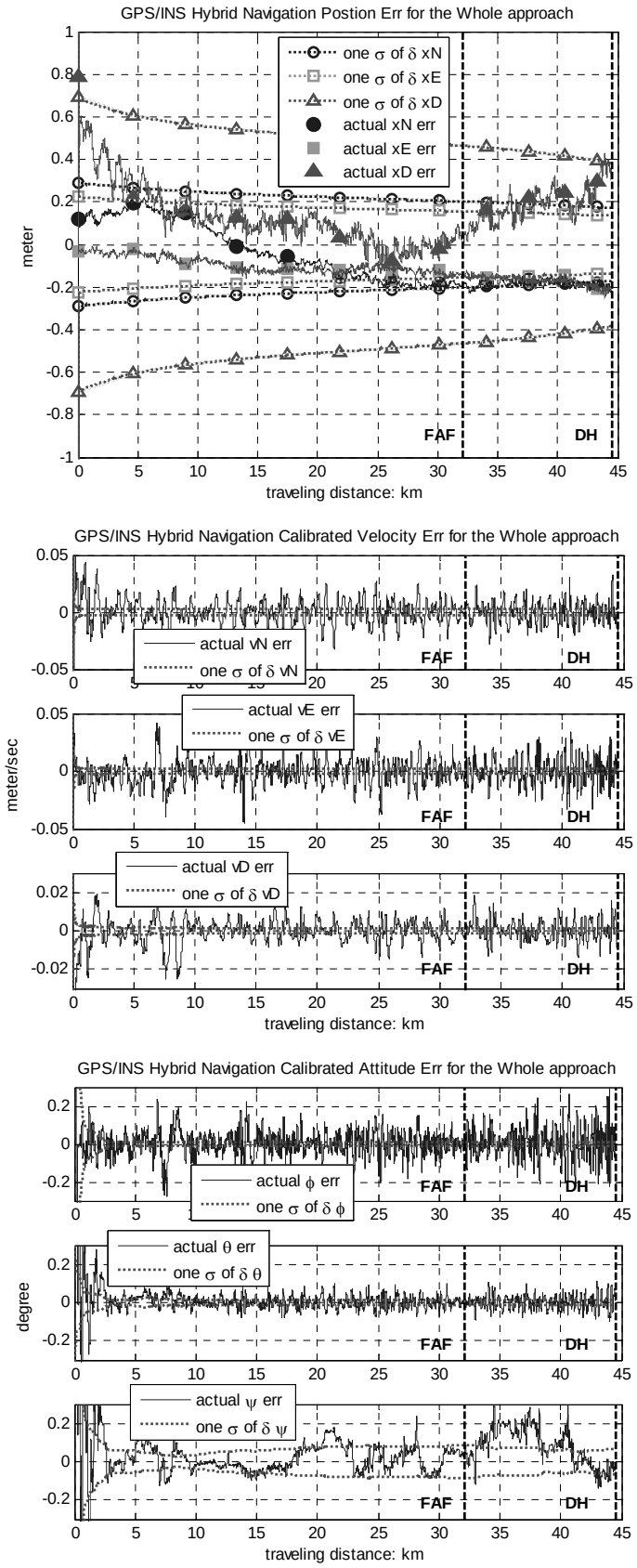

Figure D.6. GPS/INS Hybrid Navigation System Validation by Flight Data: Approach Seven.

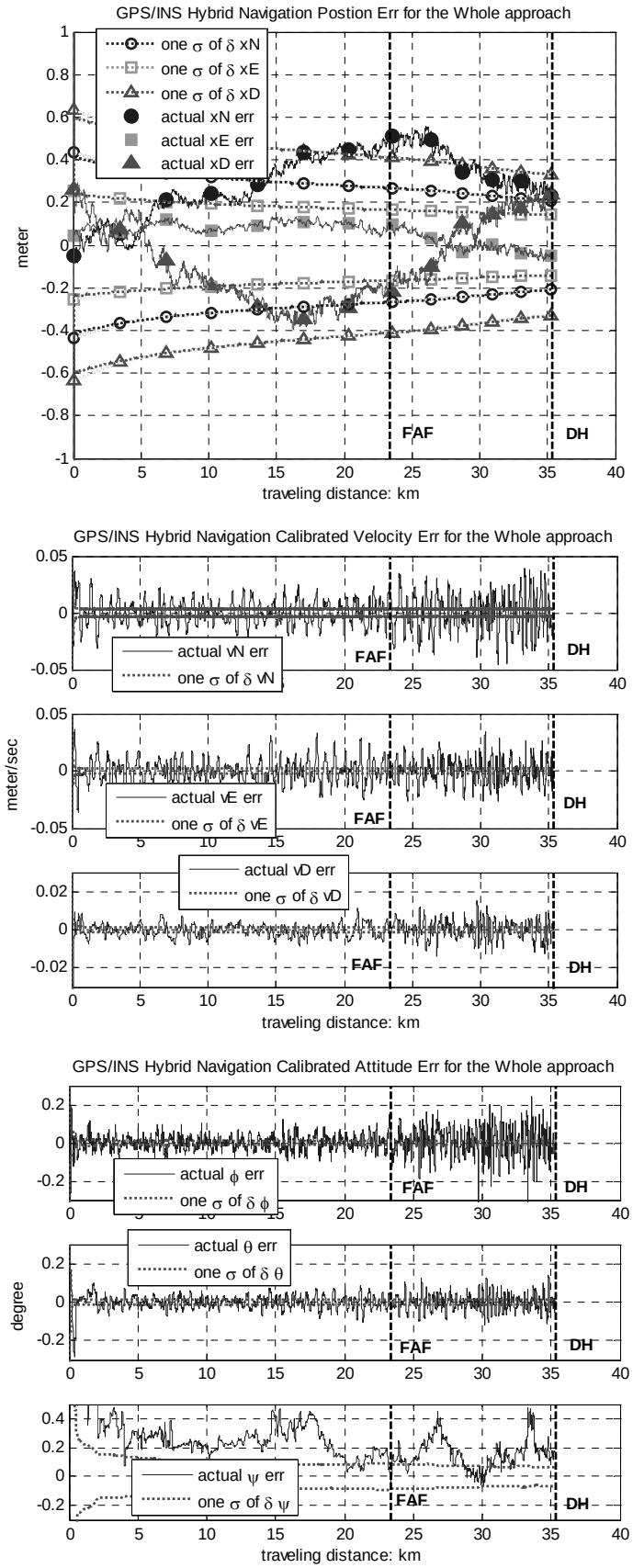

Figure D.7. GPS/INS Hybrid Navigation System Validation by Flight Data: Approach Eight.

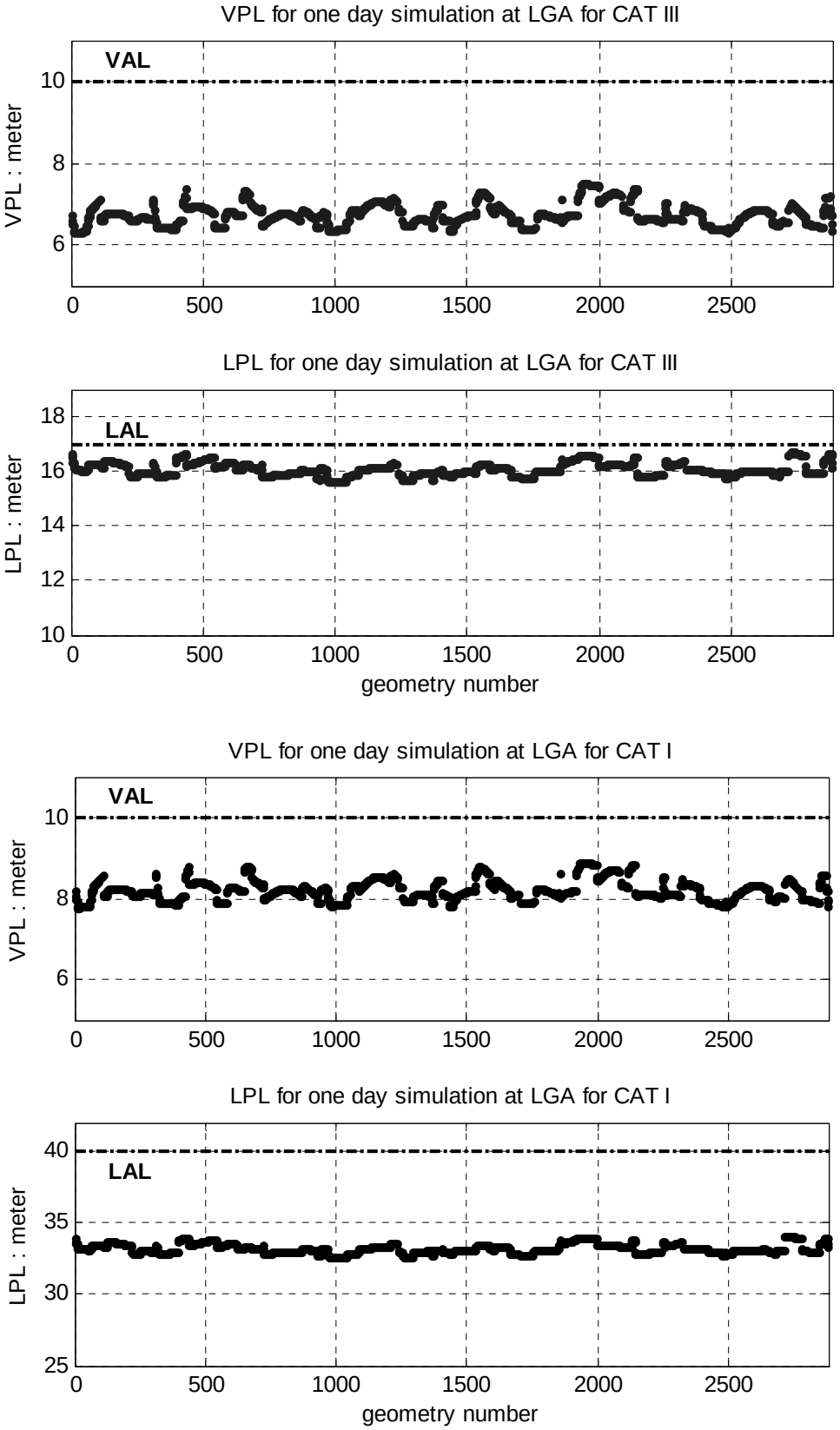

Figure D.8. Fault-free Availability Simulation Results at LGA Airport

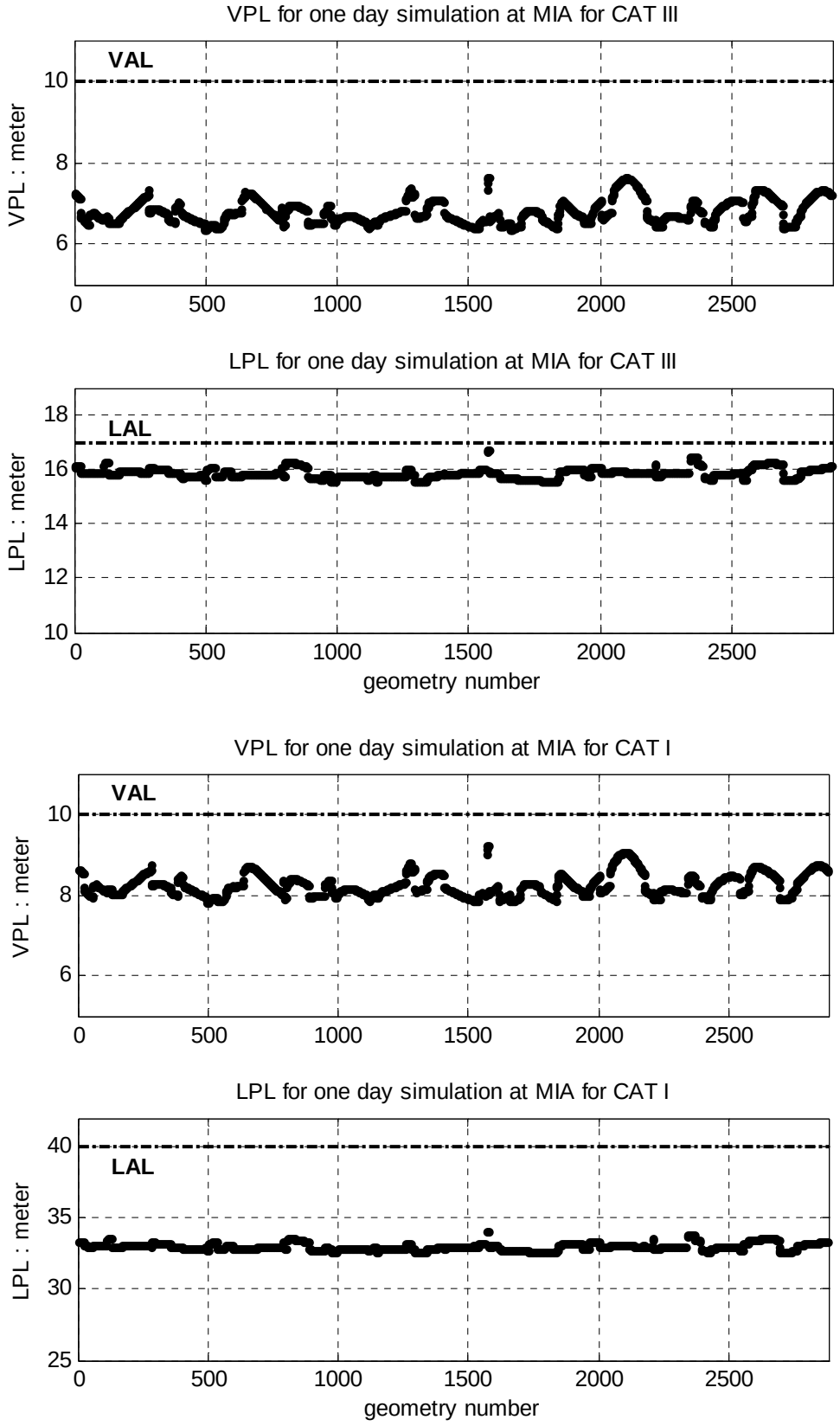

Figure D.9. Fault-free Availability Simulation Results at MIA Airport

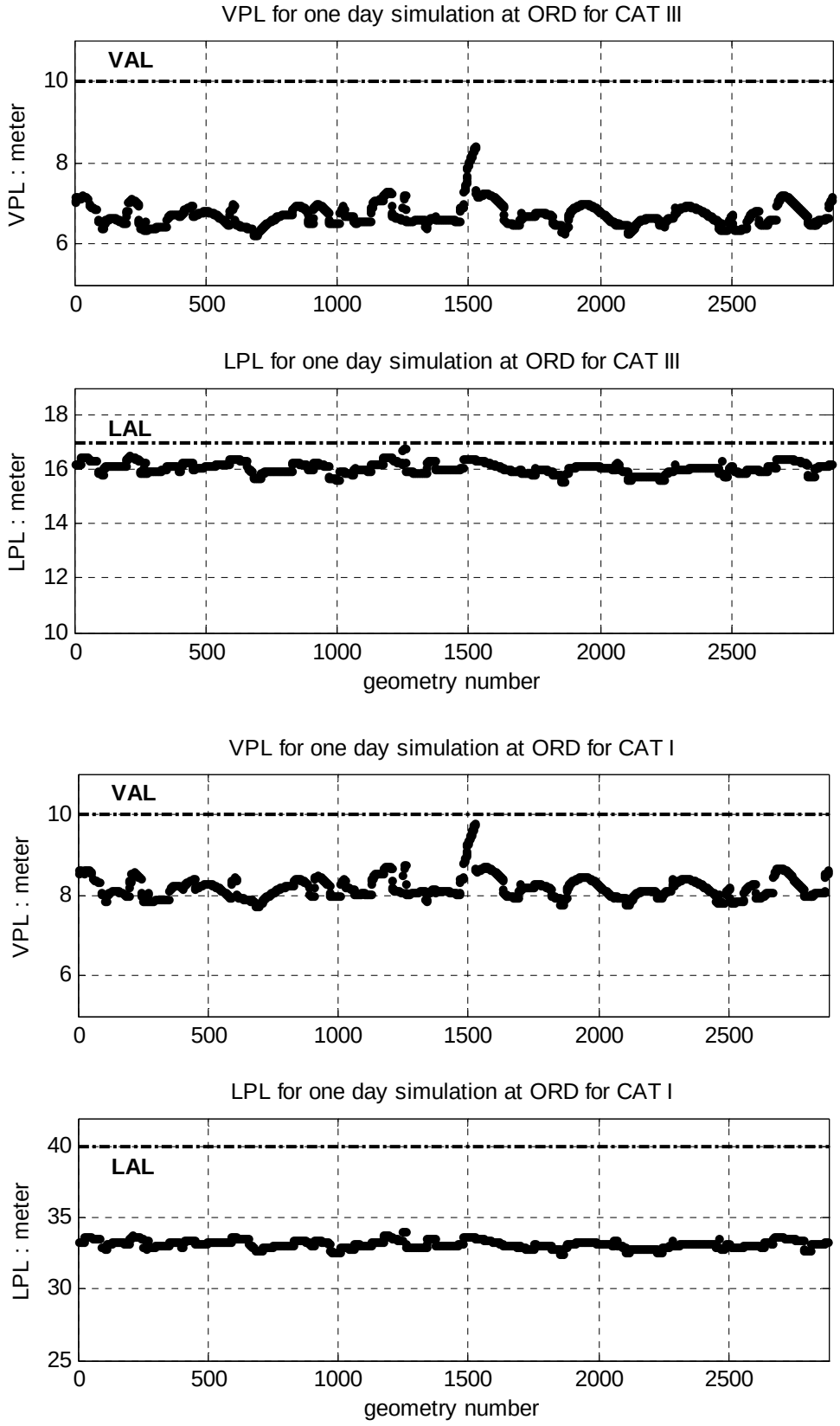

Figure D.10. Fault-free Availability Simulation Results at ORD Airport

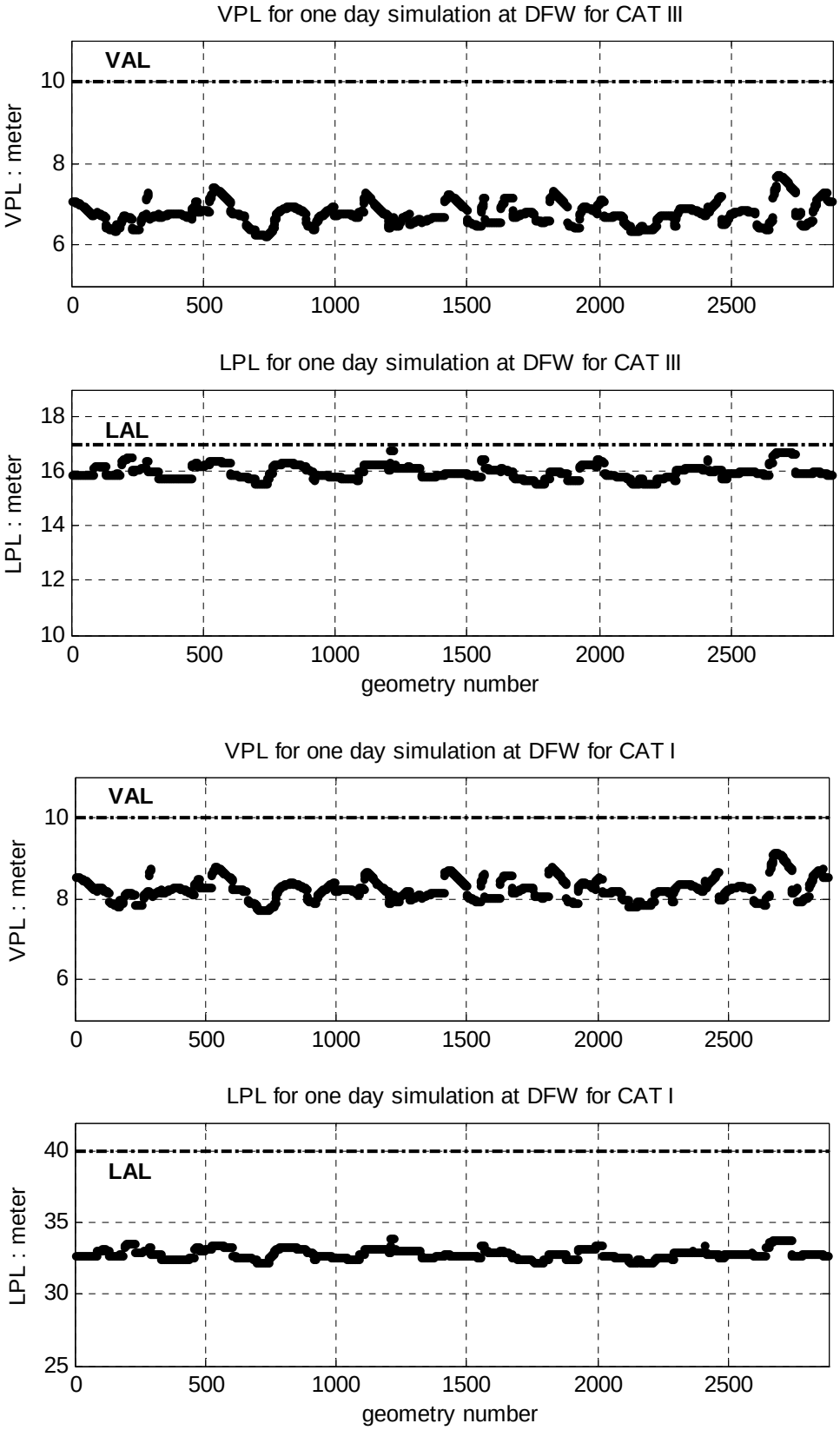

Figure D.11. Fault-free Availability Simulation Results at DFW Airport

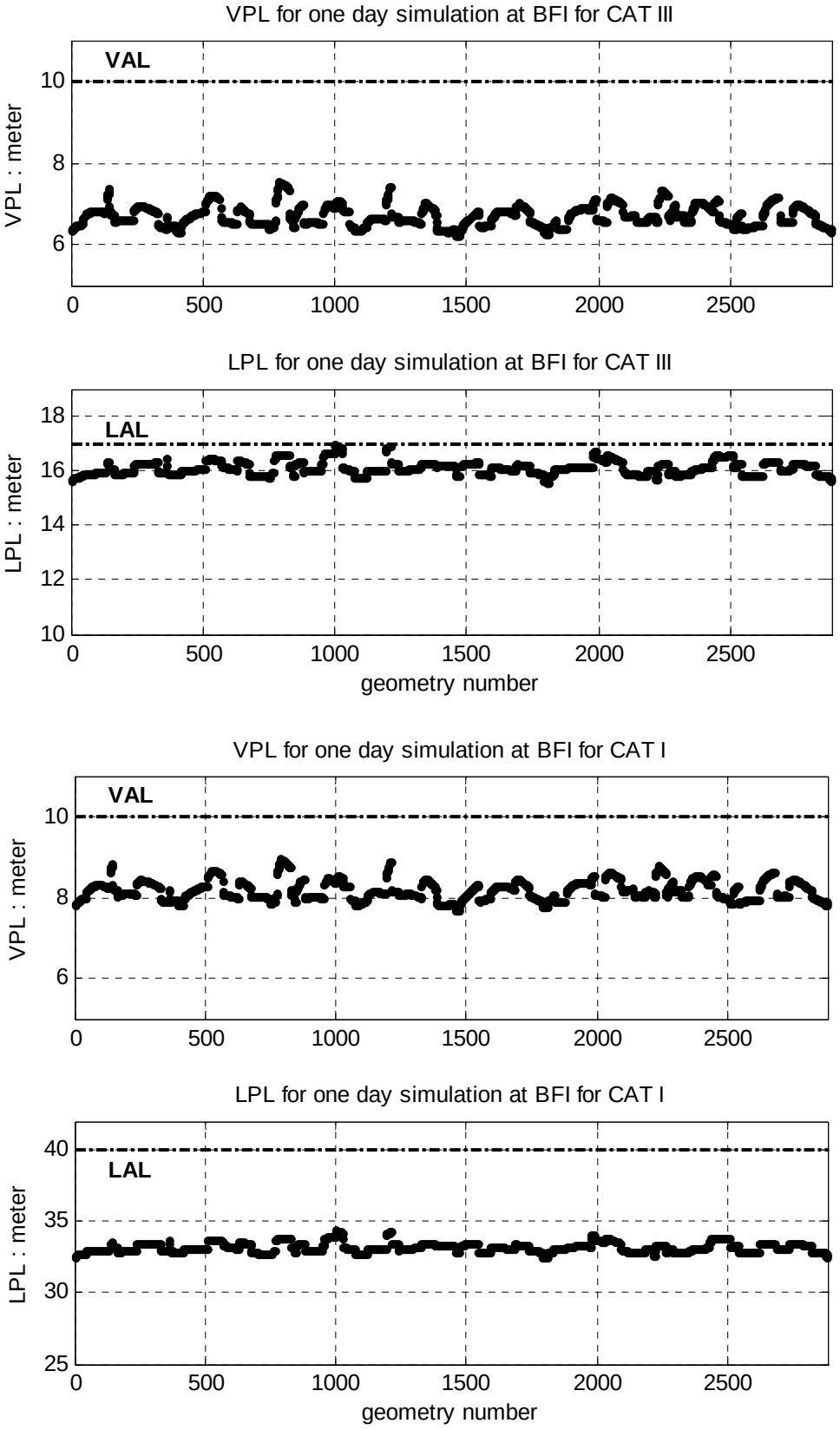

Figure D.12. Fault-free Availability Simulation Results at BFI Airport

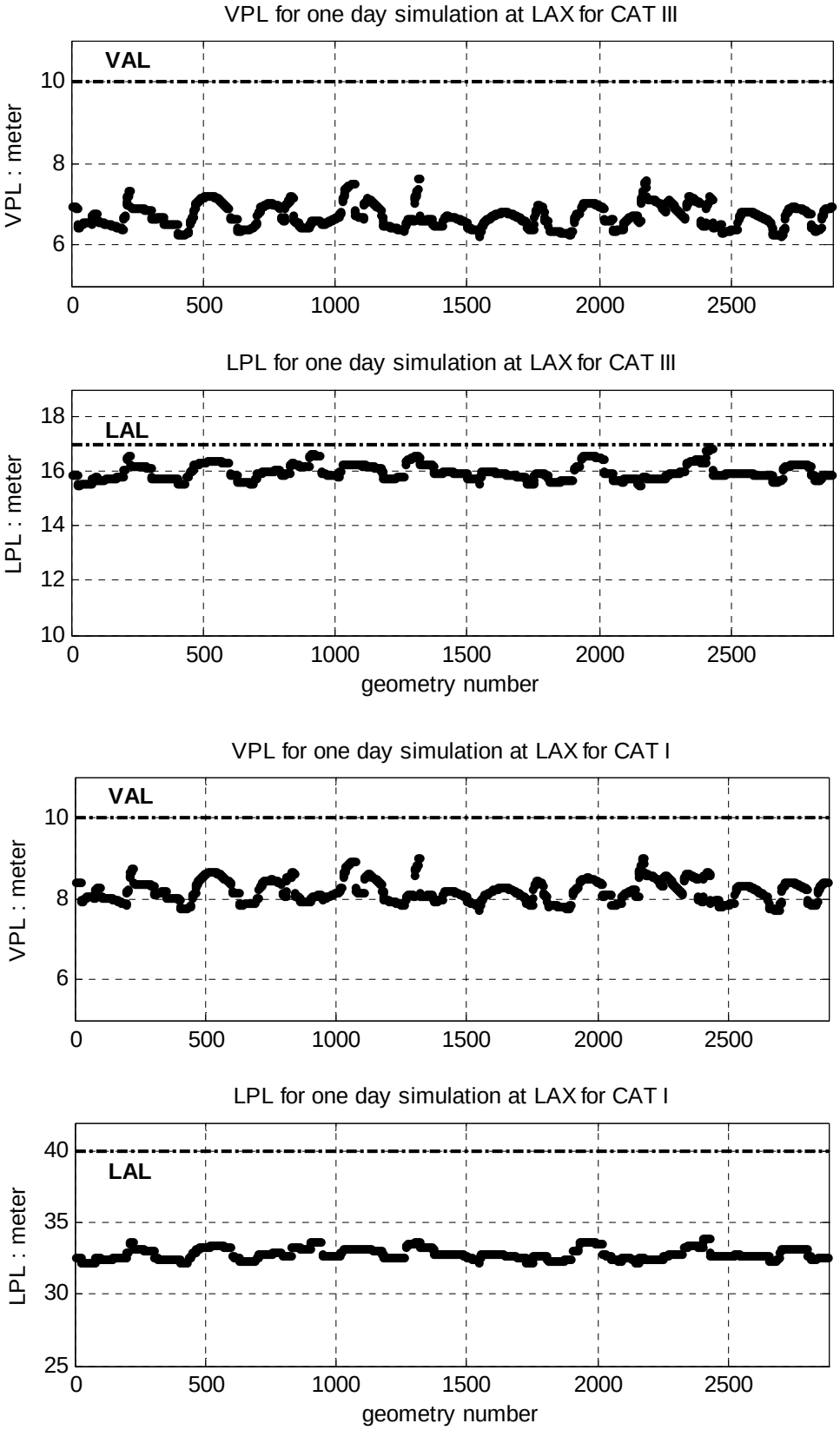

Figure D.13. Fault-free Availability Simulation Results at LAX Airport

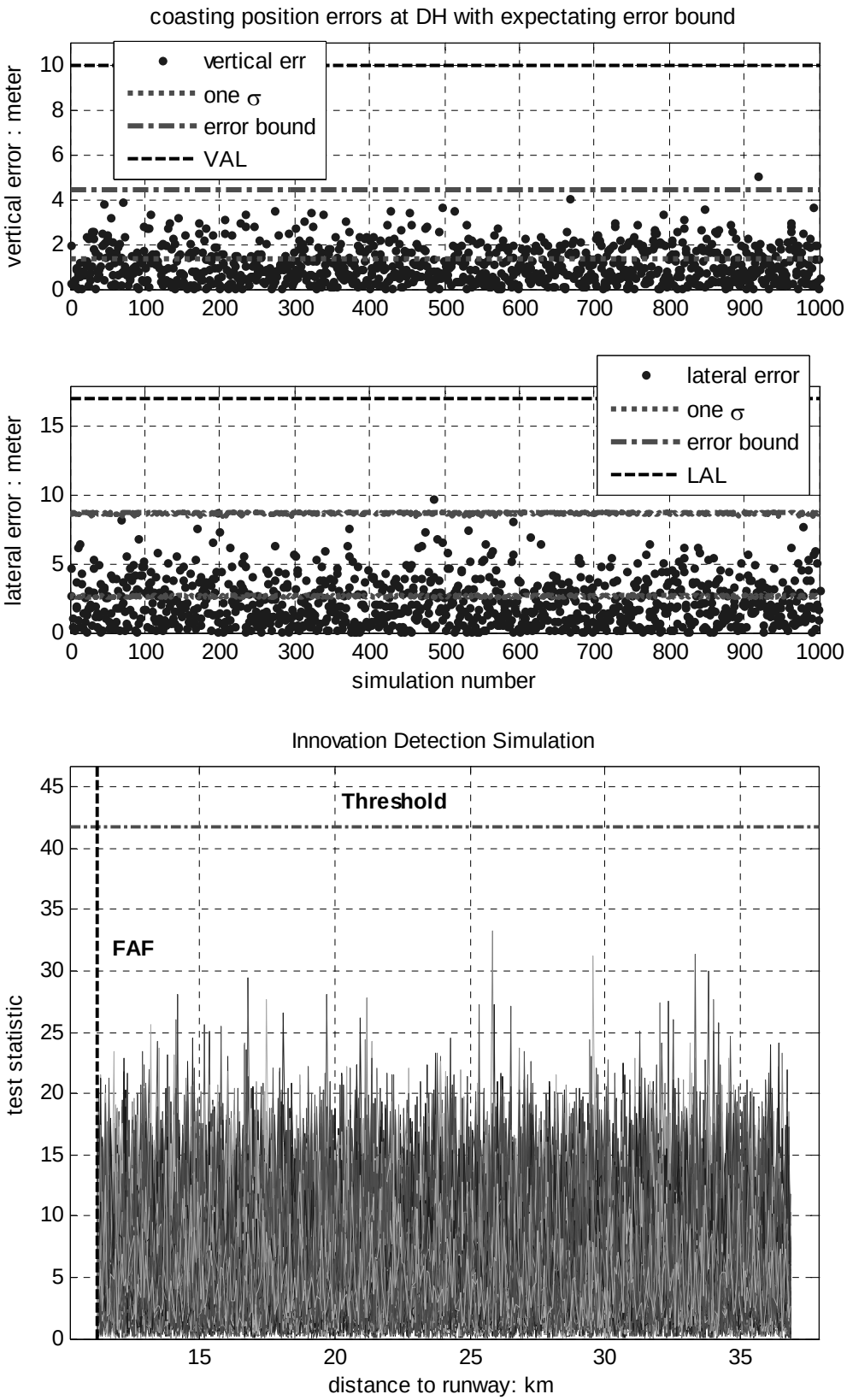

Figure D.14. 1000 Times Monte Carlo Simulation Results at ORD Airport for One Geometry (1)

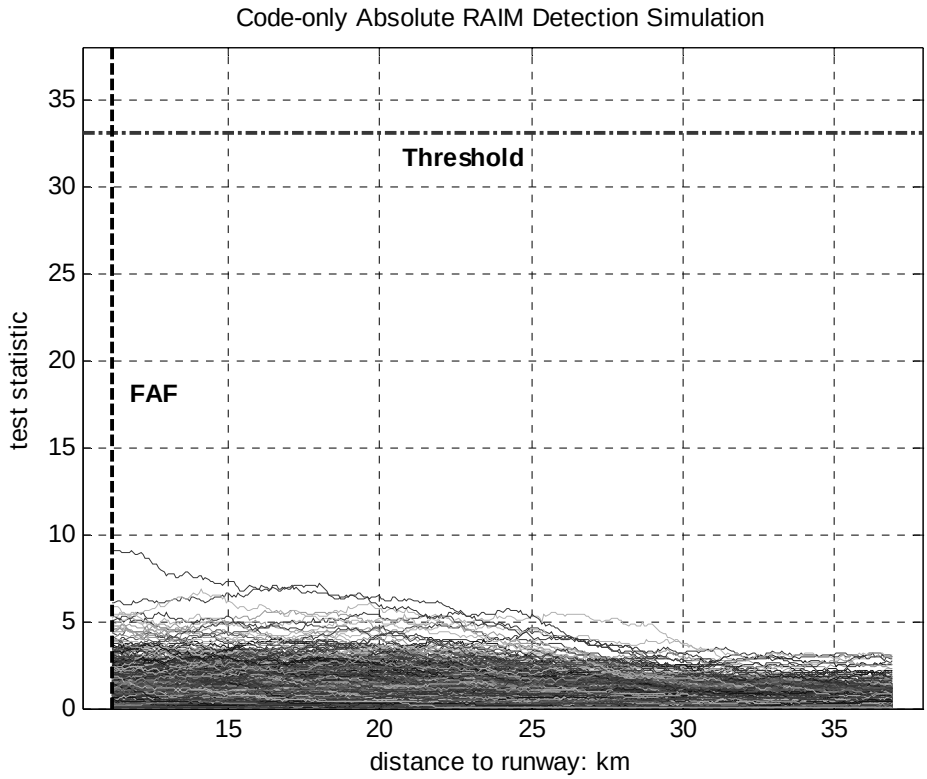

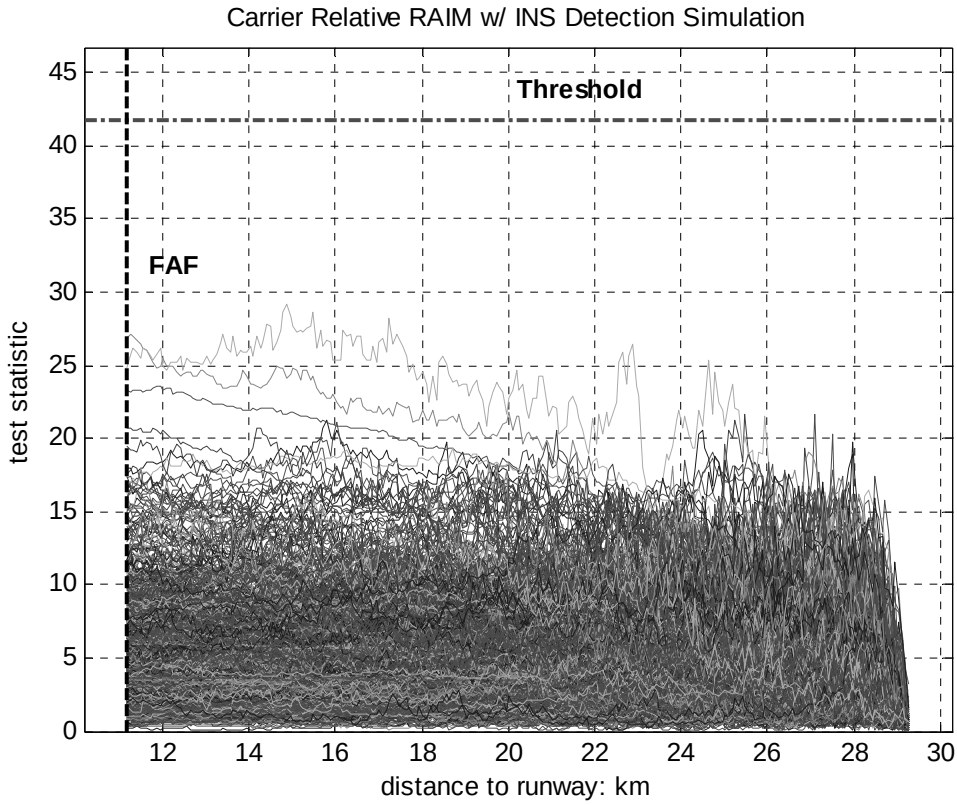

Figure D.15. 1000 Times Monte Carlo Simulation Results at ORD Airport for One Geometry (2)

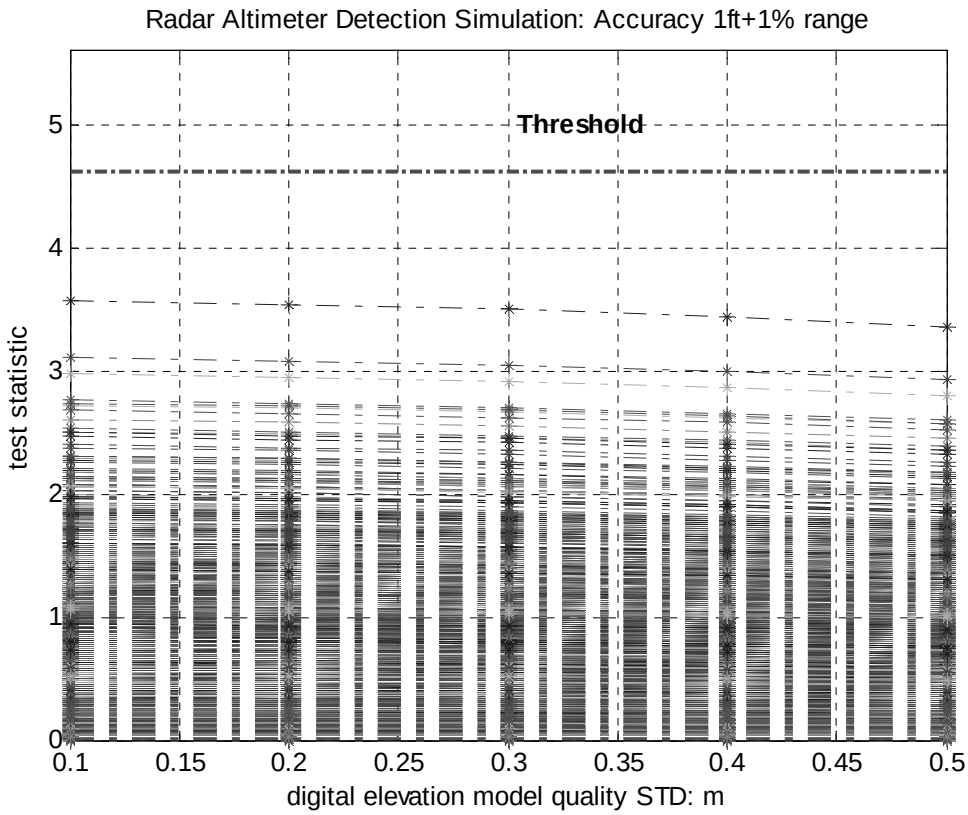

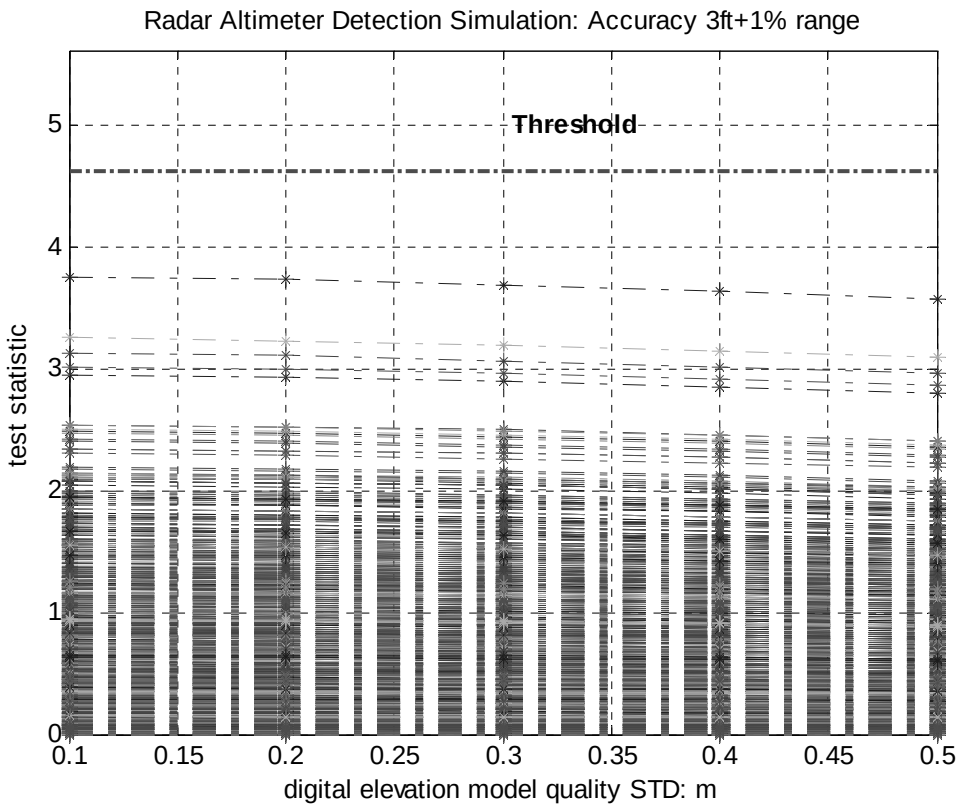

Figure D.16. 1000 Times Monte Carlo Simulation Results at ORD Airport for One Geometry (3)

BIBLIOGRAPHY

[Beser82] Beser, J., and B. Parkinson, "The Application of NAVSTAR Differential GPS in the Civilian Community." *NAVIGATION: Journal of the Institute of Navigation*. 29.2 (Summer 1982).

[Bocean99] Bocean, V., "Geodetic Determinations for the NuMI project at Fermilab." IWAA 1999, Grenoble, France (October 1999)

[Braff97] Braff, R., "Description of the FAA's Local Area Augmentation System (LAAS)." *NAVIGATION: Journal of the Institute of Navigation*. 44.4 (Winter 1997-98).

[Brenner99] Brenner, M., "Integrated GPS LAAS/Inertial Guidance System Using Multiple Kalman Filters." *Proceedings of the 12th International Technical Meeting of the Satellite Division of the Institute of Navigation*, ION GPS 1999, Nashville, TN (September 1999).

[Brown88] Brown, R. G. and P. W. McBurney, "Self-Contained GPS Integrity Check Using Maximum Solution Separation." *NAVIGATION: Journal of the Institute of Navigation*. 35.1 (Spring 1988).

[Brown92] Brown, R. G., "A Baseline RAIM Scheme and a Note on the Equivalence of Three RAIM Methods." *NAVIGATION: Journal of the Institute of Navigation*. 39.3 (Fall 1992).

[Brown01] Brown, A. and N. Gerein, "Test Results from a Digital P(Y) Code Beamsteering Receiver for Multipath Minimization," *Proceedings of the ION 57th Annual Meeting*, Albuquerque, NM (June 2001).

[Colby01] Colby, G. "JPALS Navy Program and Requirements Overview," Briefing to SRGPS Architecture Integrated Product Team (March 2001).

[Cohen96] Cohen, C. E., B. S. Pervan, H. S. Cobb, D. G. Lawrence, J. D. Powell and B. W. Parkinson, "Precision Landing of Aircraft Using Interity Beacons." *Global Positioning System: Theory and Applications* II.164, Chapter 15, American Institute of Aeronautics and Astronautics Inc., Washington (1996).

[Campbell01] Campbell, J. L. and M.U. de Haag, "Assessment of Radar Altimeter Performance When Used For Integrity Monitoring in A Synthetic Vision System." Digital Avionics Systems, DASC. The 20th Conference, 1 (Oct 2001): 2C3/1 - 2C3/9.

[Counselman79] Counselman, C., and I. Shapiro, "Miniature Interferometer Terminals for Earth Surveying." Bulletin Geodesique, 53.2 (1979): 139-163.

[Cox78] Cox, D. B., B. A. Kriegsman, W. M. Stonestreet, J. Kishel and L. V. Calicchia, "Feasibility Study of GPS-Inertial Navigation for Helicopters and Study of Advanced GPS Signal Processing Techniques." Draper Report R-981, Cambridge, MA (March 1978).

[Cox80] Cox, D. B., "Inertial Integration of GPS." *Global Position System* – Paper published in *Navigation: Institute of Navigation*, I, Alexandria, VA (1980).

[Cunningham88] Cunningham, J. R. and Z. H. Lewantowicz, "Dynamic Interaction of Separate INS/GPS Kalman Filters (Filter-driving - Filter dynamics)." *Proceedings of the Satellite Division's International Technical Meeting*, ION GPS' 88, Colorado Springs, CO (September 1988): 273-281.

[Davis93] Davis, J. M. and R. J. Kelly, "RNP Tunnel Concept for Precision Approach with GNSS Application." *Proceedings of the 49th Annual Meeting of the Institute of Navigation*, Cambridge, MA (June 1993).

[Diesel99] Diesel, J., D. Conners, and M. Talley, "Low Cost Dual-Use System for CAT I and CAT II Worldwide With Jam Resistance." *Proceedings of the 12th International Technical Meeting of the Satellite Division of the Institute of Navigation*, ION GPS 1999, Nashville, TN (September 1999).

[FAA-E-2937A] US DoT FAA, *Category I Local Area Augmentation System Ground Facility*. FAA-E-2937A, (April 2002).

[Farrell02] Farrell, J. L., "GPS/INS-Streamlined." *NAVIGATIION: Journal of Institute of Navigation*, 49.4 (Winter 2002-2003).

[Fathy99] Fathy, H. K., J. G. Thompson and P. J. Gorder, "Direct Determination of Aircraft Quaternion Parameters Using a Combined Inertial-GPS Instrumentation System." *Proceedings of the 12th International Technical Meeting of the Satellite Division of the Institute of Navigation*, ION GPS 1999, Nashville, TN (September 1999).

[Flood99] Flood, M. "Commercial Development of Airborne Laser Altimetry: A Review of the Commercial Instrument Market and its Projected Growth". *Proceedings of the ISPRS Workshop*, La Jolla, California (November 1999).

[Franklin97] Franklin, G. F., J. D. Powell and M. Workman, *Digital Control of Dynamic Systems*. 3rd edition, California: Addison-Wesley (1997).

[Gautier03] Gautier, J. D. "GPS/INS Generalized Evaluation Tool (GIGET) for the Design and Testing of Integrated Navigation Systems." Stanford University Ph.D. Dissertation, Department of Aeronautics and Astronautics, Stanford, California (June 2003).

[Gebre01] Gebre-Egziahber, D., "Design and Performance Analysis of a Low-Cost Aided Dead Reckoning Navigator." Stanford University Ph.D. Dissertation, Department of Aeronautics and Astronautics, Stanford, California (December 2001).

[Gebre03] Geber-Egziabher, D., A. Razavi, P. Enge, J. Gautier, D. M. Akos, S. Pullen and B. Pervan, "Doppler Aided Tracking Loops for SRGPS Integrity Monitoring." *Proceeding of ION GPS/GNSS 2003*, Portland, Oregon (September 2003).

[Goad74] Goad, C. C. and L. Goodman, "A Modified Hopfield Tropospheric Refraction Correction Model." *Proceedings of theFall Annual Meeting of the American Geophysical Union*, San Francisco, CA, (December 1974).

[GPSSPS] Department of Defense, *Global Positioning System Standard Positioning Service Performance Standard* (October 2001).

[Gregorius98] Gregorius, T. and G. Blewitt, "The Effect of Weather Fronts on GPS Measurements." *GPS World*, 9.5 (1998): 52-60.

[Gratton06] Gratton, L. and B. Pervan, "Carrier Phase Airborne and Ground Monitors for Ionospheric Front Detection for Category III LAAS." *Proceedings of ION GNSS 2006*.

[Greenspan96] Greenspan, R., "GPS and Inertial Integration." *The Global Positioning System: Theory and Applications*, II.163, Part IV, Chapter 7, AIAA Progress in Aeronautics and Astronautics, Washington, DC (1996).

[Grejner03] Grejner-Brzezinska, D. A., Y. Yi, C. Toth, R. Anderson, J. Davenport, D. Kopcha and R. Salman, "Enhanced Gravity Compensation for Improved Inertial Navigation Accuracy." *Proceedings of the 16th International Technical Meeting of the Satellite Division of the Institute of Navigation*, ION GPS/GNSS 2003, Portland, Oregon (September 2003).

[Hayward99] Hayward, R., A. Marchick and J. D. Powell, "Two Antenna GPS Attitude and Integer Ambiguity Resolution for Aircraft Applications." *Proceedings of the Institute of Navigation*, 1999 National Technical Meeting, San Diego, California (January 1999).

[Heo04] Heo, M., "Robust Carrier Phase DGPS Navigation For Shipboard Landing of Aircraft." Illinois Institute of Technology Ph.D. Dissertation, Department of Mechanical Material and Aerospace Engineering, Chicago, Illinois (December 2004).

[Heo06] Heo, M.-B. and B. Pervan, "Carrier Phase Navigation Architecture for Shipboard Relative GPS." *IEEE Transactions on Aerospace and Electronic Systems,* 42.2 (April 2006): 26-29.

[Hopfield69] Hopfield, H. S., "Two Quadratic Tropospheric Refractivity Profiles for Correcting Satellite Data." *Journal of Geophysical Research* 74.18 (1969): 4487-4499.

[Hou04] Hou, H., "Modeling Inertial Sensors Errors Using Allan Variance." University of Calgary Master Thesis, Department of Geomatics Engineering, Calgary, Alberta, Canada (September 2004).

[Huang06] Huang, J. and F. van Graas, "Comparison of Tropospheric Decorrelation Errors in the Presence of Severe Weather Conditions in Different Areas and Over Different Baseline Lengths," *Proceedings of ION GNSS 2006* (September 2006).

[IEEEstd97] IEEE Standard Specification Format Guide and Test Procedure, IEEE Std 952-1997 (1998).

[IONtutorial02] ION GPS-2002 Tutorial Course 501: Integration of GPS with Inertial Nav Systems, Portland, Oregeon (September 2002).

[Jekeli01] Jekeli, C., *Inertial Navigation Systems with Geodetic applications*, Berlin; New York, Walter de Gruyter (2001).

[Johnson90] Johnson, G. B. and Z. H. Lewantowicz, "Closed-Loop Operation of GPS Aided INS." *Proceedings of the 3rd International Technical Meeting of the Satellite Division of the Institute of Navigation,* ION GPS 1990, Colorado Springs, CO (September 1990).

[JPALS99] JPALS Test Planning Working Group, "Architecture and Requirements Definition: Test and Evaluation Master Plan for JPALS" (January 1999).

[Jung00] Jung, J., "High Integrity Carrier Phase Navigation Using Multiple Civil GPS Signals." Stanford University Ph.D. Dissertation, Department of Aeronautics and Astronautics, Stanford, California (August 2000).

[Kalafus86] Kalafus, R., A. J. Van Dierendonck, and N. Pealer, "Special Committee 104 Recommendations for Differential Service," *Global Positioning System*. III. Papers Published in *NAVIGATION*, Reprinted by the ION, Washington D. C. (1986).

[Kim04] Kim, U. S., D.S. De Lorenzo, D. Akos, J. Gautier, P. Enge and J. Orr, "Precise phase calibration of a controlled reception pattern GPS antenna for JPALS." *IEEE Position Location and Navigation Symposium, 2004.* PLANS 2004 (April 2004)

[Ko00] Ko, P.-Y. "GPS-Based Precision Approach and Landing Navigation: Emphasis on Inertial and Pseudolite Augmentation and Differential Ionosphere Effect." Stanford University Ph.D. Dissertation, Department of Aeronautics and Astronautics, Stanford, California (May 2000).

[Koenig02] Koenig, M., D. Gebre-Egziabher, S. Pullen, U.-S. Kim, B. Pervan, and F.-C. Chan, "Analysis of Reference Antenna Motion on the JPALS Shipboard Integrity Monitor," *Proceedings of ION National Technical Meeting,* Anaheim, CA (January 2002).

[LAASADD06] Avionics Engineering Center, Ohio University, "Algorithm Description Document (ADD) for Addressing the Troposphere in the Local Area Augmentation System," Athens, OH (August 2006).

[Landau92] Landau, H., C. Pagels and U. Vollath, "Development and Implementation of a Centimeter-Accurate Real-Time-Kinematic Positioning System." *Proceedings of the 8th International Technical Meeting of the Satellite Division of the Institute of Navigation*, ION GPS 1995, Palm Springs, CA (September 1995).

[Lawrence96] Lawrence, D. G., "Aircraft Landing Using GPS: Development and Evaluation of a Real Time System for Kinematic Position using the Global Positioning System." Stanford University Ph.D. Dissertation, Department of Aeronautics and Astronautics, Stanford, California (September 1996).

[Lawrence06] Lawrence, D., R. B. Langley, D. Kim, F. Chan and B. Pervan, "Decorrelation of Troposphere Across Short Baselines." *Proceedings of IEEE/ION Position Location and Navigation Symposium 2006*, San Diego, CA (April 2006).

[Lee99] Lee, Y. C. and D. G. O'Laughlin, "A Performance Analysis of a Tightly Coupled GPS/Inertial System for Two Integrity Monitoring Methods." *Proceedings of the 12th International Technical Meeting of the Satellite Division of the Institute of Navigation,* ION GPS 1999, Nashville, TN (September 1999).

[Lee05] Lee, Y. C., C. A. Shively and T. T. Hsiao, "Availability of LAAS to Calibrate IRS for CAT IIIB." *Proceedings of the 2005 National Technical Meeting of the Institute of Navigation*, San Diego, California (January 2005).

[Lee06] Lee, J., M. Luo, and S. Pullen, "Position-Domain Geometry Screening to Maximize LAAS Availability in the Presence of Ionosphere Anomalies." *Proceeding of ION GPS 2006,* Fort Worth, Texas (September 2006).

[Leick94] Leick, A., *GPS Satellite Surveying*, 2nd edition, New York: John Wiley & Sons, Inc. (1994).

[Lorga03] Lorga, J. F. M., Q. P. Chu and J. A. Mulder, "Tightly-Coupled IMU/GPS Carrier-Phase Navigation System." *Proceedings of the Institute of Navigation,* 2003 National Technical Meeting, Anaheim, California (January 2003): 385-396.

[Luo04] Luo, M., S. Pullen, A. Ene, D. Qiu, T. Walter, and P. Enge, "Ionosphere Threat to LAAS: Updated Model, User Impact and Mitigations." *Proceeding of ION GNSS 2004*, Long beach, California (September 2004).

[MacDoran79] MacDoran, P., "Satellite Emission Radio Interferometric Earth Surveying (SERIES) GPS Geodetic System." Bulletin Geodesique, 53.2 (1979): 117-138.

[Marti02] Marti, U., "Efforts in predicting the local gravity field." Paper presented at the EGS XXVI General Assembly 2001, Nice, France. IGeS Bulletin.

[McGraw00] McGraw, G., T. Murphy, M. Brenner, S. Pullen and A. J. Van Dierendonck, "Development of the LAAS Accuracy Models," *Proceedings of ION GPS-2000*, Salt Lake City, UT (September 2000).

[Misra01] Misra, P., and P. Enge, *Global Positioning System: Signals, Measurements, and Performance*. Ganga-Jamuna Press (2001).

[Moafipoor04] Moafipoor, S., D. G. Brzezinska and C. K. Toth, "Tightly Coupled GPS/INS/CCD Integration Based on GPS Carrier Phase Velocity Update." *Proceedings of the 2004 National Technical Meeting of the Institute of Navigation*, San Diego, California (January 2004).

[O'Connor96] O'Connor, M., G. Elkaim, and B. Parkinson, "Carrier-Phase DGPS for Closed-Loop Control of Farm and Construction Vehicles." *NAVIGATION: Journal of the Institute of Navigation*. 43.2 (Summer 1996).

[Paielli93] Paielli, R., B. McNally, R. Bach, and D. Warner, "Carrier Phase Differential GPS for Approach and Landing: Algorithms and Preliminary Results," *Proceedings of 6th International Technical Meeting of the Satellite Division of the Institute of Navigation*, Salt Lake City, Utah (September 1993).

[Pervan94] Pervan, B. S., C. E. Cohen and B. W. Parkinson, "Integrity in Cycle Ambiguity Resolution for GPS-Based Precision Landing." *Third International Conference on Differential Satellite Navigation Systems* DSNS-94, London, UK (April 1994).

[Pervan96a] Pervan, B. S., "Navigation Integrity for Aircraft Precision Landing Using the Global Positioning System." Stanford University Ph.D. Dissertation, Department of Aeronautics and Astronautics, Stanford, California (March 1996).

[Pervan96b] Pervan, B. S., C. E. Cohen and B. W. Parkinson, "Parity Space Methods for Autonomous Fault Detection and Exclusion using GPS Carrier Phase." *IEEE Position Location and Navigation Symposium,* PLANS 1996, Atlanta, GA (April 1996).

[Pervan98] Pervan, B.S., D.G. Lawrence and B.W. Parkinson, "Autonomous Fault Detection and Removal using GPS Carrier Phase." *IEEE Transactions on Aerospace and Electronic Systems,* 34.3 (July 1998): 897-906.

[Pervan03] Pervan, B. S. F.-C. Chan, D. Gebre-Egziabher, S. Pullen, P. Enge and G. Colby, "Performance Analysis of Carrier-Phase DGPS Navigation for Shipboard Landing of Aircraft." *NAVIGATIION: Journal of Institute of Navigation*, 50.3 (Fall 2003).

[Remondi85] Remondi, B., "Performing Centimeter-level Surveys in Seconds with GPS Carrier Phase: Initial Results." *NAVIGATION: Journal of the Institute of Navigation*, 32.4 (Winter 1985-86).

[Romrell95] Romrell, G., R. Brown, G. Johnson, and D. Kaufman, "FAA/FEDSIM̧E-Systems Cat IIIB Feasibility Demonstration Flight Test Preliminary Results." *Proceedings of 8th International Technical Meeting of the Satellite Division of the Institute of Navigation*, Palm Springs, CA (September 1995).

[RTCA/DO229D] RTCA Special Committee 159 Working Group 2, "Minimum Operational Performance Standards for Global Positioning System / Wide Area Augmentation System Airborne Equipment," RTCA Document Number DO-229D (December 2006).

[RTCA/DO245A] RTCA Special Committee 159, "Minimum Aviation System Performance Standards for The Local Area Augmentation System." RTCA Document Number DO-245A (December 2004).

[RTCA/DO246C] RTCA Special Committee 159, "GNSS Based Precision Approach Local Area Augmentation System (LAAS) – Signal-in-Space Interface Control Document (ICD)." RTCA Document Number DO-246C (April 2005).

[RTCA/DO253B] RTCA SC-159, "Minimum Operational Performance Standards for GPS Local Area Augmentation System Airborne Equipment." RTCA Document Number DO-253B (June 2007).

[Scherzinger00] Scherzinger, B. M., "Precise Robust Positioning with Inertial/GPS RTK," *Proceedings of 13th International Technical Meeting of the Satellite Division of the Institute of Navigation*, ION GPS 2001, Salt Lake City, UT (September 2000).

[Stockwell] Stockwell, W., "Angle Random Walk," Application Notes, Crossbow Technology, Inc.

[Soloviev04] Soloview, A., F. van Graas and S. Gunawardena, "Implementation of Deeply Integrated GPS/Low-Cost IMU for Acquisition and Tracking of Low CNR GPS Signals.", *Proceeding of ION GPS 2004*, Long beach, California (September 2004).

[SpilkerJr96a] Spilker Jr.,J. J., "GPS Navigation Data.", *Global Positioning System: Theory and Applications,* I.163, Part I, Chapter 4, American Institute of Aeronautics and Astronautics Inc., Washington (1996).

[SpilkerJr96b] Spilker Jr.,J. J., "Tropospheric Effects on GPS.", *Global Positioning System: Theory and Applications,* I.163, Part II, Chapter 13, American Institute of Aeronautics and Astronautics Inc., Washington (1996).

[Teasley80] Teasley, S., W. Hoover, and C. Johnson, "Differential GPS Navigation." *Proceedings of the IEEE Position, Navigation, and Location Symposium*, PLANS 1980, Atlantic City, New Jersey (December 1980).

[Tome99] Tomé, P., T. Cunha, S. Cunha and L. Bastos, "Integrating Multiple GPS Receivers With A Low Cost IMU For Aircraft Attitude Determination." *Proceedings of the 1999 National Technical Meeting of the Institute of Navigation*, San Diego, CA (January 1999).

[Teunissen98] Teunissen, P., D. Odijk and P. Joosten, "A Probabilistic Evaluation of Correct GPS Ambiguity Resolution." *Proceedings of 11th International Technical Meeting of the Satellite Division of the Institute of Navigation*, Nashville, TN (September 1998).

[Titterton04] Titterton, D., *Strapdown Inertial Navigation Technology*, John L.. Weston Published (2004).

[USAF002] *Operational Requirements Document (ORD) for Joint Precision Approach and Landing System (JPALS)*, USAF 002-94-I.

[vanGraas93] van Graas, F., D. Diggle, R. Hueschen, "Interferometric GPS Flight Reference/Autoland System." *Proceedings of 6th International Technical Meeting of the Satellite Division of the Institute of Navigation*, Salt Lake City, Utah (September 1993).

[vanGraas95a] van Graas, F. and S.-W. Lee, "High-Accuracy Differential Positioning for Satellite-Based Systems Without Using Code-Phase Measurements." *Proceedings of the ION National Technical Meeting*, Anaheim, CA (January 1995).

[vanGraas95b] van Graas, F. D. Diggle, M. U. de Haag, V. Wullschleger, R. Velez, D. Lamb, M. Dimeo, G. Kuehl and R. Hilb, "FAA/Ohio University United Parcel Service DGPS Autoland Flight Test Demonstration." *Proceedings of the 8th International Technical Meeting of the Satellite Division of the Institute of Navigation*, ION GPS 1995, Palm Springs, CA (September 1995).

[Volpe01] "Vulnerability Assessment of the Transportation Infrastructure Relying on the Global Positioning System." Final Report produced by the Volpe Center for the Office of the Secretary of Transportation (August 2001).

[Wallac01] K. Wallace, *Personal Communication* (August 2001).

[Warburton98] Walberton, J. and D. Lamb, "Validation of the FAA LAAS Specification Using the LAAS Test Prototype." *Proceedings of the 11th International Technical Meeting of the Satellite Division of the Institute of Navigation,* ION GPS 1998, Nashville, TN (September 1998).

[Waters01] Waters, J., P. Sousa, L. Wellons, G. Colby and J. Weir, "Test Results of an F/A-18 Automatic Carrier Landing Using Shipboard Relative GPS," *Proceedings of the ION 57th Annual Meeting*, Albuquerque, NM (June 2001).

[Yang01] Yang, Y. and J. A. Farrell, "Fast Ambiguity Resolution for GPS/IMU Attitude Determination." *Proceedings of the 14th International Technical Meeting of the Satellite Division of the Institute of Navigation*, ION GPS 2001, Salt Lake City, UT (September 2001).